THE UNIVERSITY *of* EDINBURGH

Cosmology with Underdensities of the Cosmic Web

Vasiliy Grigoriyvich Demchenko

Doctor of Philosophy
The University of Edinburgh
May 2019

Declaration

I declare that this thesis was composed by myself, that the work contained herein is my own except where explicitly stated otherwise in the text, and that this work has not been submitted for any other degree or professional qualification except as specified.

Parts of this work have been published in Demchenko et al. (2016),Brouwer et al. (2018).

(*Vasiliy Grigoriyvich Demchenko, May 2019*)

Lay Summary

Observations of our Universe have provided some outstanding revelations. One of the biggest discoveries at the turn of the millennium was that the Universe is expanding at an accelerated rate. This is a very odd discovery since we know that gravity should coalesce matter, causing the Universe to decelerate. This suggests that a previously unknown component pervades the cosmos inducing the accelerated expansion: the so-called 'dark energy.' Another interpretation arises by considering that the laws of gravity, as we know them, are insufficient, requiring a modification: known as 'modified gravity.' We believe that the Universe is composed of $\simeq$ 5% visible matter, $\simeq$ 25% 'dark matter,' and $\simeq$ 70% of dark energy. One model to explain an accelerating universe with such parameters is known as the ΛCDM model, where 'Λ' represents the dark energy and 'CDM' stands for cold (non-relativistic) dark matter. We have yet to observe or determine the nature of dark matter and dark energy, but we can measure their effects upon the visible matter. Through these observations we can test the foundations of the ΛCDM model and compare it to other models, such as modified gravity or dark energy theories.

Looking at the Universe as a whole, we find that the large-scale structure of the Universe resembles a web-like pattern with dense clusters, elongated filaments, and relatively empty voids. The majority of cosmological studies have focused on the matter that we can directly observe, such as galaxy clusters and filaments, however as our telescopes probe larger volumes of space, the 'empty' void regions begin to emerge as useful cosmological objects to investigate. The dynamics of expansion are governed by two things: matter and dark energy. Since voids are objects that contain less matter than the Universe on average, we can unravel the nature of dark energy by studying the evolutionary dynamics of voids. Furthermore, due to their underdense nature, voids present themselves as prime candidates to test theories of modified gravity. Within compact, gravity-dominated regions, such as our Solar System, we know that the fundamental theory of gravity behaves in accordance with General Relativity. Therefore, regardless of the amount of deviation from General Relativity, any theory of modified gravity must resemble General Relativity in overdense regions. This suggests that any viable theories of modified gravity will exhibit so-called 'screening mechanisms' that gradually mask any deviations from General Relativity on progressively denser scales. We can thus infer that any deviations from General Relativity will be most pronounced in the largest, most underdense

regions of our Universe. Therefore, we can use theoretical predictions of the evolved void density and compare them to the observed void density, deciphering the underlying laws of gravity and dark energy. Consequently, since the evolution of voids is intrinsically linked to the distribution and growth rate of the large-scale structure of the Universe, measurements of this distribution and growth rate will depend on the characteristics of any dark energy or modified gravity model.

This thesis focuses on understanding how we can exploit voids as probes for cosmology. In particular, it explores how we can improve the modelling of void evolution by extending it to the non-linear regime, and applying this model to extract the growth rate of structure. One of the main tools for this is 'weak gravitational lensing,' which is a phenomenon that arises as light traverses through space and interacts with matter. Through these interactions, the original, source images of galaxies become distorted by the time they reach our telescopes. Studying these distortions in a statistical manner can shed light upon the intervening matter between us and the observed galaxy. As explored towards the end of this thesis, combining this lensing signal with projected underdensities can enhance our capability to uncover the underlying cosmological parameters of our Universe.

This thesis begins with an introductory chapter that discusses cosmology as a whole, followed by a chapter overviewing the principles of gravitational lensing. The third chapter presents a model for void evolution and applies it to predicting the non-linear signal of redshift-space distortions around voids, which arise due to inhomogeneous motions of galaxies. The fourth chapter explores how to extract a crucial ingredient for this model, namely the late-time void density profile, through the weak gravitational lensing approach. The measurement of the void weak lensing signal is explored through the SLICS cosmological N-body simulations and through observational data from the KiDS and GAMA surveys. The final science chapter focuses on optimising this weak lensing signal with the use of projected, underdense apertures, extending this approach to include apertures within the full density spectrum, known as Density Split Statistics. The effectiveness of this Density Split Statistics approach to constrain cosmological parameters is then tested on *cosmo*-SLICS, which are cosmological N-body simulations constructed to mimic various theories of dark energy.

Abstract

This thesis explores the utilisation of underdense regions of the Cosmic Web as a tool for studying cosmology. Underdensities, known as cosmic voids, provide a complementary approach for understanding the large-scale structure of our Universe, as well as providing a unique environment to explore the effects of dark energy. An application of the spherical model to void evolution is presented, showcasing its ability to provide non-linear density and velocity profiles for voids. This methodology is then applied in order to reconstruct the initial conditions of the void using a late-time void density profile. Using this reconstruction, the spherical model yields non-linear late-time velocity profiles which are used to predict redshift-space distortions around voids, showing the capacity to constrain cosmological parameters using measurements in the non-linear regime. Furthermore, this thesis investigates how cosmologists can utilise the advances of weak gravitational lensing to exploit the underdensities of the Universe. A study of the weak lensing measurement around voids is presented with a focus on the SLICS simulation suite and the KiDS and GAMA surveys. A watershed void finding algorithm, ZOBOV, is applied to both the simulations and data, showing that the geometry of the GAMA survey does not lend well to extracting a weak lensing signal from voids due to limitations from both the survey volume and geometry. In contrast, projected underdensities, known as troughs, and the full, projected density spectrum, known as Density Split Statistics, are both shown to yield great potential as cosmological tools. The final chapter of this thesis investigates the use of this novel approach to explore non-ΛCDM cosmologies using the *cosmo*-SLICS simulations, showing how underdensities can potentially constrain the equation-of-state of dark energy with a higher precision than overdense regions. Chapter 1 of this thesis provides a brief overview of cosmology, while Chapter 2 introduces the theory of weak gravitational lensing. Chapter 3 discusses the spherical model applied to void evolution and redshift-space distortions around voids, while Chapter 4 explores the weak gravitational lensing signal around voids in simulations and data. Chapter 5 utilises a suite of simulations to investigate the sensitivity of Density Split Statistics to dark energy models.

Acknowledgements

I would first and foremost like to extend my gratitude to my supervisors, Yan-Chuan Cai and Catherine Heymans. Their sincere enthusiasm for my work, genuine compassion, interest in my well-being, and seemingly endless patience made my Ph.D. experience something I will recall with fondness and a smile upon my face. I'd also like to thank my Ph.D. pals at the IfA for all the merriment we've shared. In particular, I would like to thank Johanna Vos, Tom Kemp (and his wonderful family), Alex Amon, Clémence Fontanive, and Ben Giblin for their friendship and support. Edinburgh, as a whole, is a city filled with wonderful, caring communities. My time here was significantly enhanced by the yoga community (especially the amazing MUDRA Yoga community created by Demelza Feltham and Helen Gillespie), the meditation community that Mark Miller started, and the speciality coffee scene, which is filled not only with delicious artisan coffees, but with outstandingly friendly baristas.

Last but certainly not least, I'd like to thank my family. My grandparents played a crucial role in making my education a relatively smooth process, supporting me both morally and financially. And, of course, none of this thesis would've been written without my parents: the wondrous Yelena and Grigoriy Demchenko. Throughout my life, they have relentlessly fuelled my interests and supported me in all of my academic and non-academic endeavours with joy and excitement. They've made significant sacrifices throughout their lives, often at the expense of their own well-being, solely to provide the best opportunities for my happiness and success. In particular, my mother has been extremely influential in my academic path from teaching me the multiplication tables to introducing me to quantum physics. The effect she's had on my life outside of academia would require a whole thesis in and of itself. No amount of words would suffice to express my deepest gratitude and love towards my parents, so I will simply end this section by dedicating this thesis to Yelena and Grigoriy Demchenko.

Contents

List of Figures

List of Tables

Nothing in life is to be feared, it is only to be understood. Now is the time to understand more, so that we may fear less.

Marie Curie

1

Introduction to Cosmology

Cosmology is defined as the study of the origin and evolution of the Universe. Countless cultures over the history of humanity have contemplated the creation of the Universe and there is no shortage of theories regarding its creation. Although some of these theories may sound fantastical (if not comical) in the present day, the curiosity and wonder of previous civilisations lives on. We live in a particularly remarkable time where we finally have the technological prowess to put our theories of the Universe through rigorous, scientific tests.

In this chapter, I present an overview of the current state of cosmology, providing relevant equations and foundational principles. I will discuss key topics of cosmology before narrowing into finer details of the present-day large-scale structure pertaining to the core of this thesis.

Throughout this thesis, the pronouns 'we' and 'I' will both be used. 'We' will be reserved for published work and discussions regarding the cosmology community as a whole, while 'I' will be used for unpublished work. I feel that this presents the most accurate depiction of not only the work done in this thesis, but the scientific community as a whole.

1.1 The Basics

Imagine that you have found yourself sitting in a dinghy in the middle of a calm, expansive ocean. In whichever direction you look, you find a uniform, featureless ocean stretching out to the horizon. However, your acute wisdom tells you that your perceptions may be slightly illusory since you feel an ever-gentle rocking of

your dinghy. You shift your focus to a patch of water directly outside your boat finding that the seemingly uniform and featureless ocean consists of small waves behaving in a chaotic way as they lightly hit your vessel.

In this regard, our Universe is not too dissimilar from the ocean. Viewing the Universe on sufficiently large scales (several hundreds of Mpc) we find it to be relatively smooth and featureless, with gravity as the only relevant force. This idea of homogeneity and isotropy constitutes the crux of our understanding of cosmology. However, were it not for the seemingly random, chaotic, and ubiquitous features on small scales, neither you, nor me, nor even the Universe as we currently know it would exist. Einstein's Theory of General Relativity (1916) allows us to understand the evolution of isotropic, homogeneous matter by considering a finite speed of light in a much more robust way than allowed for by Newtonian dynamics. Furthermore, Einstein proposed the idea of a universe curved in a non-trivial way depending on its energy density. His famous Gravitational Field Equations[1] relate the curvature of space-time to the energy density:

$$R_{\mu\nu} - \frac{1}{2}Rg_{\mu\nu} = -\frac{8\pi G}{c^4}T_{\mu\nu}. \tag{1.1}$$

These equations are in a tensorial form and are invariant under any general coordinate transformation. The Ricci tensor, $R_{\mu\nu}$, and the Ricci scalar, R, encode derivatives of the metric tensor, $g_{\mu\nu}$, with respect to the coordinates. This metric tensor plays a central role in curved space-time geometries and provides a way to compute an effective distance in a curved space-time. The stress-energy tensor, $T_{\mu\nu}$, contains all the information about the energy density distribution within the space-time. These field equations are highly non-linear and analytic solutions only exist for some symmetric cases, with no general solution yet discovered.

Using the approximations of homogeneity and isotropy in conjunction with spherical symmetry, the metric tensor can be written as[2]:

$$ds^2 = g_{\mu\nu}dx^\mu dx^\nu = c^2dt^2 - R^2(t)[dr^2 + S_k(r)^2(d\theta^2 + \sin^2\theta d\phi^2)]. \tag{1.2}$$

In the above equation, $R(t)$, represents the scale factor, which measures how individual locations in the Universe evolve away from each other in time, t, and is independent of position due to homogeneity. This time coordinate is the proper time of an observer in free-fall, or equivalently one at rest with respect to their local matter distribution. One can also consider it as the time elapsed on clocks for which the cosmic microwave background is isotropic. The spatial coordinates

[1] Upon realising his 'biggest blunder' (Gamow, 1956), Einstein added a factor of $\Lambda g_{\mu\nu}$ to the left hand side of this equation to make sure that the solution was static. Nowadays we know this blunder as the cosmological constant (see Section 1.4).

[2] Although this metric arises from General Relativity, a neat geometrical derivation exists as well (see Longair, 2008, for a detailed example).

r, θ and ϕ are the standard spherical coordinates, where the radial coordinate, r, is chosen to be a dimensionless comoving coordinate, meaning it is synced with the expansion of the Universe. This implies that observers moving with the expansion do not change their location along the r coordinate. In order to obtain a physical (also known as proper) distance between events at time t, one multiplies the comoving coordinate by the scale factor, *i.e.* $R(t)r$. The function S_k depends on the curvature of the Universe and is given by:

$$S_k = \begin{cases} \sin r, & k = 1 \,(\text{closed}) \\ r, & k = 0 \,(\text{flat}) \\ \sinh r, & k = -1 \,(\text{open}) \end{cases} \tag{1.3}$$

with k and R related via the Friedmann Equation,

$$\left(\frac{\dot{R}}{R}\right)^2 \equiv H^2 = \frac{8\pi G}{3} \sum_i \rho_i(R) - \frac{kc^2}{R^2}, \tag{1.4}$$

where the summation occurs over all the energy-density components, ρ, of the Universe, H is the Hubble constant, G is the Newtonian gravitational constant, and c is the speed of light. The metric configuration of Eq. 1.2, known as the Friedmann-Lemaître-Robertson-Walker (FLRW) metric (Friedmann, 1922; Lemaître, 1927), is the foundation of modern cosmology. In fact, Eq. 1.4 is the solution to Eq. 1.1 with the Friedmann metric (Eq. 1.2) and a stress-energy tensor for a perfect fluid (*i.e.* a diagonal stress-energy tensor). One can view the Friedmann Equation as an energy equation: the left hand side is the kinetic energy of the expansion of the Universe, while the first term on the right hand side is the potential energy and the second term is the constant total energy in the form of curvature. This suggests that curvature (or total energy) is determined by the rest of the terms. Defining the matter content and rate of expansion of a particular universe, directly sets its energy content. This can be understood through the relation of the curvature constant, k, and the scale factor evaluated at the present time, R_0,

$$k = R_0^2 \left(\frac{8\pi G \rho_0}{3} - H_0^2 \right), \tag{1.5}$$

where H_0 is the present-day Hubble constant and ρ_0 is the present-day energy density. Although, Eq. 1.3 states that k can only take three values, by changing R_0 the energy term can vary continuously. One can see from Eq. 1.5 that for a spatially flat universe where $k = 0$, R_0 becomes undefined. Conventionally,

cosmologists redefine R_0 as a dimensionless scale factor,

$$a \equiv \frac{R(t)}{R_0}, \tag{1.6}$$

such that $a = 1$ at the present day. This allows R_0 to remain defined as the curvature scale beyond which the non-trivial geometry of space-time becomes important.

In the classic paradigm of cosmology, we consider the Universe as composed of three essential components: matter, radiation, and dark energy. These components affect the energy density of the Universe in different ways. The conservation of the stress-energy tensor, $\nabla_\mu T^{\mu\nu} = 0$, determines the behaviour of these individual components via the continuity equation,

$$\dot{\rho}_i + 3H(\rho_i + p_i/c^2) = 0, \tag{1.7}$$

where the subscript i denotes each component and p is the pressure. In order to solve the continuity equation, one needs to know the equation-of-state for each species. For the three components considered here, $p = 0$ for (cold) matter, $p = \rho/3$ for radiation, and $p = -\rho$ for dark energy. Based on the conservation of particles, as the Universe expands the density of matter changes as $\rho_\mathrm{m} \propto a^{-3}$, using the same reasoning and taking into account the relativistic nature of radiation, the radiation density changes as $\rho_\mathrm{r} \propto a^{-4}$, while dark energy maintains a constant energy density with $\rho_\Lambda = \text{constant}$[3]. This means that each component's effect on the Universe changes as the it evolves with time. For example, we see that the radiation energy density becomes diluted more quickly than matter, thus playing a less significant role in the dynamics of the Universe as time moves forward.

Given these components we can rewrite the Friedmann Equation as,

$$\left(\frac{\dot{a}}{a}\right)^2 \equiv H^2 = \frac{8\pi G}{3}\left(\frac{\rho_{\mathrm{m},0}}{a^3} + \frac{\rho_{\mathrm{r},0}}{a^4} + \rho_\Lambda\right) - \frac{k_0}{R_0 a^2}, \tag{1.8}$$

where the '0' subscript refers to the present-day value of the parameter. Furthermore, we can define dimensionless density parameters as,

$$\Omega_i(a) = \frac{8\pi G}{3H^2}\rho_i(a), \tag{1.9}$$

[3]Throughout this chapter I adopt the common assumption that the cosmological constant, Λ, is equivalent to dark energy and is the cause of expansion.

arriving at a succinct form of the Friedmann Equation,

$$\left(\frac{\dot{a}}{a}\right)^2 = H_0^2\left(\frac{\Omega_{\mathrm{m},0}}{a^3} + \frac{\Omega_{\mathrm{r},0}}{a^4} + \Omega_\Lambda + \frac{1-\Omega}{a^2}\right), \tag{1.10}$$

where $\Omega = \Omega_\mathrm{m} + \Omega_\mathrm{r} + \Omega_\Lambda$ and should include any other species considered relevant *i.e.* neutrinos.

1.2 Cosmological Redshift

Consider a galaxy located at some distance from an observer on Earth. Imagine that we measure a signal from a uniform, pulsing source located within that galaxy. Since we know that space and time are fundamentally coupled, we realise that this spatially distant signal is also a signal from the 'past' time-wise. Since we know that the Universe is expanding, we could ask ourselves how, if at all, does this expansion affect the spectral properties of the emitted signal. For this we refer back to the FLRW metric in Eq. 1.2. Since photons follow null geodesics, considering a radial ray of light, we can write the metric as,

$$0 = ds^2 = c^2dt^2 - R^2(t)dr^2. \tag{1.11}$$

We can solve for the radial distance traversed by a light ray emitted at time t_e and observed at time $t_\mathcal{O}$,

$$r = \int_{t_e}^{t_\mathcal{O}} \frac{c\,dt}{R(t)}. \tag{1.12}$$

This is the comoving radial distance between an observer and an emitter. Since we know that the comoving distance doesn't change, this expression is also valid at a later time:

$$r = \int_{t_e+\delta t_e}^{t_\mathcal{O}+\delta t_\mathcal{O}} \frac{c\,dt}{R(t)}, \tag{1.13}$$

and assuming that $\delta t_{e,\mathcal{O}}$ is short enough that $R(t)$ is almost constant over that time frame, we can equate the two equations above such that,

$$\delta t_e R(t_e) = \delta t_\mathcal{O} R(t_\mathcal{O}). \tag{1.14}$$

Defining cosmological redshift as the amount a particular wavelength has changed over time, we can write $1 + z \equiv \delta t_\mathcal{O}/\delta t_e$ and relate this to the ratio of the scale

factors at the emitted and observed times. Expressing this at the present time, cosmologists define redshift, z, as,

$$\frac{R_0}{R(t)} \equiv \frac{1}{a} = 1 + z. \tag{1.15}$$

Since redshift is directly observable and model independent, it is most convenient for cosmologists to use a or z for distances rather than a comoving coordinate from the metric.

1.3 Cosmological Distances

Now that we have a definition of redshift, we can rewrite the comoving distance between two cosmological events from Eq. 1.12 as,

$$r = \int \frac{cdt}{R(t)} = \frac{1}{R_0} \int \frac{cda}{a^2 H(a)} = \frac{1}{R_0} \int \frac{cdz}{H(z)}, \tag{1.16}$$

where the limits of the integral will depend on the desired quantity. For example, the finite speed of light creates horizons in cosmology. Assuming the Universe had a finite beginning (*i.e.* a big bang), then light must have travelled a limited distance set by the current age of the Universe. This means any observers beyond that distance are not in causal contact. The particle horizon is defined as the maximum distance light particles can have travelled since $R = 0$, thus is only valid for big bang cosmologies and is defined as:

$$R_0 r_p(z) = \int_0^t \frac{cdt}{R(t)} = \int_z^\infty \frac{cdz}{H(z)}. \tag{1.17}$$

Conversely, we can compute the event horizon, which represents the maximum comoving distance that light can travel, as:

$$R_0 r_p(z) = \int_{t_0}^\infty \frac{c\,dt}{R(t)} = \int_{-1}^0 \frac{c\,dz}{H(z)}. \tag{1.18}$$

Eq. 1.18 may or may not be finite depending on the cosmological model. For instance, in big crunch scenarios, one should replace $t = \infty$ with $t = t_{\rm crunch}$ since those universes have a finite age.

As mentioned before, $R_0 r$ is referred to as the 'physical[4]' distance, but cosmologists also define two other important distance measures: angular diameter

[4]This is somewhat of a slippery slope in the language of General Relativity. Seemingly equivalent ways to measure an 'absolute' distance may yield differing results due to the curvature

distance and luminosity distance. The angular diameter distance, $D_{\rm A}$, refers to the distance to an object of a known physical extent, l, which subtends an angle $\delta\theta$ on the sky,

$$D_{\rm A} = \frac{l}{\delta\theta} = \frac{R_0 S_k(r)}{1+z}. \tag{1.19}$$

The luminosity distance is defined as the distance that satisfies the bolometric flux - luminosity relation,

$$F = \frac{L}{4\pi D_{\rm L}^2}, \tag{1.20}$$

and can be computed from the metric in Eq. 1.2 as,

$$D_{\rm L} = (1+z) R_0 S_k(r). \tag{1.21}$$

Generally, the luminosity distance will be greater than the angular diameter distance, $D_{\rm L}/D_{\rm A} = (1+z)^2$, which is independent of cosmology. The consequences of this is that objects appear dimmer and larger[5] due to the expansion of the Universe. One can understand the increase in angular size by considering the effect of gravitational lensing due to the curvature of space-time; it's as if we observe the Universe through a massive fish-eye lens. The dimming arises due to five effects on the flux of the photons:

- From the observer's frame of reference, photons at the source pass through a sphere of proper surface area $4\pi[R_0 S_k(r)]$.
- Photon energies are redshifted, reducing the flux energy density by $(1+z)$.
- Photons arrival times are time dilated causing another reduction of $(1+z)$.
- In opposition, the bandwidth $d\nu$ is reduced by $(1+z)$, causing an increase in the flux energy density per unit bandwidth by that factor.
- A photon's observed frequency ν_0 was emitted at a frequency of $(1+z)\nu_0$.

Thus, we find that the flux density emitted by an object appears as a dimmed luminosity to the observer. Both $D_{\rm A}$ and $D_{\rm L}$ constitute useful quantities in cosmology since they are observable and can help us to unravel the fundamental cosmology of our Universe.

of space-time, thus it's safer to refer to coordinates, rather than distances, in the realm of General Relativity.

[5]Technically, this only holds true if $\Omega_{\rm m} = 0$ with a flat or open universe. If $\Omega_{\rm m} \neq 0$, then the distance-redshift relation is not monotonic and peaks at $z \simeq 1$.

1.4 Observations and the ΛCDM Model

Although the previous sections describe a general homogeneous, isotropic universe, cosmological observations suggest that we live in a universe with a particular set of parameters. The current observations of our Universe can be successfully described in the context of the ΛCDM model, often referred to as the standard or concordance model of cosmology.

The beginnings of this model manifested approximately 100 years ago when Slipher (1917) first noticed the recessional velocity of galaxies and Hubble (1929) presented a linear relation between their recessional velocity and distance. The assumptions made in the Friedmann metric (Eq. 1.2) predicts this type of behaviour such that,

$$v = H_0 x, \tag{1.22}$$

where v represents the recessional velocity, x is the distance, and H_0 is the present day value of the Hubble parameter known as the Hubble constant (which is not actually a constant since it changes with time. Please see a later footnote in Section 1.5 for a thorough rant on misnomers in astronomy). A precise and accurate measurement of the Hubble constant is an important task for cosmologists since it affects the outcomes of cosmological observations. In most cases, cosmologists tend to employ the dimensionless Hubble parameter, h, such that $H_0 = 100\,h\,\mathrm{km\,s^{-1}\,Mpc^{-1}}$.

As mentioned at the end of Section 1.3, distance measurements play a vital role in cosmology. A variety of methods exist to measure distances to an object, however techniques applicable to distance measurements in the local universe do not typically apply to the distant universe. This leads us to the creation of what's known as the distance ladder. For example, we can use Cepheid variable stars to accurately measure the distance to the nearest few galaxies. Cepheids are highly luminous, variable stars that exhibit a well defined correlation between their luminosity and the period of their pulsation. Hubble (1929) used these particular types of stars to show that the Universe is expanding. Using these Cepheids, the distance to the Large Megellanic Cloud (LMC) has been measured to an accuracy of $\sim 10\%$ (e.g. Majaess et al., 2009), securing a pivotal rung on the distance ladder[6]. Adding to the precision of Cepheid variables, the LMC had a (relatively) recent supernova explosion, SN1987A, which provided a more direct distance measure to the LMC. Using the angular extent of the material ejected due to the supernova and a measure of the ejecta's velocity allows for a highly accurate measurement of the distance to the supernova and, thus, to the LMC (Panagia, 1998). Although Cepheid distance measurements are accurate out to $\sim 10 - 20$ Mpc, we require brighter objects to add more rungs to the distance

[6] A more recent publication by Pietrzynski et al. (2019) suggest that using eclipsing binaries to measure the distance to the LMC narrows the precision to 1%.

ladder. This is where supernovae come to the cosmological stage. After stars of a certain mass eject all of their material, only their core containing carbon and oxygen remains. These objects, known as Carbon-Oxygen white dwarfs, are supported by electron degeneracy pressure. This means they have a limit as to how much mass they can support, which is known as the Chandrasekhar Mass ($\sim 1.4\,\mathrm{M}_\odot$). If their mass exceeds this limit, they will explode in what is known as a type Ia supernova. Since all type Ia supernovae explode at a similar mass, they will exhibit a relatively homogeneous set of explosion properties (*i.e.* light curve), making them standard candles in the Universe. However, this is a somewhat simplified model that ignores differences between the progenitors of these supernovae, such as their spin and metalicity. This, among other factors, makes type Ia supernovae standardisable, rather than perfect standard candles. This means the relationship between the peak flux and duration of their light curve can be calibrated and standardised. With a sufficiently large sample of type Ia supernovae, this scaling relation can be utilised to measure their distance to approximately 5% (Phillips et al., 1992). As shown in Fig. 1.1, the redshift-magnitude relation calculated from type Ia supernovae shows a remarkably tight correlation from which the Hubble constant can be estimated (e.g. Wang and Tegmark, 2005; Sollerman et al., 2009; Shafieloo and Clarkson, 2010). Current measurements suggest a Hubble constant of $H_0 \sim 70\,\mathrm{km\,s^{-1}\,Mpc^{-1}}$. However, the most important result from type Ia supernova came at the end of the 20th century when Riess et al. (1998) and Perlmutter et al. (1999) first showed that the present-day energy densities of the Universe are $\Omega_\Lambda \sim 0.7$ and $\Omega_\mathrm{m} \sim 0.3$, confirming the presence of a cosmological constant, fuelling an accelerated expansion of the cosmos. The plot shown in Fig. 1.1 suggests a flat universe with approximately a quarter of its energy density in the form of matter and three quarters in the form of dark energy (cosmological constant).

This paradigm is known as the ΛCDM model and represents the current standard model of cosmology, where Λ represents the cosmological constant and 'CDM' stands for cold dark matter. Features of this cosmology include a big bang in the past as $a \to 0$ and an infinite extension into the future as $a \to \infty$, $t \to \infty$. One of the most curious aspects of such a universe is that the total energy density $\Omega \simeq 1$, indicating a flat universe in the context of General Relativity. Fig. 1.2 shows that a larger parameter space exists for open/closed universes as compared to a flat universe, defined by the line where $\Omega_\mathrm{m} + \Omega_\Lambda = 1$. This suggests that open and closed universes are thus statistically more likely given the combinations of Ω_m and Ω_Λ that can create such universes, noted in Fig. 1.2 as 'open' and 'closed'. This is indeed quite strange and so I would now like to shift the reader's attention to contemplate the early universe in order to unravel this mystery of flatness, as well as some other interesting observations.

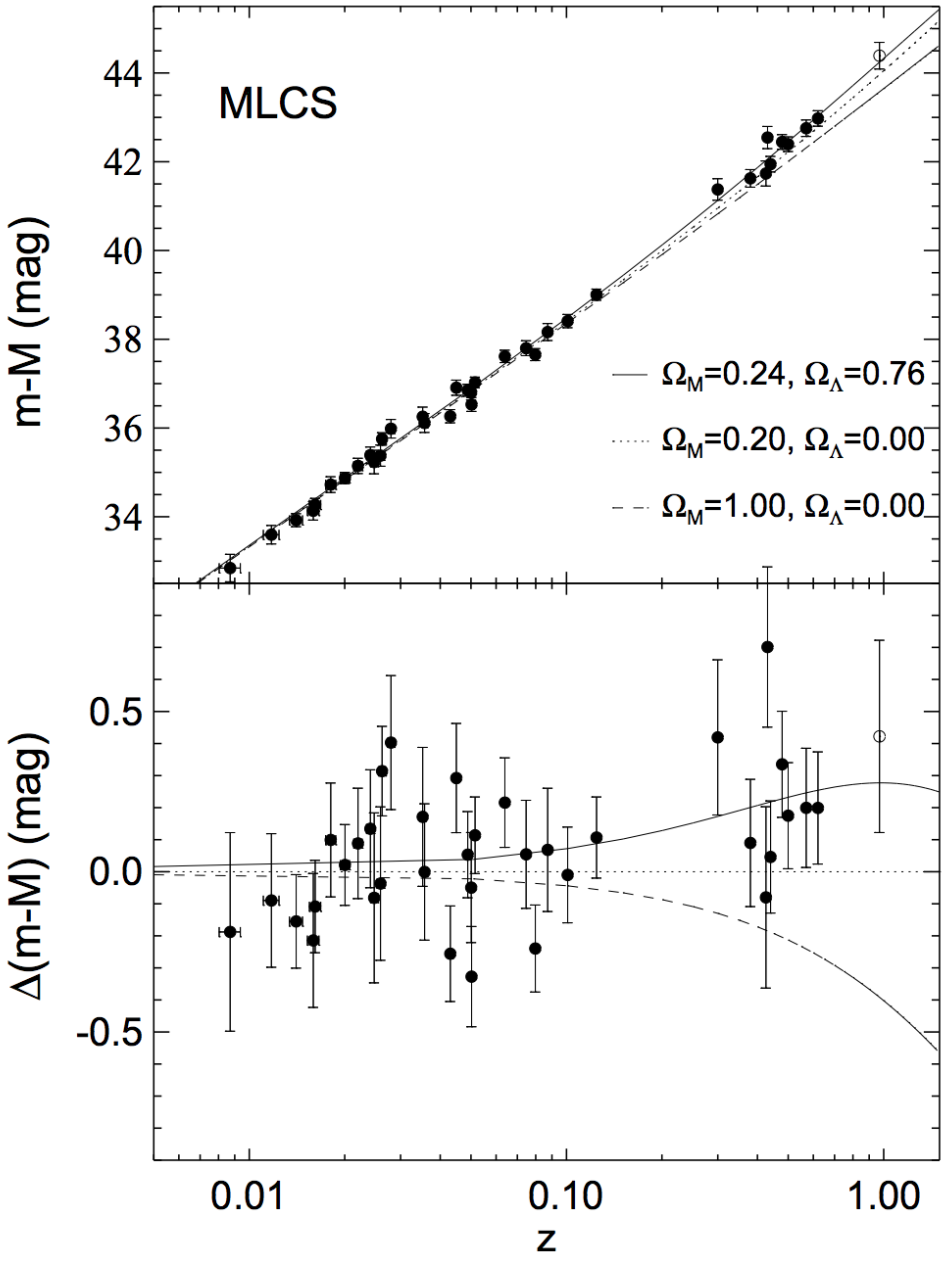

Figure 1.1 Plot from Riess et al. (1998) showing that the magnitudes of the type Ia supernovae favour a model with a non-zero cosmological constant.

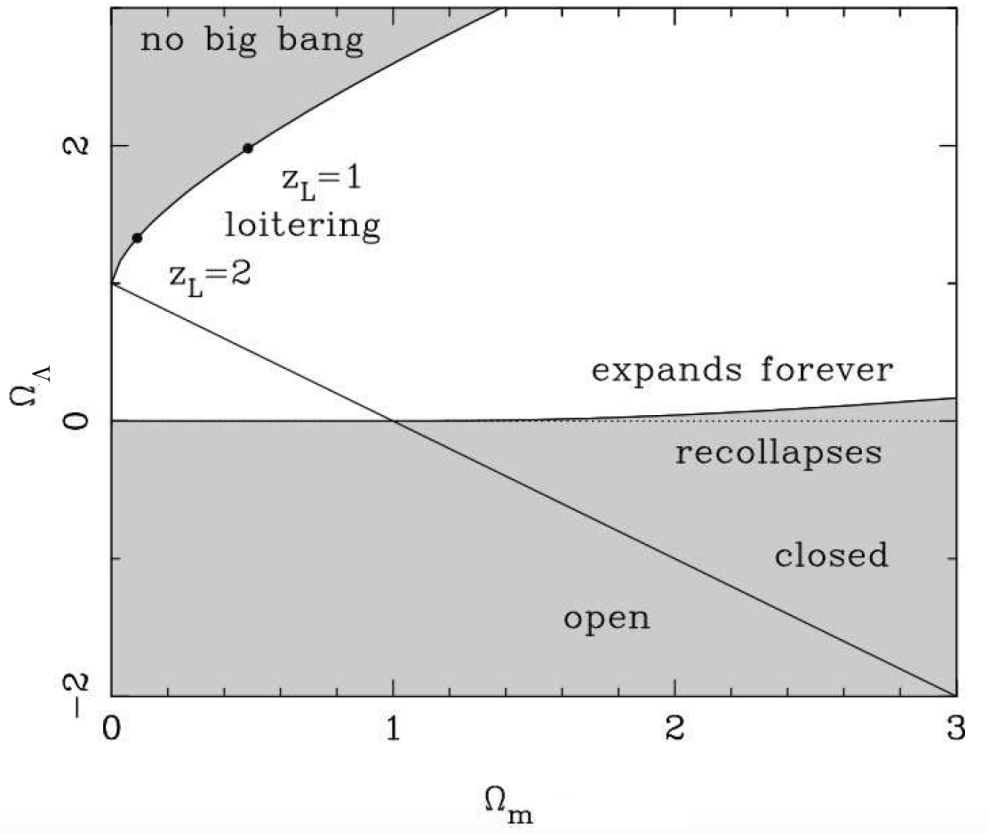

Figure 1.2 Influence of the Ω_m and Ω_Λ on the geometry and behaviour of the Universe (Peacock, 1999).

1.5 The Early Universe

Considering the paradigm of an accelerated expansion, one realises that if we could rewind this process, the Universe would look in stark contrast to what we observe today. Namely, the Universe at its infancy was extremely dense and hot. Additionally, recalling the scaling relations of matter and radiation from Section 1.1, we come to the conclusion that as we wind back the clock to $a \to 0$, radiation energy density dominated the landscape of the Universe. During this period, one can assume that the Universe followed an adiabatic expansion, such that the entropy of a given comoving region remained unchanged with time. Although this assumption has some drawbacks, such as reversibility, a key feature of this paradigm suggests that if radiation dominated the Universe at some point in the past, there must exist a crossover period when matter triumphed as the dominant form of density. A general prediction from such a construction would indicate that we should, in theory, be able to observe the light from this early, hot period. Specifically, as the Universe expands and cools, it should transition from being in a plasma-like state to a neutral state, releasing photons. The observation of photons from this period came as somewhat of an accident by Penzias and Wilson (1965), while Dicke et al. (1965) showed that this radiation is a relic of a hot big bang following a perfect black-body with a temperature of $T \simeq 3\,\mathrm{K}$ from all directions in space[7]. This came to be known as the Cosmic Microwave Background (CMB) (see Section 1.7 for more details). We should note that the total radiation energy density includes a contribution by cosmic neutrinos, which are thought to be relativistic in the early universe, thus contributing to the radiation energy density. Using the temperature of the CMB, one can estimate the radiation density as,

$$\Omega_{\mathrm{r}} = 2.5 \times 10^{-5}(1 + 0.227 n_{\mathrm{eff}}), \tag{1.23}$$

where n_{eff} represents the effective number of neutrino species, which is predicted to be $n_{\mathrm{eff}} = 3.04$ (e.g. Beutler et al., 2014).

At such an early phase of the Universe, both radiation and matter are coalesced in a plasma, however, as the Universe expands, the plasma loses its state of thermal equilibrium, and thus matter and radiation will decouple. This is the moment (although not an instantaneous one) when the photons we measure from the CMB are released into the Universe for eager observers to capture in their detectors. In cosmology, this transition period is known as the epoch of recombination[8].

[7] It's interesting to note that the earliest estimations for a temperature of space came from Guillaume (1896) and Eddington (1926), who estimated the temperature of space to follow a black body spectrum with T = 5-6 K and T = 3.18 K, respectively.

[8] Dear distinguished reader, I would like to take this opportunity to formally convey my discontentment with a rife problem in astrophysics, namely the copious amount of misnomers that plague us. Let me first address the mention in Section 1.4 regarding the Hubble constant. Now, I'm no expert in semantics, but the sheer contradiction of a *time-varying constant* makes one, not only physically, but also mentally, nauseated. In regards to 'recombination,' what is

Considering the overwhelming amount of photons compared to baryonic matter particles ($\approx 10^{10} : 1$) and that neutral atoms form by emitting a pair of photons, the decoupling redshift can be estimated as $z_{\rm dec} \sim 1100$. This event is known as last-scattering and occurs during matter domination, though not long after matter-radiation equality, which one can calculate as,

$$1 + z_{\rm eq} = 23\,900\,\Omega_{\rm m} h^2\,(T/2.73\,{\rm K})^{-4}. \tag{1.24}$$

For $\Omega_{\rm m} = 0.3$ and $h = 0.7$, this becomes $z_{\rm eq} \approx 3500$, which is not long before decoupling in terms of cosmological time scales.

Since we know that redshift and time are intimately related, we can calculate the time and size of the Universe at matter-radiation equality. Realising that during this epoch of the Universe only matter and radiation have any relevance, we can rewrite the Friedmann equation as,

$$\left(\frac{\dot{a}}{a}\right)^2 = H_0^2 \left(\frac{\Omega_{\rm m}}{a^3} + \frac{\Omega_{\rm r}}{a^4}\right). \tag{1.25}$$

During this epoch, we can ignore the effects of curvature (if any exists) and see that the Universe expands as $a \propto t^{1/2}$. However, during matter domination, the Universe expands as $a \propto t^{2/3}$, thus including both contribution at the time of equality, the relationship between time and the scale factor becomes,

$$H_0 t = \frac{2}{3}\frac{\Omega_{\rm r}^{3/2}}{\Omega_{\rm m}^2}\left[\left(\frac{\Omega_{\rm m}}{\Omega_{\rm r}}a - 2\right)\sqrt{1 + \frac{\Omega_{\rm m}}{\Omega_{\rm r}}a} + 2\right], \tag{1.26}$$

which we can simplify knowing that at equality $\Omega_{\rm m} a_{\rm eq}^{-3} = \Omega_{\rm r} a_{\rm eq}^{-4}$ therefore $a_{\rm eq} = \Omega_{\rm r}/\Omega_{\rm m}$ so that,

$$t_{\rm eq} = 13.04 \frac{\Omega_{\rm r}^{3/2}}{\Omega_{\rm m}^2}\, h^{-1}\,{\rm Gyr}. \tag{1.27}$$

it exactly that *re*combines? This is the first time atoms have combined, so why do we not call it the epoch of 'combination?' A few other notable misnomers include: planetary nebulae (no planets involved), shooting stars (no stars involved), galaxy-galaxy lensing (what's wrong with position-shear lensing?), and more! These, of course, cause endless confusion amongst students trying to fit the breadth of the Universe into their meagre human brains, but even more perplexity arises during public engagement. Peer into the disgruntled faces of keen, fellow humans as you explain to them that late-type galaxies formed first and early-type galaxies formed afterwards and you will understand the gravity (no pun intended) of this predicament. All facetiousness and melodrama aside, I appreciate that these terms arose within the particular historical context of these discoveries and I appreciate the vast windows these discoveries have opened, however that doesn't abate them from haunting me (us?) to this day.

Using this time of matter-radiation equality, we can employ Eq. 1.16 to calculate the particle horizon when the CMB was released. Continuing our assumption of a flat Universe with only matter and radiation, the particle horizon size becomes,

$$r_{\rm p}(a) = \frac{2\sqrt{\Omega_{\rm r}}}{H_0\Omega_{\rm m}}\left(\sqrt{1+\frac{\Omega_{\rm m}}{\Omega_{\rm r}}a}-1\right), \tag{1.28}$$

which means that the comoving size of the horizon at matter-radiation equality factors to,

$$r_{\rm eq} = \frac{2\sqrt{\Omega_{\rm r}}}{H_0\Omega_{\rm m}}\Big(\sqrt{2}-1\Big). \tag{1.29}$$

This suggests that at the time of the release of the CMB, the angle on the sky within which the Universe was causally connected subtended $\sim 1^\circ$. How, then, is it that the whole sky reached thermal equilibrium when it wasn't causally connected? At this point, I'd like to introduce a fascinating, yet contentious, topic in cosmology known as inflation.

1.5.1 Inflation

So far, our discussion of the Universe we inhabit has conjured several complications:

- The big bang problem: there appears to be a singularity in the Friedmann metric (Eq. 1.2) at $a = 0$, which causes a divergence in density, disappearance of coordinates, and general mathematical pandemonium, so what occurs as $a \to 0$?
- The horizon problem: a radiation dominated universe (one with $a \propto t^{1/2}$) has a finite horizon. There seems to exist no causal way for different parts of the sky to have been in thermal equilibrium and produce the homogeneity of the CMB.
- The flatness problem: why does the Universe appear to exhibit spatial flatness in the present day when flatness is an unstable, critical point in a big bang cosmology (see Fig. 1.2)?
- The expansion problem: of all the conundrums, the fact that the Universe is expanding at $t = 0$ in a smooth, uniform way creating the isotropy and homogeneity we observe on large scales in the present day poses, arguably, the greatest enigma of all.

These complications can (to some degree) be alleviated by the theory of inflation (Starobinsky, 1980; Guth, 1981; Linde, 1982). Since observations of the CMB

and the homogeneous clustering of large-scale structure strongly suggest that all of the Universe was in causal contact at last-scattering, we realise that we require a scale factor - time relation of $a \propto t^{\alpha}$ with $\alpha > 1$. Differentiating the Friedmann Equation (Eq. 1.4) and utilising the continuity equation (Eq. 1.7), we find the acceleration equation:

$$\frac{\ddot{a}}{a} = \frac{4\pi G}{3}(\rho + 3p/c^2). \tag{1.30}$$

Recognising that $a \propto t^{\alpha}$ with $\alpha > 1$ implies an accelerated expansion, we conclude that we need a negative pressure such that

$$\rho c^2 + 3p < 0. \tag{1.31}$$

This recalls the discussion of the negative pressure of dark energy in Section 1.1, hinting that the Universe may have been dark-energy-dominated at an early time. Solving the Friedmann Equation (Eq. 1.4) for a flat, dark-energy-dominated universe is known as the de Sitter solution, which has an exponential expansion in a:

$$a \propto e^{Ht}, \tag{1.32}$$

where $H = \sqrt{8\pi G \rho_{\mathrm{DE}}/3}$. This solution avoids a singularity, however it also indicates that, in principle, time could stretch back to $t \to -\infty$. This constitutes the general idea of an inflationary universe: a vacuum-like repulsion causing the Universe to expand at an exponentially increasing rate. A feature of this is that this expansion causes the Hubble flow to begin, solving the expansion problem, and solves the horizon problem by inflating a small, causally connected patch in thermal equilibrium to encompass the whole observable Universe. Additionally, inflation can potentially untangle the flatness problem. Considering the Friedmann Equation (Eq. 1.4) in a dark-energy-dominated universe, one finds that the density component increases as the Universe expands, dominating over the curvature term and causing flatness in the geometry of the Universe. One can think of this in the following terms: even if the Universe began as initially curved, inflation expanded it so much that any deviation from flatness would be so subtle that measuring the initial curvature would be extraordinarily challenging.

Despite all the potential of the theory of inflation, it raises some new fundamental questions. Not long after the theory came to life, some have called the initial conditions of inflation into question (e.g. Penrose, 1989), believing that the conditions for inflation are arguably more contrived than the ones needed for the Universe we observe in a ΛCDM paradigm. One of the biggest concerns about the initial conditions of inflation is the requirement of a relatively low entropy state, which contradicts our belief of a hot, chaotic beginning to the Universe.

Although the theory has its flaws, it nevertheless provides a powerful formalism for producing the large-scale structure of the Universe that we observe. Basically, tiny, but inevitable quantum fluctuations in space-time during the inflationary period become stretched out as the Universe expands. These tiny quantum fluctuations manifest themselves as small, but significant fluctuations in the density field. As the Universe continues to evolve and gravity takes centre stage, these inhomogeneities in the density field develop into the complex structures that we observe today. Although we could dive much deeper into the theory of inflation, such a daunting task surpasses the scope of this thesis and I would now like to explore the large-scale structure of our Universe.

1.6 Large-Scale Structure

Up to this point, we concerned ourselves with dynamics of a smooth, homogeneous Universe, however looking at the distribution of galaxies, we find a web-like structure consisting of dense clusters, filamentary structures, flattened sheets, and dauntingly empty voids, as seen in Fig. 1.3. This figure shows the distribution of galaxies observed by the Sloan Digital Sky Survey (SDSS) (Blanton et al., 2017). The colour indicates the density of galaxies with a clear, inhomogeneous, web-like pattern in the galaxy distribution. Understanding the properties of this structure in a statistical manner has been the aim of modern-day cosmology.

As mentioned in Section 1.5.1, cosmologists believe that an inflation-like period of a smooth Universe with small fluctuations sowed the seeds of the large-scale structure that we observe today. When the period of inflation ended, the imprints from these fluctuations began to grow, attracting both dark and baryonic matter into their potential wells. The evolution of the Universe then caused these seemingly insignificant perturbations to transform into the complicated structures that we observe today, as shown in Fig. 1.3. In this section of the thesis I will discuss the general idea of structure formation, two key players in the formation process: dark matter and dark energy, and then introduce some of the cosmological probes used to study our Universe.

1.6.1 Structure Formation

As we observe the local universe, we find that it does not conform to the FLRW metric. To measure and quantify the patterns in the large-scale structure (LSS) of the Universe, we define the dimensionless matter density parameter, which represents the perturbations of the density field as,

$$\delta(\mathbf{r}, t) \equiv \frac{\rho(\mathbf{r}, t) - \bar{\rho}(t)}{\bar{\rho}(t)}, \tag{1.33}$$

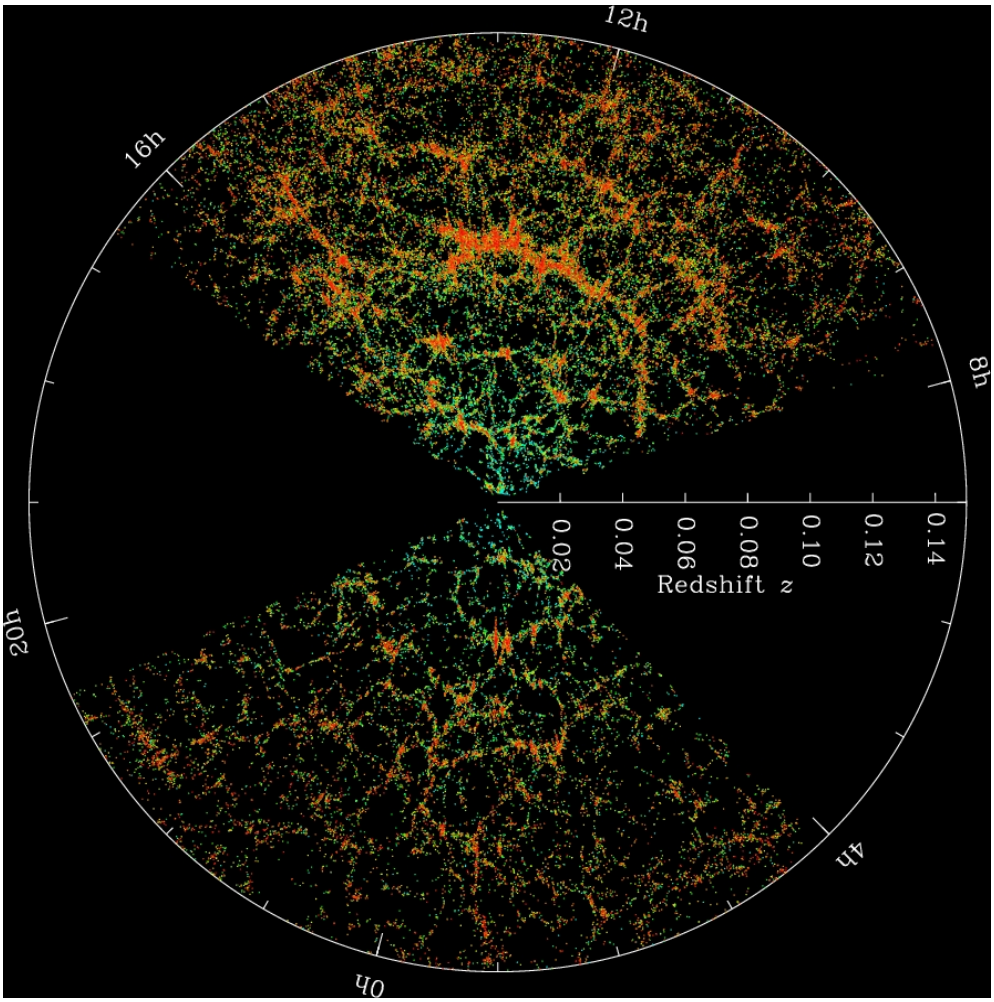

Figure 1.3 A map showing the galaxies identified in the Sloan Digital Sky Survey (SDSS) (Blanton et al., 2017) with a distinct, inhomogeneous, web-like structure.

where $\bar{\rho}(t)$ is the homogeneous mass density at time t. Although the time dependence of density perturbations is relatively well described by the laws of physics, the spatial dependence of the perturbations at a fixed time follow a random distribution. Thus, in order to extract fundamental physical properties from this stochastic distribution, cosmologists seek to understand the statistical distribution of galaxies. Rather than aiming to identify the exact location of each galaxy, any theory of LSS will instead provide an insight into the size distribution and clustering of galaxies. Thus, cosmologists tend to speak in terms of 'scales' rather than positions. The scales, $\mathbf{k}$, relate to the comoving wave-number, which is the Fourier transform of the comoving coordinate, $\mathbf{r}$. The relation between the Fourier-space and real-space is,

$$\begin{aligned} \delta_{\mathbf{k}} &= \frac{1}{V} \int \delta(\mathbf{r}) e^{-i\mathbf{k}\cdot\mathbf{r}} d^3r, \\ \delta(\mathbf{r}) &= \sum_{\mathbf{k}} \delta_{\mathbf{k}} e^{i\mathbf{k}\cdot\mathbf{r}}, \end{aligned} \tag{1.34}$$

where V represents the volume over which the Fourier transform takes place[9]. Since cosmologists are mostly interested in an average distributions of positions rather than precise, individual positions, the power spectrum provides a convenient way to define the variance of the density field over all modes of a given amplitude and is defined as,

$$P(\mathbf{k}) \equiv |\delta_{\mathbf{k}}|^2. \tag{1.35}$$

Cosmologists can also express the power spectrum in terms of a dimensionless power spectrum,

$$\Delta^2(k) \equiv \frac{V}{(2\pi)^3} 4\pi k^3 P(k), \tag{1.36}$$

which contributes power in logarithmic intervals of k and is often defined as,

$$\Delta^2(k) \equiv \frac{d\,P(k)}{d\ln k}. \tag{1.37}$$

Another related statistical quantity of particular interest for cosmology, is known as spatial variance,

$$\sigma^2 \equiv \frac{1}{V} \int \delta^2(\mathbf{r})\, d^3r. \tag{1.38}$$

[9]This volume can be taken to be infinite, which converts the summation in the lower equation into an integral.

This quantity provides a measure of how inhomogeneous the density field is when smoothed at a given scale. We can also express the variance in Fourier-space,

$$\begin{aligned}\sigma^2 &= \frac{V}{(2\pi)^3}\int |\delta^2(k)|\, d^3k, \\ &= \int \frac{V}{(2\pi)^3}\, 4\pi k^3\, P(k)\, d\ln k, \\ &= \int \Delta^2(k)\, d\ln k,\end{aligned} \tag{1.39}$$

where the final equation utilises Eq. 1.36. Cosmologists frequently use the variance of a density field smoothed by a filter of comoving size R,

$$\sigma^2(R) = \int \Delta^2(k)\, W^2(kR)\, d\ln k, \tag{1.40}$$

where $W(kR)$ represents a filter function. Of particular use in cosmology is the quantity σ_8, which is the dispersion in the linearly-extrapolated initial density field smoothed with a top-hat filter over a comoving radius of 8 h^{-1}Mpc, which gives an indication of the amplitude of clustering of matter in the Universe with that scale.

Considering minute density fluctuations ($\delta \ll 1$) that interact only through gravity, the linear evolution of the density perturbations in the matter field can be written as,

$$\ddot{\delta} + 2H\dot{\delta} = 4\pi G\bar{\rho}_{\rm m}\delta = \frac{3}{2}H^2\Omega_{\rm m}(t)\delta, \tag{1.41}$$

where $\bar{\rho}_{\rm m}$ represents the homogeneous matter density. This equation constitutes the foundation for understanding the evolution of the LSS (for examples see Peebles, 1980; Peacock, 1999). It can be regarded as Newton's law of gravity for a density perturbation, where the acceleration arises due to the perturbed density component. The 'Hubble drag' term, $2H$, also affects the perturbation and arises as the peculiar velocity declines as a function of time due to the expansion. Note that since no spatial derivatives exist, these perturbations can increase or decrease in their amplitude, but they do not change spatial position in comoving coordinates (to linear order). Additionally, Eq. 1.41 suggests that perturbations only exist in the matter component of the Universe. Perturbations in other energy density components of the Universe may be added, however that exploration exceeds the scope of this thesis, thus I will simply present the solution to this equation for a matter only Universe where $\Omega_{\rm m} = 1$. As Peacock (1999) shows, the perturbation equation has two solutions:

$$\delta(a) = Aa + Ba^{-3/2}. \tag{1.42}$$

In the above equation, the first term with $\delta(a) \propto a$ represents the 'growing mode' and corresponds to the gravitational instability of density perturbations. The first term quickly dominates over the second term (known as the 'decaying mode'), suggesting that given a small initial fluctuations in an earlier epoch, a universe with any degree of inhomogeneity can be created through this linear theory approach. Interestingly, if one considers solving Eq. 1.41 into the distant future with $\Omega_{\rm m} \to 0$, what occurs is that $\delta \to$ constant because $H \to$ constant. This means that the perturbations will cease to grow. Considering the accelerated expansion of a ΛCDM universe, such an outcome aligns with expectations since material will refrain from coalescing together and creating structure due to the expansion. This feature of ΛCDM is unique since it means that the most massive structures in our Universe have already formed within the most overdense regions since observations indicate that $\Omega_\Lambda \geq 0.6$. Another useful quantity is known as the linear growth rate of structure, defined as

$$f = \frac{d\ln\delta}{d\ln a}. \tag{1.43}$$

By construction, Eq. 1.43 requires that $f \to 1$ as $a \to 0$, however the growth rate can deviate at later times based on the underlying cosmology of the Universe. Peebles (1993) approximate the growth rate for a flat ΛCDM universe as $f \approx \Omega_{\rm m}^{0.55}(a)$. Redshift-space distortions are a key measurement of the linear growth rate and can help distinguish between different cosmologies (see Section 3.9.2).

1.6.2 Dark Matter

Having briefly discussed the fundamentals of the LSS, I now introduce its main, enigmatic constituent: dark matter. Present-day observations suggest that $\Omega_{\rm m} \sim 0.3$, however the baryon density, $\Omega_{\rm b} \sim 0.05$ (see Section 1.7), leading to the mystifying conclusion that non-baryonic mass exists in our Universe. The idea of dark matter began in the 1930s by observing the abnormally high velocity dispersion of galaxy clusters given the mass of their stellar content (Zwicky, 1933, 1937)[10]. In 1940 more evidence for dark matter appeared on galactic scales where Jan Oort found that the mass-to-light ratio of NGC 3115 suggested the presence of a 'more or less homogeneous mass of great density' (Oort, 1940). However, it wasn't until the 1970s when the infamous Vera Rubin and her collaborators measured the rotation curves of spiral galaxies finding a flat rotation curve beyond the galactic bulge, contrary to the expectations from Newtonian dynamics (Rubin and Ford, 1970; Rubin et al., 1978, 1980). Since these galaxies appeared to rotate faster than the observable baryonic matter permitted, the rotation curves of these galaxies suggest the presence of extra, 'dark' matter. In addition, measurements of the mass of galaxy clusters from weak gravitational lensing combined with the

[10]Note that this citation refers to the same publication with the only difference being the language in which they were published (1933: German, 1937: English).

spatial distribution of hot, X-ray-emitting gas, such as the Bullet cluster studies (Clowe et al., 2004; Markevitch et al., 2004), provide evidence for dark matter on cosmological scales.

Several candidates to explain dark matter have arisen over the years. MACHOs (MAssive Compact Halo Objects) (Griest, 1991) were one of the first suggestions. Essentially, the term MACHOs encompasses any low-luminosity, baryonic matter that has not been detected, such as low-mass stars, planets, or black holes. However, at the turn of millennium, they have been ruled out as a potential dark matter candidate (e.g. Alcock et al., 2000; Tisserand et al., 2007)[11]. Particle physicists have also attempted to understand the fundamental nature of dark matter and proposed two types of fundamental particles as candidates: WIMPs (Weakly Interacting Massive Particles) (Jungman et al., 1996) and axions (Peccei and Quinn, 1977). In short, WIMPs are a type of particle that has no electromagnetic interaction, but interacts through the weak nuclear force and gravity. If such particles were to exist and have a weakly-interacting cross-section, then their mass would be ≈ 10 GeV, or ten times heavier than a proton or neutron. Another potential particle candidate, axions, have an interesting theoretical foundation. Quantum chromodynamics predicts no fundamental mechanism for a symmetry between the charge and parity of particles, however no violation to this symmetry has been detected. This is known as the charge-parity problem. Axions alleviate this problem by acting as oscillating particles of a charge-parity violating field (Peccei and Quinn, 1977). These axions are predicted to have a light mass (< 1 eV) and were never in thermal equilibrium with the rest of the Universe.

However, leaving these equivocal acronyms[12] and terrifyingly small-scale-physics behind us, the main concern for this thesis resides in the velocity, or, more precisely, the free-streaming length of whatever constitutes this fantastical, yet highly pervasive dark matter. Since particles of different masses will decouple at different times and low mass particles will tend to be relativistic for longer, they affect the underlying cosmology and the formation of structure in direct ways. For example, low mass particles would delay the onset of matter domination compared to heavier particles. Furthermore, while particles are relativistic, they erase perturbations on the length scale that they were able to travel relativistically (*i.e.* the free-streaming length). There are essentially 3 'flavours' to dark matter particles: hot, warm, and cold. Hot dark matter (HDM) particles decouple whilst relativistic with a number density similar to that of photons and a mass of ~ 1 eV, warm dark matter (WDM) particles decouple while semi-relativistic with a characteristic mass of 1-10 keV, while cold dark matter (CDM) decouple when

[11]It should be noted that after the gravitational wave detection (see Section 1.6.4) a resurgence of interest into stellar-mass black holes arose (e.g. Bird et al., 2016), so MACHOs may not totally be ruled out yet.

[12]For the sake of brevity (and the author's sanity), we leave the exploration of RAMBOs (Moore and Silk, 1995), which is perhaps the most dubiously named dark matter candidate, for the distinguished reader's leisure. Sigmund Freud would surely have had an exuberant time studying the cause for such metaphorical-Castration-anxiety-inducing acronyms.

non-relativistic and their number density can be exponentially suppressed with a particle mass in the MeV - GeV ranges. The 'warmer' the dark matter particle, the smoother the density of the LSS, meaning that since cosmologists can observe structures below certain scales, such as dwarf galaxies, we can place a constraint on the velocity of the dark matter particle(s) at decoupling. Observations and simulations seem to suggest that the Universe consists of dark matter particles that decoupled while non-relativistic, hence the CDM in ΛCDM, however we require more studies to fully confirm this (e.g. Gao and Theuns, 2007; Iršič et al., 2017; Wang et al., 2017; Berlin et al., 2018). If our particle physicists colleagues conclude that 10 GeV WIMPs are indeed the dark matter particle, this will fit well with the present-day cosmological paradigm of a 'cold' dark matter particle.

1.6.3 Dark Energy

The accelerated expansion of the late-time Universe (discussed in Section 1.4) presents several mysteries in need of a resolution. Mathematically, acceleration arises by adding a constant to Einstein's Field Equations (Eq. 1.1) such that,

$$R_{\mu\nu} - \frac{1}{2}Rg_{\mu\nu} + \Lambda g_{\mu\nu} = -\frac{8\pi G}{c^4}T_{\mu\nu}. \tag{1.44}$$

Although this constant alters the 'gravitational' side of the equation, the magnitude of Λ required to explain the present day acceleration is so small that it has no detectable effect on the scales of individual galaxies. Despite explaining present-day observations to a high degree of accuracy, the purest of physicists may scoff at the crude idea of arbitrarily adding a constant of nature that alters gravity without sound, fundamental reasoning. Another way to explore the acceleration phenomenon is by modifying the stress-energy tensor, rather than the gravity, of Einstein's Field Equations. In this manner, the same acceleration arises by effectively introducing a new fluid into the Universe with $p = -\rho$ and $\dot{\rho_\Lambda} = 0$. A benefit of this approach is that this constant energy is predicted by Quantum Field Theory (QFT) and is known as vacuum energy. However, in order to produce a finite value for ρ_Λ, an energy cut-off scale needs to be chosen. Unfortunately, the most sensible cut-off scale, which is the Planck energy scale of $\sim 10^{18}$ GeV, yields a density of vacuum energy that's discrepant by $\sim 10^{120}$ with what cosmologists observe for dark energy[13]. This discrepancy between the predicted and observed value of ρ_Λ is known as the cosmological constant problem (Weinberg, 1989). Although the discovery of the accelerated expansion of our Universe and the use of a cosmological constant to explain it seemed shocking, Weinberg (1987) predicted it over a decade before its measurement (Riess et al., 1998; Perlmutter et al., 1999). The argument by Weinberg (1987) was anthropic by nature: if indeed the true value of ρ_Λ exceeds the observed value by $\sim 10^{120}$, such strong

[13]It's worth noting that part of the reason for such a large discrepancy is because the energy is raised to the power of four in the calculation of the vacuum energy density, which exaggerates the offset. Although a 10^{30} difference is still worrisome.

acceleration would disallow for the formation of the structure that we see, which means no observers would exist in the Universe to observe it. Weinberg (1987) argues that the Universe we inhabit has a cosmological constant that's as large as possible without preventing the growth of structure that we observe. Various groups have followed this line of reasoning (e.g. Peacock, 2007) finding that the most likely value of the vacuum energy density from the anthropic point of view is $\Omega_\Lambda \sim 0.7$.

Aside from the cosmological constant or vacuum energy, the acceleration of the Universe could result from a set of theories termed Dark Energy (see Copeland et al., 2006, for a review). Generally, these theories rely on the idea that there exists symmetry in the Universe, which sets the value of the vacuum energy close to zero, while some factor causes the dark energy to create late-time acceleration. As introduced in Section 1.1, the pressure-density relation of the various components of the Universe can be described as: $p = w\rho$, where w is the equation-of-state parameter. For cosmological constant or vacuum energy $w = -1$. Dark Energy models either keep w constant or allow it to vary over time, which changes the strength of the acceleration and affects the growth of structure. The most current observations suggest that $w = -1$, consistent with a cosmological constant or vacuum energy model (Planck Collaboration et al., 2018a). However, regardless of whether or not the equation-of-state for dark energy is constant or time varying, a physical explanation of the underlying mechanism of dark energy is needed. One of the most generalised ways to explain dark energy is to introduce a canonical or non-canonical scalar field, known as quintessence or k-essence, respectively (Caldwell et al., 1998; Chiba et al., 2000; Copeland et al., 2006; Joyce et al., 2016). With the discovery of the Higgs Boson, which arises from a fundamental scalar field, these types of models seem to provide the highest potential as explanations of dark energy.

1.6.4 Modified Gravity

Generally speaking, dark energy acts as a contribution to the stress-energy tensor side of Einstein's Field Equations, however modifications to the the gravity side of these equations can achieve a similar effect. Such theories, known as modified gravity theories[14], disobey the Strong Equivalence Principle and Lovelock's Theorem (Lovelock, 1971). Lovelock's Theorem states that Einstein's Field Equations are a unique solution satisfying local gravity with second order derivatives in the metric of a four dimensional space. Therefore, a theory of modified gravity will violate one (or more) of these conditions. A myriad of modified gravity theories exist that behave in fundamentally different ways, taking forms of scalars, vectors, tensors, and other higher-order fields (see Clifton et al., 2012; Joyce et al., 2016, for a review). Since these theories introduce new degrees of freedom into the gravitational sector, invoking an effective fifth force, they

[14]This section will only refer to modified gravity theories aimed at explaining cosmic acceleration, not to theories replacing the need for dark matter.

must also employ some mechanism to pass local tests of gravity and appear as General Relativity on Solar System scales (Will, 2014). These mechanisms, called screening mechanisms, can affect the effective gravitational potential in various ways, such as changing the first or second order derivatives of the potential. Some of the most well-studied screening mechanisms are Chameleon and Vainshtein Screening (Khoury and Weltman, 2004; Vainshtein, 1972).

However, arguably the most revolutionary astrophysical observation of the 21st century has upended the field of modified gravity and dark energy. On the 14th of September 2015, the two detectors of Advanced LIGO (LIGO Scientific Collaboration et al., 2015) identified the first gravitational wave signal, which occurred from the merging of two black holes (Abbott et al., 2016). Fortunately, we did not need to wait long until Advanced LIGO yielded and even more exciting detection. On August 17th, 2017 the Advanced LIGO and Advanced Virgo (Acernese et al., 2015) detectors observed the gravitational wave signal of two merging neutron stars. This astrophysical phenomenon created a gamma ray burst, which was identified by The Fermi Gamma-ray Burst Monitor ~ 1.7s after the detection of the gravitational signal, becoming the first multi-messenger detection of gravitational waves (Abbott et al., 2017). An extensive campaign of approximately 70 observatories spanning the full electromagnetic spectrum identified the signal from this merger event. One of the main conclusions from this observation is that the speed of gravitational waves is essentially the same as the speed of light, resulting in a significant subset of modified gravity and dark energy theories with $c_{\text{grav wave}} \neq c_{\text{light}}$ to be inconsistent with observations (e.g. Lombriser and Taylor, 2016; Baker et al., 2017). This constraint puts a strain on the viability of any theory that claims that the speed of propagation of gravitational waves differs from the speed of light, such as multiple scalar-tensor theories suggest (Baker et al., 2017).

1.7 Cosmological Probes

A vast variety of cosmological probes exist to test the ΛCDM model. In this section, I intend to introduce a non-exhaustive list of these probes giving both a historical and present-day context.

1.7.1 Cosmic Microwave Background

The Cosmic Microwave Background (CMB) is the thermal radiation left over after recombination. Since density fluctuations during the epoch of the CMB directly translate to temperature fluctuations through physical processes such as the Sachs-Wolfe effect and the Doppler effect, cosmologists can observe and study the temperature fluctuations of photons propagating through the Universe. The first postulation of the CMB occurred in 1948 when Ralph Alpher and Robert Herman

(Alpher and Herman, 1948) responded to a couple of publications by George Gamow on big bang nucleosynthesis (Gamow, 1948a,b). However, it wasn't until approximately two decades later that two Soviet physicists claimed that the CMB is a measurable phenomenon (Doroshkevich and Novikov, 1964)[15]. In 1964, Todd Wilkinson, Robert Dicke, and their colleagues set out to measure the CMB using a radiometer, however it didn't take long for Arno Penzias and Robert Wilson to serendipitously measure the CMB (Penzias and Wilson, 1965), for which they received the Nobel Prize in 1978. There was some push back from the scientific community (as there always is with new ideas), but throughout the 1970s the seemingly infinite brain power of cosmology heavyweights, such as Jim Peebles, Yakov Zel'dovich, and Rashid Sunyaev, calculated what effect inhomogeneities in the early Universe would have on the CMB. Finally, in 1992 the COBE mission confirmed the existence of the CMB showing that the expected and observed power spectrum of the temperature fluctuations agree to an astonishingly high precision (Smoot et al., 1992).

Fast forward to the present day where Figs. 1.4 & 1.5 show the most up-to-date map of these temperature fluctuations and the temperature power spectrum from the Planck collaboration (Planck Collaboration et al., 2018a,b). Fig. 1.4 shows an all-sky temperature map of the CMB with fluctuations on the μK scales, while Fig. 1.5 shows the power spectrum of these temperature fluctuations (red points) and their agreement with the theoretical prediction for a flat ΛCDM universe (blue curve). These temperature fluctuations strongly depend on the underlying cosmology of the Universe, providing us with an opportunity to explore the Universe at its earliest stages. The CMB suggests a flat geometry of the Universe with $\Omega = 1$. The observation of flatness, as well as the homogeneity and isotropy of the CMB, suggest some process of early rapid inflation to bring the whole observable Universe in causal contact. All CMB experiments suggest that the content of baryonic matter is $\Omega_{\rm b} \simeq 0.05$, which aligns with big bang nucleosynthesis. Furthermore, the total matter content can be calculated since it directly affects the epoch of matter-radiation equality. The CMB suggests that $\Omega_{\rm m} \simeq 0.3$, which supports hypothesises of dark matter and dark energy. But despite the precision of the present-day CMB experiments, an air of tension pervades within the cosmological community because the total matter density and galaxy clustering evaluated from the early-time Universe of the CMB somewhat disagrees with measurements of the late-time Universe, such as weak gravitational lensing, by $\sim 2\sigma$. Adding to the drama, a discrepancy of $\sim 4\sigma$ between the different values of the present-day Hubble constant evaluated from the CMB and supernovae raises some questions (Riess et al., 2016, 2019). But while the statistics and particle physics communities mockingly smirk at cosmologists as we quibble over 2σ, if the tension is indeed real and not due to systematic errors, a whole Pandora's box of new physics may soon reveal itself.

[15]It should be well noted that there were other scientists in the 1950s who effectively measured the CMB, but perhaps without realising it or unable to fully confirm it. These people include: Émile Le Roux, T. A. Shmaonov, and William Rose (see Kragh, 1999; Naselsky et al., 2006, for more historical context).

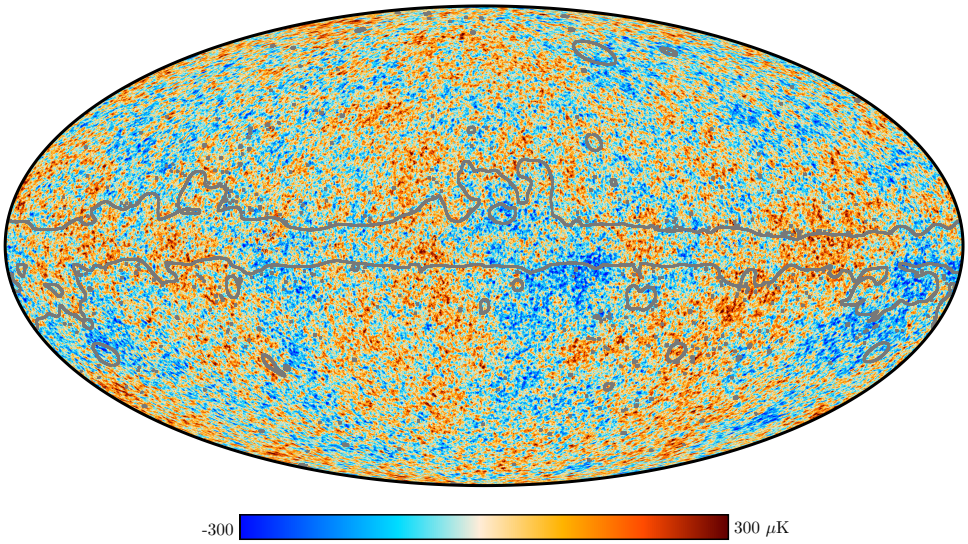

Figure 1.4 An all-sky map of the temperature fluctuations of the CMB as observed by Planck (Planck Collaboration et al., 2018b). The grey contour represents the extent of the confidence mask.

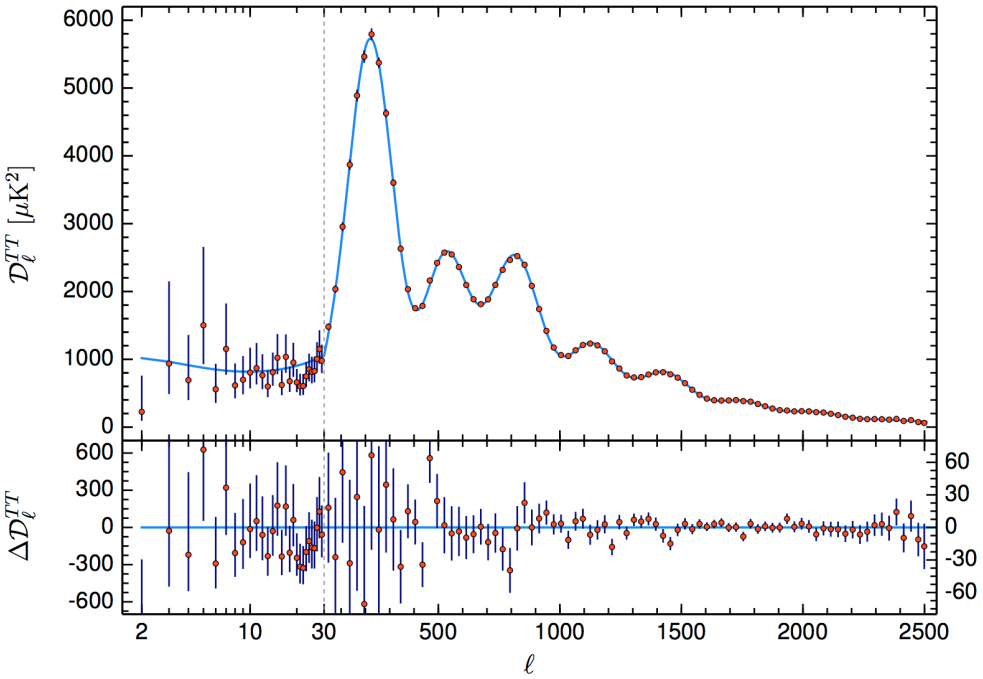

Figure 1.5 The temperature power spectrum of CMB as observed by Planck (Planck Collaboration et al., 2018a). The blue curve represents the theoretical prediction with concordance cosmology parameters.

1.7.2 Weak Gravitational Lensing

Weak gravitational lensing (WL, see Chapter 2 for a thorough overview) occurs when massive objects, such as galaxy clusters, bend the trajectory of light as it propagates through space-time (see Bartelmann and Schneider, 2001, for a review). Theoretically, WL provides a way to measure the matter power spectrum directly in an unbiased way, making it the only cosmological probe (so far) to do so. Knowing the matter density can help identify the number density of galaxy clusters as a function of mass or redshift, both of which significantly depend on the background cosmology (e.g. Madhavacheril et al., 2017). In addition, WL provides an opportunity to use the correlation of galaxy shapes, known as cosmic shear, as a probe of cosmology (e.g. Hildebrandt et al., 2017; Troxel et al., 2017; Hikage et al., 2018; Hildebrandt et al., 2018). Cosmic shear is the distortion of galaxies by the LSS. Measuring galaxy shapes from cosmic shear, can uncover properties and evolution history of the LSS, helping to unravel the nature of dark matter and dark energy. Comparing lensing maps of dark matter distribution with X-ray or optical maps of galaxies and gas can expose the connection between dark matter and baryonic matter (e.g. Clowe et al., 2004; Markevitch et al., 2004). However, lensing is sensitive to the change in the density along the line of sight, which can be altered by the total clustering (σ_8) or the total matter density (Ω_m), creating a degeneracy between σ_8 and Ω_m. Currently, there are 3 main WL surveys which are the Kilo-Degree Survey (KiDS) (de Jong et al., 2013), the Dark Energy Survey (DES) (Diehl et al., 2014), and the Hyper Suprime-Cam survey (HSC) (Miyazaki et al., 2012). Fig. 1.6 shows cosmic shear results from these three surveys, which clearly shows the degeneracy and the aforementioned 2σ offset from the CMB measurements.

Tremendous effort has been exerted to understand the systematics of WL and to prepare for the next generation of surveys, which are expected to have first light in the next couple of years. The efforts by Euclid (Laureijs et al., 2011), the Large Synoptic Survey Telescope (LSST) (LSST Science Collaboration et al., 2009), and the Wide Field Infrared Space Telescope (WFIRST) (Green et al., 2012) will shine new light on systematic errors or potential new physics that may cause cosmological discrepancies.

1.7.3 Baryon Acoustic Oscillations

The period before matter-radiation equality consisted of a tumultuous time in the Universe. Due to the immense temperatures and pressures, matter and radiation existed in a hot plasma state connected by Thompson scattering and gravitational interactions. These two competing forces pushed and pulled the plasma around: just as overdense regions began to draw together due to their gravitational pull, radiation pressure began to increase and push the plasma back. These counteracting forces created oscillatory sound waves in the coupled plasma, which became imprinted in the matter power spectrum. The CMB can constrain the

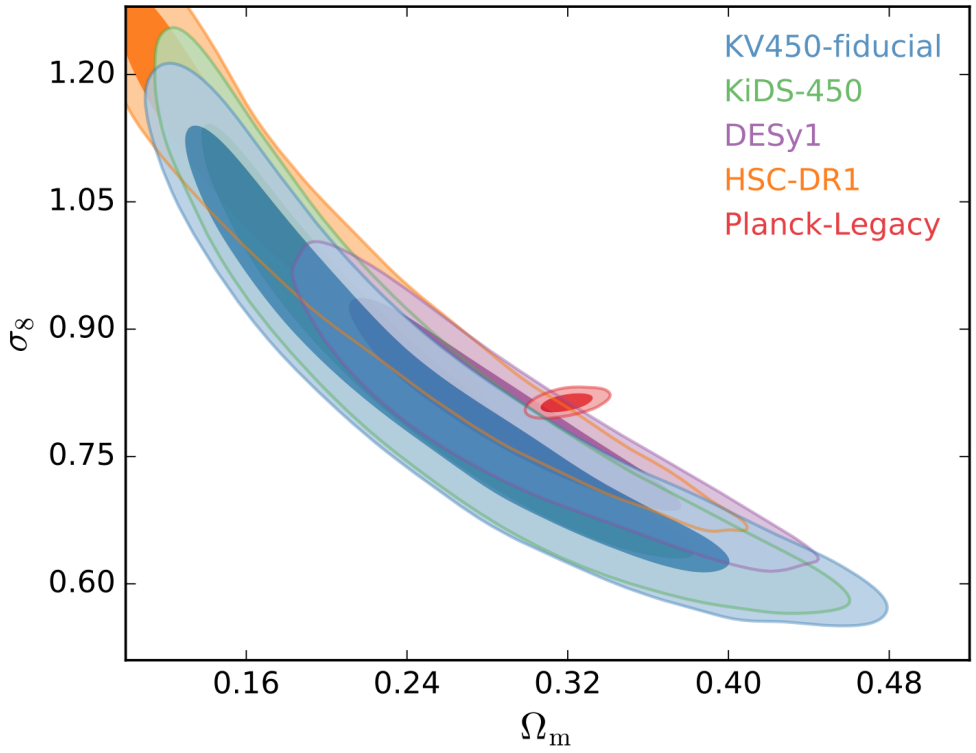

Figure 1.6 Cosmic shear results from KiDS showing the degeneracy between galaxy clustering σ_8 and the total matter density Ω_m (Hildebrandt et al., 2018). The red contour shows the results from the Planck mission discussed in Section 1.7.1.

comoving size of these oscillations, known as Baryon Acoustic Oscillations (BAO) (Eisenstein, 2005; Eisenstein et al., 2005), since they directly emerge as hot/cold spots in the temperature fluctuations. The CMB temperature fluctuations in Fig. 1.5 show the prominence of BAOs at scales of $30 \lesssim l \lesssim 2000$. In a similar fashion that type Ia supernovae act as standard candles (see Section 1.4), so too can BAOs act as a standard ruler for cosmology. In effect, measuring the scale of the most prominent peak of the BAO can constrain cosmology in a complementary way to the full power spectrum.

1.7.4 Redshift Space Distortion

The LSS of the cosmic web in Fig. 1.3 shows a distinct anisotropy in the distribution of galaxies. One of the main culprits contributing to this anisotropy is the fact that galaxies have peculiar velocities and so the measurement of their location given an angular position and redshift is only an approximation when mapping between real space and the observed redshift space. This anisotropy along the line-of-sight direction, known as the Fingers-of-God effect (Jackson, 1972), occurs since virialised galaxies in a dense environment tend to scatter towards, or away from, an observer in redshift-space, which causes these structures to appear elongated along the line of sight, creating the Fingers-of-God feature. This anisotropy in redshift space means that the power spectrum will have different amplitudes in the density fluctuations measured perpendicular and parallel to the line-of-sight direction.

However, Fingers-of-God isn't the only effect creating anisotropic behaviour in redshift space. Even though an individual galaxy's peculiar motions may cause an elongation and a Fingers-of-God effect, if galaxies reside in a dense cluster, they tend to coherently migrate in towards the centre of the cluster. In redshift space, this tends to manifest as a flattening, rather than an elongation, and is known as the Kaiser effect (Kaiser, 1987; Hamilton, 1998). The squashing due to the Kaiser effect occurs on much larger scales than the Fingers-of-God effect and tends to be subdominant. Fig. 1.7 shows a 2D galaxy correlation function from the 2dF Galaxy Redshift Survey (Peacock et al., 2001), clearly exhibiting both the flattening of the Kaiser effect on large scales and the elongation of the Fingers-of-God effect on small scales.

Kaiser (1987) was the first to calculate the linear relationship between the matter power spectrum in real-space and redshift-space:

$$\Delta_{\mathrm{s}}^2(k,\mu) = (1 + f_{\mathrm{g}}\mu^2)^2\Delta^2(k), \tag{1.45}$$

where Δ_{s} refers to the power spectrum in redshift space, k is the wave number, $\mu = \cos\theta$ where θ is the angle to the line of sight, and f_{g} is the linear theory growth rate from Eq. 1.43. The effect that arises from the expression in Eq. 1.45 boosts the power of modes along the line-of-sight direction due to their peculiar velocities,

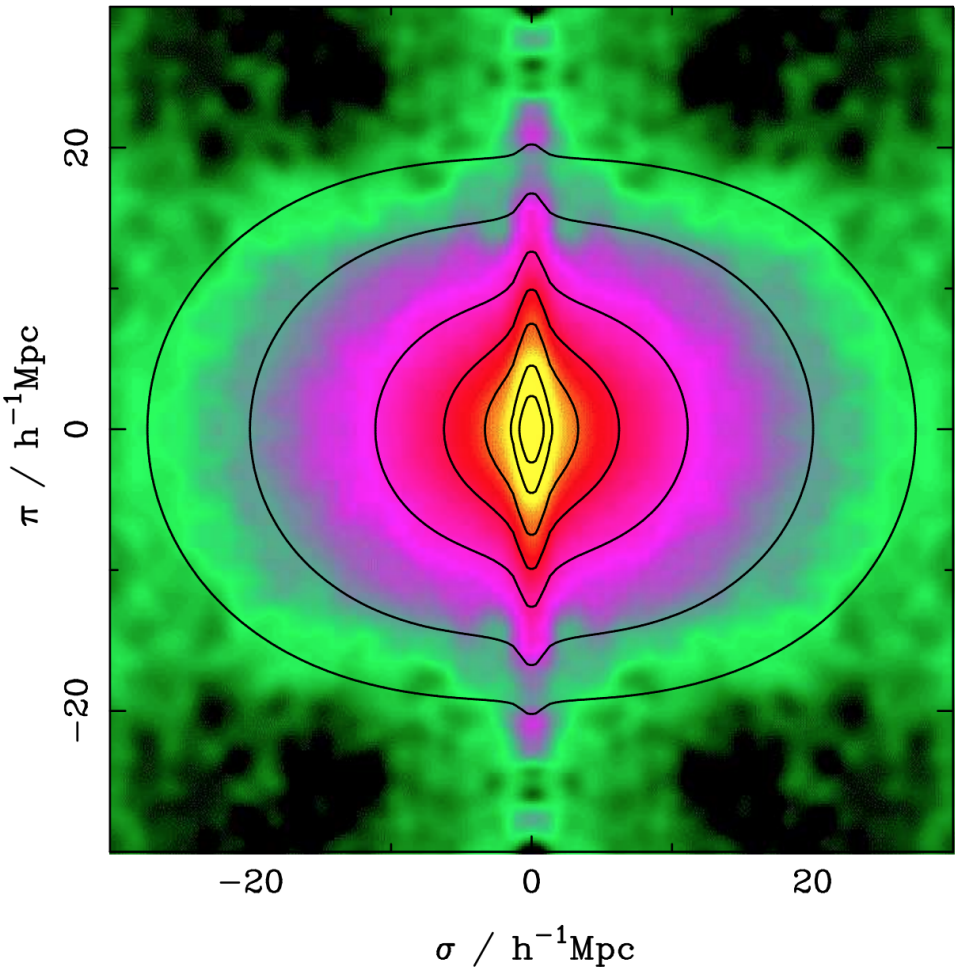

Figure 1.7 Redshift-space correlation function from the 2dF Galaxy Redshift Survey (Peacock et al., 2001). This figure shows the correlation function using the transverse, σ, and radial, π, pair separation. Both the Fingers-of-God on small scales and Kaiser effect of large scales are evident.

which enhances clustering in redshift space. More realistically, this expression should account for biased tracers (*i.e.* galaxies). The simplest approach is to assume that galaxies are linearly biased tracers of the matter field and thus,

$$\Delta^2_{\mathrm{s,g}}(k,\mu) = b^2(1+\beta\mu^2)^2\Delta^2(k), \tag{1.46}$$

where b is the linear bias and $\beta = f_{\mathrm{g}}/b$. Since galaxy redshift surveys observe $\Delta_{\mathrm{s,g}}(k,\mu)$, a Redshift-Space Distortion (RSD) analysis constrains β. However, independently obtaining the bias of the galaxy sample paves the way for RSDs to directly constrain the growth rate, making it an ideal probe to test theories of modified gravity and dark energy.

One of the most common ways to extract β from the 2D correlation function involves decomposing the correlation function into Legendre Polynomials (Cole et al., 1994), such that,

$$\Delta^2_{\mathrm{s}}(k,\mu) = \sum_{l=0}^{\infty} P_l(\mu)\,\Delta^2_l(k), \tag{1.47}$$

from which the multipole moments can be computed using the inversion formula,

$$\Delta^2_l(k) = \frac{2l+1}{2}\int_{-1}^{1} P_l(\mu)\,\Delta^2_{\mathrm{s}}(k,\mu)\,\mathrm{d}\mu. \tag{1.48}$$

Due to symmetries in μ, the odd l integrals will vanish, leaving only the even ones. In practice, cosmologists usually only utilise the first 3 even multipoles, namely the monopole, quadrupole, and hexadecapole. In linear theory (Kaiser, 1987), the ratio of the quadrupole to the monopole can be used to directly constrain β, which will in turn constrain the growth rate if the galaxy bias is known.

However, to the great dismay of cosmologists everywhere, RSDs tend to behave in quite finicky ways. Non-linearities strongly affect redshift space, requiring elaborate models to understand the small-scale physics (e.g. Scoccimarro, 2004; Matsubara, 2008; Jennings et al., 2011) and even raising questions about the feasibility to do so (Kimura et al., 2018). Accounting for velocity dispersion is key and several analysis methods exist to do so (see de la Torre and Guzzo, 2012, and references therein for more details). In Chapter 3 we explore a method to calculate the full non-linear behaviour of RSDs in cosmic voids, constraining cosmology without the assumption of linearity.

1.7.5 Alcock-Paczyński Test

Related to RSDs, the Alcock-Paczyński (AP) test (Alcock and Paczynski, 1979) exploits spherical geometry to constrain cosmology. In principle, a perfectly

spherical object will have an equal ratio of its angular size to its radial size at a given redshift. Since isotropy of the Universe indicates that objects should have no preferential orientation to the line of sight, a measurement of the angular and radial size of spherical objects will be equal, given the underlying cosmological parameters are correct. However, since redshift does not actually measure the radial distance, peculiar velocities will affect the radial size of objects in redshift space. This requires an accurate understanding of RSDs in order to properly constrain cosmological parameters using the AP test. In theory, cosmic voids, which tend towards sphericity as they evolve, can be used as objects for the AP test (Ryden, 1995; Lavaux and Wandelt, 2012; Sutter et al., 2014; Mao et al., 2017; Nadathur et al., 2019b). However, to fully exploit voids in the AP test, their non-linear RSD dynamics need to be understood (see Section 3.6).

1.8 Cosmic Voids

1.8.1 A Brief History of Voids

Galaxy redshift surveys in the late 1970s first revealed voids observationally (Gregory and Thompson, 1978; Joeveer and Einasto, 1978), with the term 'void' first coined in 1978 (Chincarini, 1978; Chincarini and Rood, 1980). A seminal study by Zeldovich et al. (1982) linked the first observationally identified voids to the theory of structure formation. Around the same time, observations were underway of the canonical Bootes Void (Kirshner et al., 1981, 1987), with the results of the CfA redshift survey solidifying voids' place in both theory and observations of the LSS (de Lapparent et al., 1986). Some of the earliest theoretical studies of voids include explorations of perfectly spherical, isolated depressions in a uniform background (Hoffman and Shaham, 1982; Blumenthal et al., 1992) as well as evolution of 'holes' in an Einstein-de Sitter universe (Bertschinger, 1985). van de Weygaert and van Kampen (1993) expanded this idea, exploring voids as 'Super-Hubble Bubbles' forming and evolving in a hierarchical manner. Alongside the theoretical work, cosmologists also approached voids numerically. Some of the earliest numerical studies focused on the spherical tendency of voids (Icke, 1984), while others focused on exploring voids as bubble networks (Regos, 1991) and a hierarchical merging of spherical voids (Dubinski et al., 1993). At the turn of the century, the hierarchical picture of voids began to solidify with Goldberg and Vogeley (2004) simulating growth of voids in a FLRW Universe. At around the same time, Sheth and van de Weygaert (2004) introduced their seminal approach to void evolution by combining the spherical evolution model with the excursion set approach. As computing power increased, cosmologists' abilities to study the hierarchical model of void formation also increased (Aragon-Calvo and Szalay, 2013; Wojtak et al., 2016). One of the biggest questions regarding voids is how to define and identify voids in observations and simulations. The general definition of a void as a large, underdense region of the cosmic web gives cosmologists ample opportunity to flex

their creativity. When it comes down to technical definitions and identifications of voids, not all methods yield the same result. To address this issue, Colberg et al. (2008) decided to compare the 10 most prominent void finding algorithms available and test them on the same region of the Millennium simulation (Springel et al., 2005). As evident in Fig. 1.8, different methodologies define and identify voids in a varied manner. This figure shows the dark matter distribution of a 5 h^{-1}Mpc slice of the Millennium simulation (Springel et al., 2005) in the upper left panel with the galaxy distribution of that slice in the upper middle panel. The remaining panels show the locations of the largest void (with dark matter particles inside the void marked green), its centre (red circle), and all void galaxies (blue dots) identified by 10 different void finders. We see that the shape, size, and centre of the void varies amongst the 10 void finders. No full consensus exists as to which methodology reigns supreme, and in fact, the most optimal void finder may differ from science case to science case. One of the most widely used methods for void finding relies of the watershed technique. These void finders do not assume any geometry or shape of a void and allow the cosmic web to define the void and minimise parameters. Some example of these void finders are WVF (Platen et al., 2007), ZOBOV (Neyrinck, 2008), and VIDE[16] (Sutter et al., 2012b). In Section 4.2.1, I provide more thorough details on the watershed void finder ZOBOV.

As the cosmological community began to fully realise the potential of voids as sensitive probes of cosmology, a surge of interest for voids arose. Furthermore, as more and more observations came to light, Tully et al. (2008) showed that the Milky Way lies at the edge of our Local Void and moves away from it at ~ 260 km/s, so studying void dynamics directly aides us in understanding the behaviour of galaxies in our Local Group. Interestingly, as such observations accumulated, Peebles (2001) suggested that the lack of faint galaxies in void regions poses a challenge to the current cosmological paradigm. This environment-dependent scarcity became known as the Void Phenomenon. However, subsequent studies suggest that the mass of the dark matter halo, rather than the environment of the halo, drives galaxy formation, naturally explaining the Void Phenomenon in a ΛCDM cosmology (Tinker and Conroy, 2009). As discussed in Section 1.8.3, voids have emerged as unique cosmic laboratories to probe dark energy and modified gravity. Furthermore, they constitute pristine regions in which astrophysicists can explore the formation and evolution of galaxies. But before we explore the plethora of applications for voids, I will introduce a model for void evolution that will be used in Chapter 3.

1.8.2 Evolution of Voids - Much Ado About Nothing

The spherical evolution model (Gunn and Gott, 1972) describes the formation of overdense halos, and can also describe the evolution of underdense voids (Peebles, 1980; Blumenthal et al., 1992; Sheth and van de Weygaert, 2004). Applying

[16] VIDE is actually based on ZOBOV with some modifications.

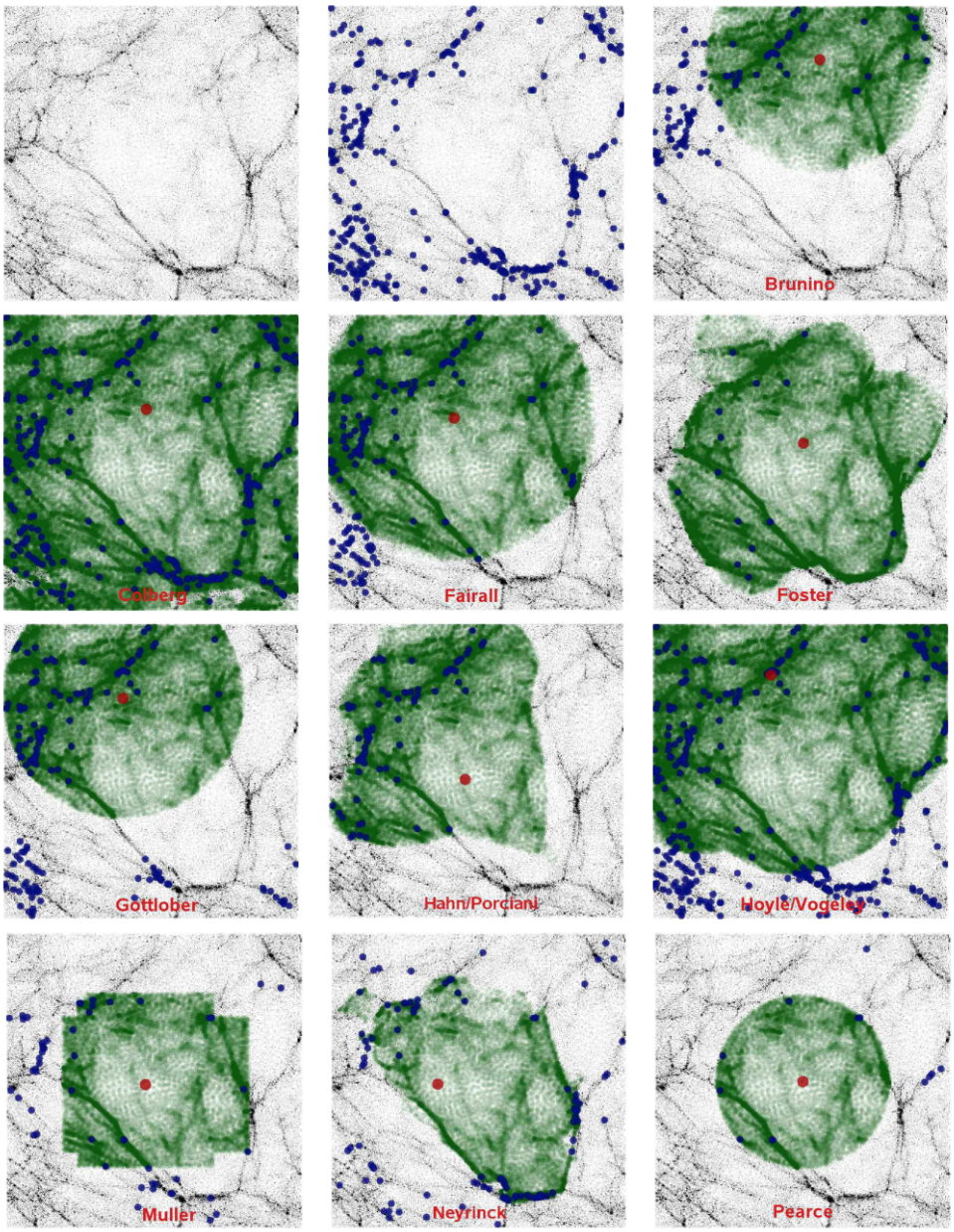

Figure 1.8 Comparison of 10 out of 13 void finders from Colberg et al. (2008) on the same patch of the Millennium simulation. The red dot defines the centre of each void, with the dark matter particles associated with the void identified in green and the void galaxies in blue. This figure clearly shows the myriad of ways to identify the same underdense region of the Universe.

this analytical evolution model, a statistical framework of collapsed, virialised objects was derived by Press and Schechter (1974) and further developed by other groups (Epstein, 1983; Bond et al., 1991) to constitute the *excursion set approach*, explaining the origin of hierarchical, gravitational clustering. The excursion set approach provides a tool to count the number of collapsed and virialised objects, accounting for mis-counting of virialised objects due to the cloud-in-cloud problem (Bardeen et al., 1986). The cloud-in-cloud problem states that in a hierarchical model of structure formation, larger halos (clouds) contain smaller ones within them leading to a mis-count of the number of distinct halos. Despite being originally developed for halos, voids accept the excursion set approach more easily (Sheth and van de Weygaert, 2004). In the hierarchical model discussed here, a void is defined as a primordial underdensity that reaches the shell-crossing regime (Blumenthal et al., 1992; Dubinski et al., 1993; Sheth and van de Weygaert, 2004). Unlike the evolution of a density peak, underdense perturbations tend to become more spherical as they expand and approach a shape better described by a spherical top-hat profile (technically speaking, an inverse top-hat) (Icke, 1984). It has been argued that applying a hierarchical excursion set model of evolution to voids, rather than to halos, describes the LSS more accurately since halos tend to clump together to form complex structures, such as walls, sheets, and filaments, whereas voids evolve to a more spherical shape (Sheth and van de Weygaert, 2004). Evolution of the structure from a void-based model suggests that structure forms as voids expel matter from their inner regions creating a boundary wall around the void. As neighbouring voids expand, they squeeze matter into sheets and filaments as their walls intersect (Icke, 1984; Regos, 1991; van de Weygaert, 1991; Dubinski et al., 1993; van de Weygaert and van Kampen, 1993; van de Weygaert, 2002). Eventually, these colliding voids merge into a single, larger void, however this merging depends on the definition of a void (Aragon-Calvo and Szalay, 2013).

This hierarchical formation of voids raises an issue: not only do smaller voids disappear as they combine to form larger ones (analogous to the cloud-in-cloud problem for halos), but they also disappear if a small void exists within a larger overdensity, making the statistical evolution of voids a two-barrier problem (Sheth and van de Weygaert, 2004). This introduces more complications since now the excursion set approach must account for both the void-in-void and the void-in-cloud problems. Fig 1.9 provides a visual representation of the excursion set formalism for both halos and voids. The following provides a row-by-row overview of the figure:

- Cloud-in-cloud scenario: the random walk of density fluctuations (left panel) crosses the halo formation barrier twice, meaning that separate overdense regions (middle panel) collapse to form a more massive overdense region at a later time (right panel).
- Cloud-in-void scenario: the random walk initially crosses the halo formation barrier and then the void formation barrier, thus an overdense region virialises within larger underdensity. As the middle and right panels show,

the formation of a bona-fide void does not destroy a halo that has formed within it.

- Void-in-void scenario: the random walk crosses the void formation barrier twice, suggesting that smaller voids combine to form a larger void. This is analogous to the cloud-in-cloud process. One difference between void-in-void and cloud-in-cloud scenarios is that subvoids within other voids remain separate in position, while clouds-in-clouds are subhaloes, distinct only in phase space.

- Void-in-cloud scenario: the random walk crosses the void formation barrier and then the halo formation barrier, meaning that a void has formed within a larger overdense region that is destined to become a halo. As the middle and right panels show, the formation of the halo squeezes the void, eventually destroying it completely.

From this figure we see that unlike halos (clouds), which are conserved in number even if they form within voids, voids can become eradicated if they reside within a larger, overdense field, making void evolution a two-barrier problem. Using this approach leads to some interesting conclusions. Since a virialised halo signifies a collapsed object, by definition it cannot host a void inside itself. Therefore, if the random walk crosses the barrier for collapse, $\delta_{\rm c} = 1.686$, before it crosses the void formation barrier, $\delta_{\rm v} = -2.81$, a large halo will contain a smaller void within it[17]. As this region collapses, the void diminishes and eventually no longer exists, so it should not be counted as a genuine void. There exists a subtlety though in the void-in-cloud problem. This arises with the choice of $\delta_{\rm c}$: if the collapse barrier equals to the turnaround density, *i.e.* $\delta_{\rm c} = \delta_{\rm ta} = 1.06$, then the collapsing halo has not yet destroyed the void inside it, but choosing the density contrast value for full collapse, $\delta_{\rm c} = 1.686$, then all voids inside halos are eliminated. In either of these cases, a void counting issue arises since the former underestimates the abundance of large voids, whereas the latter overestimates the typical size of the void (Sheth and van de Weygaert, 2004). Fundamentally, the excursion set approach allows us to distinguish between voids and halos by suggesting that: although it is possible to have a cluster within a void, having a void within a cluster does not make physical sense.

As presented by Sheth and van de Weygaert (2004), the spherical evolution model assumes a single, isolated void with particular evolutionary characteristics described below:

- *Expansion* - unlike overdense regions which collapse, a void expands in comoving coordinates as it evolves. If a void were fully isolated, it would never stop expanding since no neighbouring structure would limit its expansion[18].

[17] The values for $\delta_{\rm c}$ and $\delta_{\rm v}$ come from the spherical evolution model (Gunn and Gott, 1972).

[18] This is only true for open or flat universes. In a closed universe, the void would eventually collapse upon itself.

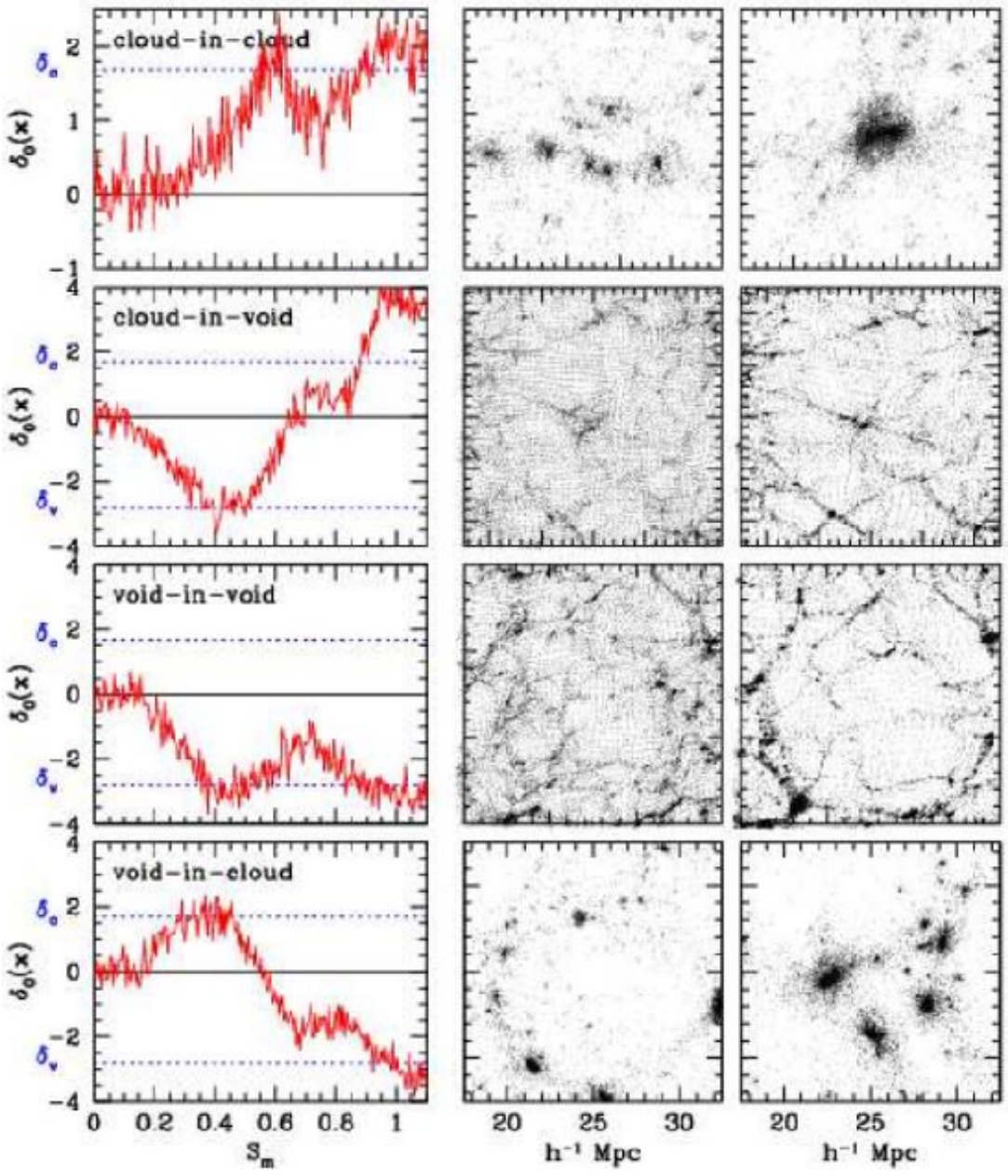

Figure 1.9 The plots in this figure show the 4 mode extended excursion set approach for both halos and voids. The left panels show a random walk of the density perturbation as a function of the parametrised mass smoothing scale, S_m defined by Eq. 1.40, whereas the middle and right panels show the evolution of particle distribution (Sheth and van de Weygaert, 2004).

- *Evacuation* - as a void expands, its inner density decreases. This occurs because the inner mass redistributes itself to the edges creating filaments and sheets, fuelled by the void's expansion. Mass loss to surrounding overdensities also decreases the density, which manifests as a second order, non-linear effect.

- *Spherical geometry* - the evolution of an expanding void tends towards a spherical geometry regardless of any initial asphericity. As a void expands and pushes material to its outskirts, its most underdense region lies within the centre of the void and becomes less underdense as a function of the void's radius.

- *Top-hat density profile* - since the effective outward repulsion of matter decreases as the distance from the centre increases, an initial inverse top-hat density profile can model the evolution of an expanding void. Because the interior matter distribution given by this profile is homogeneous, the peculiar velocity field diverges in a Hubble-like manner. This means that a void can effectively be described as a mini-FLRW universe making it a 'Super-Hubble Bubble.'

- *Suppressed structure growth* - since a void resembles an underdense universe, its density inhomogeneities become suppressed with less matter coalescing in a void as compared to the Universe on average. This causes a suppression in the growth of structure within voids.

- *Boundary ridge* - over time, the matter evacuating from the interior of the void accumulates and forms a boundary ridge defining its edges. As a result of the outward repulsion, the velocity field diverges from the interior of the void, causing the inner shells to move with a larger velocity than the outer ones.

- *Shell crossing* - eventually, the inner shells catch up to and overcome the outer ones inducing the epoch of shell crossing. This shell crossing regime, alongside the formation of a boundary ridge, defines a void in the hierarchical formalism described in Sheth and van de Weygaert (2004). Fig 1.10 shows the evolution of the density profile for a single, isolated void. This figure shows that as $a \to 1$, the interior of the void becomes more underdense as a ridge-like feature forms at the void's boundary.

Nevertheless, certain caveats and assumptions limit this formalism. The assumption of an isolated void poses a highly theoretical and unphysical scenario. In reality, voids will collide with other nearby voids, as well as other structures, complicating this model. Furthermore, since this model follows conservation of mass for a particular shell, it fails once it evolves into the shell crossing regime. This failure occurs due to a violation of conservation of mass within the spherical shells, where material from neighbouring shells crosses between shell boundaries and changes the initial mass of shells. Despite these idealised assumptions, this model for void evolution applies well to more generic, less

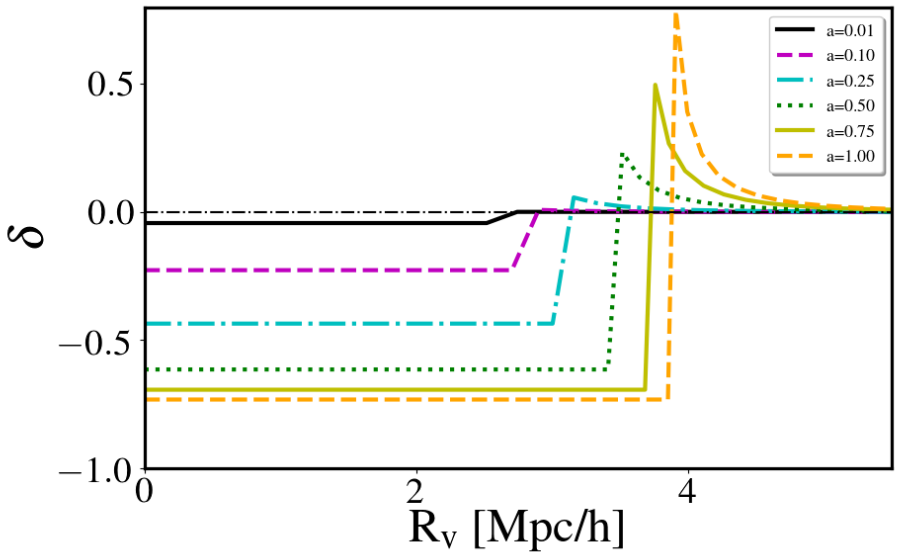

Figure 1.10 The evolution of the density profile for a single, isolated void following the characteristics described above.

symmetric circumstances and *N*-body simulations have shown that it can predict the hierarchical formation of voids (Dubinski et al., 1993; van de Weygaert and van Kampen, 1993; Demchenko et al., 2016).

1.8.3 Applications of Voids

RSDs and AP Test with Voids

A stacked sample of voids is on average intrinsically spherical in real space, thus voids constitute favourable candidates for the AP test (Ryden, 1995; Lavaux and Wandelt, 2012; Sutter et al., 2012a, 2014; Pisani et al., 2014; Hamaus et al., 2015, 2016; Mao et al., 2017). Lavaux and Wandelt (2012) forecasted that stacking voids could surpass BAO measurements in constraining cosmological parameters through the AP test. Sutter et al. (2014) apply this technique to SDSS Data Release 7 sample as well as Data Release 10 LOWZ and CMASS samples and find evidence for the AP test using this data. However, as discussed in Cai et al. (2016), RSDs can have a significant affect on the AP test by altering the shape of voids and thus need to be taken carefully into account. Since stacked voids are much more spherical as compared to galaxies or galaxy clusters and since the accuracy of the AP test relies on understanding the RSDs around voids, extensive work has gone into modelling and measuring the RSD signal around voids to constrain the growth rate (Hamaus et al., 2015; Cai et al., 2016; Hamaus et al., 2017; Achitouv, 2017; Achitouv et al., 2017; Hawken et al., 2017; Nadathur and Percival, 2019; Nadathur et al., 2019a). Several methods exist to extract the growth rate from the redshift-space void-galaxy correlation

function. For example, some groups (Cai et al., 2016; Hamaus et al., 2017) adopt the multipole decomposition approach discussed in Section 1.7.4, while others choose to employ the Gaussian streaming model (Hamaus et al., 2016; Achitouv et al., 2017; Hawken et al., 2017). Currently, the analysis of RSDs around voids from the SDSS BOSS data provides the tightest constraint from voids alone on $\Omega_{\rm m}$ (10% accuracy) and on β (12% accuracy) (Hamaus et al., 2017). However, some issues arise in this analysis, namely the enhancement of the growth rate measured from voids in the LOWZ sample, which is a counter-intuitive result since a suppression of the growth rate is expected. Such a result can arise from several reason, such as modified gravity or systematics within the data, but one known caveat of this analysis is the assumption of linearity for the RSD modelling. This assumption fails within the void, where the most non-linear dynamics exist. Clearly, cosmologists require more accurate models to measure the growth rate from void RSDs. Nadathur and Percival (2019) made some improvements by retaining higher order terms from the linear theory and including velocity dispersions, but they still keep the assumption of linearity between the density and peculiar velocity. The spherical model can overcome this assumption of linearity since the dynamics of the spherical evolution model yield non-linear density and velocity profiles (Demchenko et al., 2016; Massara and Sheth, 2018). In Section 3.6 I describe the application of the spherical model to constrain cosmology using non-linear RSDs around voids.

Weak Lensing and Modified Gravity with Voids

Several groups have also studied WL around voids (Amendola et al., 1999; Krause et al., 2013; Melchior et al., 2014; Clampitt and Jain, 2015; Sánchez et al., 2016; Cai et al., 2017; Davies et al., 2018). Although these studies use different techniques and void finding algorithms, they all show that WL of stacked voids can provide a statistically significant lensing signal. Optimising the geometry of voids, Cautun et al. (2015) provide a novel way to stack voids by using the distance from a void's boundary rather than its centre, which increases the lensing signal by up to two times. However, WL of voids poses several issues due to systematics in WL data itself (see Section 2.4 for more details), in addition to differences amongst various void finding algorithms and void definitions. Since WL measures the projected mass density, a stronger signal is expected from projected underdense regions as compared to 3D voids (Gruen et al., 2016; Friedrich et al., 2018; Gruen et al., 2018; Brouwer et al., 2018). These projected underdensities, known as troughs, take advantage of the projection of WL to increase the signal-to-noise of lensing around underdense regions. In order to understand the lensing signal from troughs, Friedrich et al. (2018) created a model that uses perturbation theory to predict this signal for a given cosmology. One of the benefits of WL from voids and troughs is that their measured density profiles can be compared to predicted density profiles from various theories of modified gravity (Li et al., 2012; Cai et al., 2015; Zivick et al., 2015; Lam et al., 2015; Barreira et al., 2015; Falck et al., 2018; Cautun et al., 2018; Baker et al., 2018). Since voids may not succumb to the

effects of screening mechanisms (see Section 1.6.4), their density profiles can show deviations between the lensing and Newtonian potentials (Cautun et al., 2018; Baker et al., 2018). In fact, Cautun et al. (2018) explored how modified gravity affects the density profiles obtained from lensing for both voids and troughs. They find that both voids and troughs can distinguish between different theories of gravity, however, since lensing is a projected effect, troughs have a higher amplitude in their signal-to-noise and distinguish between theories of gravity better than voids do (Cautun et al., 2018). Furthermore, since modifications to General Relativity will affect the expansion of voids, the RSD signal around voids will change due to its sensitivity to velocities. This means that the growth rate will also differ between theories of gravity, placing more significance on the importance of theoretical modelling for RSDs around voids. In addition, studies suggest that a combination of WL and RSDs with overlapping datasets can help diminish cosmic variance and increase the constraining power of cosmological surveys (Bernstein and Cai, 2011; Cai and Bernstein, 2012). Thus, as presented in Chapter 3, the combination of WL and RSDs around voids has the potential to provide power constraints on cosmological parameters.

Integrated Sachs-Wolfe Effect with Voids

The signal of the Integrated Sachs-Wolfe (ISW; Sachs and Wolfe, 1967) effect from voids has also been explored (Granett et al., 2008; Nadathur et al., 2012; Flender et al., 2013; Planck Collaboration et al., 2014; Ilić et al., 2013; Cai et al., 2014; Kovács and Granett, 2015; Planck Collaboration et al., 2015; Aiola et al., 2015; Kovács, 2018; Kovács et al., 2019). The ISW effect arises as a secondary imprint of hot and cold spots on the CMB, emerging from the evolution of gravitational potentials as the universe expands. Potentials that decay due to the accelerated expansion of the universe heat (cool) photons that pass through clusters (voids), creating a secondary imprint of hot (cold) spots. Some studies using the ISW effect find significant deviation of the signal from the predicted ΛCDM signal (Granett et al., 2008; Nadathur et al., 2012), while others do not (Flender et al., 2013; Hotchkiss et al., 2015). This tension likely stems from different groups using different definitions of voids, nevertheless there are strong indications that an accurate measure of the ISW signal can provide powerful constraints on the nature of dark energy.

Dark Energy with Voids

To that effect, several groups have explored the effect of the dark energy equation-of-state, w, on voids. Since dark energy dominates the evolutionary behaviour of voids, various expansion histories of dark energy, for example a constant or time-dependent equation-of-state, alter the void number function and ellipticity (Lee and Park, 2009; Lavaux and Wandelt, 2010; Bos et al., 2012; Sutter et al., 2015; Pisani et al., 2015). In this vein, Lavaux and Wandelt (2012) have shown

that even if individual voids have non-spherical shapes, due to the isotropy and homogeneity of the Universe, the average shape of stacked voids is expected to be spherical. They show that the AP test is particularly sensitive to the present day equation-of-state, w_0, and knowing w_0 to a few percent accuracy could make the AP test of stacked voids outperform cosmological constraints from traditional galaxy clustering methods.

Neutrinos with Voids

As observations and simulations increase in their accuracy, unravelling the mass of neutrinos arises as a compelling, yet enigmatic and elusive aspect of the standard model of cosmology. The discovery of neutrino oscillations solidified the belief that neutrinos must have mass (see Ahmed et al., 2004, and references therein), with cosmology placing stringent constraints on the sum of neutrino species' masses (e.g. Planck Collaboration et al., 2018a). Neutrinos tend to behave similarly to CDM, contributing to structure formation on scales larger than their free-streaming length, which itself depends on the neutrino species' masses. Conveniently, the typical size of voids span the range of free-streaming lengths for neutrinos and due to the underdense nature of voids, they are particularly sensitive to neutrinos as compared to overdense regions (Massara et al., 2015; Banerjee and Dalal, 2016; Kreisch et al., 2018). The void number function, void shape distribution, and void clustering are all sensitive probes to the underlying properties of neutrinos. For example, Kreisch et al. (2018) show how galaxy bias affects void clustering for different neutrino masses.

Galaxy Evolution with Voids

In addition to all the benefits voids provide to the cosmological community, they are also an important concept for the galaxy evolution community. Since the formation of galaxies is a highly complex process, difficulties arise when astrophysicists try to disentangle the various components contributing to galaxy evolution. However, since galaxies within voids reside in isolated conditions, these galaxies evolve in a self-similar way. According to the hierarchical model of structure formation, voids contain relatively under-developed galaxies since it's statistically less likely that these galaxies will interact with other galaxies. Overall, galaxies within voids tend to be blue, star-forming spiral galaxies (Grogin and Geller, 1999; Rojas et al., 2004; van de Weygaert et al., 2011; Ricciardelli et al., 2014). As discussed above, modified gravity affects the structure and evolution of voids, thus directly affecting the properties of galaxies between underdense and overdense regions (Hui et al., 2009; Zhao et al., 2010; Jain, 2011; Jain and VanderPlas, 2011; Cabré et al., 2012). An uncertainty persists within the galaxy formation community as to whether the local or global density plays

the most significant role in galaxy evolution (e.g. Kraljic et al., 2018)[19]. Upcoming surveys, such as Euclid and WFIRST, alongside advancement in hydrodynamical simulations, will soon disentangle this mystery and voids will play a crucial role in this endeavour.

A variety of other studies on voids exist such as: coupled dark energy (Pollina et al., 2016), the nature of dark matter (Yang et al., 2015), BAO in void clustering (Achitouv and Blake, 2015; Kitaura et al., 2016; Liang et al., 2016; Zhao et al., 2018), and halo bias (Neyrinck et al., 2014) and galaxy bias around voids (Pollina et al., 2018). Overall, voids exhibit potential to constrain the nature of gravity and dark energy from a variety of methods and constitute an active area of research. The advantages of using voids as probes of the dark universe includes their underdense nature providing a 'mini-FLRW' universe, in which dark energy domination begins at an earlier epoch compared to the universe as a whole, and their tendency towards a generally spherical geometry. Despite these advantages, several issues persist, such as the lack of a coherent void definition and the lack of consistency between void finding algorithms.

Recognising the need for accurate modelling to describe the non-linear regime of voids and to place constraints on modified gravity and dark energy, I embark upon a journey to provide such a model. In this thesis, I describe my contribution to the field of cosmic voids by expanding upon the basic theory of void evolution, using it to present a non-linear model for RSDs around voids. Seeing the need to test this model with observable measurements, I then explore the possibility of weak lensing with voids in the spectroscopic galaxy redshift survey, GAMA. Finally, I analyse the cosmological dependence of projected underdensities, exposing the aptitude of the underdense regions of our Universe to constrain cosmology.

[19]Global refers to the location within the large-scale structure (such as clusters, voids, or filaments), while local refers to the individual halo properties.

Even if I knew that tomorrow the world would go to pieces, I would still plant my apple tree.

Martin Luther

2

Gravitational Lensing

According to Einstein's theory of relativity, photons propagate along null geodesics, where the FLRW metric (Eq. 1.2) describes the homogeneous, isotropic space-time through which the photons propagate. According to the theory of relativity, the gravitational fields of massive objects perturb the path of the light ray causing the initially straight path to curve. This phenomenon is known as gravitational lensing and can, for majority of astrophysical cases, be described by the geometry of a gravitational lens. In this chapter, I will present the basic principles of gravitational lensing, in particularly focusing on the weak gravitational lensing regime. There are several thorough reviews on the principles and application of gravitational lensing (e.g. Wambsganss, 1998; Bartelmann and Schneider, 2001; Bartelmann, 2010; Kilbinger, 2015; Mandelbaum, 2018), however throughout this chapter I will follow the notation of Bartelmann and Schneider (2001).

2.1 The Fundamentals of Lensing

Fig. 2.1 presents a schematic diagram of a typical lensing system. In this representation, a concentrated amount of mass at the 'lens plane,' located at an angular diameter distance D_l from the observer, deflects light rays from a source at the 'source plane' located at D_s from the observer. I will refer to the foreground mass causing the distortion as the *lens* and the luminous, background mass being distorted as the *source*. A common assumption, known as the thin lens approximation, assumes that the lens instantaneously deflects the light from the source (see Seitz et al., 1994). Although, strictly speaking this is not true,

in most astrophysical systems considered, the size of the lens along the line-of-sight direction is much smaller than the angular diameter distances considered, validating this approximation.

As indicated by Fig. 2.1, the foreground lens displaces the perceived location of the source from its true position. Observers do not know the true location of the source, however the deflection angle, $\hat{\boldsymbol{\alpha}}$, relates to the impact parameter ξ such that,

$$\hat{\boldsymbol{\alpha}} = \frac{4GM}{c^2\xi}, \tag{2.1}$$

where G is the gravitational constant, c is the speed of light, and M is the mass of the lens, considered as a point mass. This equation holds only if the impact parameter is much larger than the Schwarzschild radius of the lens *i.e.* $\xi \gg R_{\rm s} \equiv 2GMc^{-2}$. We note that this deflection angle is exactly twice of the angle obtained from Newtonian gravity. This equation shows that the amount of distortion due to gravitational lensing relates not only to the mass of the lens, but also to the radial proximity of the source to the lens. Were the source to align directly behind the lens, the distorted image would appear circular, known as an Einstein Ring. The radius of this ring, known as the Einstein Radius, $\theta_{\rm E}$, relates to the mass of the lens via,

$$\theta_{\rm E} = \frac{4GM}{c^2}\frac{D_{ls}}{D_l D_s}. \tag{2.2}$$

If there were no lens in between the source and the observer, the observer would see the source at angle $\boldsymbol{\beta}$, however the presence of the lens deflects the light by an angle $\hat{\boldsymbol{\alpha}}$, causing the observer to see the source at angle $\boldsymbol{\theta}$. In most typical lensing situations, all of these angles are small. With the small angle approximation, the geometry in Fig. 2.1 yields the lensing equation,

$$\boldsymbol{\theta} D_s = \boldsymbol{\beta} D_s - \hat{\boldsymbol{\alpha}} D_{ls}, \tag{2.3}$$

which reduces to,

$$\boldsymbol{\theta} = \boldsymbol{\beta} - \boldsymbol{\alpha}, \tag{2.4}$$

by defining $\boldsymbol{\alpha} = \hat{\boldsymbol{\alpha}} D_{ls}/D_s$. From this equation, we can relate the observed angular position of the image, $\boldsymbol{\theta} = \xi/D_l$, to the reduced deflection angle, $\boldsymbol{\alpha}$.

Considering an isolated distribution of mass, $\rho(\mathbf{r})$, we can approximate the deflection angle produced by the total mass distribution as the sum of the deflection angles produced by a series of point masses constituting the full mass distribution. We assume that a deflected light ray passing through the

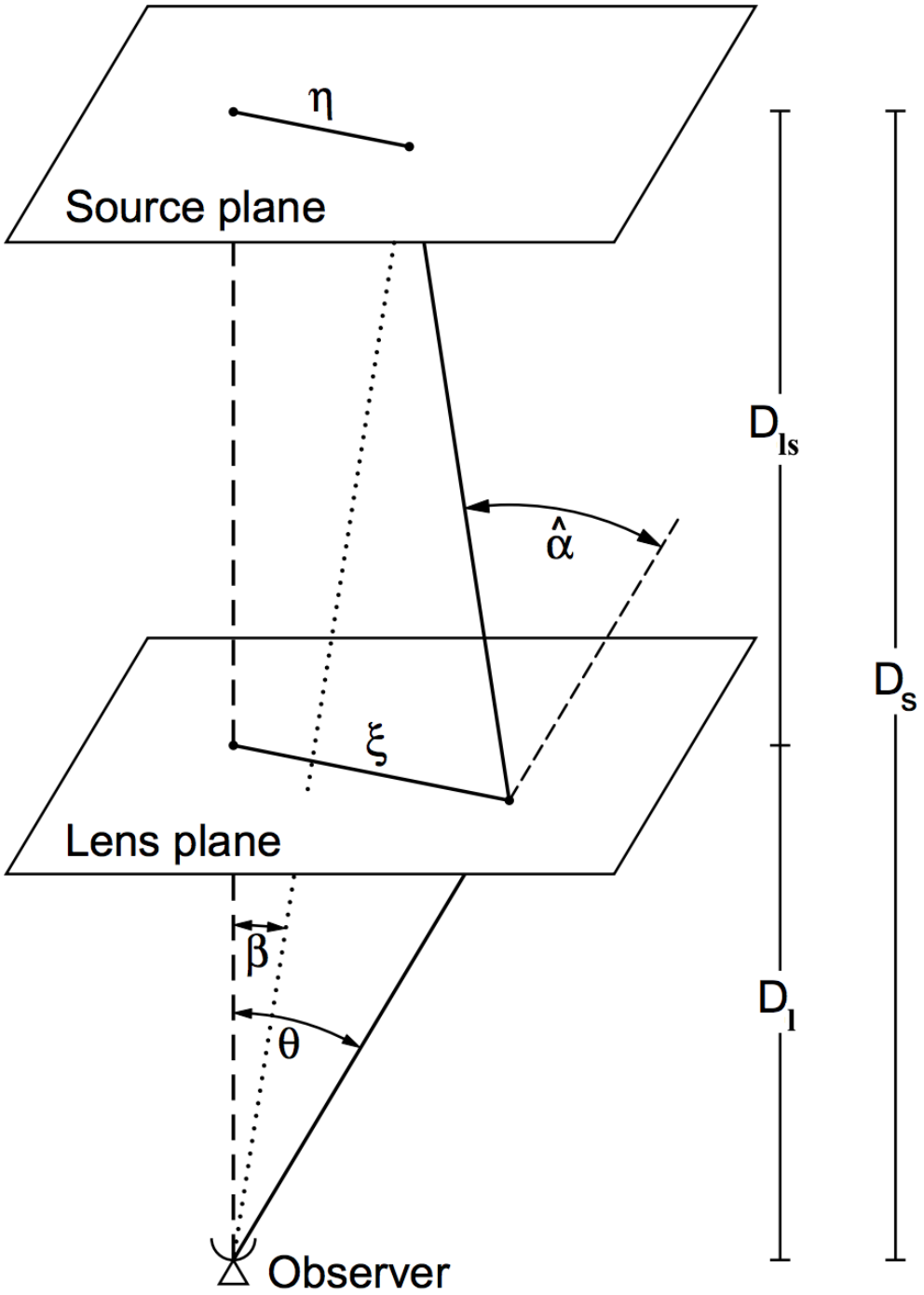

Figure 2.1 A sketch representing a typical gravitational lensing system adapted from Bartelmann and Schneider (2001). The lens located at the lens plane deflects the light as it propagates from the source located at η. Were there to be no lens, the observer would see the source at angle $\boldsymbol{\beta}$, however the deflection angle $\hat{\boldsymbol{\alpha}}$ and the impact parameter ξ make the source appear at angle $\boldsymbol{\theta}$ to the observer. D_s, D_l, and D_{ls} represent the angular diameter distances to the source, the lens, and between the source and lens, respectively.

distribution propagates in a straight line in the region of the deflected mass. This corresponds to the Born approximation (Born, 1926) and applies as long as the true deviation of the light ray from a straight line within the mass distribution is small compared the scale at which the mass distribution changes significantly. From this, Bartelmann and Schneider (2001) rewrite the deflection angle as,

$$\hat{\boldsymbol{\alpha}}(\xi) = \frac{4GM}{c^2} \int d^2\xi' \Sigma(\xi') \frac{\xi - \xi'}{|\xi - \xi'|^2}, \tag{2.5}$$

defining the 2D surface mass density of the lens as,

$$\Sigma(\xi) = \int \rho(\xi, z) dz, \tag{2.6}$$

where ρ represents the 3D mass density and z is the line-of-sight direction. This approximation holds true under the thin lens approximation, which allows us to assume that the whole lensing mass lies on a 2D plane. Using the previous two equations, Bartelmann and Schneider (2001) rewrite the reduced deflection angle as,

$$\boldsymbol{\alpha} = \frac{\Sigma}{\Sigma_{\rm crit}} \boldsymbol{\theta}, \tag{2.7}$$

where $\Sigma_{\rm crit}$ represents the critical surface mass density of the lens, defined as,

$$\Sigma_{\rm crit} = \frac{c^2}{4\pi G} \frac{D_s}{D_l D_{ls}}. \tag{2.8}$$

In the case of $\boldsymbol{\alpha} = \boldsymbol{\theta} = \boldsymbol{\theta}_{\rm E}$, we can define $\Sigma = \Sigma_{\rm crit}$.

We can further introduce a generalised, dimensionless surface mass density, known as convergence, κ,

$$\kappa(\boldsymbol{\theta}) = \frac{\Sigma(\xi)}{\Sigma_{\rm crit}}. \tag{2.9}$$

If the surface mass density exceeds the critical surface mass density, *i.e.* $\kappa \geq 1$, the lens will produce multiple source images, known as the strong lensing regime. Thus, we utilise convergence as a distinguishing quantity between strong ($\kappa \geq 1$) and weak ($\kappa \ll 1$) lensing regimes.

Integrating over the convergence, Bartelmann and Schneider (2001) define the lensing potential as,

$$\psi(\boldsymbol{\theta}) = \frac{1}{\pi} \int \kappa(\boldsymbol{\theta'}) \ln|\boldsymbol{\theta} - \boldsymbol{\theta'}| d^2\theta', \tag{2.10}$$

such that lensing potential relates to the reduced deflection angle as,

$$\boldsymbol{\alpha}(\boldsymbol{\theta}) = \nabla_\theta \psi(\boldsymbol{\theta}), \tag{2.11}$$

i.e. the deflection angle is the gradient of the deflection potential. As the Laplacian of the lensing equation satisfies Poisson's equation, $\nabla^2_\xi \Phi = 4\pi G \rho(\xi, z)$, where Φ represents the gravitational potential,

$$\begin{aligned} \nabla^2_\theta \psi &= \frac{D_l D_{ls}}{D_s} \frac{2}{c^2} \int \nabla^2_\xi \Phi \\ &= 2\frac{\Sigma(\xi)}{\Sigma_{\rm crit}} = 2\kappa(\boldsymbol{\theta}). \end{aligned} \tag{2.12}$$

Having briefly introduced the basic concepts of gravitational lensing, I will now focus on the weak lensing regime.

2.2 Weak Lensing Theory

In this section, I will summarise the fundamental aspects of weak gravitational lensing, referring the reader to Bartelmann and Schneider (2001) and Schneider (2005) for a more thorough analysis.

Given that lensing conserves surface brightness (Kristian and Sachs, 1966), as gravitational lensing increases the area of a source image, the observer sees a magnification, μ, such that,

$$\mu = \frac{\text{image area}}{\text{source area}} = \frac{\delta\theta^2}{\delta\beta^2}, \tag{2.13}$$

where part of the source $\delta\beta^2$ maps onto an area of the image $\delta\theta^2$. Practically, lensing adds photons onto a section of the image plane that would have been devoid of photons without the effect of gravitational lensing. Given a source small enough such that the convergence does not change across the image, there exists a mapping between the source and image plane,

$$\delta\beta_i = A_{ij}\delta\theta_j, \tag{2.14}$$

where A_{ij} is the lensing Jacobian defined as,

$$\begin{aligned} A_{ij} &= \frac{\delta\beta_i}{\delta\theta_j} = \frac{\delta}{\delta\theta_j}[\theta_i - \alpha_i(\boldsymbol{\theta})], \\ &= \delta_{ij} - \frac{\delta\alpha_i\boldsymbol{\theta}}{\delta\theta_j}, \\ &= \delta_{ij} - \frac{\delta^2\psi\boldsymbol{\theta}}{\delta\theta_i\delta\theta_j}. \end{aligned} \tag{2.15}$$

This leads to the distortion matrix, **A**, defined as:

$$\mathbf{A} = \begin{pmatrix} 1-\kappa-\gamma_1 & -\gamma_2 \\ -\gamma_2 & 1-\kappa-\gamma_1 \end{pmatrix}, \tag{2.16}$$

where γ represents the complex magnitude of shear at orientation ϕ induced by the lensing potential:

$$|\gamma| = \gamma_1 + i\gamma_2 = e^{2i\phi}, \tag{2.17}$$

where

$$\gamma_1 = \frac{1}{2}(\psi_{11} - \psi_{22}) = |\gamma|\cos(2\phi), \tag{2.18}$$

$$\gamma_2 = \psi_{12} = \psi_{21} = |\gamma|\sin(2\phi). \tag{2.19}$$

In the two equations above, the nomenclature of e.g. $\psi_{11} = \partial_1^2\psi$ represents the second derivative of the lensing potential. Using the complex gradient operator, $\partial = \partial_1 + i\partial_2$, Bartelmann and Schneider (2001) succinctly relate the shear to the convergence showing that shear is the second order gradient of the lensing potential: $\gamma = \partial^2\psi$. Using this same notation, they then rearrange Eq. 2.12 to compactly define convergence as,

$$\kappa(\boldsymbol{\theta}) = \frac{\psi_{11} + \psi_{22}}{2}. \tag{2.20}$$

They then define the magnification as the determinant of the inverse of the distortion matrix, $\mathrm{A} = 1/\det(\mathbf{A})$,

$$\mu = \frac{1}{(1-\kappa)^2 - \gamma^2}. \tag{2.21}$$

Fig. 2.2 shows how shear and convergence affect an originally circular image. As shown in the right image of Fig. 2.2, convergence enlarges the original image in

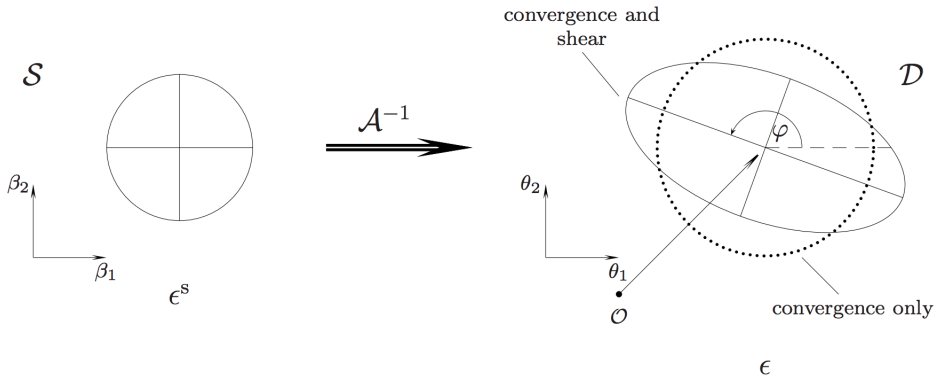

Figure 2.2 Diagram from Schneider (2005) of the effect of shear and convergence in a lensed image (right), compared to the original, circular image (left). The shear stretches an image, while the convergence cause an enlargement in the radial direction.

the radial direction, while shear stretches it, causing an ellipsoidal image whose orientation depends on the amplitude of the individual shear components. Fig. 2.3 shows the orientation and distortion of an originally circular image based on the amplitude of the shear components. We see that $\gamma \rightarrow -\gamma$ results in a 90° rotation and that γ_2 is at a 45° angle to γ_1. There are higher order terms that affect the shape of the lensed image, however since I do not exploit these higher order terms, I will not introduce them and refer the reader to Bacon et al. (2006).

To summarise the relation between shear and convergence, Schneider and Seitz (1995) introduce the reduced shear,

$$g(\boldsymbol{\theta}) = \frac{\gamma(\boldsymbol{\theta})}{1 - \kappa(\boldsymbol{\theta})}, \tag{2.22}$$

such that

$$A = (1 - \kappa) \begin{pmatrix} 1 - g_1 & -g_2 \\ -g_2 & 1 + g_1 \end{pmatrix}, \tag{2.23}$$

which clarifies that convergence functions as a scalar and thus only affects the size/magnification of the lensed image, whereas the shear affects the shape (ellipticity) of the lensed image (see Fig. 2.2).

Observationally, we can only measure the shape of a lensed galaxy and thus, according to Eq. 2.23, only obtain information about its reduced shear. Fig. 2.3 shows the relationship between the ellipticity components and we note that for a perfect ellipse, these components relate to each other through the axial ratio, β, and the position angle, ϕ, measured from the x-axis in the counter-clockwise

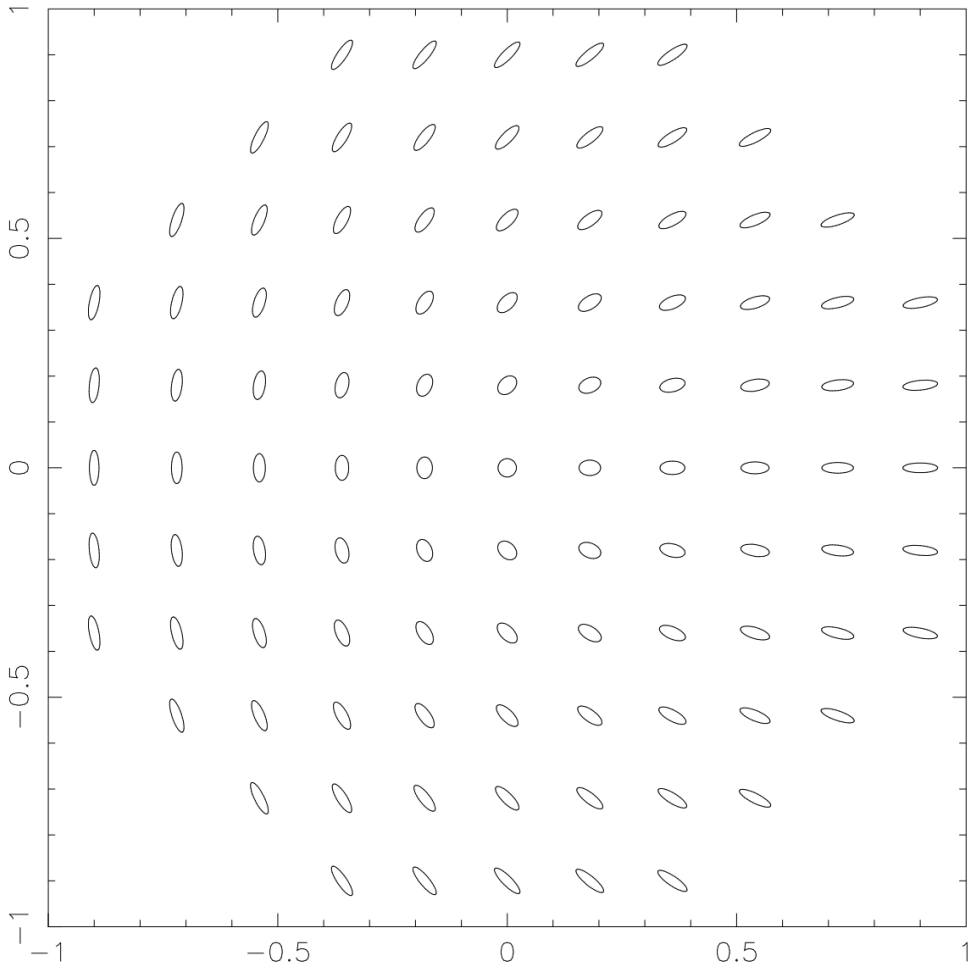

Figure 2.3 Shear orientations of an originally circular image ($\gamma_1 = \gamma_2 = 0$) depending on the amplitude of the shear components. The x-axis represents the γ_1 component and the y-axis represents the γ_2 component (Schneider, 2005).

direction such that,

$$\begin{pmatrix} e_1 \\ e_2 \end{pmatrix} = \frac{\beta^2 - 1}{\beta^2 + 1} \begin{pmatrix} \cos 2\phi \\ \sin 2\phi \end{pmatrix}. \tag{2.24}$$

Mapping the ellipticity of the image to the ellipticity of the source, the image is transformed by the lensing Jacobian in Eq. 2.23 yielding a complex source ellipticity, e^{s}, derived by Seitz and Schneider (1997),

$$e^{\mathrm{s}} = \frac{e - g}{1 - g^* e}, \tag{2.25}$$

where g^* represents the complex conjugate of g. In the weak lensing regime, since $\kappa \ll 1$ and $|\gamma| \ll 1$, we can approximate the reduced shear as $|g| \sim |\gamma|$ and $g^2 \approx 0$, therefore reducing the source ellipticity to its linear form,

$$e_i \approx e_i^{\mathrm{s}} + g. \tag{2.26}$$

We can assume that the intrinsic ellipticity of the sources is random, thus with a sufficiently large amount of imaged source galaxies, $\langle e^{\mathrm{s}} \rangle = 0$. Averaging over many sources with a constant shear and taking the case where all the source images are perfectly circular, $e^{\mathrm{s}} = 0$, we arrive at a relationship between shear and ellipticity,

$$\gamma \simeq \langle e \rangle \equiv e_1 + i e_2, \tag{2.27}$$

which I will use throughout this thesis when analysing both simulations and observational data.

2.3 Weak Lensing Estimation

In this section, I introduce the two key weak lensing estimators: cosmic shear and galaxy-galaxy lensing. This section's aim is to familiarise the reader with the estimators and measurements of weak lensing, but an in-depth discussion of these appears in *e.g.* Bartelmann and Schneider (2001); Schneider (2005).

2.3.1 Correlation Function - Power Spectrum Relationship

There are two main ways to estimate weak gravitational lensing through two-point statistics: the correlation function, $\xi(r)$, and the power spectrum, $P(k)$, where k is the wave number as introduced in Section 1.6.1. The power spectrum

(more precisely the matter power spectrum) describes the density contrast, or clumpiness, of matter on various scales (high k represents small physical scales and vis-a-versa). Correlations of galaxy shapes as a function of angular separation on the sky can be utilised to derive the matter power spectrum (e.g. Bartelmann and Schneider, 2001; Schneider, 2005). On large scales, linear theory dominates structure growth and the density field follows a Gaussian distribution, thus the power spectrum alone can describe the density field. However, on scales where gravitational collapse becomes non-linear (such as within a galaxy where $k \gtrsim 10$), higher order statistics such as the bispectrum or trispectrum become necessary to understand the density field to a higher precision. In order to define the relation between these two statistics, we can consider a homogeneous and isotropic density field, $\delta(\mathbf{x})$, which, by definition, statistically cannot depend on orientation or location in the field. Thus the two-point correlation function only depends on the absolute distance between the two points, $r = |\mathbf{x} - \mathbf{x}'|$, such that,

$$\xi(r) = \langle \delta(\mathbf{x}) \delta^*(\mathbf{x}') \rangle. \tag{2.28}$$

We can now define the Fourier transform of δ in n dimensions as,

$$\begin{aligned} \hat{\delta}(\mathbf{k}) &= \int d^n x \, \delta(\mathbf{x}) e^{i\mathbf{x}\cdot\mathbf{k}}, \\ \delta(\mathbf{x}) &= \frac{1}{(2\pi)^n} \int d^n \hat{\delta}(\mathbf{k}) e^{-i\mathbf{x}\cdot\mathbf{k}}, \end{aligned} \tag{2.29}$$

where the correlation function in Fourier space is,

$$\langle \hat{\delta}(\mathbf{k}) \hat{\delta}^*(\mathbf{k}') \rangle = \int d^n x e^{i\mathbf{x}\cdot\mathbf{k}} \int d^n x' e^{i\mathbf{x}'\cdot\mathbf{k}'} \langle \delta(\mathbf{x}) \delta^*(\mathbf{x}') \rangle. \tag{2.30}$$

We can redefine the above equation knowing that $\mathbf{x}'$ is independent of $\mathbf{x}$,

$$\langle \hat{\delta}(\mathbf{k}) \hat{\delta}^*(\mathbf{k}') \rangle = \int d^n x e^{i\mathbf{x}\cdot\mathbf{k} - \mathbf{k}'} \int d^n r e^{-i\mathbf{r}\cdot\mathbf{k}'} \xi(r). \tag{2.31}$$

Letting $f(\mathbf{k}) = \delta_D(\mathbf{k} - \mathbf{k}')$, where δ_D represents the Dirac delta function, we can take the Fourier inverse of $f(\mathbf{k})$ so that,

$$f(\mathbf{x}) = \frac{1}{(2\pi)^n} \int d^n k \, \delta(\mathbf{k} - \mathbf{k}') e^{-i\mathbf{x}\cdot\mathbf{k}} = \frac{1}{(2\pi)^n} e^{-i\mathbf{x}\cdot\mathbf{k}'}. \tag{2.32}$$

Using Eq. 2.29, we can write,

$$\delta_D(\mathbf{k} - \mathbf{k}') = \frac{1}{(2\pi)^n} \int d^n x e^{i\mathbf{x}\cdot(\mathbf{k} - \mathbf{k}')}, \tag{2.33}$$

which we can plug into Eq. 2.31 and simplify it to,

$$\begin{aligned}\langle\hat{\delta}(\mathbf{k})\hat{\delta}^{*}(\mathbf{k}')\rangle &= (2\pi)^{n}\delta_{D}(\mathbf{k}-\mathbf{k}')\int d^{n}r e^{-i\mathbf{r}\cdot(\mathbf{k}')}\xi(|\mathbf{r}|),\\ &= (2\pi)^{n}\delta_{D}(\mathbf{k}-\mathbf{k}')P(|\mathbf{k}'|),\end{aligned} \tag{2.34}$$

defining the power spectrum of a homogeneous, isotropic, random field, $P(|\mathbf{k}|)$, as the Fourier transform of the two-point correlation function, $\xi(|\mathbf{r}|)$,

$$P(|\mathbf{k}|) = \int d^{n}r e^{-i\mathbf{r}\cdot(\mathbf{k})}\xi(|\mathbf{r}|). \tag{2.35}$$

Thus, estimating two-point statistics allows us to access the power spectrum. In terms of weak lensing, the two statistics I will discuss, cosmic shear and galaxy-galaxy lensing, are functions of the effective convergence power spectrum, P_{κ}, which directly relates to the matter density power spectrum, P_{δ}, from which we can constrain cosmological parameters such as Ω_{m} and σ_{8}.

2.3.2 Cosmic Shear

Cosmic shear refers to a correlation in the imaged shapes of two galaxy pairs at an angular separation of $\theta \rightarrow \theta \pm \Delta\theta$. This correlation occurs because the cosmic web continuously deflects a light ray propagating from a source galaxy to our detectors. The statistics of these distortions and alignments directly relate to the underlying matter distribution that caused them. Considering that these distortions have a sub-percent effect on the galaxy shape, only through a sufficiently large sample of galaxies, with proper systematic error corrections, can we statistically measure this effect. It was initially measured at the turn of the millennium (Bacon et al., 2000; Van Waerbeke et al., 2000; Wittman et al., 2000). With the evolution of ever-deeper, wider, and more robust observations, as well as refined imaging techniques, cosmic shear has provided competitive constraints on cosmological parameters (e.g. Hildebrandt et al., 2017; Troxel et al., 2017; Hikage et al., 2018; Hildebrandt et al., 2018). Although cosmic shear cannot utilise the thin lens approximation since the cosmic web does not behave as a single lens plane, we can assume that the deflection angle is small, resulting in a convergence that depends on the redshift of the source, and thus measure the two-point correlation function from which we can deduce constraints on cosmological parameters. A benefit of cosmic shear is its independence from baryonic systematics such as galaxy bias. Moreover, cosmic shear helps to reduce degeneracies on cosmological constraints when compared to measurements from the CMB. Combining the constraints from these two observables helps hone in on fundamental cosmological parameters (Hildebrandt et al., 2017; Troxel et al., 2017; Hikage et al., 2018). However, since the intrinsic ellipticity of a single galaxy dominates any distortion to its

shape, we cannot measure cosmic shear for a single galaxy and have to rely on a large sample of source galaxies with the assumption that their ellipticities are randomly oriented on the sky. Thus, we can measure the cosmic shear signal in a statistical manner over many galaxies to reduce shape noise and assume that the mean intrinsic shape of galaxies will be circular. It can then be deduced that any deviation from sphericity results from weak lensing, however, due to systematic complications of the telescope and measurement pipelines (discussed in Section 2.4), measurement complications arise.

2.3.3 Galaxy-Galaxy Lensing

Alongside cosmic shear, which measures the correlations of the shapes of galaxies across the sky, we can obtain a correlation of the location of a lens galaxy with the shapes of source galaxies. Given a galaxy, or galaxy cluster, the images of source galaxies will align in a circular pattern around the lens with the intensity of distortions decreasing as a function of radial distance from the lens. As we measure the lensing distortion pattern of source galaxies around a lens in increasingly larger circular annuli, we paint a picture of the density profile of the lens, which informs us of the mass distribution of the lens itself. This lens position - source shape correlation is known as galaxy-galaxy lensing (GGL) (Valdes et al., 1983). Just as with cosmic shear, since the distortion signal in galaxy-galaxy lensing is weak, we need to approach this measurement in a statistical manner in order to reduce the effects of shape noise.

Theory

The shear $\gamma_{1,2}$ in Eqs. 2.18 and 2.19 is defined relative to a Cartesian coordinate system. For a GGL analysis it is more convenient to define these two shear components relative to the lens that the sources are centred on. We therefore define the tangential and cross shear components, $\gamma_{\rm t}$ and $\gamma_{\times}$, respectively, as:

$$\begin{aligned} \gamma_{\rm t} &= -\mathcal{R}[-\gamma e^{-2i\phi}] = -\cos(2\phi)\gamma_1 - \sin(2\phi)\gamma_2, \\ \gamma_{\times} &= -\mathcal{I}[-\gamma e^{-2i\phi}] = \sin(2\phi)\gamma_1 - \cos(2\phi)\gamma_2, \end{aligned} \tag{2.36}$$

where ϕ represents the angle between the lens and source image as shown in Fig. 2.4.

From Eq. 2.36 and from Fig. 2.4, we see that a massive lens will yield a positive tangential shear signal. For underdensitites such as voids, which constitute the majority of this thesis, the induced tangential shear signal is purely negative. In regard to galaxies or clusters, we can think of the GGL signal for voids (VGL) as an anti-lensing signal producing radially aligned sources with respect to the void origin. In both cases, however, the cross shear signal cannot be induced

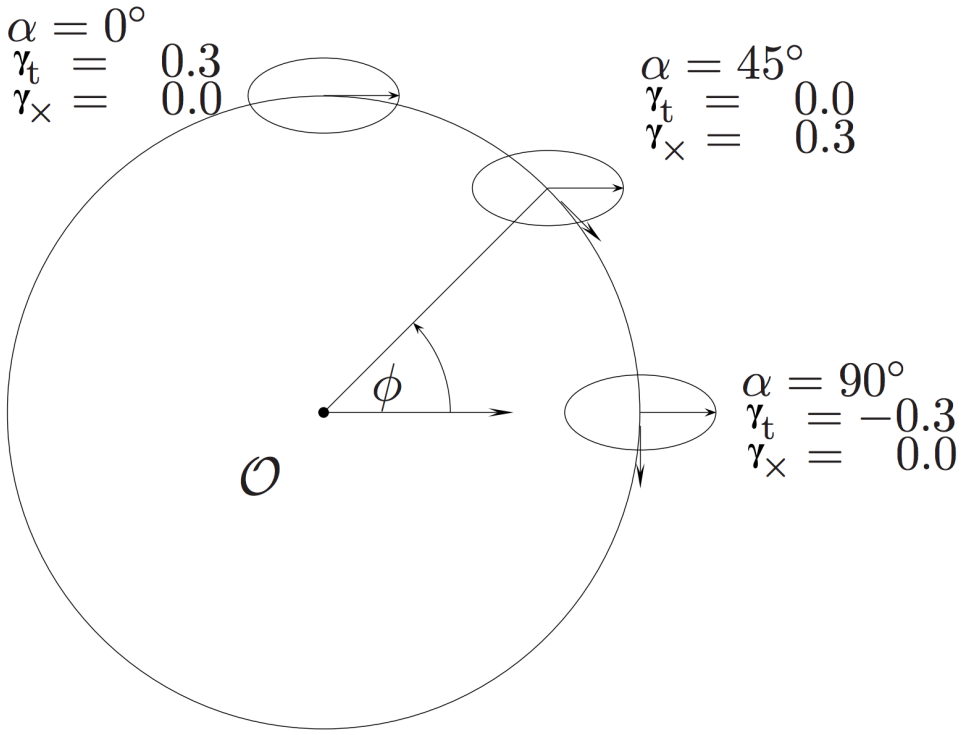

Figure 2.4 Illustration adapted from Schneider (2005) showing the tangential and cross shear components for a circular lens located at $\mathcal{O}$ with the source located at angle ϕ relative to the horizon. For pure tangential alignment, the tangential shear, γ_t, is positive while the cross shear, $\gamma_\times$, is zero. If γ_t is negative, as is the case in underdensities, then the source is radially, aligned with the lens. If $\gamma_t = 0$, this means that the source images is at a 45° angle to the lens.

by lensing and the measurement of such a signal serves as a useful null test to measure any systematic errors in the data.

Considering that lensing is a projection effect, we can relate the galaxy location - shape correlation, $\xi_{\rm gm}(\mathbf{r})$, to the projected surface mass density, Σ, of galaxies within a comoving projected radius, R, as,

$$\Sigma(R) = \rho_{\rm m,0} \int_0^{\chi(z_s)} \xi_{\rm gm}(\sqrt{R^2 + [\chi' - \chi(z_l)]^2}) {\rm d}\chi', \tag{2.37}$$

where $\chi(z_s)$ and $\chi(z_l)$ represent the comoving distances to the source and lens galaxies, respectively, $\rho_{\rm m,0}$ is the present day matter density of the Universe, and χ is the comoving line-of-sight separation. Furthermore, we can define the average surface mass density within comoving radius, R, as:

$$\overline{\Sigma}(\leq R) = \frac{2}{R} \int_0^R \Sigma(R') R' {\rm d}R'. \tag{2.38}$$

We can then follow Mandelbaum et al. (2005) and define the comoving excess surface mass density, also known as the surface density contrast, as

$$\Delta\Sigma(R) = \overline{\Sigma}(\leq R) - \Sigma(R), \tag{2.39}$$

which relates to the tangential shear of the background source galaxies as,

$$\Delta\Sigma(R) = \gamma_{\rm t} \Sigma_{\rm c}, \tag{2.40}$$

where $\Sigma_{\rm c}$ functions as a geometrical term that accounts for the lensing efficiency by utilising the lens galaxy's redshift and is known as the comoving critical surface mass density:

$$\Sigma_{\rm c} = \frac{c^2}{4\pi G} \frac{\chi(z_s)}{\chi(z_l)\chi(z_l, z_s)(1 + z_l)}, \tag{2.41}$$

where z_l represents the redshift to the lens, $\chi(z_l)$ is the comoving radial coordinate of the lens at redshift z_l, and $\chi(z_l, z_s)$ is the comoving distance between the lens and source. Note that Eq. 2.41 is the same as Eq. 2.8, but defined in comoving coordinates. As is thoroughly described in Appendix C of Dvornik et al. (2018), the previous equations can simply be converted to proper coordinates rather than using the comoving coordinates. I introduce the excess surface mass density definition in the comoving coordinates since I utilise this definition for the work conducted in this thesis. As Dvornik et al. (2018) discuss, the choice of proper versus comoving coordinates depends on the science case. Since the density profile

of galaxies is approximately stationary in proper coordinates, proper transverse distances should be used in the definitions above. However, using comoving distances for large-scale correlations is more sensible since the galaxy-matter correlation function on large scales is expected to be preserved (Dvornik et al., 2018) . It is also worth mentioning that there are slightly varying definitions of the projected surface mass density (Eq. 2.37). Some groups (e.g. Mandelbaum et al., 2010; Viola et al., 2015; de la Torre et al., 2017) replace $\xi_{\rm gm} \rightarrow (1 + \xi_{\rm gm})$ in the integrand of Eq. 2.37. Although this extra term does not fold through to the definition of $\Delta\Sigma$ and has no impact on the measured results, as Dvornik et al. (2018) point out, this term adds the line-of-sight integrated density of the Universe, which is already accounted for in the FLRW metric.

Estimators

In practice, the estimator for tangential shear comes in the form of tangential ellipticity defined in Eqs. 2.26 & 2.27, where averaging azimuthally over tangential ellipticities yields an unbiased measurement of the shear, barring systematic effects. Therefore, we can write this galaxy-galaxy lensing estimator as a weighted sum of the ellipticities, $\epsilon_{\rm t}$, as function of angular separation, θ,

$$\gamma_{\rm t}(\theta) = \frac{\sum_{jk}^{\rm N_{pairs}} w_{\rm s}^{j} \epsilon_{\rm t}^{jk}}{\sum_{jk}^{\rm N_{pairs}} w_{\rm s}}, \tag{2.42}$$

where $w_{\rm s}$ represents the weight on the source galaxy provided by a shape measurement pipeline.

Using this tangential shear estimator, we follow the definition in Amon et al. (2017) to write the estimator of the excess surface mass density as a function of projected radius, R, from the lens and the spectroscopic redshift of the lens, $z_{\rm l}$,

$$\overline{\Delta\Sigma}(R, z_{\rm l}) = \frac{\gamma_{\rm t}(R/\chi_{\rm l})}{\overline{\Sigma_{\rm c}^{-1}}(z_{\rm l})}. \tag{2.43}$$

The lens galaxies are split by redshift and the inverse of the critical surface mass density is calculated per the source-lens plane,

$$\overline{\Sigma_{\rm c}^{-1}}(z_{\rm l}) = \frac{4\pi G}{c^2}(1 + z_{\rm l})\chi(z_{\rm l})\eta(z_{\rm l}), \tag{2.44}$$

where $\eta(z_{\rm l})$ represents the lensing efficiency,

$$\eta(z_{\rm l}) = \int_{z_{\rm l}}^{\infty} N(z_{\rm s}) \left(\frac{\chi(z_{\rm l}, z_{\rm s})}{\chi(z_{\rm s})} \right) {\rm d}z_{\rm s}, \tag{2.45}$$

where $N(z_s)$ is the normalised redshift distribution. This accounts for the dilution of the lensing signal due to possibility of a source being located in front of the lens due to redshift uncertainties. I will use this estimator for VGL throughout the rest of this thesis.

2.4 Measurement Techniques and Systematic Uncertainties

The measurement of weak gravitational lensing poses distinct challenges due to the subtle nature of its distortion coupled with the myriad of galaxy-shape-changing effects that need to be accounted for (e.g. atmosphere, cosmic rays, astrometry, discreteness of detectors, intrinsic alignments). As shown in Fig. 2.5, as the light from a galaxy propagates through our atmosphere and detectors, the galaxy image undergoes a severe change in shape and clarity that needs to be taken into account before a proper analysis can convene. In this section, I briefly introduce some of the systematic issues that we need to correct for when accurately extracting the lensing signal from galaxy images.

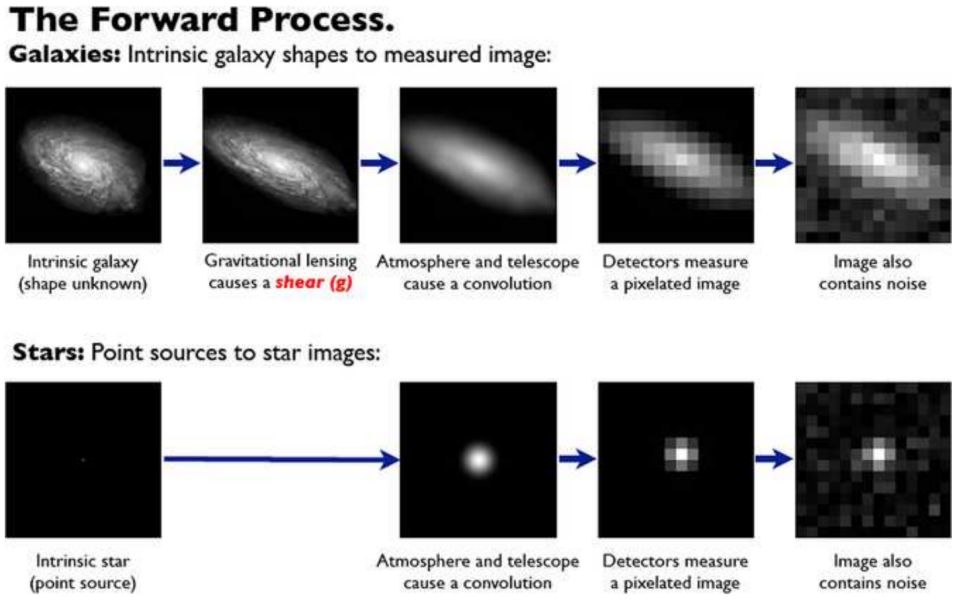

Figure 2.5 *Upper:* Illustration showing the progression of a galaxy's image quality as it becomes distorted from the atmosphere and telescope noise. *Lower:* Showing how the same effects that alter a galaxy's image change the image of a point-like source. This illustration is from Bridle et al. (2009).

2.4.1 PSF & Seeing

One of the main systematic difficulties for weak lensing occurs when the telescope generates patterns that correlate with galaxy ellipticities, imitating a lensing signal. This effect is generally known as the point-spread function (PSF). For ground-based telescopes, the largest contributor to the PSF arises due to the turbulent nature of Earth's atmosphere. Since temperature affects the optical refractive indices, if the particular portion of the atmosphere through which an astrophysical observation occurs has a temperature gradient, plane waves from a distant source will undergo a distortion when passing through this section of the atmosphere. The most common measurement of this in astronomy, known as seeing, is the Full Width at Half Maximum (FWHM) measurement, which identifies the width of a function at half of that function's maximum amplitude. Since distant stars and quasars behave like point-like sources, the measurement of these objects' FWHM (seeing) informs us of the atmospheric distortions and the PSF. The lower panel of Fig. 2.5 shows a general effect of PSF on an image, while Fig. 2.6 shows the PSF and seeing of stars in a particular observation in KiDS (de Jong et al., 2015), which is an optical survey in the *ugri* bands based at the VLT and covers two strips of $\sim 10\,\mathrm{deg} \times 75\,\mathrm{deg}$ on the celestial equator and around the South Galactic Pole (see Section 4.4.2 for a full description of the survey). Since we know that stars should be circular, any distortions to the shape of stars is due to the PSF, which can be modelled and corrected for.

Although space-based telescope do not suffer from atmospheric effects, a gradual degradation of their CCD chips can induce an excess PSF. Cosmic rays constantly bombard these observatories causing 'charged traps' in the silicon surface of the CCD to manifest as trail-like objects around the images. This effect, known as charge-transfer inefficiency (CTI) (Rhodes et al., 2010), will affect upcoming surveys such as Euclid and WFIRST, however substantial effort has been made at modelling and correcting for this effect (e.g. Massey et al., 2014).

2.4.2 Intrinsic Alignment

One of the more challenging astrophysical effects that the weak lensing community must overcome arises from the fact that galaxies tend to exhibit correlations in their orientation. In regards to galaxy formation, two dominant mechanisms exist that can cause nearby galaxies to intrinsically align. The first mechanism states that as gas and dust collapse under gravitational instability to form a galaxy, the tidal field of nearby proto-galaxies transfers angular momentum to the collapsing system, causing the formation of a disk-like galaxy with a rotation angle perpendicular to that of the angular momentum (Heavens et al., 2000). The second mechanism manifests in the form of common tidal interactions experienced by galaxies that share a single dark matter halo (Heavens et al., 2000; Croft and Metzler, 2000; Catelan et al., 2001; Mackey et al., 2002). In this picture, a spherical dark matter halo undergoing gravitational collapse is embedded within

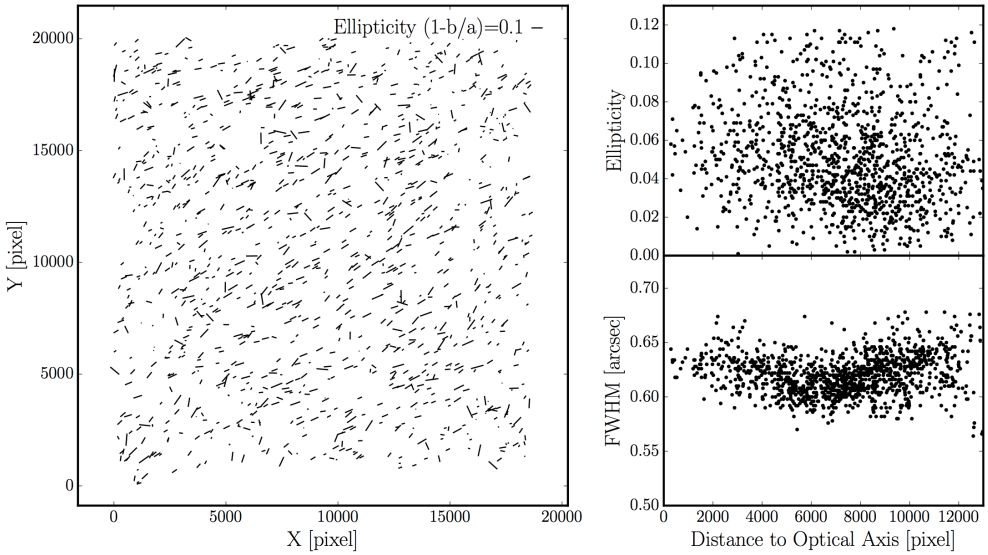

Figure 2.6 An example of the Point Spread Function (PSF) observed in the Kilo-Degree Survey (Kuijken et al., 2015). *Left:* In this figure, each tick mark represents the magnitude and orientation of the ellipticity of stars in the field. *Right:* The PSF ellipticity (upper) and FWHM size (lower) as a function of the distance from the image's centre. This is an example of a relatively simple PSF that can be modelled and accounted for without significantly affecting the measured ellipticity of galaxies, while delivering a seeing of $0.6''$ over the full distance range.

a large-scale, constant tidal field. Since this halo will experience an asymmetric gravitational force due to the tidal field, the halo will become oblate. Considering that the galaxies within this oblate halo perceive the same tidal field, they too will exhibit an intrinsic elongation in their shape. This alignment of nearby galaxies is known as the 'intrinsic-intrinsic' (II) correlation and is due to the fact that galaxies are not point-like sources, but are extended objects interacting with their environment. It has been shown that this alignment of galaxies produces a 'lensing-like' effect of approximately 10% of the shear signal (Croft and Metzler, 2000; Heymans and Heavens, 2003), however Johnston et al. (2018) recently showed that the effect of the II signal highly varies with galaxy colour, redshift, and binning. For example, they show that the intrinsic alignment signal for a red galaxy sample will likely dominate the shear in a low redshift bin, however the alignment of blue galaxies at all redshifts is $< 10\%$.

Unfortunately, the II correlation is not the sole contributor to intrinsic alignments. Hirata and Seljak (2004) showed that the foreground matter field experiences local gravitational interactions over a relatively short spatial distance, inducing an alignment signal to source galaxies. This interaction can essentially anti-align galaxies that are separated along the line of sight, causing a correlation between the foreground galaxies and background sources known as 'galaxy-intrinsic' (GI) correlation. This GI term is, in fact, the main culprit responsible for intrinsic alignment, outweighing the effect of the II correlation (Hirata and Seljak, 2004).

Since weak lensing assumes that any coherent alignment of galaxy shapes occurs solely due to lensing, intrinsic alignments of galaxies can contaminate the lensing analysis if not properly accounted for. The difficulty in modelling this alignment signal comes from the fact that, while simulations and analytic models show that dark matter halos exhibit an alignment signal, we cannot use these simulations to test the inherent alignment of baryonic matter (galaxies), which is what we observe. This poses an issue since the amplitude of alignment can vary by several orders of magnitude depending on the assumptions of the galaxy population and alignment model (Heymans et al., 2006). Furthermore, both data and simulations show that the galaxy shape measurement method also affects the amplitude of the intrinsic alignment signal (Singh and Mandelbaum, 2016; Hilbert et al., 2017).

Although still a concern for current and future surveys, such as LSST, Euclid, and WFIRST, there has been an exceptional amount of effort in the lensing community to model and mitigate the effect of intrinsic alignments. Studies have focused on understanding the behaviour and treatment of small-scale effects of intrinsic alignments using the halo model approach (e.g. Schneider and Bridle, 2010) and exploiting semi-analytical models (e.g. Joachimi et al., 2013), as well as building more unified models that incorporate large-scale effects (e.g. Blazek et al., 2015). Recent studies have also focused on the dependence of intrinsic alignments as a function of wavelength (Georgiou et al., 2018) and as a function of galaxy colour (Samuroff et al., 2018), showing that proper modelling of intrinsic alignments can shift cosmological parameters in the current datasets by approximately 0.5σ (Samuroff et al., 2018).

2.4.3 Photometric Redshifts

Amongst all the difficulties surrounding a weak lensing analysis, the most dominant source of systematic error arises from inaccurately measured galaxy redshifts. Inaccurately estimated redshift distributions can cause significant shifts in cosmological parameters and there has been a significant amount of effort by various groups to obtain accurate redshifts for source galaxies (e.g. Bonnett et al., 2016; Hoyle et al., 2018; Hildebrandt et al., 2018). There are two main methods of estimating a galaxy's redshift. The first method obtains redshift information from a galaxy's spectrum, known as spectroscopic redshifts (spec-z). The second method, known as photometric redshifts (photo-z), uses a galaxy's flux in multiple, broad band filters providing an effective low-resolution spectrum (see Salvato et al. (2018) for a review). Photo-z probe galaxies at a much fainter magnitude than spec-z and can estimate the redshift for a significantly larger number of galaxies given the same amount of telescope time. Furthermore, combining flux measurements from multiple wavelength filters provides higher signal-to-noise images than spectroscopy, however such broad filters yield a crude estimate of the object's spectrum and redshift. Thus, photo-z are not as accurate as spec-z measurements and need proper calibration. But before calibrating photo-z, one needs to overcome several hurdles. For example, since the PSF tends

to differ between bands, aperture photometry will likely yield an inaccurate colour estimation, therefore techniques such as PSF-matched aperture photometry are used (Hildebrandt et al., 2012). Despite the challenges of photo-z estimation, due to the ever-increasing size of surveys for weak lensing, we need to understand and constrain the systematic errors in uncertainties of photo-z otherwise they may dominate all the other uncertainties in future experiments (see Huterer et al., 2006), limiting our ability to exploit these data.

Hildebrandt et al. (2010) discuss various methods of estimating photo-z, but the two main approaches currently employed rely either on template-fitting techniques or machine learning algorithms. Template-fitting methods utilise a set of templates that represent a galaxy's spectral energy distribution (SED), which can predict a galaxy's photometry as a function of redshift when enough, accurate templates are combined. The template-predicted photometry can then be compared to with the observed photometry (Ilbert et al., 2006). One of the main setbacks for this method is that not enough templates exist to fully describe the data we observe. The second main approach exploits machine learning algorithms to learn the relationship between photometry and redshift from a 'training set' of galaxies. The main issue for these types of methods arises when the training set does not resemble the observed data, thus making the machine learning algorithm less accurate for a generalised data set. Using spec-z data to set priors on the photometry-redshift relations significantly improves the accuracy of the estimated photo-z (Benítez, 2000). If there existed a large, representative sample of spec-z galaxies to the depth of current and upcoming lensing surveys, the issues with photo-z uncertainty would be nearly eliminated (Newman et al., 2015). Surveys such as DESI (DESI Collaboration et al., 2016), MOONS (Taylor et al., 2018), and PFS (Takada et al., 2014) are promising candidates to address the concern of representative datasets in the next few years.

A recent analysis by Hildebrandt et al. (2018) shows the importance of properly calibrated photo-z redshifts and the effect of a non-representative sample for calibration. Due to limitations of deep spec-z redshifts, most cosmic shear studies calibrate their redshifts with the COSMOS sample (Ilbert et al., 2009; Laigle et al., 2016), which is a high-quality, 30-band photometric survey. Hildebrandt et al. (2018) find that despite the high-quality of the COSMOS-2015 catalogue (Laigle et al., 2016), it has a non-Gaussian distribution in the photo-z scatter with an outlier rate of 6% at magnitudes of $23 < i < 24$. This outlier rate is significantly larger than the outlier rate of the spec-z samples used in the redshift calibration ($\approx 1\%$). They show that using only the COSMOS-2015 catalogue lowers the mean redshift of all tomographic bins, as compared to when including the highest-redshift spectroscopic survey in the calibration sample. This causes an upward shift in S_8, which is an estimator that combines Ω_m and σ_8 such that $S_8 \equiv \sigma_8\sqrt{\Omega_\mathrm{m}/0.3}$, by approximately 0.6σ. This produces a stronger agreement with other cosmic shear results that use the COSMOS-2015 catalogue without high-redshift spectroscopic samples for their redshift calibration (Troxel et al., 2017; Hikage et al., 2018). Seeing the effect of a more representative, less biased redshift calibration sample on cosmic shear results echoes the need for large,

representative spec-z surveys as discussed in Newman et al. (2015).

2.4.4 Shape Measurements

Correcting for the above systematics (as well as others not mentioned in these thesis; see Mandelbaum (2018) for a more complete list) poses a somewhat daunting, but necessary, task in order to accurately extract cosmological information from weak lensing. In this section, I will briefly introduce two main approaches used for measuring the shapes of galaxies (moments-based and model-fitting) and discuss two pipelines currently used by the KiDS (*lens*fit) and DES (METACALIBRATION) collaborations.

One of the most common approaches to extracting the shape of a galaxy image is to measure the moments of the galaxy's surface brightness distribution. Of most importance to weak lensing studies is the quadrupole moment, which encodes the ellipticity of the image. Since most images contain some amount of noise, the most common approach is to add a weight function to the moments, where the ellipticity is calculated as a weighted quadrupole:

$$Q_{ij} = \frac{\int \mathrm{d}^2\theta\, \mathrm{W}(\boldsymbol{\theta}) I(\boldsymbol{\theta})\, \theta_i \theta_j}{\int \mathrm{d}^2\theta\, \mathrm{W}(\boldsymbol{\theta}) I(\boldsymbol{\theta})}, \tag{2.46}$$

where $I(\boldsymbol{\theta})$ is the galaxy surface brightness with the galaxy image centred at $(\theta_1, \theta_2) = (0, 0)$. For a perfectly elliptical image, the ellipticity parameters, ϵ_i, relate to the weighted quadrupole moments as,

$$\begin{pmatrix} \epsilon_1 \\ \epsilon_2 \end{pmatrix} = \frac{1}{Q_{11} + Q_{22} + 2(Q_{11}Q_{22} - Q_{12}^2)^{1/2}} \begin{pmatrix} Q_{11} - Q_{22} \\ 2Q_{12} \end{pmatrix}. \tag{2.47}$$

Since sky noise propagates into this measurement, these methods introduce a weight function $W(\boldsymbol{\theta})$ to mitigate the effect of noisy pixels biasing the unweighted ellipticities to higher values. This moments-based approach marks the foundation for one of the most widely-used shape estimations methods, known as the Kaiser-Squires-Broadhurst (KSB) method. Originally introduced by Kaiser et al. (1995), Luppino and Kaiser (1997) included seeing corrections, while Hoekstra et al. (1998) folded in astrometric distortions and updated some derivations to the original KSB method. Despite KSB's simplistic, Gaussian assumption regarding the PSF (Kaiser, 2000), it has been tremendously successful in accurately recovering the shapes of galaxies, rivalling newer methods. However, complications arise when using KSB on areas where data is missing or where light from nearby objects interjects onto the image. Over time, several extensions to KSB have been implemented (e.g. Bacon et al., 2000; Heymans et al., 2005), as well as other approaches in the vein of KSB, but with differing weight functions (e.g. DEIMOS Melchior et al., 2011).

Another approach to estimating the shape of a galaxy relies on an attempt to fit models to the galaxies surface brightness distribution. These methods, broadly known as model-fitting techniques, generally rely on the assumption that a galaxy exhibits either a circular or elliptical shape and thus any excess to the chosen model's ellipticity arises from shear. Unlike KSB, this approach accounts more thoroughly for the PSF, which is usually convolved with the galaxy model. One particularly interesting model fitting procedure is known as shapelets (Bernstein and Jarvis, 2002; Refregier, 2003; Refregier and Bacon, 2003). Unlike KSB, this method benefits from using an analytical expression for the PSF and shear, which increases the precision and speed of the calculations. However, a downside is that it assumes a Gaussian distribution of the light profile of galaxies, thereby poorly constraining the wings of the distribution. Other similar methods attempt to overcome this problem by modelling the galaxy brightness as a sum of Gaussians (Kuijken, 1999; Bridle et al., 2002; Voigt and Bridle, 2010) or using the Sérsic approach (Sersic, 1968) to model a galaxies brightness profile (Ngan et al., 2009). Nevertheless, model-fitting tends to suffer from a need of many parameters to fit the galaxy profile before noise and PSF convolutions are added. If the model does not meet this requirement, it exhibits a model bias (Bernstein, 2010). Another significant source of bias arises from noise in the non-linear regime of the models. This noise bias plays a particularly important role in low signal-to-noise galaxies and is difficult to predict (Hirata et al., 2004; Refregier et al., 2012; Melchior and Viola, 2012). Thus, in order to calibrate these models image simulations are usually required.

A different technique to galaxy shape measurement relies on Bayesian statistics to predict the shape from the full posterior distribution of ellipticities. This method is the basis of the *lens*fit algorithm (Miller et al., 2007; Kitching et al., 2008; Miller et al., 2013), employed by the KiDS collaboration. By marginalising over several parameters that do not pertain to the measurement of weak lensing, *lens*fit manages to individually model each galaxy image as a combination of two Sérsic profiles to describe the bulge and disk components, producing a likelihood distribution for the shape. One caveat of this approach, and all other Bayesian-based methods, is that it requires a prior on the galaxy shape as an input into the model. This is not a trivial task since the choice of prior can significantly affect the posterior distributions in a Bayesian framework. Furthermore, there is no guarantee that the morphologies of these model galaxies fully represent the morphologies of the observed galaxies. Thus, in order to calibrate a method like *lens*fit, we require image simulations (e.g. Fenech Conti et al., 2017; Kannawadi et al., 2018). Another successful model-fitting, Bayesian inference code worth mentioning is `Im3shape` (Zuntz et al., 2013). Similarly to *lens*fit, it measures the shape of a galaxy using two (or more) Sérsic profiles, calculates the maximum likelihood for parameter values, and corrects for noise bias. It has been successfully implemented by the DES Collaboration to create weak lensing shape catalogues (Zuntz et al., 2018).

The most recent technique to measure galaxy shapes is known as METACALIBRATION (Huff and Mandelbaum, 2017; Sheldon and Huff, 2017), which uses a shape

measurement, such as KSB, as its basis and then re-calibrates the shapes. In this approach, the observed galaxy image receives a small, known distortion to the shear and PSF, after which a response of the shear estimator to that added distortion is calculated. An ensemble average of the responses is then used to estimate the true shape of each galaxy. The advantage of METACALIBRATION is that no prior knowledge about the galaxy shear or morphology is needed. It can also correlate and correct for the noise across an image, which becomes a dominant source of error for faint objects (Sheldon and Huff, 2017). Furthermore, this method does not require calibration on images simulations since it only measures the response function of the added shear distortion. The assumptions made in this method are similar to those in other shape measurement methods. For example, METACALIBRATION assumes a linear relationship between the image and the true surface brightness on the sky. It also relies on single, de-blended galaxies, thus metacalibrating a response for a galaxy that has two shears or is blended with another galaxy will be problematic. These issues plague most shape measurement techniques, however, and so do not severely limit the quality and accuracy of shapes using METACALIBRATION (Sheldon and Huff, 2017).

Knowledge is like a sphere, the greater its volume, the larger its contact with the unknown.

Blaise Pascal

3

Void Modelling

We study the spherical evolution model for voids in ΛCDM, where the evolution of voids is governed by dark energy at an earlier time than that for the whole universe or in overdensities. We show that the presence of dark energy suppresses the growth of peculiar velocities, causing void shell crossing to occur at progressively later epochs as Ω_Λ increases. We apply the spherical model (Sections 3.2 & 3.3) to evolve the initial conditions of *N*-body simulated voids and compare the resulting final void profiles (Section 3.4). We find that the model is successful in tracking the evolution of voids with radii greater than 30 h^{-1}Mpc, implying that void profiles could be used to constrain dark energy. We find that the initial peculiar velocities of voids play a significant role in shaping their evolution. Excluding the peculiar velocity in the evolution model delays the time of shell crossing.

We then introduce the concept of redshift-space distortions around voids (Section 3.6). Recognising that the spherical model provides a crucial, missing ingredient for the prediction of a non-linear RSD measurement, *i.e.* non-linear peculiar velocity profiles, we use the spherical model to reconstruct these profiles (Section 3.7). We then present how the non-linear model for RSDs around voids compares to other models (Section 3.8), before showing how we can apply this model to constrain cosmological parameters (Section 3.9). This chapter then concludes with a discussion about the possible future and limitations of our approach (Section 3.10).

Sections 3.1 - 3.5 are published in Demchenko et al. (2016). The analysis presented in Sections 3.1 - 3.3 was first submitted, in a preliminary form, as part of my MSc thesis. The text and figures have been updated as part of this Ph.D. study, with Sections 3.4 & 3.5 constituting a significant addendum to the MSc work.

3.1 Void Introduction

The cosmic web, consisting of halos, voids, filaments, and walls in large-scale structure is predicted by the cold dark matter model (Bond et al., 1996; Pogosyan et al., 1998) and confirmed by large galaxy surveys (e.g. de Lapparent et al., 1986; Colless et al., 2003; Alam et al., 2015). Among these large-scale structures, the underdensities of the universe, *i.e.* cosmic voids, have been shown to have great potential for constraining dark energy and testing theories of gravity via several measurements. These measurements include: distance measurement via the Alcock-Paczyński Test (AP) (Ryden, 1995; Lavaux and Wandelt, 2012; Sutter et al., 2014), weak gravitational lensing of voids (Krause et al., 2013; Melchior et al., 2014; Clampitt and Jain, 2015; Gruen et al., 2016; Sánchez et al., 2016), the signal of the Integrated Sachs-Wolfe (ISW) effect associated with voids (Sachs and Wolfe, 1967; Granett et al., 2008; Nadathur et al., 2012; Flender et al., 2013; Planck Collaboration et al., 2014; Ilić et al., 2013; Cai et al., 2014; Kovács and Granett, 2015; Planck Collaboration et al., 2015; Aiola et al., 2015), void ellipticity as a probe for the dark energy equation of state (Lee and Park, 2009; Lavaux and Wandelt, 2010; Bos et al., 2012; Sutter et al., 2015; Pisani et al., 2015), void abundances and profiles for testing theories of gravity and cosmology (Li et al., 2012; Clampitt et al., 2013; Lam et al., 2015; Cai et al., 2015; Zivick et al., 2015; Barreira et al., 2015; Massara et al., 2015), coupled dark energy (Pollina et al., 2016), the nature of dark matter (Yang et al., 2015), baryon acoustic oscillations in void clustering (Kitaura et al., 2016; Liang et al., 2016), and redshift-space distortions in voids (Hamaus et al., 2015, 2016; Cai et al., 2016). Despite their popularity and great potential as a cosmological tool, a gap of knowledge between the evolution of individual voids through simulations and observations versus theory still persists. How voids evolve from the initial conditions and how dark energy or alternative theories of gravity shape this process still lacks a complete analytical understanding. As with the formation history of halos, the initial conditions and evolution history of voids sets the base for their two fundamental properties: profile and abundance. As these are crucial for constraining cosmological parameters, it is therefore important to bridge the gap between theory and observations. This is the main goal of our study.

The spherical evolution model has commonly been applied in theoretical studies of voids (Peebles, 1980; Blumenthal et al., 1992; Sheth and van de Weygaert, 2004). However, voids are usually assumed to start evolving from a spherical top-hat underdensity or some smooth functional form, which are not perfect descriptions for the initial underdenisties arising from random Gaussian fluctuations. Also, the analytical solution for the model is only found for the Einstein de-Sitter (EdS) universe. Solutions for the specific regimes of shell-crossing and turn-around in overdensities in a ΛCDM universe were given in Eke et al. (1996). The condition for shell crossing in voids is different from that in overdensities making the solution in Eke et al. (1996) inapplicable for shell crossing in voids. All these factors limit the application of the spherical evolution model and make it an unlikely candidate to describe observations or even simulations. In this study,

we take steps to extend the model by generalising it to cosmologies with dark energy and by going beyond simple assumptions for the void profile. Using the evolution equation to evolve initial void profiles from N-body simulations we find that, given the correct initial density and velocity profiles, the spherical model can reproduce late time void profiles from N-body simulations for void radii > 30 h^{-1}Mpc.

During the preparation of our manuscript, Wojtak et al. (2016) published a paper on a similar topic, studying void properties (e.g. ellipticity, size and density profile) using simulations. However, our focus for this publication is on comparing void profiles in simulations with the spherical model, so the two studies are complementary.

The structure of this publication is as follows: Section 3.2 introduces the spherical model for an EdS cosmology, Section 3.3 extends the model to ΛCDM and provides a comparison between the different cosmologies, Section 3.4 compares the theoretical ΛCDM model to results from N-body simulations and includes a discussion on the impact of peculiar velocities on void profiles, and Section 3.5 summarises the study.

3.2 The Spherical Model

The spherical evolution model was originally introduced to describe the evolution of overdensities (Gunn and Gott, 1972). This model assumes a spherical underdensity, ρ_i, embedded in an expanding, homogeneous background with density, $\bar{\rho}$. The evolution of each radius is determined by the total mass, M, contained within the proper radius, R, via the acceleration equation in the Newtonian regime.[1] The model makes no assumption about the background cosmology with the evolution governed by Friedmann acceleration equation (Eq. 1.30). This equation applies to an unperturbed region, which yields the expansion history of the universe. The spherical model has been applied to solve the evolution of overdensities and underdensities (e.g. Gunn and Gott, 1972; Peebles, 1980; Lilje and Lahav, 1991; Sheth and van de Weygaert, 2004). Using the spherical model, the evolution equation in a $\Lambda = 0$ universe becomes:

$$\ddot{R} = -\frac{GM}{R^2}. \tag{3.1}$$

To solve the above equation, the initial density and velocity profiles are needed. For the case of an overdensity, which eventually collapses and virialises as a halo, the initial density profile is usually taken to be a spherical top-hat and the initial velocity is assumed to be the Hubble flow at the initial time t_i. We will use the subscript i to indicate quantities at the initial time throughout the publication. With these assumptions, the equation can be solved analytically and the solution

[1] The Newtonian regime implies that $\dot{R} \ll c$ and $R \ll R_c \sim c/H$.

for the size of the radius as a function of time takes the following parametric form (Gunn and Gott, 1972; Lilje and Lahav, 1991):

$$\begin{aligned} R &= A(1-\cos\theta), \\ t+T &= B(\theta-\sin\theta), \\ A^3 &= GMB^2, \end{aligned} \tag{3.2}$$

where A, B, and T are constants that can be fixed once the initial conditions are fixed and θ is an indicator of time. For voids with the same initial settings, the analytical solutions can also be found by taking an inverse top-hat model for the density profile (Gunn and Gott, 1972; Lilje and Lahav, 1991; Peebles, 1980; Sheth and van de Weygaert, 2004):

$$\begin{aligned} R &= A(\cosh\theta-1), \\ t+T &= B(\sinh\theta-\theta), \\ A^3 &= GMB^2. \end{aligned} \tag{3.3}$$

Note that the parametric solutions above apply to any $\Lambda = 0$ universe. For this study we use the flat EdS cosmology.

There are noteworthy differences between halos and voids in this model. For halos, the overdensity begins expanding with a slower rate than that of the background universe. Since the local density is higher than the background, the effective Hubble rate is higher. The overdensity keeps expanding until it reaches a maximum radius, at which point it turns around and collapses into a singularity. The well-known turnaround radius ($R_{\rm ta} = R_{\rm i}/1.771$) and the density contrast when the over density collapses (linearly extrapolated $\delta_{\rm sc} = 1.686$) are found based on these exact assumptions, where δ is defined as $\delta = \rho/\bar{\rho} - 1$. Note that provided shell crossing does not occur before turnaround, which is unlikely, these values do not depend on the interior initial density profile.

For voids, matter shells will keep expanding from the initial conditions at a faster rate than the background universe. This expansion rate increases as the local density decreases. With this (unrealistic) assumption of a single, isolated void, a void's expansion is unaffected by its surrounding environment. The expansion of matter shells at radii smaller than the edge of the top-hat, R_t, are slightly faster than for those at $R > R_t$. This causes an overdense ridge to build up at the edge of the void. At some point the inner shells catch up with the outer ones. This defines shell crossing for voids, beyond which the analytical model fails. The evolution of such a case in terms of density contrasts and peculiar velocities is shown in Fig 3.1. In the EdS universe (dashed lines), the comoving radius of the underdensity would have expanded by a factor of 1.7 when shell crossing occurs, and the corresponding density contrast is $\delta = -0.8$, as shown by the dashed curve in Fig 3.2, which shows the evolution of the density contrast as a function of scale factor for an EdS universe, ΛCDM, and linear theory (see also Blumenthal et al., 1992; Sheth and van de Weygaert, 2004). These analytical values are successfully reproduced by our numerical solver for the acceleration equation (Eq 3.1).

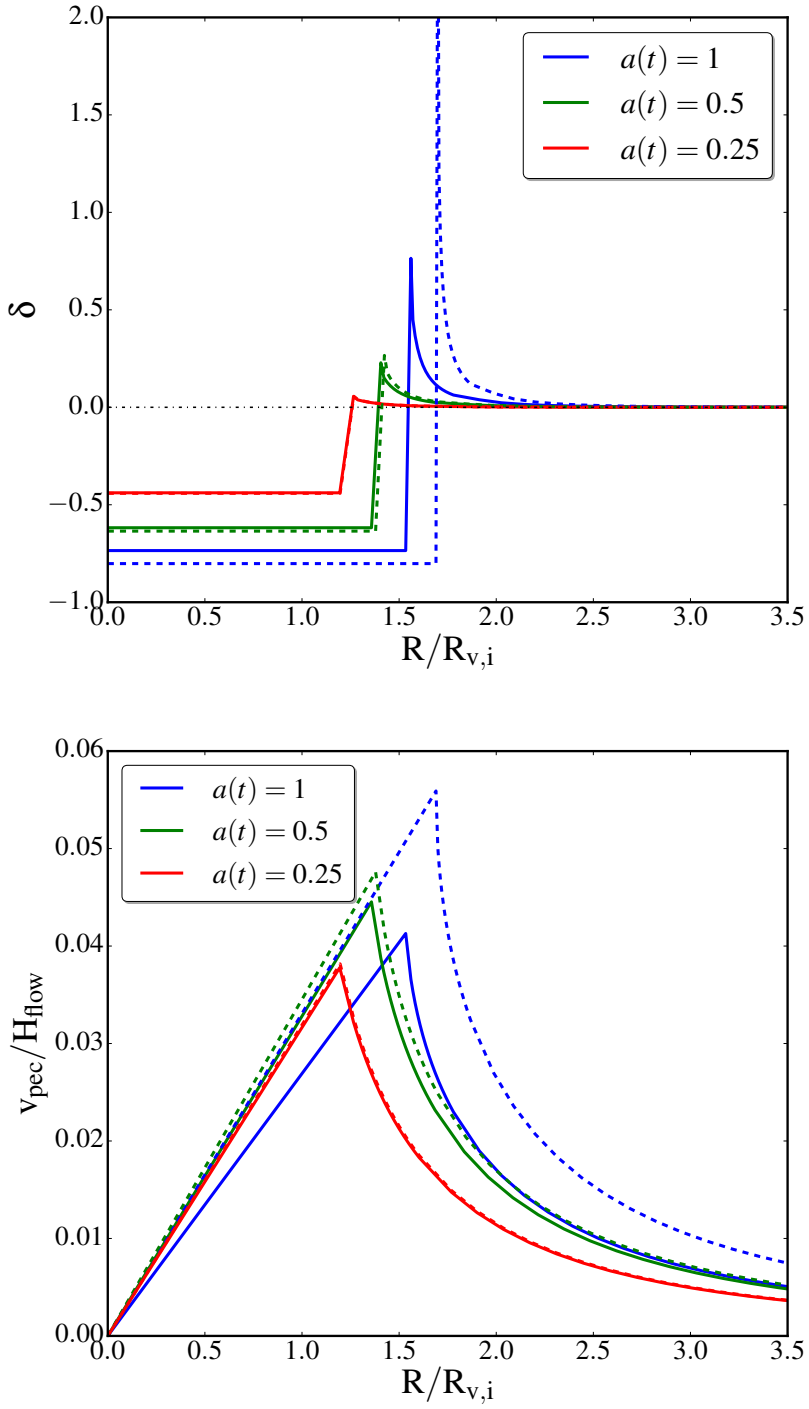

Figure 3.1 Numerically evolved density (upper) and proper peculiar velocity (lower) profiles of a spherical underdensity for both a ΛCDM (solid) and EdS (dashed) universe. These profiles are shown at three different epochs ($a = 0.25$, $a = 0.5$, and $a = 1.0$ from left to right) as a function of comoving radius normalised by their initial sizes. Peculiar velocities are normalised by the initial Hubble flow. The initial density contrast is chosen such that the inner most shell approaches, but not reach, shell crossing for the EdS cosmology.

Technically, we achieve the examples given in Figs 3.1 & 3.2 by numerically solving Eq 1.30 for spherical underdensities, requiring both the initial densities and velocities. We set up an inverse top-hat density contrast, δ_i, with a comoving radius of, $R_{v,i}$, at the epoch, a_i, so the mass at a given radius, R, from the centre is:

$$M_i(< R_i) = \begin{cases} \frac{4\pi}{3}\bar{\rho}_i R_i^3(1+\delta_i) & \text{if } R_i \leq R_{v,i} \\ \frac{4\pi}{3}\bar{\rho}_i R_i^3\left(1+\frac{R_{v,i}^3}{R_i^3}\delta_i\right) & \text{if } R_i > R_{v,i}, \end{cases} \tag{3.4}$$

where $\bar{\rho}$ is the background matter density of the universe. For the example of EdS, we integrate Eq 3.1 over t once to obtain:

$$\frac{1}{2}\dot{R}^2 = \frac{GM}{R^2} + E, \tag{3.5}$$

where M is a function of R and R is a function of t. The constant of integration E at the initial time t_i is set by the initial kinematic energy, *i.e.* $E_i = \frac{1}{2}v_i^2$, and the initial total velocities, v_i, are set to be the same as the Hubble flow, i.e. $v_i = H_i R_i$. We discuss the impact of other choices of initial velocities in Section 3.4.1. Note that in cosmologies with Λ, there will be a contribution from Ω_Λ in the above equation. In non-flat universes, the curvature contributes to the energy term in Eq 3.5, but Eq 1.30 remains the same.

With the above setup, we integrate Eq 3.5 for $R(t)$ and use it to solve for the average density contrast within R, $\Delta(a, < R)$, defined as:

$$1 + \Delta(a, < R) = M(< R) \Big/ \frac{4\pi}{3} R^3 \bar{\rho}, \tag{3.6}$$

and we see that $1 + \Delta(a, < R) \propto (a/R)^3$. We then differentiate $1 + \Delta(a, < R)$ to obtain the density contrast of each spherical shell at R, $\delta(a, R)$. We track the evolution of 30 consecutive shells equally spaced from the void centre to $3.5 \times R_{v,i}$ from $a_\mathrm{i} = 0.01$ to $a = 1$. We choose an initial density contrast such that the void approaches, but does not enter, the shell-crossing regime in an EdS universe. We solve the background expansion history, $a(t)$, with the same setup, apart from setting $\delta_i = 0$ and an arbitrary choice of radius. We note that for all the theoretical calculations in the different cosmologies used in this publication, their initial conditions are equal at a fixed a_i and follow the same framework to solve the acceleration equation. We find excellent agreement between the EdS results from our numerical solver and the analytical EdS solution, providing a benchmark from which we generate void models for other cosmologies.

The density contrast at shell crossing, $\delta = -0.8$, has been taken as a default choice of theoretical density threshold (Sheth and van de Weygaert, 2004). It is worth noting that the acceleration equation and the form of the solutions are general to any initial density profiles for both voids and halos, *i.e.* the top-hat profile assumption need not to be taken. However, quantitatively, the shell-crossing time and density contrast $\delta = -0.8$ are relevant when assuming an inverse spherical

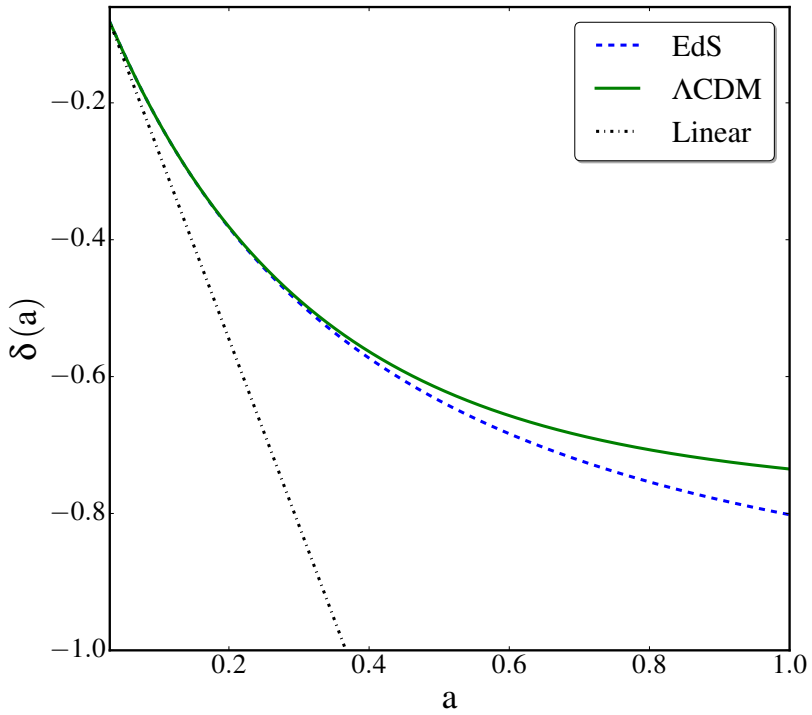

Figure 3.2 Density contrast of a void versus scale factor for EdS (dashed) and ΛCDM (solid). The prediction from linear theory is shown in the dot-dashed line.

top-hat density profile and an EdS universe. Relaxing any of those assumptions may lead to changes in those values. The sharp transition at the edge of the top-hat is somewhat unnatural and unrealistic. The time and density contrast for shell crossing is likely to be altered if a different (slower varying) initial density profile is assumed. It is the main goal of our publication to test the performance of the spherical evolution model by going beyond these overly simplistic assumptions.

3.3 Spherical Model Extended to ΛCDM and Beyond

In this section, we investigate the spherical evolution model in cosmologies with dark energy. We keep the inverse top-hat profile assumption for the initial density for the purpose of comparing solutions with those in an EdS cosmology. Switching from a $\Lambda = 0$ to a ΛCDM cosmology, the dark energy term is added to the acceleration equation, such that we can rewrite Eq. 1.30 as,

$$\ddot{R} = -\frac{GM}{R^2} + \Omega_\Lambda H_0^2 R, \tag{3.7}$$

where Ω_Λ is the present-day dimensionless density parameter for the cosmological constant Λ, and H_0 is the present-day Hubble constant. We chose the density

parameters adopted in Li et al. (2012) which are $\Omega_m = 0.24$ and $\Omega_\Lambda = 0.76$, for the purpose of comparing the model with voids in N-body simulations of the same cosmological parameters in Section 3.4. The dark energy term is positive, counteracting the effect of gravity. The presence of dark energy acts as a damping term, suppressing the growth of the peculiar velocity compared to the case in EdS, as shown in the lower panel of Fig 3.1. This effect partly quenches the velocity gradient between the inner and outer shells, hence delaying shell crossing. ΛCDM voids can therefore expand for longer without reaching the epoch of shell-crossing, as compared to EdS voids. This can be seen in the upper panel of Fig 3.1 and in Fig 3.2 where voids start from the same scale factor and initial density contrast in both the EdS and ΛCDM universes and are evolved to the same final redshifts. The two voids in different cosmologies follow closely to each other at the early times, but the evolution of the ΛCDM void slows at late times, having a relatively smaller void radius and smaller amplitude of density contrast at both the interior and the edge of the void. By $a = 1$, the void in the EdS cosmology is about to reach shell crossing. The comoving radius of the void in ΛCDM is smaller by $\approx 6\%$. We compare the comoving void radii for different values of Ω_m at $a = 1$ in flat ΛCDM universes in Fig 3.3. Again, we find that the void radius decreases as the amplitude of the dark energy term increases.

For general cases where the dark energy equation of state w is not necessarily -1, Eq 3.7[2] becomes

$$\ddot{R} = -\frac{GM}{R^2} - \frac{\Omega_\Lambda H_0^2 R}{2}(1+3w)a^{-3(1+w)}. \tag{3.8}$$

An example of void profile at $a = 1$ for $w = -0.5$ is compared with the fiducial dark energy model, shown in Fig 3.4. With $w = -0.5$, the universe has been expanding faster than the case of $w = -1$ until $a = 1$. The void experiences stronger background expansion from the dark energy term, which suppresses the development of peculiar velocities when compared to the fiducial ΛCDM case. It therefore appears to be smaller and shallower at the interior. In contrast, for $w < -1$, the void will be more evolved than the case in ΛCDM. The distinction between different models of dark energy in terms of the density and velocity profiles suggests that voids have the potential to constrain dark energy parameters.

To further investigate the effect of dark energy on the expansion history of voids, we plot the contribution of acceleration from the mass part and dark energy part on the RHS of Eq 3.7, shown in Fig 3.5. It is interesting to see that the amplitudes of these two terms are equal at $a \approx 0.4$ or $z \approx 1.5$ in voids. This is an earlier time than the epoch when dark energy starts to dominate the dynamics of the universe as a whole ($a \approx 0.67$ or $z \approx 0.5$). This is expected as the void region is a 'bubble' with lower dark matter density as compared to the average of the Universe. Since the dark energy density is thought to be the same regardless of matter density

[2]It should be noted that any effect of curvature is taken into account by the Friedmann Equation (Eq. 1.10) and mathematically arises as a constant of integration of this acceleration equation.

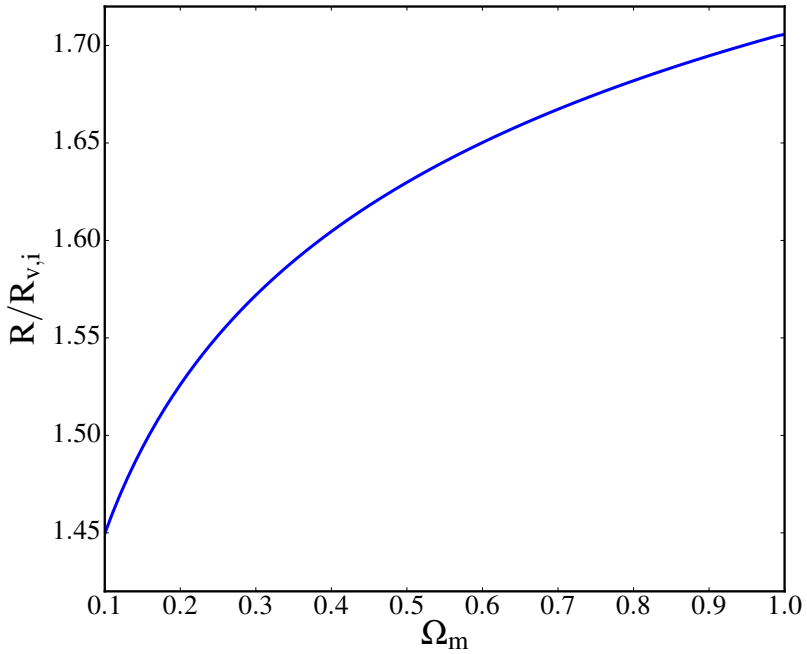

Figure 3.3 Comoving void radius at $a = 1$ normalised by its initial size as a function of $\Omega_{\rm m}$ in flat ΛCDM universes.

environment, it is more dominant in void regions and has been dominating for a longer time than in the Universe as a whole. Because the dynamics of voids are affected more strongly and for a longer time by dark energy, they are a potentially powerful laboratory to test the nature of dark energy.

Finally, we have checked that with the same top-hat initial void profiles, when allowing the void to evolve to shell crossing in the ΛCDM universe, the density contrast at shell crossing is the same as that in the EdS. This occurs at a later epoch hence the proper physical radius of the void would be greater than its EdS counterpart.

3.4 Comparison to N-body Simulation Results

With the numerical solver for the spherical evolution model applied for different cosmologies in the previous sections, we now use it to solve the evolution for voids with initial conditions taken from N-body simulations.

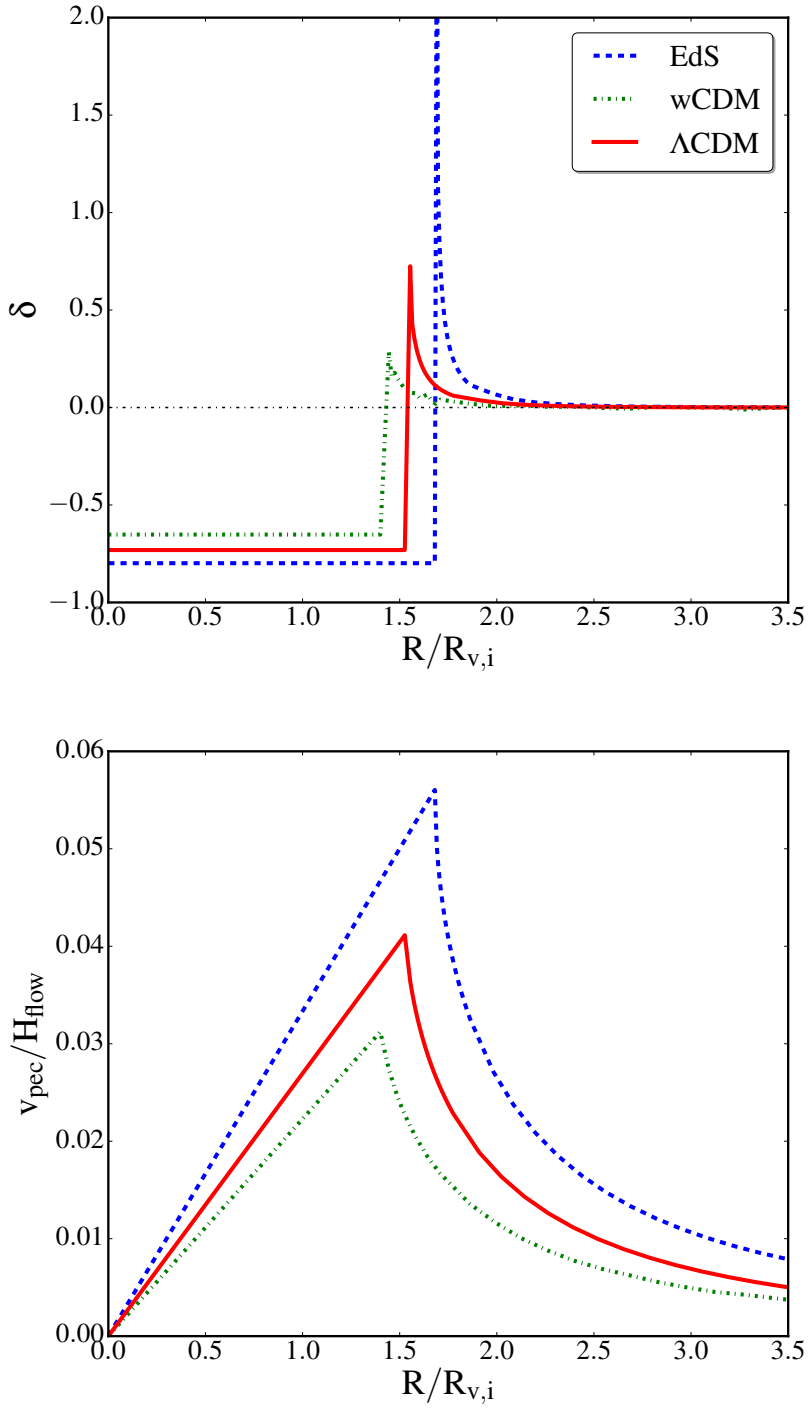

Figure 3.4 *Upper*: The density contrast at $a = 1$ for three different cosmologies labelled by the legend. The fiducial ΛCDM model has $\Omega_\Lambda = 0.74$, and the wCDM model has $w = -0.5$, while the rest of parameters are the same as the fiducial model. *Lower*: Velocity profiles at $a = 1$ for the same cosmologies normalised by the initial Hubble flow.

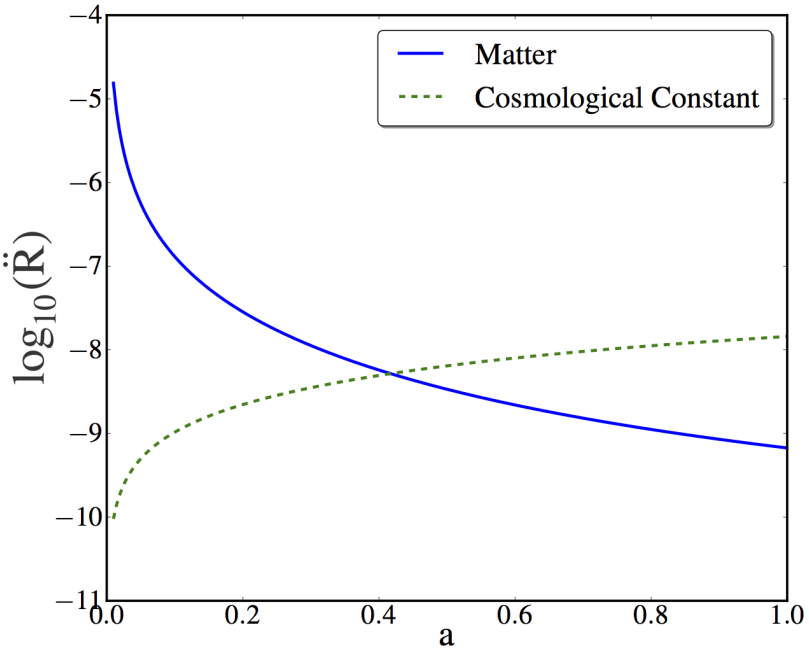

Figure 3.5 Contributions of dark matter (solid line) and dark energy (dashed line) to the acceleration of spherical shells shown in Eq 3.7, as a function of scale factor. The dark energy component dominates over the acceleration at $a \approx 0.4$, where the initial density contrast is chosen such that a void in EdS is on verge of shell crossing at $a = 1$. This value can be compared to the scale factor at which dark energy is dominant in our Universe, which is $a \approx 0.67$ (Frieman et al., 2008).

3.4.1 *N*-body Simulation

We employ *N*-body simulations of a ΛCDM model with the following parameters: $\Omega_{\rm m} = 0.24$, $\Omega_\Lambda = 0.76$, $h = 0.73$, $n_{\rm s} = 0.958$, and $\sigma_8 = 0.80$ from Li et al. (2012). The volume of the simulation box is $(1\ h^{-1}\,{\rm Gpc})^3$. We identify voids using all halos above a minimum halo mass of $M_{\rm min} = 10^{12.8}\ h^{-1}{\rm M}_\odot$ to ensure that each halo contains at least 100 particles. Voids are found in the halo field with the spherical underdensity algorithm described in Cai et al. (2015), which is based on the algorithm of Padilla et al. (2005). In the void algorithm, maximal spheres are grown from a set of grid points, within which the number density of halos satisfies the criterion $\Delta \leq 0.2$. Void candidates are ranked in decreasing order of radius. Spheres that overlap with a neighbour by more than 50% of the sum of their radii are rejected. Technical details on the void catalogue can be found in Cai et al. (2015).

With the void centres defined at $a = 1$ from simulations, we measure the dark matter density and velocity profiles around them. To ensure that the voids from the simulations are close to spherical, we stack 1491, 393, and 268 voids with radii in a narrow range of 40, 30, and 20 h^{-1}Mpc, respectively, at $a = 1$. We then use the same void centres in comoving coordinates to measure the stacked density and velocity profiles at $a = 0.1$ and $a = 0.5$. The density and velocity profiles at $a = 0.1$ are treated as the initial conditions used by our numerical solver.

Before proceeding to evolve the profiles, we have verified that the peculiar velocities measured from the simulation at $a = 0.1$ can be accurately reproduced using the density profiles via the linear relation (Peebles, 1993):

$$v_{\rm pec} = -\frac{1}{3} aHf\bar{\delta}(r) r_p, \tag{3.9}$$

where $f \equiv d\ln D/d\ln a$ is the linear growth rate, D is the linear growth factor, H is the Hubble constant at a, $\bar{\delta}(r)$ is the cumulative density profile from the model, and r_p is the physical radius. The initial density and velocity profiles of our chosen voids satisfy the linearised continuity equation and can be considered as linear. It is important to note that we need to include these non-zero peculiar velocities in our solver for the acceleration equation in order to obtain a sufficient level of accuracy in the density contrast profiles between the spherical model and *N*-body simulation. Setting the initial peculiar velocity to zero for the analytical solutions with the top-hat model may seem reasonable since the peculiar velocity is usually negligibly small compared to the Hubble flow in the linear regime, however our results suggest that this is not the case. This can be understood by the fact that *N*-body simulations use the total velocity as the initial condition *i.e.* Hubble flow plus peculiar velocities, rather than just the Hubble flow alone. Excluding peculiar velocities at the initial condition is equivalent to setting the initial growth rate of a void to be zero due to a cancellation of the growing and decaying modes *i.e.*, $\dot{\delta} = 0$. The subsequent evolution of a void with this setting, assuming only the growing mode, will have a prefactor of 3/5 in the amplitude of density fluctuations compared to the case where the initial peculiar velocity is

set according to linear theory. Fig 3.6 shows the $\Delta\delta$ (upper) and Δv_{pec} (lower) between the *N*-body simulation and profiles which include an initial peculiar velocity (solid lines) and profiles that only use the Hubble flow (dashed lines) as the initial velocity. As shown in Fig 3.6, setting the peculiar velocity to be zero at the initial time largely slows down the evolution of the density and makes the predicted void profiles shallower than the simulation results. In our analysis (Fig 3.7) we use the linearly derived peculiar velocity (Eq 3.9) plus the Hubble flow instead of the peculiar velocity from the simulation. Although we find that using the peculiar velocity from the simulation as initial conditions for the model makes the results agree slightly better at small radii, we perform our analysis with the linearly calculated peculiar velocity because it is simple to obtain, requiring only a knowledge of the density contrast.

Having understood the effect of peculiar velocities in *N*-body simulations, we then calculate the evolved profiles at $a = 0.5$ and $a = 1$ and compare them to the simulation results. Fig 3.7 depicts the density profiles and peculiar velocity profiles as a function of comoving void radius at the three epochs, where the dotted lines are the simulation and the solid lines are the model. We find that the void profiles at the initial time have a slower slope at their edges than that of a top-hat. For the relatively large voids, $R_v = 40$ and 30 h^{-1}Mpc, we find good agreement between the spherical model and the *N*-body simulations for the void density profiles at all epochs, as shown by the comparisons of the dashed curves versus the solid curves on the left-hand panel of Fig 3.7. For smaller voids with $R_v = 20$ h^{-1}Mpc however, the agreement between the spherical model and *N*-body simulations at the late time degrades. We suspect that this is due to mis-centering between the voids at the late time versus their initial conditions, caused by the void's non-zero bulk motions, *i.e.* simulated voids may have been moving throughout their evolution history from $a = 0.1$ to $a = 1$; the amplitudes of such motions have been shown to be larger for smaller voids (Ceccarelli et al., 2016). This scenario would qualitatively explain the fact that the model prediction for smaller voids has a shallower density profile interior and a less-pronounced density ridge, compared to that from *N*-body simulations at the late time. It may be possible to further improve the agreement between the model and simulation profiles at the late time for smaller voids, if one accurately tracks void centres back to their initial positions. We also suspect that smaller voids may be less spherical (Sheth and van de Weygaert, 2004) and more affected by tidal forces from their large-scale environments. This is not accounted for by the spherical evolution model hence it may diminish the agreement between the model and *N*-body simulations. We leave the investigation of small voids for future work.

Regarding peculiar velocities, the spherical model generally underpredicts their amplitudes by a few percent up to nearly 10% at the peak of the outflow for $R_v = 40$ and 30 h^{-1}Mpc, and by a larger amount for $R_v = 20$ h^{-1}Mpc. It might seem surprising that these deviations for the predicted peculiar velocity are not reflected as deviations in the predicted density profiles. This can be understood as follows: the evolution of the density profiles is determined by the total velocity (peculiar velocity plus Hubble flow). At the scale of our interest, the

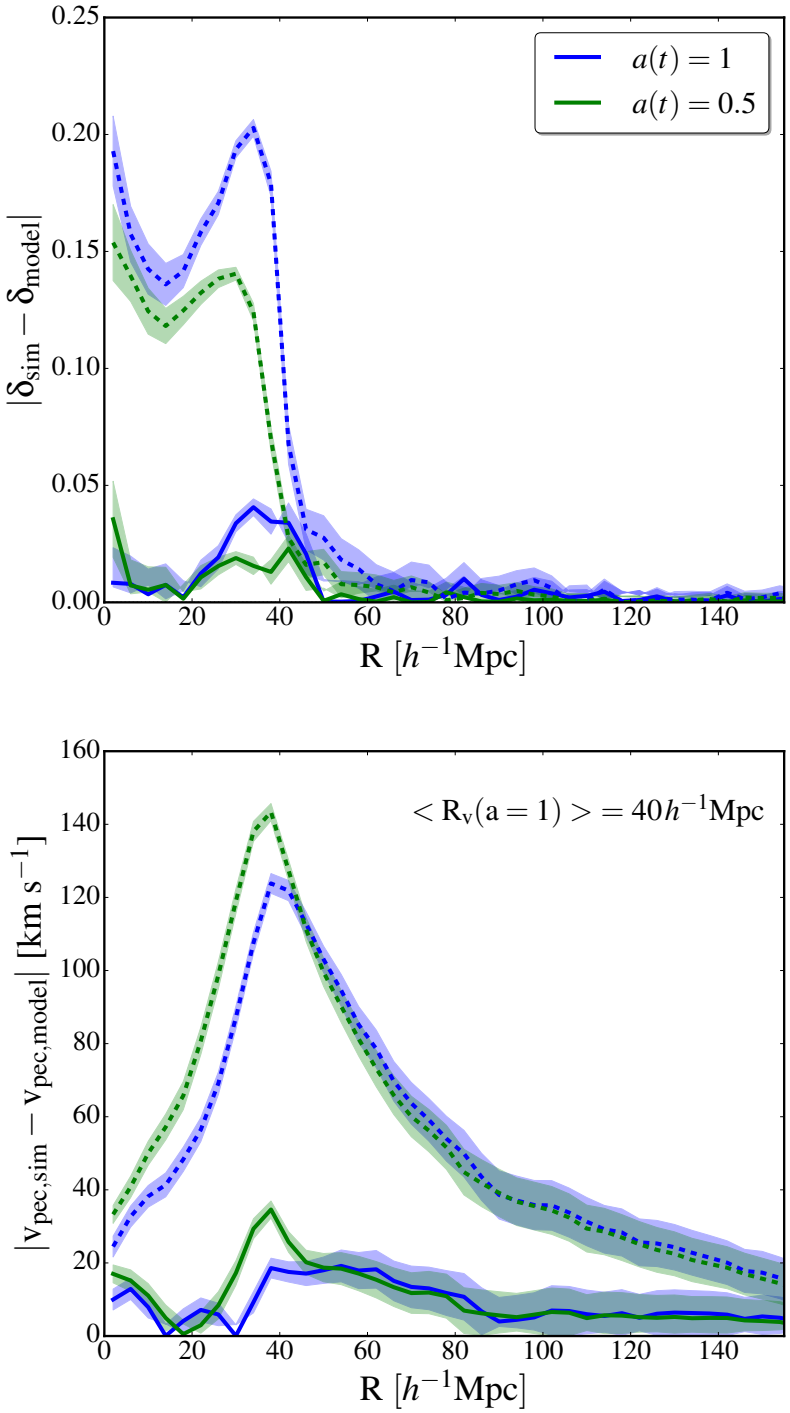

Figure 3.6 Effect of various velocities as initial conditions on the absolute difference in density contrast (upper) and peculiar velocity (lower) profiles for 268 voids with average an average radius of 40 h^{-1}Mpc. The solid lines show the absolute difference if the initial velocity includes the peculiar velocity from the N-body simulation, whereas the dashed lines show the absolute difference if only Hubble flow is used as the initial velocity. Blue and green represent $a = 1$ and $a = 0.5$, respectively. The shaded regions represent a 1σ errors on the N-body simulation curves. The features within the void radius are likely due to shot noise at those scales.

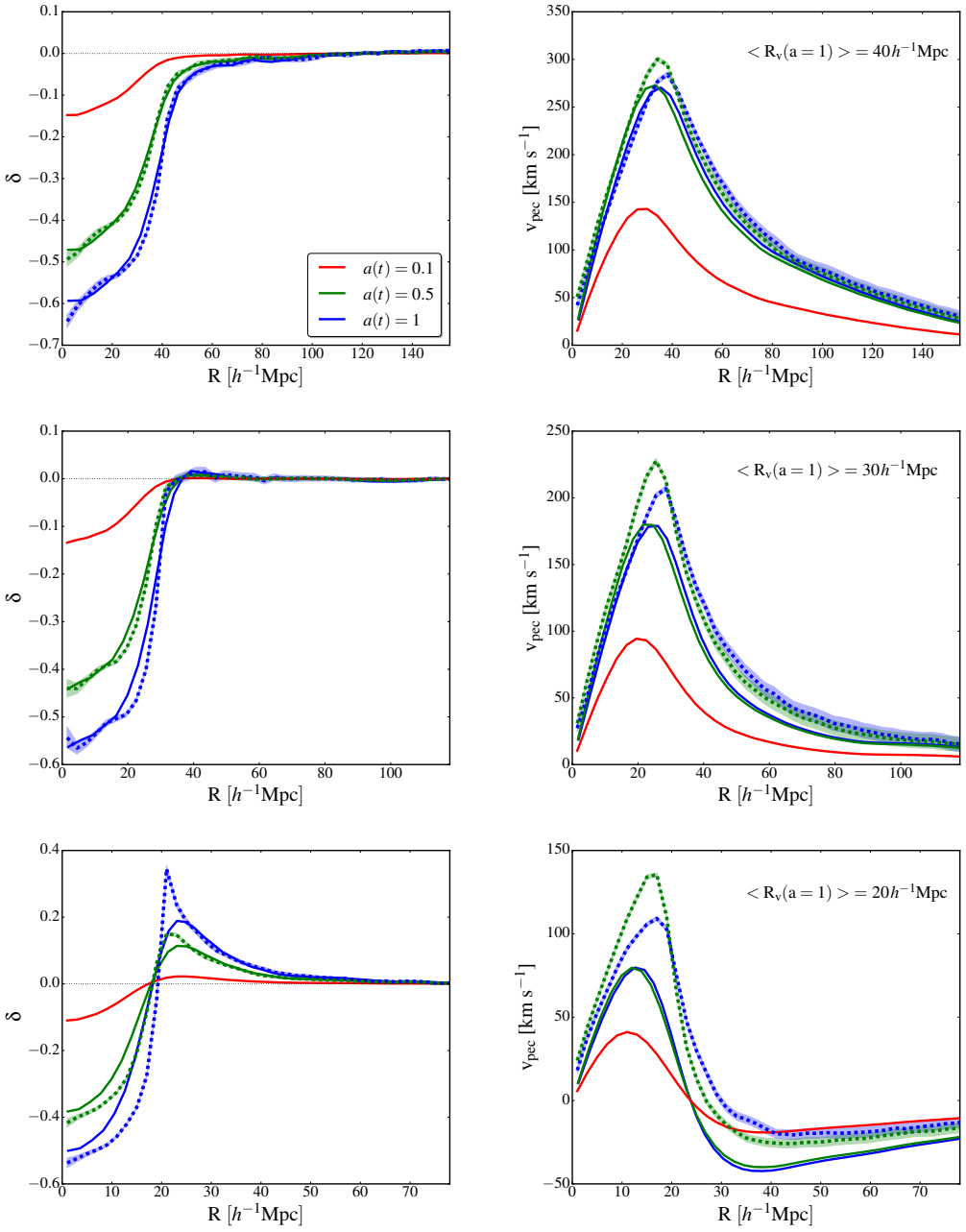

Figure 3.7 Evolved void profiles in terms of density contrast (left) and peculiar velocity (right) predicted from the spherical model (solid) compared to N-body simulations (dashed). The rows from upper to lower represent voids with average radii of 40, 30, and 20 h^{-1}Mpc, respectively, at $a = 1$. Solid curves of different colours show results from the model at different epochs labelled by the legend. The red curve at $a = 0.1$ is the initial profile measured in the N-body simulations and used as input to the spherical model. The shaded regions represent 1σ errors on the N-body simulation curves.

Hubble flow dominates over the peculiar velocity, thus small deviations in peculiar velocities are inconsequential to the resulting density profile. Also, any differences will manifest themselves in the density profile integrated over a sufficiently long period of time, so we expect the difference in the density profile to show up at a later epoch as compared to when the difference starts to emerge in the velocity profiles.

It is worth noting that if one simply applies linear theory to evolve the density profiles from the initial conditions, the amplitudes of the density profiles are largely overpredicted. This suggests that the spherical model successfully describes the dynamics for large voids, *i.e.* the growth of the density contrast in voids has to slow down and is significantly slower than predicted by linear theory. We also note that even though the initial peculiar velocities seem negligibly small compared to the Hubble flow, they need to be included in our solver for the acceleration in order to obtain a sufficient level of accuracy in the density contrast profiles between the spherical model and N-body simulation.

3.5 The Spherical Model Conclusions

We investigate the spherical evolution model for voids in different cosmologies and compare voids in Einstein-de Sitter, ΛCDM, and wCDM cosmologies. We start with the assumption that the initial density of voids can be modelled with an inverse spherical top-hat profile. We find that the presence of dark energy damps the effect of gravity sourced by dark matter and suppresses the growth of peculiar velocities. This causes the same void to decrease in size by a few percent when comparing EdS to ΛCDM at the epoch when shell crossing is about to occur in the EdS universe. In general, the impact of dark energy for the evolution of voids increases as the dark energy density increases relative to the dark matter component. This implies that its impact is stronger for voids than for the whole universe on average. The dynamics of voids have been affected by dark energy for a longer time and therefore the imprint of dark energy is stronger within them. This makes voids potentially powerful candidates for constraining dark energy.

With the success of the generalised model demonstrated, we compare the model to N-body simulations. Using the initial conditions from the simulation, we evolve voids of different sizes using the spherical model and compare the final density and peculiar velocity profiles with simulation outputs. We show that the model successfully reproduces the density and velocity profiles for voids with radii of 30 and 40 h^{-1}Mpc, with the agreement for the velocity profiles being slightly worse, *i.e.* the model underpredicts results from simulations by a few percent and up to 10% at the peak. The success of the spherical model for tracking the evolution of large voids opens up the possibility of using it to constrain dark energy. The performance of the model is not as successful for smaller voids, which may be due to mis-centring errors in our determination of the position of void centres within the simulation when the initial conditions are measured with the evolved

late time void centres.

After the publication of Demchenko et al. (2016)[3], Massara and Sheth (2018) explored the evolution of void density and velocity profiles taking into account the evolution of the bias of large-scale tracers. They identify void centres at the initial condition and create a model that follows their evolution in Lagrangian coordinates. Identifying voids and void centres at the late-time, rather than 'proto-voids' at an earlier epoch, does not require accounting for the evolution of the large-scale bias. As mentioned in Section 3.4.1, void centres move and disregarding that motion can affect the accuracy of the spherical model, especially for small voids such as the ones studied in Massara and Sheth (2018). They also find that void motions are approximately independent of void size, which means that the bulk motion of voids affects voids of smaller sizes more significantly than the larger ones, which explains why the spherical model doesn't recover the N-body simulation profile for smaller voids in Fig. 3.7. If one wishes to study small voids (*i.e.* $R_{\rm v} \lesssim 25\ h^{-1}$Mpc), then indeed modelling the bulk motion of voids similar to Massara and Sheth (2018) improves upon our work.

3.6 Redshift-Space Distortions Around Voids

Having successfully modelled the evolution of density and velocity profiles of voids, we now turn our attention to investigate how these profiles may change due to redshift-space distortions (RSDs; discussed in Section 1.7.4) around voids. Linear RSDs in the galaxy correlation function (Kaiser, 1987; Hamilton, 1998) have been employed to measure the growth rate of the LSS for almost three decades (e.g. Hamilton, 1992; Cole et al., 1994; Peacock et al., 2001; Beutler et al., 2012; Reid et al., 2012; Blake et al., 2013; de la Torre et al., 2013; Samushia et al., 2014; Okumura et al., 2016; de la Torre et al., 2017; Wang et al., 2018). Recently, Cai et al. (2016) apply this model to measure the RSDs around voids and Nadathur and Percival (2019) expanded it to include higher order terms. In the next few sections, we introduce these linear and quasi-linear RSD approaches before showing the improvements gained by using the non-linear spherical model approach described in Section 3.3.

3.6.1 Linear and Quasi-Linear RSDs Around Voids

To begin with, we explore the linear model for the void-galaxy correlation function as presented in Cai et al. (2016). Unlike the galaxy-galaxy correlation function, the void-galaxy correlation function considers the relative peculiar velocities of dark matter halos with respect to one location, namely the void centre. We assume that this central point remains stationary and thus the bulk motion of voids will have negligible effect on the void-galaxy correlation function within

[3]This paragraph does not appear in the published version of Demchenko et al. (2016)

scales where the bulk velocity field remains coherent. Utilising the plane-parallel approximation, $|v/(raH)| \ll 1$, where v represents the peculiar velocity, r is the comoving distance from the observer, a represents the scale factor, and H is the Hubble constant at a, the relation between real-space and redshift-space density is,

$$1 + \delta^{\mathrm{s}}(\mathbf{r}) = [1 + \delta(\mathbf{r})]\,[1 + u(\mathbf{r})]^{-1}, \tag{3.10}$$

where the parameters have their standard definitions described above and $\mathbf{r}$ represents a radial vector originating at the void centre. In what follows, the s superscript will denote parameters in redshift space. From the plane-parallel approximation, the line-of-sight separation component between redshift-space and real-space is,

$$s = r + \frac{v(r)}{aH}, \tag{3.11}$$

where s represents the location in redshift space. When perturbations are small, meaning when $\delta(\mathbf{r}) \ll 1$ and $|\partial v(\mathbf{r})/\partial \mathbf{r}| \ll aH$, Eq. 3.10 simplifies to linear order as,

$$\delta^{\mathrm{s}}(\mathbf{r}) = \delta(\mathbf{r}) - u(\mathbf{r}). \tag{3.12}$$

The term $u(\mathbf{r})$ functions as an effective distortion term and represents the gradient of the radial peculiar velocity profile, $v(\boldsymbol{r})$, along the void centre projected along the line of sight:

$$\begin{aligned} u(\mathbf{r}) &= \hat{\mathbf{z}} \cdot \frac{1}{aH} \frac{\partial[\hat{\mathbf{z}} \cdot \hat{\mathbf{r}} v(\mathbf{r})]}{\partial \mathbf{r}} \\ &= (1 - \mu^2) \frac{1}{aH} \frac{v(r)}{r} + \mu^2 \frac{1}{aH} \frac{\partial v(r)}{\partial r}, \end{aligned} \tag{3.13}$$

where $\hat{\mathbf{z}}$ is the unit vector along the line of sight, $\mu = \cos(\theta)$, and θ is the angle subtended between $\mathbf{r}$ and $\hat{\mathbf{z}}$ (Cai et al., 2016). It is this term that induces distortions between real and redshift space. Taking the derivative of the linear theory peculiar velocity in Eq. 3.9 with respect to r yields,

$$\frac{\partial v(r)}{\partial r} = -faH\Big[\delta(r) - \frac{2}{3}\Delta(< r)\Big], \tag{3.14}$$

where f is the linear growth rate defined in Eq. 1.43 and $\Delta(< r)$ is the cumulative

density contrast defined as,

$$\Delta(< r) = \frac{3}{r^3} \int_0^r \delta(r')\, r'^2\, \mathrm{d}r'. \tag{3.15}$$

Substituting Eqs. 3.13 and 3.14 into Eq. 3.12 provides,

$$\xi^s_{\rm vg}(\mathbf{r}) = \delta(r) + \frac{1}{3} f\Delta(< r) + f\mu^2[\delta(r) - \Delta(< r)], \tag{3.16}$$

where instead of $\delta^s(\mathbf{r})$, we use the notation of $\xi^s_{\rm vg}(\mathbf{r})$. We justify this change of notation since the density fluctuation, $\delta(r)$, is equivalent to a void-galaxy cross-correlation at separation r. The above equation states that, in linear theory, unlike the galaxy-galaxy auto-correlation function, the void-galaxy cross-correlation contains only the monopole and quadrupole, with no hexadecapole.

Adhering to the approach of Hamilton (1998), the monopole and quadrupole of the void-galaxy correlation function are defined as,

$$\begin{aligned} \xi^s_0(r) - \frac{3}{r^3}\int_0^r \xi^s_0(r')r'^2 dr' &= \Big(1 + \frac{f}{3}\Big)[\xi(r) - \bar{\xi}(r)], \\ \xi^2_2(r) &= \frac{2f}{3}[\xi(r) - \bar{\xi}(r)]. \end{aligned} \tag{3.17}$$

Since for linear theory the hexadecapole is zero, Cai et al. (2016) write the redshift-space correlation function as a combination of the two multipoles,

$$\begin{aligned} \xi^s(r,\mu) &= \xi^s_0(r) + \frac{3\mu^2 - 1}{2}\xi^s_2(r) \\ &= \Big(1 + \frac{f}{3}\Big)\xi(r) + \frac{f(3\mu^2 - 1)}{3}[\xi(r) - \bar{\xi}(r)] \\ &= \xi(r) + \frac{1}{3}f\bar{\xi}(r) + f\mu^2[\xi(r) - \bar{\xi}(r)]. \end{aligned} \tag{3.18}$$

In order to estimate the growth rate from the above multipoles of the correlation function, Cai et al. (2016) define a growth rate estimator as,

$$\begin{aligned} \tilde{G}(f) &= \frac{\xi^s_2(r)}{\xi^s_0(r) - \frac{3}{r^3}\int_0^r \xi^s_0(r')r'^2 dr'} \\ &= \frac{2f}{3+f}. \end{aligned} \tag{3.19}$$

Using this definition of the growth rate, Cai et al. (2016) show how RSDs around voids can constrain the growth rate. With this approach, they place a constraint of $\beta = f/b$ at $r > R_v$ in a volume of 3 $(h^{-1}\,\mathrm{Gpc})^3$ at 9% precision, while including the contribution from velocity dispersions into this model allows them to probe scale of $r > 0.5\,R_v$ and increases the constraining power by a factor of two.

Nadathur and Percival (2019) extend upon this linear approach by retaining higher-order terms from Eq. 3.10, arguing that since, by definition, the density contrast of a void is $\delta(r) \sim -1$, we need to retain additional terms in the redshift-space correlation function. Using this assumption allows us to rewrite Eq. 3.10 as,

$$1 + \xi^s_{\rm vg}(s) = (1 + \xi_{\rm vg}(r))\Big[1 - \frac{1}{3} f\Delta(< r) + f\mu^2(\delta(r) - \Delta(< r))\Big]^{-1}. \tag{3.20}$$

Expanding this equation and retaining terms of order $\xi\delta$ and $\xi\Delta$ yields,

$$\begin{aligned}\xi^s_{\rm vg}(s,\mu) = \xi_{\rm vg}(r) &+ \frac{1}{3} f\Delta(< r)(1 + \xi_{\rm vg}(r)) \\ &+ f\mu^2[\delta(r) - \Delta(< r)](1 + \xi_{\rm vg}(r)),\end{aligned} \tag{3.21}$$

where s is redefined to include the $\xi\delta$ and $\xi\Delta$ terms, which alters the line-of-sight separation vector and Eq. 3.11 becomes,

$$r = s\Big[1 + \frac{1}{3} f\Delta(< s)\mu^2\Big]. \tag{3.22}$$

This coordinate shift between real-space, r, and redshift-space, s, arises due to the retention of higher-order terms from the Taylor expansion in ξ,

$$\xi(r) = \xi(s) + \xi'(s)\frac{f}{3} s\,\Delta(< s)\mu^2 + \ldots. \tag{3.23}$$

In order to extract the monopole and quadrupole, Nadathur and Percival (2019) use the above Taylor expansion in Eq. 3.21 obtaining,

$$\begin{aligned}\xi^s_{\rm vg}(s,\mu) \simeq \xi_{\rm vg}(s) &+ \frac{1}{3} f\Delta(< s)(1 + \xi_{\rm vg}(s)) \\ &+ f\mu^2[\delta(s) - \Delta(< s)](1 + \xi_{\rm vg}(s)) + \frac{f\mu^2}{3} s\,\xi'_{\rm vg}(s)\Delta(< s).\end{aligned} \tag{3.24}$$

The original linear theory for RSD (Kaiser, 1987) does not include these higher-order terms (Hamilton, 1998). Their inclusion induces an altered mapping

between the real and redshift-space coordinates, as shown in Eq. 3.22. As discussed by Nadathur and Percival (2019), the effect of this coordinate shift manifests as an elongation along the line-of-sight direction within the void. This elongation competes with the flattening effect arising from the $f\Delta/3 + f\mu^2(\delta - \Delta)$ term presented in Cai et al. (2016). Although this approach extends the scales on which linear theory is accurate by including higher-order terms in the correlation function, it still makes the crucial assumption that the peculiar velocity follows linear theory (*i.e.* Eq. 3.9). Because of this assumption we refer to this quasi-linear method as Linear Approximation for the Velocity (LAV).

Extending from the quasi-linear LAV approach to the full non-linear RSD modelling requires a knowledge of the non-linear peculiar velocity profile, $v(r)$, and its gradient to solve,

$$\xi^s_{\rm NL}(s) = (1 + \xi^r(r)) \left[1 + (1 - \mu^2) \frac{1}{aH} \frac{v(r)}{r} + \mu^2 \frac{1}{aH} \frac{\partial v(r)}{\partial r} \right]^{-1} - 1, \qquad (3.25)$$

which is a combination of Eq. 3.10 and Eq. 3.13. In Sections 3.2 & 3.3 we developed a methodology to predict the non-linear peculiar velocity profiles using the spherical model. A caveat of this approach is that it requires a knowledge of the density profile from an earlier time as an initial condition. In the next section, we present our method to predict this initial, early-time density profile.

3.7 Initial Density Reconstruction

As presented in Section 3.2 the spherical evolution model can provide the non-linear peculiar velocity and density around spherical regions, however to predict the late-time non-linear peculiar velocity, we need a way of obtaining the initial conditions (*i.e.* the initial density profile). To do this, we present the following approach. Given a late-time density profile, we can employ the spherical model (Eqs. 3.4 - 3.6) to trace this profile back to an earlier epoch where linear dynamics dominated the Universe (*i.e.* $z \sim 10$). Although we arbitrarily choose the exact time/redshift to define our initial condition, we need to make sure that this epoch is sufficiently dominated by linear dynamics since we define the initial peculiar velocity from linear theory (Eq. 3.9) as discussed in Section 3.4.1. Within the spherical evolution formalism, each initial density will evolve to a unique late-time density, for an assumed cosmology. This is guaranteed by mass conservation, thus the mapping works up to the shell-crossing regime. This means that for a given cosmology we can easily map between the final and initial density profiles as shown in Fig. 3.8. The late-time density profile in this figure comes from the simulations used in this analysis (Section 3.8.1) and is linearly spaced in radial bins.

Each line in Fig. 3.8 shows the unique evolutionary trajectory of the density

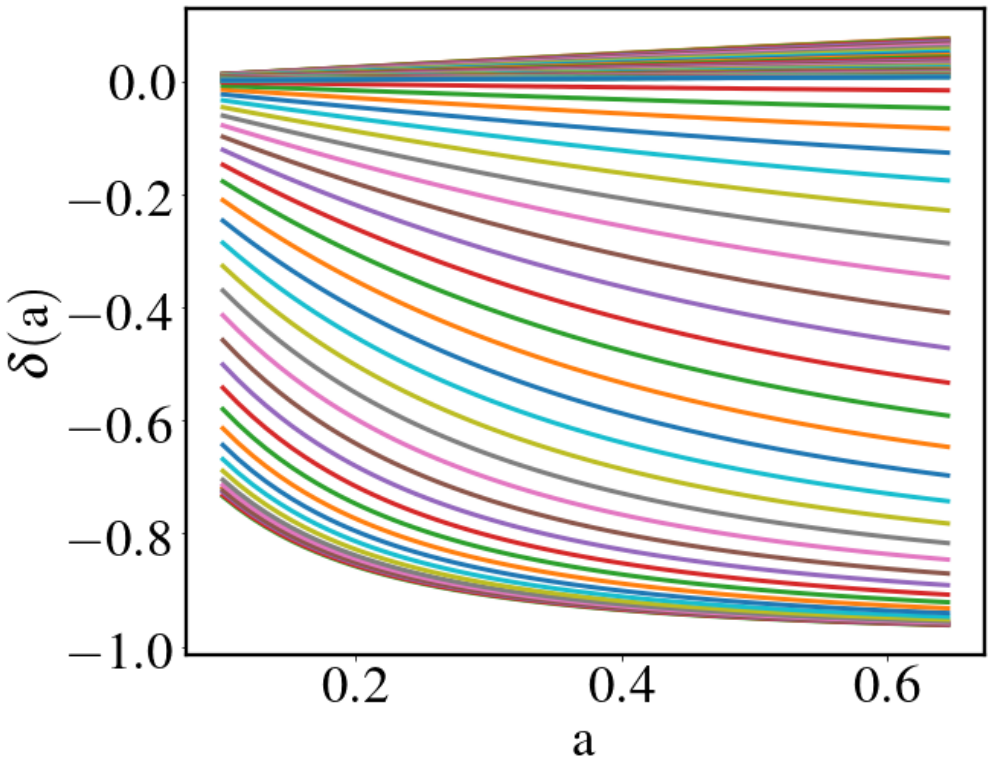

Figure 3.8 Evolution of 80 spherical shells from $a = 0.1$ and $a = 0.645$. These shells are linearly spaced in radius spanning the density range of $-0.73 < \delta(a = 0) < 0.01$. Within the spherical model formalism, the initial density can be obtained from the final density if the underlying cosmology is known.

contrast of a given spherical shell. Having mapped between the late-time and initial densities, we can use conservation of mass to calculate the initial physical radii of the spherical shells,

$$r_{p,i} = \left(\frac{r_{p,f}^3 \left(\delta_f + 1\right) \bar{\rho}_{\rm f}}{\left(\delta_i + 1\right) \bar{\rho}_i} \right)^{1/3}, \tag{3.26}$$

where the subscript p represents the physical radius, the subscripts f and i represents the evolved and initial quantities, respectively, and $\bar{\rho}$ is the mean density of the Universe at the time indicated by the subscripts.

After reconstructing the late-time density profile to the initial density profile, we can evolve this initial profile to a later epoch. As shown in Fig. 3.9, this methodology recovers the late-time density profile even if we choose a cosmology that differs from the fiducial cosmology. In the upper panel, we see that using our reconstruction technique, we obtain an initial density profile (red), which evolves to a late-time density profile (cyan and black) by construction. The lower panel of Fig. 3.9 shows the cosmological dependence of the initial profile. Note that all of the initial profiles in this panel, denoted by the colorbar, evolve to the same late-time profile represented by the black curve. Having used the spherical model to evolve the initial density profile to a later time, we now have a cosmology-dependent, non-linear velocity profile corresponding to our late-time density profile. This non-linear velocity constitutes the main missing ingredient needed to predict the non-linear RSDs around voids using Eq. 3.25. The upper panel of Fig. 3.10 compares the evolved non-linear peculiar velocity profile (black) with the late-time linear theory velocity from Eq. 3.9 (red). From Section 3.4 and Fig. 3.7 we see that the non-linear velocity profiles are more accurate than the linear profiles, particularly for large voids. We have compared the non-linear velocity profiles with the velocity profiles from the *N*-body simulations used in this analysis (Section 3.8.1) and see no deviations on large scales, therefore we do not require a large-scale bias correction term as discussed by Massara and Sheth (2018). The lower panel of Fig. 3.10 shows the cosmological dependence of the non-linear velocity profile. This clear cosmological dependence of the velocity profiles will create distinct, cosmology-dependent RSDs around voids.

As expected, the linear and non-linear profiles deviate on scales within the void, but as shown in Fig. 3.10, the deviation begins on scales outside the void radius. Since both of these velocity profiles depend on the density profile, different types of voids (*i.e.* compensated; void-in-cloud or uncompensated; void-in-void) will exhibit different relations between the linear and non-linear theory. This dependence on the density profile suggests the relationship between the velocity profiles will vary amongst void types (Cai et al., 2016). Furthermore, differences in cosmology will affect the linear and non-linear velocity profiles in different ways. For example, consider a background cosmology with an extra force term that behaves as an effective change to the gravitational constant, such as the nDGP model (e.g Falck et al., 2018). If a modification affects the gravitational

constant by enhancing it, in order for a void's lensing mass (*i.e.* late-time density profile) to remain constant, the dynamical mass must decrease, which will lead to a suppression of the peculiar velocity. Basically, our model assumes that the temporal and spatial potentials may vary, but the total remains the same. This behaviour leads to different RSDs and allows us to place tight constraints on parameters, such as the gravitational constant, using the non-linear velocity profile (see Section 3.8). This further suggests that any RSD modelling that relies upon the linear theory assumption for the velocity (such as the LAV model discussed in Section 3.6) will not have the capability to differentiate between different cosmologies as accurately as the full non-linear model. In summary, our method provides a reconstruction of the non-linear velocity profiles using only the late-time density profiles. These non-linear profiles will then increase the model accuracy by employing fully non-linear dynamics and probing all scales, including $R < R_{\rm v}$, allowing us to differentiate between various cosmologies.

3.8 Simulations and Model Comparison

In this section, we present the simulations used in this analysis as well as introducing how we extract the monopole and quadrupole for our data vector.

3.8.1 Simulations for Void Density Profiles

To forecast the constraining power on cosmology using non-linear RSDs around voids, we utilise cosmological *N*-body simulations. In particular, we use simulations created using the TreePM method (Bagla, 2002; White et al., 2002; Reid et al., 2014) with the Rockstar halo finder (Behroozi et al., 2013). These simulations were constructed by Martin White and described in Alam et al. (2017b)[4]. They consist of 10 ΛCDM ($\Omega_{\rm m} = 0.292$, $h = 0.69$) realisations of a periodic box with side length 1380 h^{-1}Mpc and 2048^3 particles evolved to $z = 0.55$. This simulation box volume corresponds to approximately one half of the effective volume of the DR11 CMASS survey (Bolton et al., 2012) that Alam et al. (2017b) employed for their analysis. The halos in these simulations are populated with mock galaxies following the Halo Occupation Distribution (HOD) prescription (see Section 4.1.2 for more details). Alam et al. (2017b) show that the parameters chosen for the HOD populate galaxies such that the clustering measurement of the *N*-body simulations and the BOSS CMASS sample that these simulations are meant to mimic, agrees to within 1σ. For the purposes of our analysis, we use one of the 10 boxes and identify voids using the zobov void finding algorithm (see Section 4.2.1). The voids are then selected on two criteria: the density of the void core cell is less than zero, $\delta_{\rm c} < 0$, and the void size $R_{\rm v} > 20\ h^{-1}$Mpc. After these void cuts, 28,381 voids remain for our analysis.

[4]These simulations are not publicly available and were provided to us by Shadab Alam.

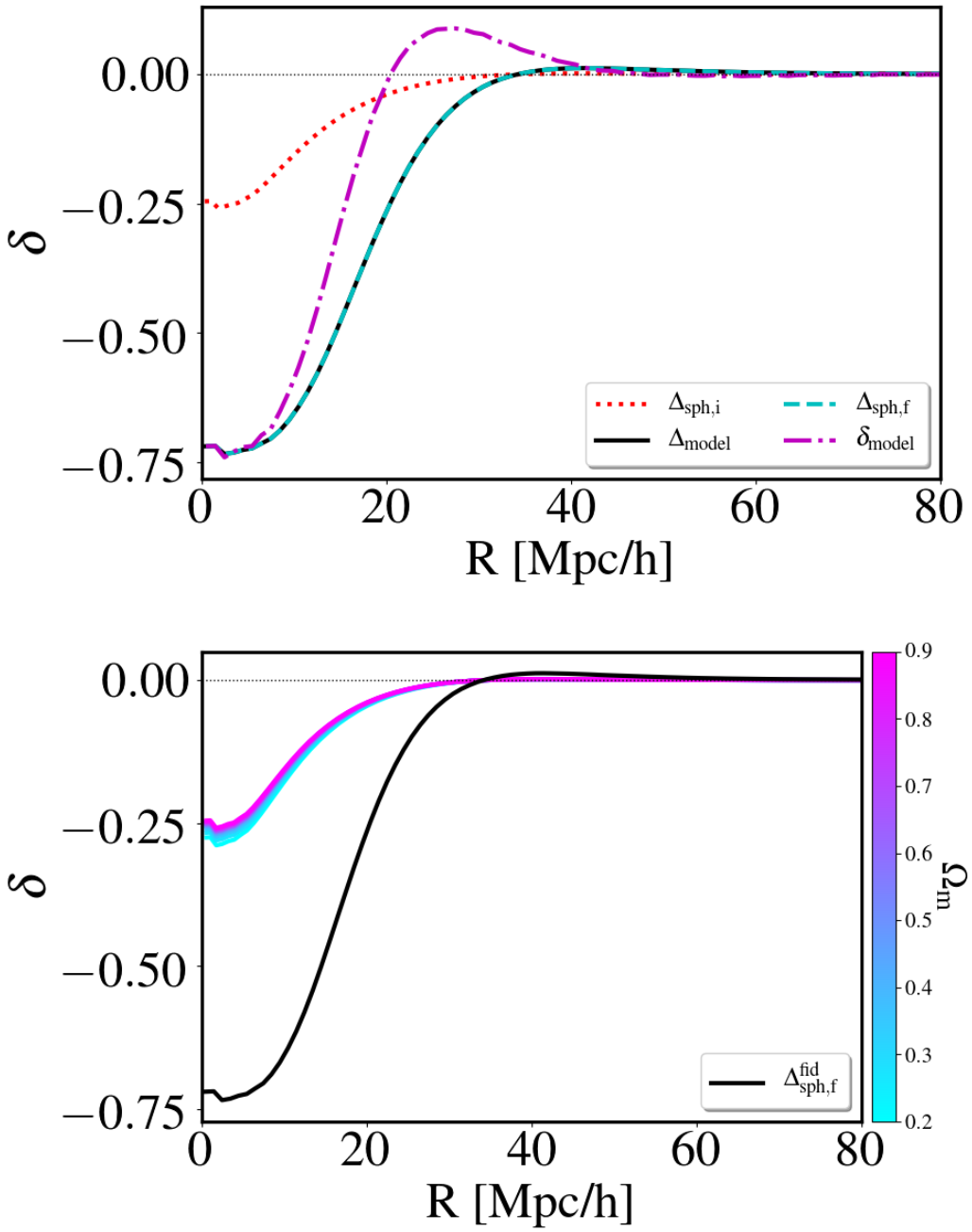

Figure 3.9 *Upper*: The dot-dashed magenta line represents our late-time differential profile and the solid black line represents the corresponding cumulative profile. The dotted red line represents the initial density profile mapped from the late-time profile, and the dashed cyan line shows the evolved version of the initial profile, which aligns with the late-time profile as expected. *Lower*: Initial differential density profiles from cosmologies with a varied Ω_m (colorbar) that correspond to the same late-time density profile (black).

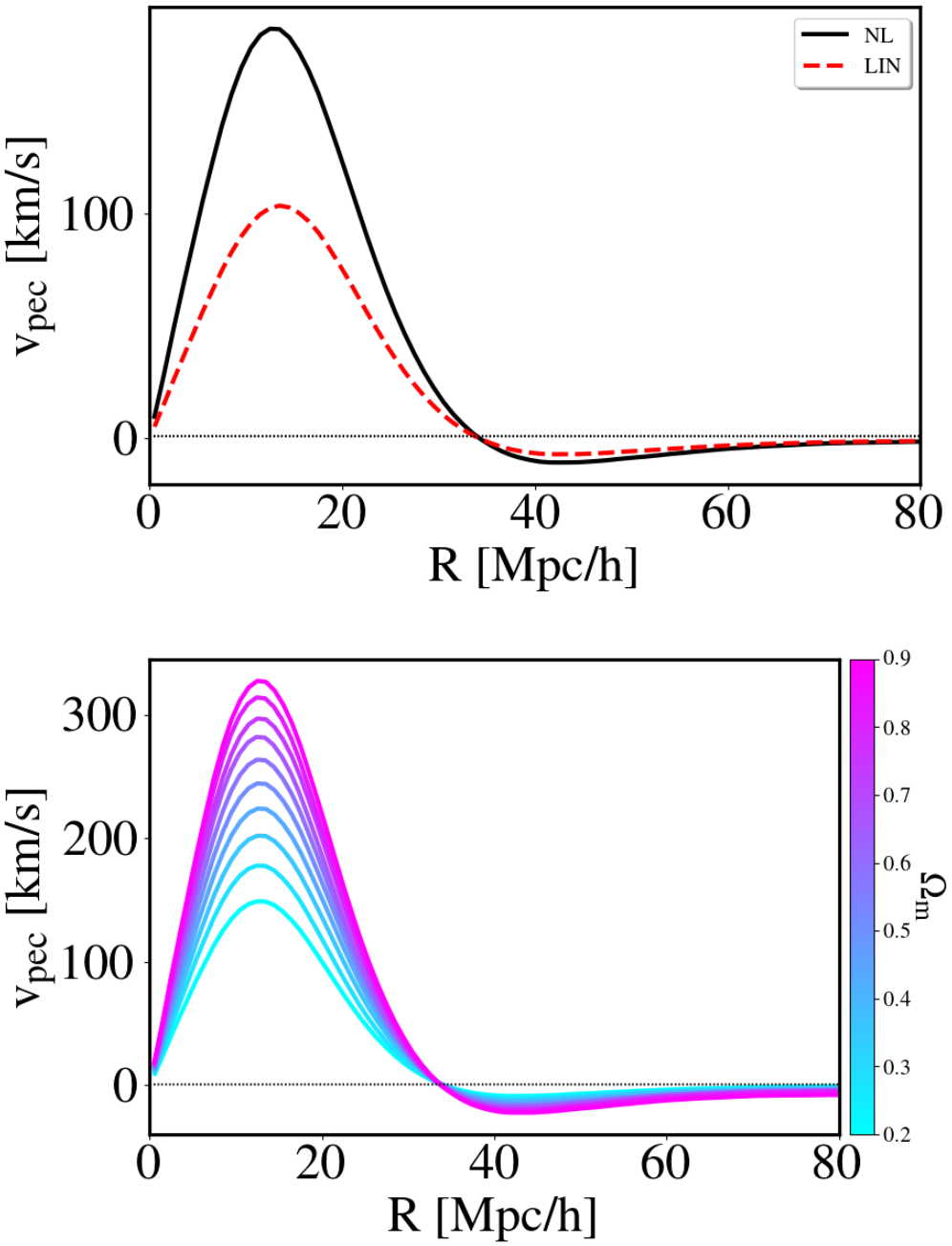

Figure 3.10 *Upper*: Comparison of the linear theory peculiar velocity (red) with the non-linear (black) version from the spherical model. *Lower*: Non-linear, late-time peculiar velocity profiles as a function of Ω_m corresponding to the late-time density profile in Fig. 3.9.

We use the average density profile of these voids as our late-time profile (black curve in Fig. 3.9) and calculate the covariance for the monopole-quadrupole data vector by decomposing the 2D correlation function for each individual void.

3.8.2 Multipole Decomposition

In this analysis we've explored three ways of constructing the 2D void-galaxy correlation function: linear theory in Eq. 3.16, the LAV approach in Eq. 3.20, and the non-linear model in Eq. 3.25.

Since we've obtained the non-linear peculiar velocity from the spherical model, we can take the derivative to obtain $\partial v(r)/\partial r$ without relying upon linear theory assumptions. In Fig. 3.11 we show the 2D correlation functions for the non-linear model (upper panel) and the LAV model (lower panel), highlighting several contours to show the various elongation and flattening characteristics (Cai et al., 2016). By eye, virtually no difference between the two panels exists, hence we show the difference between each pixel of these correlation functions in Fig. 3.12, which shows a distinct difference between the two models. From this figure, we see that along the line-of-sight direction the non-linear model produces enhanced clustering on scales within the void, and a slight suppression on scales around the mean void radius.

To quantify the differences between these models, we decompose the 2D correlation functions into their multipoles. We use Eq. 1.48 and fit for the monopole ξ_0, quadrupole ξ_2, and hexadecapole ξ_4 using,

$$P(\mu) = \xi_0 + \frac{3\mu^2 - 1}{2}\,\xi_2 + \frac{35\mu^4 - 30\mu^2 + 3}{8}\,\xi_4. \tag{3.27}$$

In practice, we loop over radial bins and calculate the mean of the 2D correlation function in 10 equally spaced μ^2 bins. This provides the measured multipoles per radial bin. In Fig. 3.13 we show the redshift-space monopole with the real-space monopole subtracted (upper) and the quadrupole (lower) for the three models we consider. We do not show the hexadecapole since its amplitude is negligible. We have tested our fitting procedure by removing the hexadecapole component from Eq. 3.27 finding no significant differences.

The two panels in Fig. 3.13 show three models: non-linear (NL, solid black), LAV (dashed magenta), and linear theory (LIN, dot-dashed green). Since the LAV model retains some higher order terms, we find that the monopole from this model resembles the non-linear model better than linear. The main differences in the monopole between LAV and the non-linear model arise at the void interior and the void boundary. This is expected since these are the most non-linear regions of a void. The quadrupole also shows distinctions amongst the three models. Just as with the monopole, LAV aligns with non-linear model better than linear model, however a noticeable offset in the amplitude of the quadrupole peak exists. The linear model has an increased amplitude on scales inside the void radius as compared to non-linear. The subtle differences between the monopole and quadrupole will vary with cosmology. We do not compare to the monopole and quadrupole directly with the simulations for several reasons. First, there is still debate within the void RSD community as to whether we should identify

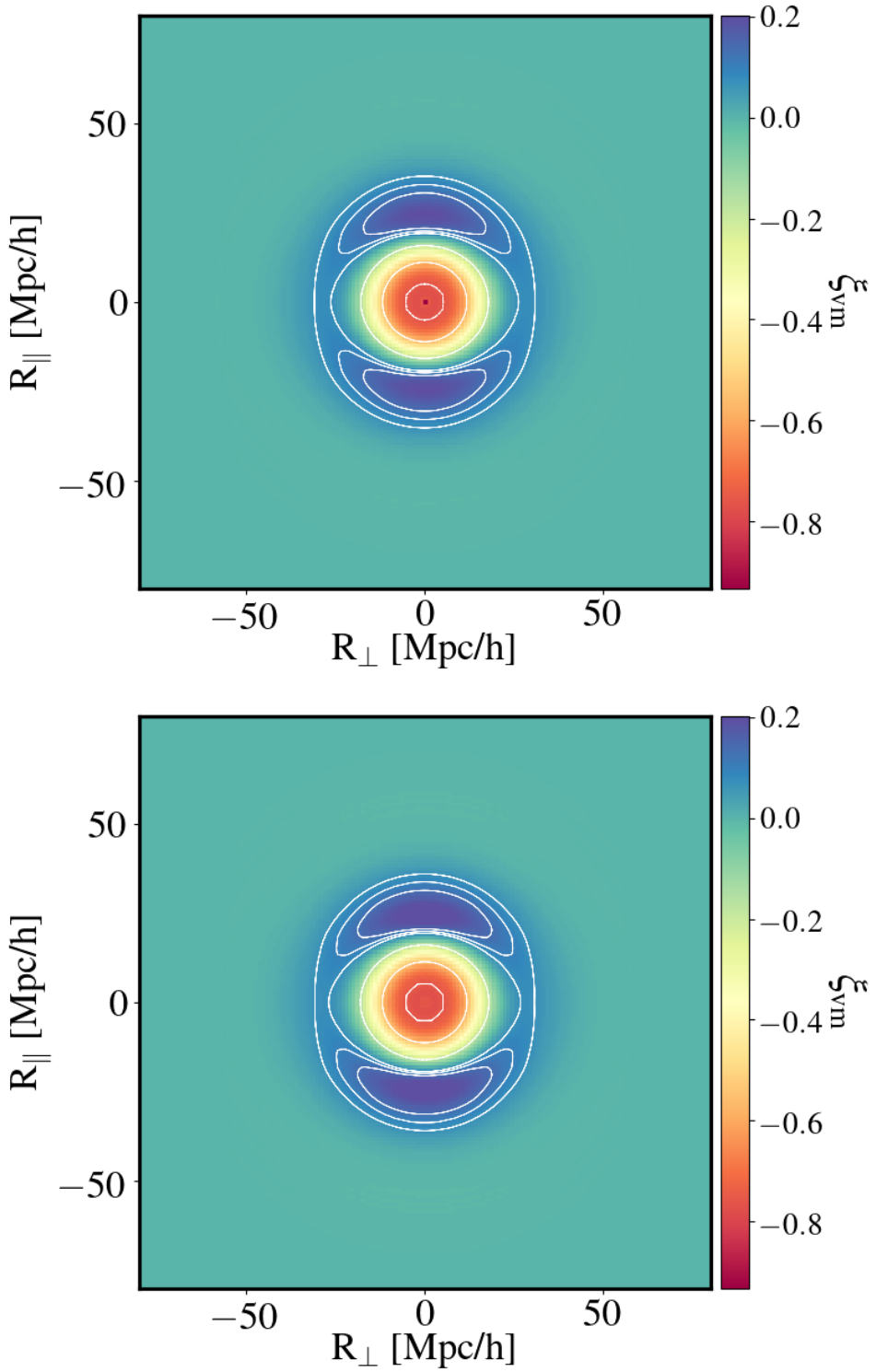

Figure 3.11 2D void-matter correlation functions with the non-linear modelling approach (upper) and LAV approach (lower) as described by Eqs. 3.25 and 3.20, respectively. These correlation function are at $z = 0.55$ for the cosmology of the N-body simulation described in Section 3.8.1. The central bin with lowest density in the non-linear model is an artefact of binning.

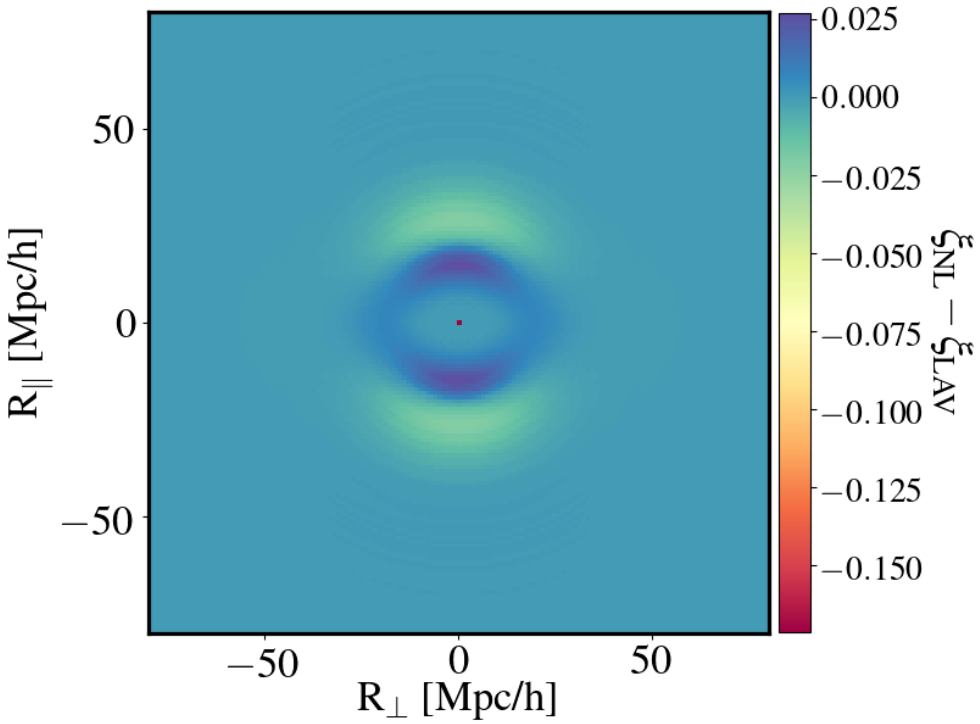

Figure 3.12 Difference between the upper and lower panels in Fig. 3.11, highlighting the differences between the non-linear and LAV models. The central bin with lowest density is an artefact of binning.

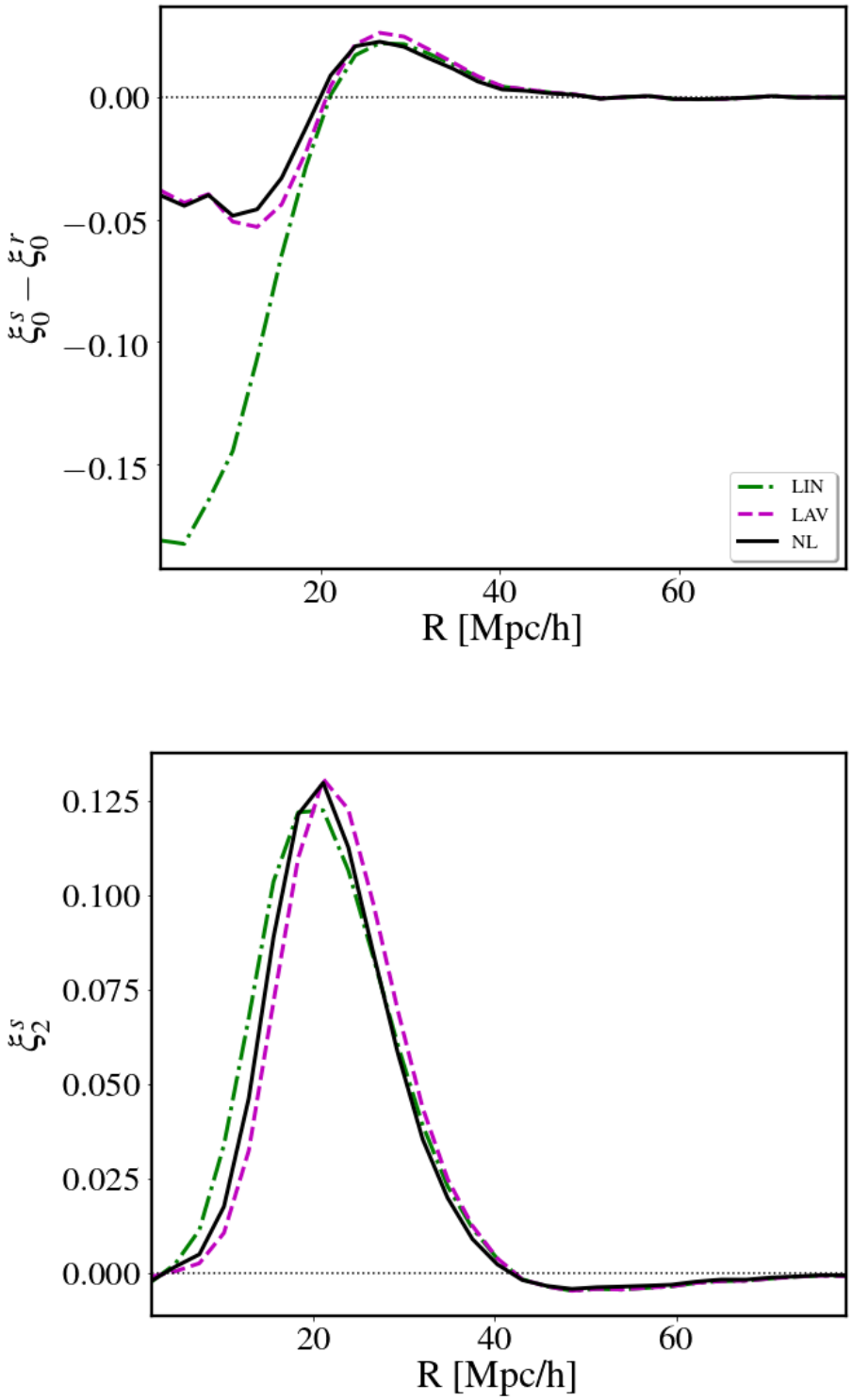

Figure 3.13 The monopole (upper) and quadrupole (lower) decompositions comparison between the linear (dot-dashed), LAV (dashed), and non-linear (solid) models. The profiles for these decompositions come from the simulations described in Section 3.8.1. Note that the upper panels shows the difference between redshift-space and real-space monopole for a clearer comparison between the models.

voids in redshift space or real space, which would affect the multipoles (Nadathur and Percival, 2019). Furthermore, although the non-linear model outperforms the LAV model, its accuracy is still disputable. We conducted preliminary tests showing that the non-linear model (Eq. 3.25) shows some level of deviation from RSDs around voids using a Monte Carlo galaxy distribution. Because of these complications, we know that the non-linear model and the simulations will disagree at the high precision level and, since our main focus is to compare the non-linear model to the LAV model, we leave the exploration of this disagreement for future work.

3.9 RSD and Lensing Combined Probes

Up to this point, we have presented a model to predict non-linear RSDs around voids using only the late-time density profile. In Section 3.9.2, we show the capabilities of our model to constrain cosmological parameters using the late-time density profiles extracted from the simulations introduced in Section 3.8.1. However, in order to apply this model to data, we need an observable late-time density profile. To this end, in Section 3.9.1 we discuss incorporating WL around voids (see Chapter 4), which provides an unbiased, late-time density profile, into our model. We provide a summary of our method in the flowchart in Fig. 3.14. This figure provides a high-level overview of our approach, where the hexagons indicate observables and rectangles with rounded edges represent our model. Using voids identified from a galaxy redshift survey, we propose to measure the WL signal around those voids, obtaining an unbiased, late-time density profile. We can then use that profile as an input into our non-linear RSD model and compare it to the RSDs measured around the voids from the galaxy redshift survey. In practice, we can employ the Landy-Szalay estimator (Landy and Szalay, 1993) to obtain the redshift-space 2D void-galaxy correlation function from observational data (Achitouv et al., 2017; Hamaus et al., 2017). This estimator combines all possible correlations between the data, D, and randoms, R, such that

$$\xi^s(r,\mu) = \frac{\langle D_\mathrm{v} D_\mathrm{g}\rangle - \langle D_\mathrm{v} R_\mathrm{g}\rangle - \langle D_\mathrm{g} D_\mathrm{v}\rangle + \langle R_\mathrm{v} R_\mathrm{g}\rangle}{\langle R_\mathrm{v} R_\mathrm{g}\rangle}, \tag{3.28}$$

where angled brackets denote normalised pair counts at separation r and μ. In the next section, we present the motivation for combining RSDs around voids with WL.

3.9.1 Combined Probes Motivation

In present-day cosmology, optimising survey strategies to extract the maximum amount of information from our Universe presents a powerful approach for making

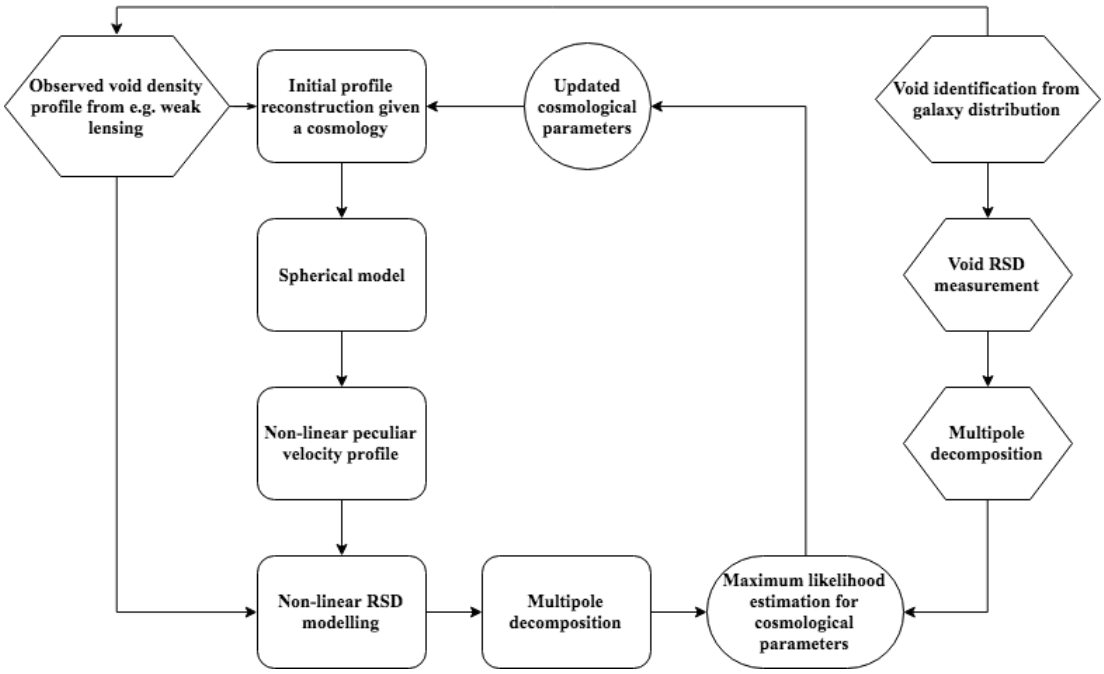

Figure 3.14 Flowchart describing our methodology for using the late-time density profile for cosmological constraints. The hexagons represent observables, the rectangles with rounded edges represent our modelling method, and the circle and oval represent an MCMC and its output.

accurate measurements. One way to accomplish this is for surveys to probe the same area of the sky using different survey strategies. This means that surveys can use each others' data, such as spectroscopic galaxy redshifts, to mitigate systematic effects and mutually improve the quality of each survey's analysis. An example of such collaboration is when lensing surveys overlap with spectroscopic galaxy redshift survey, such as the KiDS - GAMA overlap (see Chapter 4). A benefit of such symbiosis arises by using different measurements of the same density field, such as WL from KiDS and galaxy clustering from GAMA, to evade the effects of sampling variance (Bernstein and Cai, 2011; Cai and Bernstein, 2012; Hamaus et al., 2012; Alarcon et al., 2018). In fact, Bernstein and Cai (2011) show that combining an overlapping galaxy redshift survey with a WL survey has the potential to increase the constraints on the linear growth rate tenfold. The combinations of these overlapping surveys can lessen the effect of cosmic variance, which reduces the uncertainties of the growth rate measurement from RSDs (McDonald and Seljak, 2009; White et al., 2009). Since RSDs only measure $\beta = f/b$, a precise knowledge of the galaxy bias b needs to be accounted for to improve constraints on the growth rate. In principle, cross-correlating galaxy convergence from a WL survey with galaxy clustering provides a measurement of galaxy bias (Pen, 2004). Technically, cross-correlating a spectroscopic galaxy sample with an overlapping WL signal occurs in the transverse modes, while an RSD analysis of the spectroscopic galaxy sample will occur over the non-transverse modes over the same volume (Cai and Bernstein,

2012). This allows a high accuracy measurement of the large-scale modes in the linear regime (Bernstein and Cai, 2011).

As discussed in Section 1.8.3, voids provide a complementary tool for cosmology. Voids present a particularly interesting case study for RSDs since they are non-linear objects with potentially simpler dynamics than galaxies or galaxy clusters, if they have not evolved into the shell-crossing regime. Furthermore, since voids tend to become more spherical as they evolve, they constitute useful objects upon which to apply the AP test if their RSD signal is well understood. In fact, Cai et al. (2016) applied the linear theory RSD formalism to voids showing that RSDs around voids can independently provide a constraint on the growth rate. Moreover, they show that information from the quasi-linear regime of voids (*i.e.* $R \gtrsim 0.5R_{\rm v}$) can be exploited if applying the velocity dispersion model. Taking this approach, several other groups have measured the constraints on the growth rate using RSDs around voids from currently available datasets (Achitouv et al., 2017; Hawken et al., 2017). The tightest cosmological constraints from voids come from the analysis of Hamaus et al. (2017). They use a linear theory multipole decomposition approach with the SDSS BOSS data finding constraints on $\Omega_{\rm m}$ at 10% accuracy and β at 12% accuracy. More recently, Nadathur et al. (2019b) made a similar measurement to Hamaus et al. (2017), where they combined the void-galaxy correlation function with BAO and RSD measurements, showing how voids help to break degeneracies in the parameter space for these measurements.

However, to fully extract cosmological information from small scales, we need models that extend beyond linear scales. This extension to non-linear scales is of particular importance for RSD analyses since it increases the number of perturbation modes one can use in the analysis, increasing the constraints for cosmology. Due to the strong non-linear mapping between real space and redshift space, even large-scales become affected by higher order contributions. Consequently, linear theory lacks sufficient accuracy to describe the evolution of the large-scale density and velocity field, which requires sophisticated modelling (e.g. Scoccimarro, 2004; Matsubara, 2008; Jennings et al., 2011). Several models exist to further the RSD analysis into beyond-linear regimes such as the Gaussian Streaming model (e.g. Reid and White, 2011), perturbation theory approaches (e.g. Crocce and Scoccimarro, 2006; Matsubara, 2008; Taruya et al., 2010; Seljak and McDonald, 2011; Carlson et al., 2013; Wang et al., 2014), and other methods that use the moments expansion approach or a Lagrangian perturbation theory approach (see Vlah and White, 2018, for more details). Despite the continuous advances in modelling of RSDs, there is no consensus within the RSD community as to which approach provides the highest accuracy, with a persisting need for models that can accurately probe the non-linear regime.

One of the major restrictions of current theories is obtaining accurate, non-linear velocity profiles. As discussed in Section 3.7, we have introduced a methodology to reconstruct non-linear velocity profiles for cosmic voids, given only a late-time density profile from *e.g.* weak lensing. We showed how to utilise the spherical expansion model to trace the late-time density profile back to the initial

profile for an assumed background cosmology and then evolve this early-time profile to recover the non-linear velocity profile corresponding to the late-time density profile. Using this method, we showed how to predict the fully non-linear modelling of the RSD signal around voids, although ignoring the effect of velocity dispersions. In the next section, we present the capability of our model to place constraints on cosmological parameters using the simulations from Section 3.8.1.

3.9.2 Cosmological Constraints from RSDs Around Voids

Having constructed a methodology to measure the non-linear RSD signal around voids, we explore the potential of this method to constrain cosmological parameters using the void profiles from the simulations discussed in Section 3.8.1. To do this, we take the following steps. First, we select our late-time density profile, which we assume we have measured from WL, but for this forecast we obtain it directly from the simulations (see Section 3.8.1). We then apply the profile reconstruction technique (see Section 3.7) to extract the non-linear velocity profile. Since this relies on the spherical model, we can freely choose the underlying cosmology (*i.e.* $\Omega_{\rm m}$, Ω_Λ, $\Omega_{\rm k}$, G, w, etc.). By construction, the late-time density profile will always be the same for each cosmology, however the non-linear velocity will since it depends on the reconstructed initial density profile, which is cosmology-dependent (see lower panel of Fig. 3.9). Next, we use the evolved velocity and density profiles to construct the 2D void-galaxy correlation function in redshift-space as given by Eq. 3.25, which provides the theoretical model that we would compare to a direct measurement from observations (Eq. 3.28). From the 2D correlation function, we extract the monopole and quadrupole using the approach presented in Section 3.8.2 to combine the monopole and quadrupole into a single data vector. For the covariance, we use the simulations to measure of the 2D void-galaxy correlation function for each void. In practice, after identifying the voids, we use the particle distribution to compute each particle's transverse and line-of-sight distance to the void centre, bin each particle based on those distances, and then normalise to obtain a redshift-space 2D void-galaxy correlation function per void. Finally, we decompose these correlation functions into the monopole-quadrupole data vector and calculate the covariance as,

$$C^{ij} = \frac{1}{N-1}\sum_{n=1}^{N}(\xi^i_{{\rm vec},n} - \overline{\xi}^i_{\rm vec})(\xi^j_{{\rm vec},n} - \overline{\xi}^j_{\rm vec})\,, \tag{3.29}$$

where N is the number of voids, $\xi^i_{\rm vec}$ is the monopole-quadrupole data vector in the i-th radial bin of the n-th void, and $\bar{\xi}^i_{\rm vec}$ is the monopole-quadrupole data vector average of the i-th bin from all voids. Using the above covariance, we then

calculate the χ^2,

$$\chi^2 = \sum_c^N \Delta_c \, C^{-1} \, \Delta_c^\intercal, \tag{3.30}$$

where $\Delta_c = \xi_{\rm vec}^c - \xi_{\rm vec}^{fid}$, $\xi_{\rm vec}^c$ is the monopole-quadrupole vector for cosmology c, $\xi_{\rm vec}^{fid}$ is the monopole-quadrupole vector for the fiducial cosmology from the simulations, which serves as our mock data vector, and $\Delta_c^\intercal$ represents the transpose of Δ_c. Finally, we convert the χ^2 to the log-likelihood,

$$\ln\mathcal{L} \propto -\frac{\chi^2}{2}. \tag{3.31}$$

Utilising this set up, we run a Markov chain Monte Carlo (MCMC) analysis to find constraints on cosmological parameters using our non-linear void RSD model. We use the EMCEE sampler (Foreman-Mackey et al., 2013), which is a PYTHON implementation of an affine invariant ensemble sampler for MCMC proposed by Goodman and Weare (2010). This approach, known as a 'stretch move' algorithm, is an improvement on the standard Metropolis-Hastings algorithm (Hastings, 1970) in terms of autocorrelation time (Foreman-Mackey et al., 2013).

In essence, our fiducial, mock data vector represents a shape-noise-free measurement from a survey with approximately half the volume of CMASS. We recognise the need to include intrinsic shape noise into the covariance for a fully robust analysis, however, for this study, we explore the possible cosmological constraints our model provides in an idealised, shape-noise-free setting. Fig. 3.15 shows the constraints on $\Omega_{\rm m}$, $G_{\rm factor}$, and w. $G_{\rm factor}$ denotes the factor by which we alter the Newtonian gravitational constant,

$$G_{\rm factor} = \frac{G_{\rm true}}{G}, \tag{3.32}$$

where $G_{\rm true}$ represents the true gravitational constant of our Universe.

The priors used in Fig. 3.15 are $\Omega_{\rm m} : [0.2, 0.9]$, $G_{\rm factor} : [0.9, 1, 1]$, and $w : [-1.25, -0.75]$, and we find that the fiducial values lie within the 68% confidence intervals. We do not find a significant constraint on w in this analysis, however we do find a slight degeneracy in the $w - \Omega_{\rm m}$ plane, similar to the degeneracy seen by BAO measurements (see Fig. 6 of Suzuki et al., 2012). In Fig. 3.16 we extend our analysis by exploring the constraints on the curvature of the Universe, $\Omega_{\rm k}$. To do this, we explore the $\Omega_{\rm m} - G_{\rm factor} - \Omega_\Lambda$ parameter space with $\Omega_\Lambda : [0.1, 0.9]$. This analysis shows that our model provides tight constraints on $\Omega_{\rm m}$, which propagates to tight constraints on $G_{\rm factor}$. Furthermore, we see our model has the potential to constrain the geometry of the Universe through a combination with other probes, such as BAOs and supernovae, to break degeneracies in the $\Omega_{\rm m} - \Omega_\Lambda$ plane (see

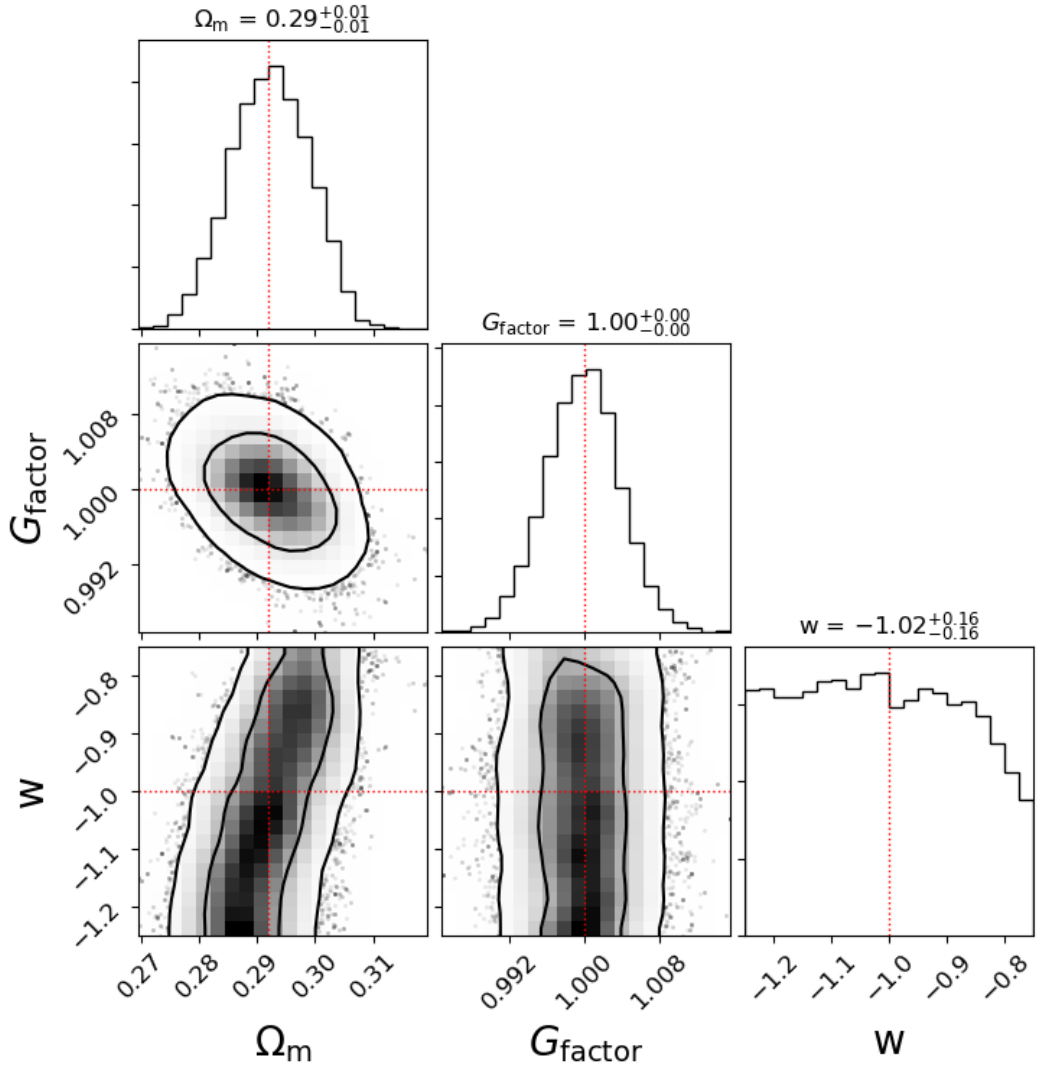

Figure 3.15 MCMC constraints for Ω_m, G_{factor}, and w using the spherical model to create non-linear 2D void-galaxy correlation functions and using the decomposition method discussed in Section 3.8.2 to extract the monopole-quadrupole data vector. The red-dotted lines show the fiducial values and the contours show the 68% and 95% confidence intervals.

Fig. 5 of Suzuki et al., 2012). In contrast, Fig. 3.17 shows the constraints in the same parameter space using the LAV model. Since this figure shows essentially no constraints on $G_{\rm factor}$ and a much broader constraint on both $\Omega_{\rm m}$ and Ω_Λ, this suggests that the LAV model does not have the constraining power of the non-linear approach. In Section 3.10, we discuss the differences between these two models as well as the potential of the non-linear model to single-handedly break degeneracies within the $\Omega_{\rm m} - \Omega_\Lambda$ plane without relying on external datasets.

3.10 RSDs Around Voids Discussion and Conclusions

We have shown that, using the spherical model, we can create a non-linear 2D void-galaxy correlation function in redshift space that captures the non-trivial flattening and elongation distortions. As explained by Cai et al. (2016), understanding and modelling these distortion patterns is necessary to understand the RSDs around voids and apply the AP test. Several groups have shown that linear and quasi-linear models can be used to measure the RSD signal around voids (Achitouv et al., 2017; Hamaus et al., 2017; Hawken et al., 2017; Nadathur et al., 2019b), however their modelling is insufficient to account for the non-linear regimes. Figs. 3.12 and 3.13 show the difference between our non-linear model and other, less accurate models. Although the differences between non-linear model and LAV do not appear significant by eye, these small deviations, particularly on small scales, could lead to a mis-estimation of the growth rate. It's also important to remember that different sizes and types of voids will exhibit different deviations from the non-linear theory in both the monopole and quadrupole.

Analysing the cosmological constraints, we find that the RSD decomposition into the monopole-quadrupole vector places stringent constraints on cosmological parameters as seen in Figs. 3.15 - 3.17. Our study suggests that combing WL and RSDs around voids identified in redshift space from a shape-noise-free CMASS-like survey at $z = 0.55$ with a volume of $(1380\ h^{-1}{\rm Mpc})^3$ can constrain the gravitational constant to within 0.4%, which can place constraints on modified gravity theories that deviate from this value (Falck et al., 2018). However, as shown by the LAV constraints in Fig. 3.17, such precision on cosmological parameters only comes from exploiting the full non-linear information. As shown in Fig. 3.18, a distinct shift in the $\Omega_{\rm m} - \Omega_\Lambda$ degeneracy exists between the LAV model (dot-dashed blue) and the non-linear model (solid black). This shift enables the non-linear model to constrain $\Omega_{\rm m}$ to a higher precision as compared to the LAV model. Figs. 3.16 and 3.17 show that the non-linear model provides significantly tighter, unbiased constraints, while the LAV model shows a biased distribution with larger errors. We attribute this bias to the fact that LAV uses a linear velocity profile and does not fully exploit the non-linear information in the interior of the void. This causes a greater degree of freedom within the evolution equation, leading to the LAV model's inability to constrain $G_{\rm factor}$, and since

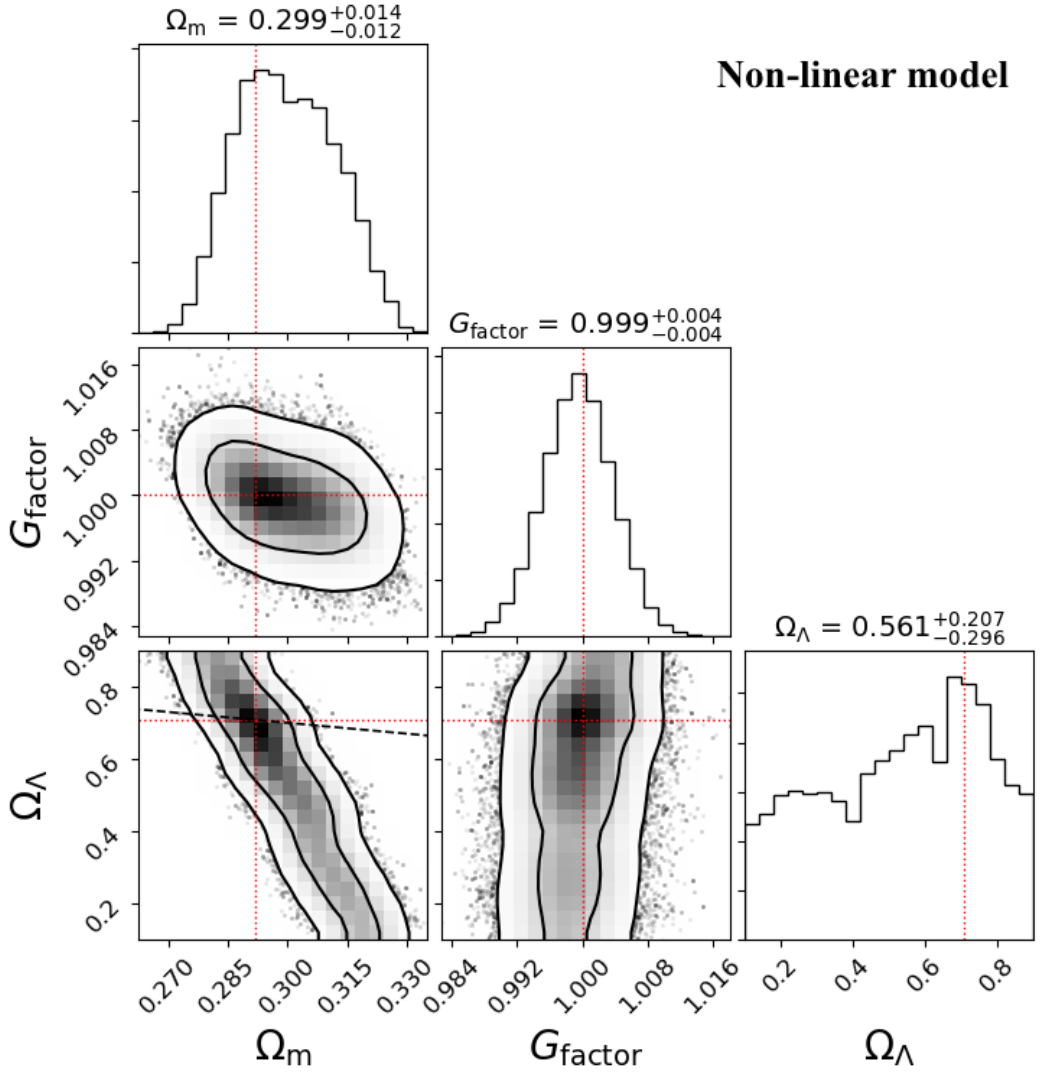

Figure 3.16 MCMC constraints for Ω_m, G_{factor}, and Ω_Λ using the spherical model to create non-linear 2D void-galaxy correlation functions and using the decomposition method discussed in Section 3.8.2 to extract the monopole and quadrupole. The red-dotted lines show the fiducial values, the black dashed line represents a flat universe, and the contours show the 68% and 95% confidence intervals.

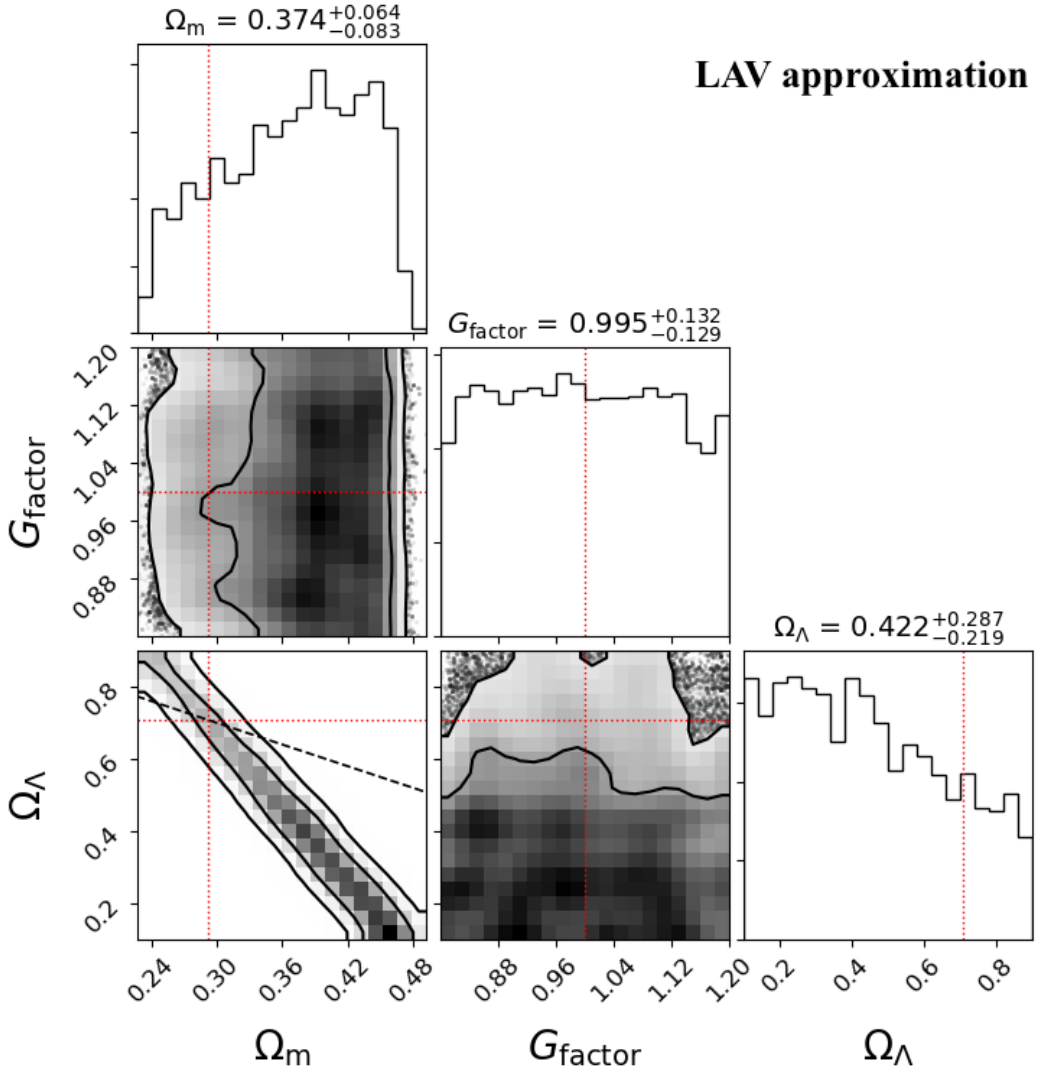

Figure 3.17 MCMC constraints for Ω_m, G_{factor}, and Ω_Λ using the LAV approach to model 2D void-galaxy correlation functions and using the decomposition method discussed in Section 3.8.2 to extract the monopole and quadrupole. The red-dotted lines show the fiducial values, the black dashed line represents a flat universe, and the contours show the 68% and 95% confidence intervals.

$\Omega_{\rm m}$ can vary to a larger degree than the non-linear case, the effect of the $G_{\rm factor}$ becomes negligible. We can understand this through the evolution equation (Eq. 3.8), where we see that matter and the gravitational constant are degenerate with one another.

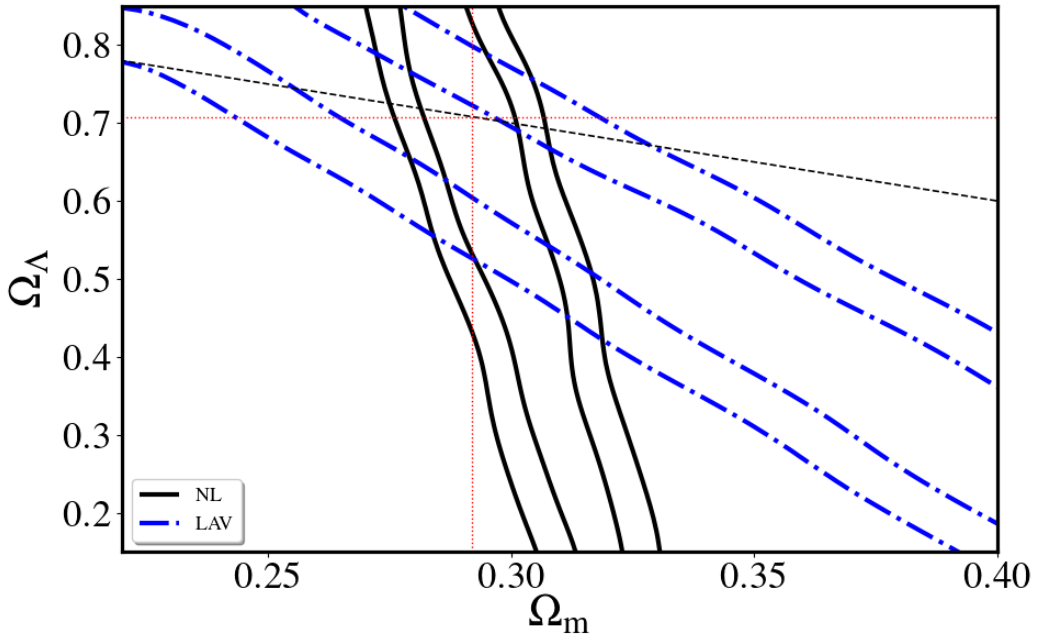

Figure 3.18 Comparison of the contours from the non-linear model (solid black) to the LAV model (dot-dashed blue). We find that the rotation in the degeneracy caused by non-linear information places a tighter constraint on $\Omega_{\rm m}$ as compared to using the LAV approximation. The dashed black line represents a flat universe and the dotted red lines represent the fiducial parameter values.

Furthermore, our methodology can be extended to possibly constrain $G_{\rm factor}$ or the curvature of the Universe using the RSDs around voids without the addition of measurements from external data such as the CMB, BAOs, and supernovae. Considering the evolution equation Eq. 3.8, we recognise that as mass decreases, the influence of Ω_Λ increases. This suggests that, with a tight prior on G, different regions within the void can independently constrain $\Omega_{\rm m}$ and Ω_Λ. In Fig. 3.19 we explore how different void scales affect the precision on these cosmological parameters. The upper panel in this figure shows how the constraint on $G_{\rm factor}$ changes as we use information from different scales. As shown in Fig. 3.9 the peak density of our void sample occurs at $\sim 25\ h^{-1}$Mpc thus we divide the interior of the void into two scales: $0 < R < 12.5\ h^{-1}$Mpc (dotted cyan) and $12.5 < R < 25\ h^{-1}$Mpc (dashed magenta). As the upper panel of Fig. 3.19 shows, these two sets of scales provide independent information with a different degeneracy. The small scale behaviour can be understood as follows: since the inner part of the void has relatively less matter compared to other scales, the dynamics will be dominated by the expansion factor of the evolution equation. This means that constraints on $\Omega_{\rm m}$, and correspondingly on $G_{\rm factor}$, will be broad. However, as

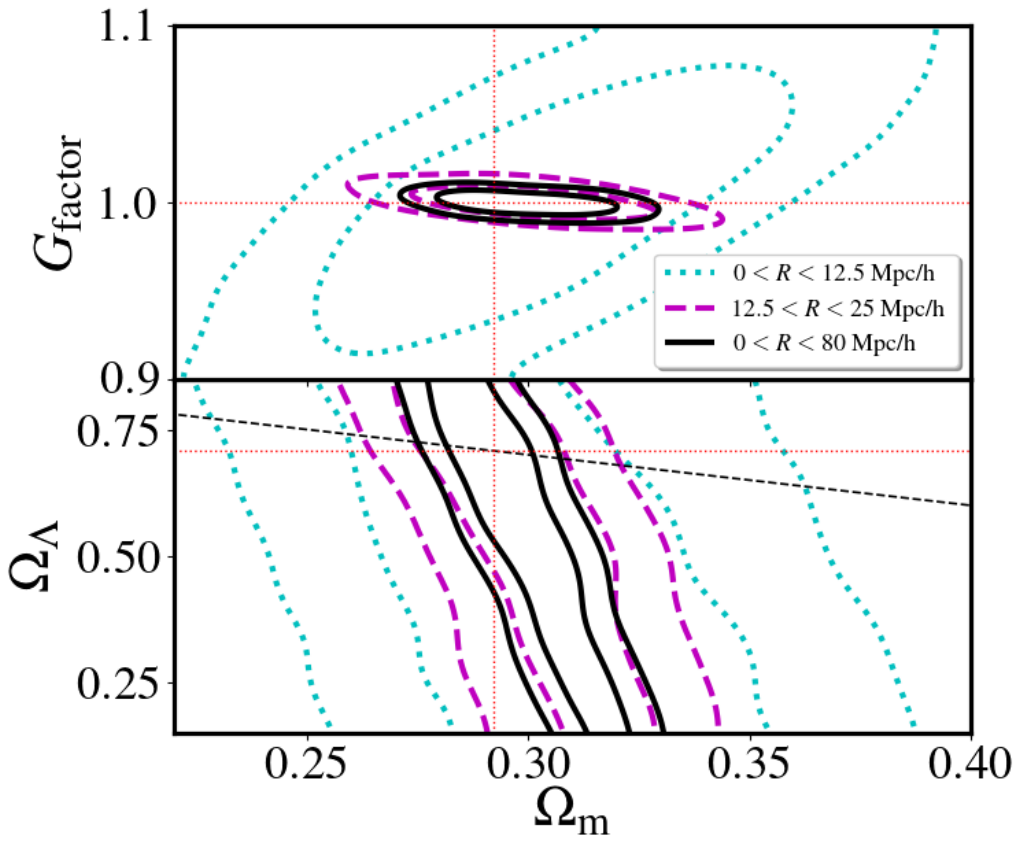

Figure 3.19 Constraints on the $\Omega_{\rm m} - G_{\rm factor}$ plane using different range of scales indicated in the legend. *Lower*: similar to the upper panel but showing constraints on the $\Omega_{\rm m} - \Omega_\Lambda$ plane. The dashed black line represents a flat universe. For both panels, the contours represent 68% and 95% confidence intervals and the crossing points of the red-dotted lines represent the fiducial values.

we begin to include more mass, the balance between the matter and dark energy parts of the evolution begins to shift, which creates tighter constraints for all three parameters. As presented in the lower panel in Fig. 3.19, including more scales significantly improves the constraint on $\Omega_{\rm m}$. In theory, we also expect a rotation in the degeneracy direction between the various scales since different aspects of the evolution equation will dominate on different scales. To test this, we calculate the covariance matrix from all 10 simulation boxes, to simulate a larger survey area and decrease the errors by a factor of ~ 3.

As shown in Fig. 3.20, although using the covariance from all 10 simulation realisations reduces the errors on our measurement with significantly tighter constraints, we do not see a rotation of degeneracy in the $\Omega_{\rm m} - \Omega_\Lambda$ plane for different void scales. Our void selection criteria could be the cause of this. Since we select all voids with $R > 20\ h^{-1}$Mpc, we effectively mix various void profiles into one. From Fig. 3.7, we see how the density profiles of voids varies as a function of size. In order to fully investigate the degeneracy rotation, we could split our void sample into smaller, compensated voids that exhibit a distinct

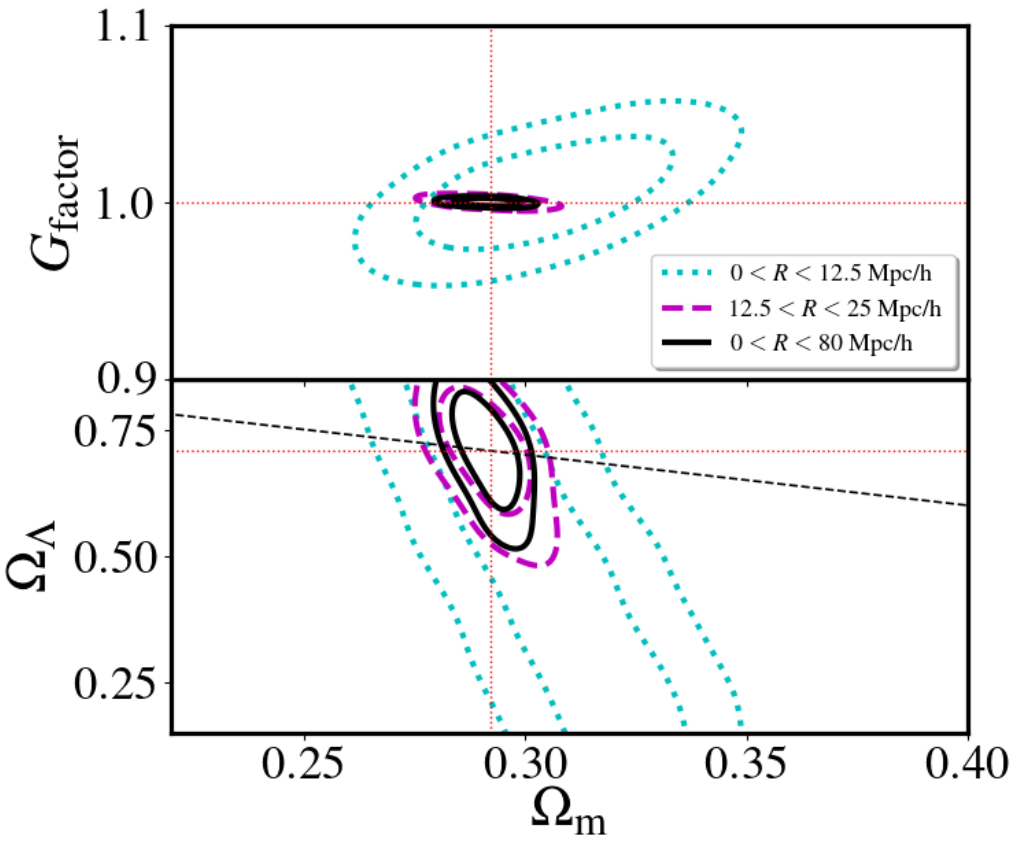

Figure 3.20 Same as Fig. 3.19, except using the covariance from all 10 simulation realisations. This effectively reduces the errors on the measurement by a factor of ~ 3.

ridge feature in their density profiles, and larger, uncompensated voids with no ridge feature. This split would provide more refined and uniform void samples to investigate the balance between the matter and dark energy components of the evolution equation. Furthermore, we have not accounted for any intrinsic shape noise from WL. This will cause an uncertainty to the late-time density profile, which we have thus far assumed to be measured noise-free, and will need to be incorporated into the covariance. Since our aim for this chapter is to demonstrate the machinery of our method, we leave this detailed investigation for future work. In the end, we show that the constraints in the $\Omega_{\rm m} - \Omega_\Lambda$ plane from RSDs around voids using a fully non-linear model clearly show a degeneracy direction not seen by other probes. This suggests that combing this measurement with other probes, such as the CMB, BAOs, or supernovae, could further our knowledge of the geometry of the Universe by including a measurements from the underdense regions.

3.10.1 Limitations and Further Studies

One of the main limitations of our approach, as discussed in Section 3.5, is the fact that we do not take into account any random movement of the void centre, assuming it to follow the bulk motion of surrounding matter. Although that may be true to large voids that do not have much matter near the void centre, such is not the case for smaller voids. This is one of the reasons that we do not find as good agreement between our model and the simulations for voids with $R_{\rm v} = 25$ h^{-1}Mpc in Fig. 3.7. We do expect the void centre for smaller voids to move more than for larger voids since these voids are more susceptible to tidal forces from nearby overdensities, tend to exhibit a higher degree of asphericity, and are prone to reside within larger overdense regions (void-in-cloud). Furthermore, we note the distinct differences in identifying voids in Lagrangian space vs Eulerian space. As discussed in Massara and Sheth (2018), the spherical model does not account for the evolution of large-scale structure tracers. Identifying voids in at an earlier epoch and following their evolution in Lagrangian space would require a proper correction for the evolution of tracer bias, which would impact the void centre location. However, we note that our model and reconstruction method only requires the late-time density profile in Eulerian space. We have compared our late-time non-linear peculiar velocity profiles with those from the N-body simulations finding no deviations on large scale, indicating that our model does not suffer from tracer evolution bias on large scales.

In terms of our RSD analysis, there is still a debate as to whether or not identifying voids in redshift space affects the monopole-quadrupole decomposition. Nadathur et al. (2019a) present a method for reconstructing void density profiles from redshift space into real space. Technically, identifying void profiles in real space mitigates the effect of void mis-centring and allows for a more accurate measurement of the Alcock-Paczyński test. However, if we rely upon WL to measure void density profiles, this measurement will inherently be in real space since any distortions to the shapes of galaxies due to foreground matter will manifest in real space. If future studies do indicate that we need to identify voids in real space, Nadathur et al. (2019b) have made their reconstruction method public and surely more methods will come to light if the community requires such reconstruction techniques for accurate constraints. Another considerable over-simplification of our analysis is our treatment of the late-time density profile. In our analysis, we assumed that we had a shape-noise-free, late-time density profile, however since we propose to obtain this profile through WL, it will come with errors (see Chapter 4). For a more robust analysis and for applying our method to data, we would need to incorporate the errors from the WL measurement into our covariance, which would broaden the constraints in Fig. 3.16. The effect of lensing noise will depend on the quality of the data and the size of the overlap region between the lensing and galaxy redshift survey, hence we need more overlap between such surveys to fully exploit the power of void WL (Pisani et al., 2019).

As a look to the future, our model could be enhanced to account for modified gravity theories (e.g. Falck et al., 2018). Falck et al. (2018) investigate if

voids could be used to test gravity models that employ a Vainshtein screening mechanism, which does not depend on halo mass or environment. They show a way of analytically incorporating an effect mimicking an nDGP gravity model by adding a modification to the matter component of the acceleration equation (first term in Eq. 3.8), which functions as an effective change to the Newtonian gravitational constant, G. Our exploration of deviations to G in Section 3.9.2 are essentially a simplified version of the modification in Falck et al. (2018). Since we have shown the capability of our model to constrain G, the next step would be to implement the more advanced, scale dependent alteration, which could place constraints on modified gravity theories relying on Vainshtein screening. Furthermore, we could include massive neutrinos into our cosmological modelling. Several groups (Massara et al., 2015; Kreisch et al., 2018) have shown how massive neutrinos affect the void clustering, number counts, and density profiles. By allowing a varying neutrino mass in our model, we could potentially use the late-time density profile to constrain the mass of neutrinos. Kreisch et al. (2018) found that increasing the neutrino mass induces a shift in the peak of the void auto-correlation function to larger scales and boosts this correlation. In principle, our model can detect a shift in the peak particularly since that will affect the peak of the monopole and quadrupole of the RSDs. As we allow more parameters to vary in our model, we will require a way to quickly and efficiently sample a higher-dimension parameter space. To assist with this, we could employ the emulator approach of (e.g. Giblin et al., 2019) who have shown the accuracy of their emulator with the *cosmo*-SLICS simulations discussed in Chapter 5. Such a technique would facilitate the inclusion of more parameters into our model, providing constraints on modified gravity and neutrino mass using physics on non-linear scales.

In summary, we have applied the spherical model in a ΛCDM cosmology showing its ability to reproduce evolved density and velocity profiles for voids from an N-body simulation. We also extended this approach to a generalised cosmology and presented a methodology to reconstruct initial void density profiles from late-time profiles and obtain the non-linear velocity profile corresponding to the late-time density profile. Using these non-linear density and velocity profiles, we can predict the RSDs around voids using a fully non-linear model and showed the possibility of our model to constrain cosmological parameters. In the following chapter, we turn our attention to the main missing ingredient for our model: obtaining void density profiles from WL data.

If we could read the secret history of our enemies, we should find in each man's life sorrow and suffering enough to disarm all hostility.

Henry Wadsworth Longfellow

4

Void Weak Lensing

This chapter explores the weak lensing measurement from voids in the KiDS and GAMA surveys, as well as from simulations that mimic these surveys. To begin, in Section 4.1 I describe the simulations used for this analysis. Then, in Section 4.2, I describe the void finding algorithm employed to identify voids. In Section 4.3 I present the measurement of the void WL signal from the simulations, while Section 4.4 shows the results from observational data. Section 4.5 concludes this chapter by providing an overview of my findings.

4.1 SLICS

This section provides a brief overview of the *Scinet LIght Cone Simulations* (SLICS hereafter) (Harnois-Déraps and van Waerbeke, 2015; Harnois-Déraps et al., 2018). Section 4.1.1 describes the dark matter N-body simulations and their construction whereas Section 4.1.2 describes the mock lens galaxy catalogues created using HOD prescriptions and 4.1.3 describes the mock source galaxy catalogue used. The content of these sections comes from Harnois-Déraps et al. (2018), of which I am a co-author, however I have re-written them in my own terms.

4.1.1 Dark Matter Simulations

The simulations used for the analysis of the void weak lensing signal are the SLICS (Harnois-Déraps and van Waerbeke, 2015). The SLICS suite was specifically

designed for weak lensing signal and covariance estimation for the KiDS-450 analysis (Hildebrandt et al., 2017), thus making it an ideal set of mock simulations for a void weak lensing analysis. The SLICS consist of a series of 1025 N-body simulations generated by the CUBE^{3}PM gravity solver (Harnois-Déraps et al., 2013). Out of the 1025 simulations, 817 realisations can be used for a full probe weak lensing analysis with each realisation containing 1536^3 particles in a comoving cubic box of side length $L_{\rm box} = 505\ h^{-1}$Mpc, $N_{\rm cell} = 3072$ grid cells, and a particle mass of $m_p = 2.88 \times 10^9\, h^{-1}{\rm M}_\odot$, which resolves dark matter halos above $10^{11}\, h^{-1}{\rm M}_\odot$. Using the Zel'dovich approximation for the initial conditions (Zel'dovich, 1970), the N-body code then computes non-linear evolution of collisionless dark matter particles from $z_i = 120$ down to $z = 0$ while generating on-the-fly halo catalogues and mass sheets in order to create a full lightcone. Using the Born approximation, 18 flat sky convergence and shear maps are extracted from $z = 3$ to $z = 0$ through a multiple-plane tiling technique (see Vale and White, 2003, for more detail). As the simulation reaches a certain lens redshift, z_l, particles from half of the cosmological volume are projected along the line of sight using a 'cloud-in-cell' methodology (Hockney and Eastwood, 1981). These redshifts are chosen such that half the volumes fill the space in $0 < z < 3$. Using this approach, the first mass plane represents a projected comoving volume at 252.5 h^{-1}Mpc starting from the observer at redshift $z = 0$, which is half of the box size. This first mass plane is assigned to the centre of the box, which corresponds to 126.25 h^{-1}Mpc or $z_l = 0.042$. The second mass plane then corresponds to the volume in 252.5 - 505 h^{-1}Mpc with its centre at 378.75 h^{-1}Mpc and $z_l = 0.130$. Table 4.1 shows the lens planes, z_l, and the corresponding source planes, z_s. The lightcone itself is constructed by tracing rays on a regular grid consisting of 7745^2 pixels with an opening angle of 100 deg^2. This opening angle contains the full box up to $z = 1.36$ after which period boundary conditions are implemented to extend the lightcone to $z = 3$. From these projected mass sheets Harnois-Déraps et al. (2018) calculate the overdensity mass maps, $\delta_{\rm 2D}(\boldsymbol{\theta}, z_{\rm l})$, using a linear interpolation of the mass overdensity sheets onto mock pixels, $\boldsymbol{\theta}$, after randomly shifting the origins in order to minimize repeated structure across redshift when constructing the full lightcone. Fig. 4.1 shows a projected overdensity map constructed in the redshift range of the SDSS LOWZ survey, showing a complex structure of halos. Using these mass maps as a discrete set of thin lenses at comoving distance, $\chi_{\rm l}$, and discrete source distribution, $n(z)$, with bins of width $\chi_{\rm s}$, Harnois-Déraps et al. (2018) construct convergence maps, $\kappa(\boldsymbol{\theta})$:

$$\kappa(\boldsymbol{\theta}) = \frac{3H_0^2\Omega_{\rm m}}{2c^2} \sum_{\chi_{\rm l}=0}^{\chi_{\rm H}} \delta_{\rm 2D}(\boldsymbol{\theta}, \chi_{\rm l})(1+z_{\rm l})\chi_{\rm l}\Big[\sum_{\chi_{\rm s}=\chi_{\rm l}}^{\chi_{\rm H}} n(\chi_{\rm s})\frac{\chi_{\rm s}-\chi_{\rm l}}{\chi_{\rm s}}\Delta\chi_{\rm s}\Big]\Delta\chi_{\rm l}, \qquad (4.1)$$

where H_0 is the Hubble constant at the present day, $\Omega_{\rm m}$ is the present day matter density, c is the speed of light, $\chi_{\rm H}$ is the comoving distance to the horizon, $n(\chi) = n(z){\rm d}\chi/{\rm d}z$, and $\Delta\chi_{\rm l} = L_{\rm box}/N_{\rm cell}$. Since the lens redshifts are associated with the natural source redshifts ($z_{\rm s}$ in Table 4.1) that correspond to infinitely thin planes

Table 4.1 Lens and source redshifts used by Harnois-Déraps et al. (2018) to generate lightcones from the observer at $z = 0$ to $z \approx 1.5$ by stacking half boxes with a comoving thickness of 252.5 h^{-1}Mpc per box. The source planes lie at the end of the half box, whereas the lens planes lie at the centre of the half box.

z_l	0.042	0.130	0.221	0.317	0.418	0.525	0.640	0.764	0.897	1.041	1.199	1.373
z_s	0.086	0.175	0.268	0.366	0.471	0.582	0.701	0.829	0.968	1.118	1.283	1.464

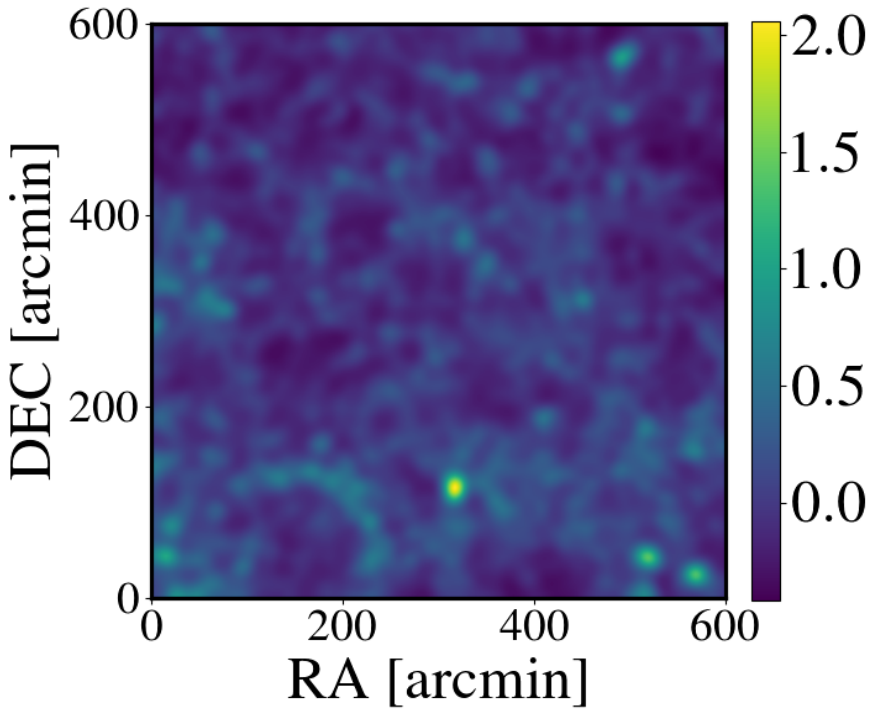

Figure 4.1 Projected overdensity map for one realisation of the SLICS simulation. The map is constructed in the redshift range of $0.15 < z < 0.43$ to resemble the LOWZ sample.

located right behind the half box, no interpolation is required in the line-of-sight direction to build the convergence maps and thus 18 such maps are generated per lightcone, with the assumption that $n(z) = \delta(z - z_\mathrm{s})$. This approach, however, explicitly breaks the correlations in the matter field between boxes. The effect of this feature will be discussed in Section 4.3.

The fiducial cosmological parameters of these simulations are that of the best fit WMAP9 + SN + BAO (Hinshaw et al., 2013), which are: $\Omega_\mathrm{m} = 0.2905$, $\Omega_\Lambda = 0.7095$, $\Omega_\mathrm{b} = 0.0473$, $h = 0.6898$, $\sigma_8 = 0.826$, and $n_\mathrm{s} = 0.969$. These parameters are used throughout this chapter, unless otherwise stated.

4.1.2 Mock Lens Galaxy Catalogues

The construction of the SLICS lens samples aims to reproduce the galaxy clustering as well as the galaxy-galaxy lensing signal of the CMASS and LOWZ samples (Reid et al., 2016), which are part of the Baryon Oscillation Spectroscopic Survey (BOSS, Alam et al., 2017a), as well as the Galaxy And Mass Assembly (GAMA, Liske et al., 2015) spectroscopic survey. The mock lens galaxies in these catalogues have a similar galaxy clustering, galaxy bias, and redshift distribution as the surveys themselves. Harnois-Déraps et al. (2018) achieve this by populating the dark matter halos of SLICS with mock galaxies using a Halo Occupation Distribution (HOD) framework (Peacock and Smith, 2000; Seljak, 2000; Zehavi et al., 2011). The HOD formalism is a statistical approach that utilises the virial mass of a dark matter halo, M_h, to populate N galaxies within the halo. This approach effectively describes the relationship between the number of galaxies and the mass of the underlying dark matter halo:

$$\langle N_{\rm cen}(M_{\rm h})\rangle = \frac{1}{2}\Big[1 + {\rm erf}\Big(\frac{\log M_{\rm h} - \log M_{\rm min})}{\sigma_{\rm logM}}\Big)\Big], \tag{4.2}$$

$$\langle N_{\rm sat}(M_{\rm h})\rangle = \langle N_{\rm cen}(M_{\rm h})\rangle \Big[\frac{M_{\rm h} - M_0}{M_1}\Big]^{\alpha}. \tag{4.3}$$

In the above equations, $N_{\rm cen}$ and $N_{\rm sat}$, introduced by Kravtsov et al. (2004) and Zheng et al. (2005), describe the number of central and satellite galaxies, respectively, populated in a halo of mass $M_{\rm h}$ within the HOD formalism, where ${\rm erf}(x)$ is the error function, $M_{\rm min}$ regulates the minimum mass of a halo that can host a central galaxy, $\sigma_{\rm logM}$ represents the the scatter about this minimum mass, M_0 is the cutoff mass scale, M_1 corresponds to the average mass required for a halo to host at least one satellite, and α is the slope that regulates the number of satellites as a function of halo mass. As noted from Eq. 4.2, the ${\rm erf}(x)$ function ensures that each halo receives a probability between zero and one central galaxies. The mean number of satellite galaxies, $\langle N_{\rm sat}(M_{\rm h})\rangle$, is then dependent on the probability of the central galaxy, where halos with no central galaxy also have no satellite galaxies. The sum of $\langle N_{\rm cen}(M_{\rm h})\rangle$ and $\langle N_{\rm sat}(M_{\rm h})\rangle$ yields the total number of galaxies in a halo, $N_{\rm tot}$. Fig. 4.2 shows an example of mean halo occupation for the following set of HOD parameters: $M_{\rm min} = 10^{11.57}\,h^{-1}M_{\odot}$, $\sigma_{\rm logM} = 0.17$, $M_0 = 10^{12.23}\,h^{-1}M_{\odot}$, $M_1 = 10^{12.75}\,h^{-1}M_{\odot}$, and $\alpha = 0.99$. As seen in Fig. 4.2, there are no satellite galaxies below $M_0 = 10^{12.23}\,h^{-1}M_{\odot}$ and every halo above $M_1 = 10^{12.75}\,h^{-1}M_{\odot}$ has at least one satellite galaxy. Harnois-Déraps et al. (2018) place the central galaxy at the location of the density peak of the halo and then distribute any satellites using a spherically symmetric NFW profile (Navarro et al., 1996),

$$\rho(r) = \frac{\rho_0}{\frac{r}{R_{\rm s}}\Big(1 + \frac{r}{R_{\rm s}}\Big)^2}, \tag{4.4}$$

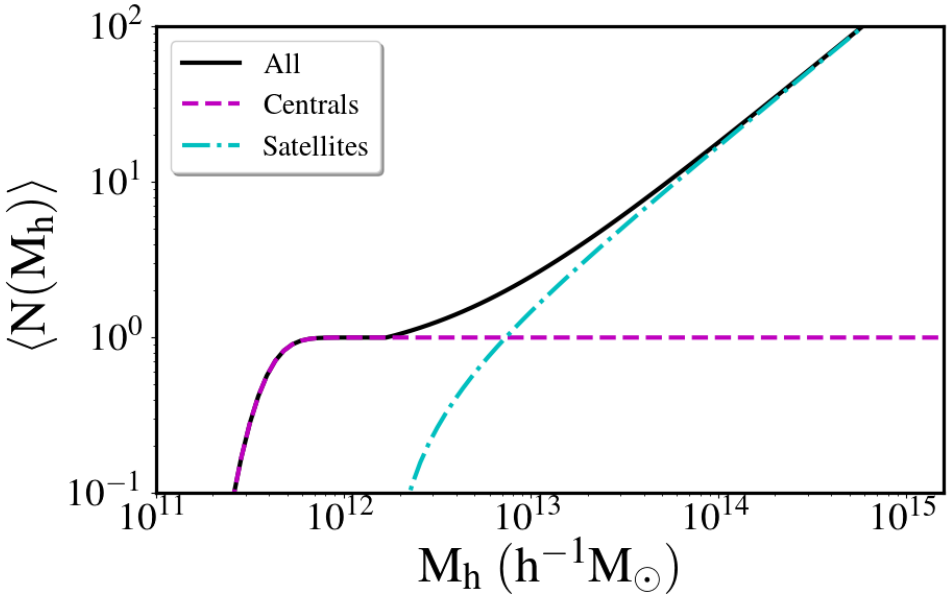

Figure 4.2 The mean halo occupation from Eqs. 4.2 and 4.3 for a set of HOD parameters from Zehavi et al. (2011).

where ρ_0 is the mean density and R_s is a scale radius. A crucial aspect of the NFW profile is the concentration-mass parameter, $c(M)$. This parameter defines the concentration of satellite galaxies as a function halo mass and relates the scale radius, R_s, to the virial radius of a halo, R_{vir}. Since Harnois-Déraps et al. (2018) chose to reproduce particular observables of each galaxy sample, they used the same $c(M)$ models as the original HOD prescriptions. This means that the Bullock et al. (2001) relation was used for CMASS and LOWZ HODs (as in Alam et al., 2017b), and the Macciò et al. (2007) relation was implemented for the GAMA HOD (as in Cacciato et al., 2013). Through a manipulation of the 5 HOD parameters and a proper concentration model, galaxies can populate halos to reproduce the desired observables of a chosen survey.

CMASS and LOWZ HOD Galaxies

In order to construct HOD mock galaxies that represent the CMASS and LOWZ samples, Harnois-Déraps et al. (2018) optimise the prescription of Alam et al. (2017b), as introduced in Section 3.8.1, to increase the agreement between the measured clustering of the mock galaxies and SDSS galaxies. The difference in the target selection between the northern and southern Galactic caps is large enough that different calibration techniques are needed between the two samples (Reid et al., 2016). Since the northern Galactic patches of BOSS cover a larger volume than the southern ones, the CMASS and LOWZ HODs were calibrated on the northern patches. CMASS is a volume-limited sample and in order to generate a similarly volume-limited mock galaxy catalogue, Harnois-Déraps et al. (2018) randomly down-sample the high-redshift tail of the mocks. The top row of Table

5 in Harnois-Déraps et al. (2018) shows the HOD parameters used as inputs for Eqs. 4.2 and 4.3, which are then used as mean values for a Poisson distribution in order to get the number of central and satellite galaxies for each halo. After the down-sampling approximately a third of the galaxies in the redshift range $0.6 < z_{\rm spec} < 0.7$, the mean redshift between the mock sample and data reaches a 2% agreement, and so does the number density of galaxies.

The mock LOWZ sample follows the same approach as CMASS with the HOD parameters shown in the bottom row of Table 5 of Harnois-Déraps et al. (2018). There was no down-sampling performed for LOWZ and the mean redshift of the mocks agrees with the data within 3%, while the effective number density agrees within 2%.

GAMA HOD

Unlike the CMASS and LOWZ samples, the GAMA survey is not a volume-limited sample but a magnitude-limited one. This means that in order to reproduce the redshift distribution and clustering of this spectroscopic dataset, the HOD requires a more complicated modelling, which reproduces the apparent magnitude of GAMA. In order to match an HOD to the magnitude-limited GAMA sample, Harnois-Déraps et al. (2018) implement the prescription of Smith et al. (2017), which uses a conditional luminosity function (CLF) approach. Through the CLF methodology, the number of central and satellite galaxies depends not only on the mass of the halo, but also on the luminosity range. In practice, this works by choosing an absolute magnitude range, which Harnois-Déraps et al. (2018) set to $[-26.7 < M_{\rm r} < -18.0]$, and then obtaining the number of central galaxies by integrating the central CLF in the luminosity range corresponding to the absolute magnitude. All of the HOD parameters in Eqs. 4.2 and 4.3 now depend not only on halo mass, $M_{\rm h}$, but also on the minimum luminosity threshold, $L_{\rm min}$. In modelling the mean luminosity-mass function Harnois-Déraps et al. (2018) use the model of Zehavi et al. (2011) and the parameters of Smith et al. (2017):

$$\langle L_{\rm cen}(M_{\rm h}, z)\rangle = L_{\star}\Big[A_{\rm t}\Big(\frac{M_{\rm h}}{M_{\rm t}}\Big)^{\alpha_{\rm M}}\exp\Big(\frac{-M_{\rm t}}{M_{\rm h}}+1.0\Big)\Big]\times 10^{0.4Q(z-0.1)}. \qquad (4.5)$$

The mean of the luminosity-mass function in Eq. 4.5 exhibits the behaviour of a power law with index, $\alpha_{\rm M}$, at the high-mass end and is exponentially suppressed at the low-mass end. The transition from between low-mass and high-mass occurs at $M_{\rm t}$ and is modulated by amplitude parameter, $A_{\rm t}$, which has units of $L_{\star}$. The parameter Q encodes the redshift evolution making the mean luminosity-mass relation dependent on both halo mass and redshift. Setting this parameter to zero removes any redshift dependence.

As noted by the subscript on the left-hand-side of Eq. 4.5, the mean luminosity-mass relation assigns a luminosity only to central galaxies and not to satellite

galaxies. In order to compute the number of satellites as a function of both halo mass and luminosity, Harnois-Déraps et al. (2018) split the absolute magnitude range into 30 bins and use the CLF per bin yielding:

$$\langle N_{\rm sat}^{\rm bin} \rangle = \langle N_{\rm sat}(> L_{\rm max}|M_{\rm h})\rangle - \langle N_{\rm sat}(> L_{\rm min}|M_{\rm h})\rangle, \tag{4.6}$$

where $L_{\rm min}$ and $L_{\rm max}$ are the bin boundaries. A luminosity randomly drawn from the bin is then assigned to each satellite in that bin. Once each galaxy, central and satellite, have been identified and assigned a luminosity, Harnois-Déraps et al. (2018) convert each luminosity to an apparent and absolute magnitude applying a K-correction (Hogg et al., 2002). This K-correction is applied to every galaxy's apparent magnitude as a function of its spectroscopic redshift. In practice, this K-correction shifts higher redshift galaxies to a brighter apparent magnitude and provides a more accurate fit to the data when a magnitude selection is applied to the galaxies:

$$\begin{aligned} k(z) &= a_0 z^4 + a_1 z^3 + a_2 z^2 + a_3 z + a_4, \\ m_r(z) &= m_r + k(z). \end{aligned} \tag{4.7}$$

The coefficients a_x in Eq. 4.7 represent polynomial coefficients that were fitted to account for the degeneracy of the K-correction with the redshift dependence of the luminosity function. After applying the K-correction, the GAMA mock data is selected with $z < 0.5$ and $m_r < 19.8$. This produces an 11% and a 6% agreement between the mock catalogues and the GAMA data (Robotham et al., 2011; Taylor et al., 2011; Baldry et al., 2018) for the redshift distribution and number density, respectively.

4.1.3 Mock Source Galaxy Catalogues

In order to build a mock catalogue of source galaxies, Harnois-Déraps et al. (2018) place galaxies at random angular coordinates within each SLICS 100 deg^2 lightcone, while matching the redshift distribution, $n(z)$, and the number density, $n_{\rm gal}$, with the KiDS-450 data. This section discusses the source galaxies generated using the $n(z)$ and $n_{\rm gal}$ of the KiDS-450 dataset, however this methodology can be applied to any weak lensing survey. The galaxies are populated with a number density of $n_{\rm gal} = 8.53$ gal/arcmin^2, which matches the effective number density of the KiDS-450 sample after being weighted by similar noise properties as described in Kuijken et al. (2015). The $n(z)$ in the mocks follows the most accurate redshift estimation method identified in the KiDS-450 analysis, namely the 'DIR' method, which re-weights spectroscopically-matched sub-samples of the KiDS-450 dataset that span 2 deg^2 (see Section 4.4.2 for more details). The mocks also contain photometric redshifts, $z_{\rm B}$. These are assigned to each mock galaxy from a joint PDF, $P(z_{\rm B}|z_{\rm spec})$, with a given $z_{\rm spec}$ for that galaxy. Since the DIR method of

galaxy redshift estimation covers a relatively small area that may or may not be representative of the dataset as a whole, it is affected by sampling variance. This means that when populating the mocks, a residual difference occurs causing a mismatch between the tomographic bins of the mocks and of the KiDS-450 dataset, as shown in Table 4.2. This slight offset in $n_{\rm gal}$ does not affect the agreement between the $n(z)$ of the DIR method and the mocks when split into tomographic bins.

After assigning the galaxy coordinates and redshift, Harnois-Déraps et al. (2018) calculate the weak lensing shear components, $\gamma_{1,2}(\boldsymbol{\theta})$, using shear planes calculated from the convergence planes discussed in Section 4.1.1. This takes advantage of the coupling between the convergence/shear planes and the gravitational potential, as discussed in Chapter 2 (Eq. 2.12). Since the SLICS are flat sky mocks, a fast Fourier transform technique can be applied for this calculation (Harnois-Déraps et al., 2012; Harnois-Déraps and van Waerbeke, 2015). The shear components are then linearly interpolated from the shear planes to each galaxy coordinate and redshift. This interpolation is along the line-of-sight direction, not the pixel direction, meaning that galaxies that have the same redshift residing in the same pixel have the same shear component values. However, in data we observe galaxy ellipticity rather than shear, so the source catalogues include the observed ellipticity defined as:

$$\epsilon^{\rm obs} = \frac{\epsilon^{\rm int} + \gamma}{1 + \epsilon^{\rm int}\gamma^*} + \eta \approx \frac{\epsilon^{\rm n} + \gamma}{1 + \epsilon^{\rm n}\gamma^*}, \tag{4.8}$$

where ϵ, η, and γ are complex numbers (i.e. $\gamma = \gamma_1 + i\gamma_2$). $\epsilon^{\rm int}$ represents the intrinsic ellipticity and γ the shear, whereas $\epsilon^{\rm obs}$ is also affected by measurement noise, η. In order to stay as consistent with the data as possible, Harnois-Déraps et al. (2018) chose not to differentiate between intrinsic shape noise and that introduced through the measurement itself. Therefore, the noisy ellipticity, $\epsilon^{\rm n}$, is an approximation of both intrinsic and measurement shape noise, which is assigned by drawing a random number from a Gaussian distribution with $\sigma = 0.29$ per component, consistent with the weighted ellipticity distribution found in the KiDS-450 dataset.

Harnois-Déraps et al. (2018) test these source mocks by comparing two-point correlation functions of the mocks to those estimated from theoretical prescriptions,

$$\xi_{\pm}^{\alpha\beta}(\theta) = \frac{\sum_{i,j} w_i w_j \left[\epsilon_{\rm t}^i \epsilon_{\rm t}^j \pm \epsilon_{\rm x}^i \epsilon_{\rm x}^j\right]}{\sum_{i,j} w_i w_j}, \tag{4.9}$$

which defines the position-shape correlation function that was estimated using ATHENA (Kilbinger et al., 2014). In Eq. 4.9, α and β represent tomographic bins, the summation extends over all galaxy pairs i,j separated on the simulated sky in the range $[\theta \pm \Delta\theta/2]$, $\epsilon_{\rm t,x}$ represent the tangential and cross components of the ellipticity, whereas the weights w_i encompass the quality of the shape

Table 4.2 The number of source galaxies, $n_{\rm gal}$, for the KiDS-450 dataset (middle column) (Hildebrandt et al., 2017) and for the KiDS-450 mocks (right column) (Harnois-Déraps et al., 2018) split by tomographic bins, $Z_{\rm B}$. The mocks match the DIR $n(z)$ of each tomographic bin despite having differences in $n_{\rm gal}$. The shape noise of each bin has been set to $\sigma = 0.29$.

$Z_{\rm B}$ Cut	KiDS-450 Data	KiDS-450 Mocks
0.1-0.3	2.354	2.098
0.3-0.5	1.856	2.062
0.5-0.7	1.830	1.968
0.7-0.9	1.493	1.419
0.9-10	0.813	0.690
No Cut	8.53	8.53

measurement for galaxy i. Using ATHENA with input predictions for the matter power spectrum from HALOFIT (Takahashi et al., 2012), Harnois-Déraps et al. (2018) find that angular scales larger than 1 arcmin for ξ_+ agree with the predictions to better than 5% when taking the finite box effect into account, whereas smaller scales suffer due to limitations in particle mass resolution.

4.2 Void Finding

As discussed in Section 1.8.1, identifying voids poses a non-trivial task. Voids can be identified in three tracers of the density field: through the halos, the galaxies, or the dark matter density field itself. Some finders use the watershed technique to identify the voids from the density field (e.g., Platen et al., 2007; Neyrinck, 2008), some finders use galaxies to find empty regions that are spherical (e.g., Hoyle and Vogeley, 2002), and others use the eigenvalues of the tidal field (Hessian of the potential) to identify the voids (e.g., Hahn et al., 2007). Naturally, variations among the size, shape, and amount of voids will exist between these void finders. Allowing voids to contain galaxies or not, or conducting theoretical studies on the dark matter distribution complicates the comparison to observations, which rely on galaxies. There are, however, certain criteria for voids that the community does agree on. These are: that voids are underdense (with respect to the average of the universe) at their centres and that the outer edges of the voids are characterised by a steep increase of galaxies (Colberg et al., 2008).

Although many void finders exist in the community, I chose the public, watershed-based void finder ZOBOV (Neyrinck, 2008) described below. The fundamental reason for this selection lies in ZOBOV's ability to identify physically motivated objects, *i.e.* irregularly shaped underdensities within the galaxy density field as well as its well-documented behaviour.

4.2.1 ZOBOV

ZOBOV (ZOnes Bordering On Voidness) (Neyrinck, 2008) is a parameter free algorithm that identifies underdensities (voids) without any assumption on the shape of the voids. In order to identify voids from a set of galaxies, ZOBOV carries out the following steps: density estimation, zoning, void identification, and void probability estimation.

First, ZOBOV estimates the density of the field using the Voronoi Tessellation Field Estimator (VTFE) (Schaap, 2007). The Voronoi tessellation method divides the space between a given set of particles into individual cells, where each cell contains the region of space that is closest to that particular particle, as opposed to another particle (Okabe et al., 2000; van de Weygaert and Schaap, 2009). Upon completion of the tessellation and division into cells, the density is estimated as $1/V_i$, where V_i is the volume of the cell associated to particle i. The Voronoi tessellation provides a set of neighbouring particles for each particle. These are particles whose cells neighbour i's cell. In the second step of the void identification process ZOBOV uses these neighbour particles to further segment the particles into zones around each density minimum. ZOBOV defines a minimum as a particle with a lower density than any of its surrounding Voronoi neighbours. ZOBOV traces the density of each particle towards its lowest density neighbour until eventually a minimum is reached. The Voronoi cells of all the particles that 'flow' towards a particular density minimum defines a *zone*. The zone's 'core' is defined as the minimum density particle associated to that particular zone. Due to shot noise, these zones could, in theory, be spurious minima and therefore ZOBOV combines several zones to construct voids. In the third step, ZOBOV joins neighbouring zones to construct voids. The process of joining particles into zones, and joining the zones themselves, is based in the watershed technique (e.g. Platen et al., 2007). The watershed technique can be thought of in the following terms. For each zone, the 'water level' is set to the zone's minimum density and then gradually increased. As the water level rises, it may cross over neighbouring Voronoi boundaries, overflowing into adjacent zones and including them into the *void* identified around a zone. This water rising process concludes when the water overflows into a zone with a deeper density than the original zone. If, for example, the original zone happens to be the most underdense zone, then the watershed process concludes when the entire field is flooded with water. A void is then defined as the set of all zones flooded with water before the water overflows into a deeper density minimum. Once ZOBOV identifies a void with this process, it selects the core particle (*i.e.* the particle which is the density minimum) of the original zone as the core particle of the void itself. If a zone does not join with any neighbouring zones to create a void, ZOBOV considers that zone a void. Through this process, ZOBOV can identify subvoids, which reside in larger voids. Although ZOBOV is a parameter-free algorithm, the user can introduce a density parameter to stop the growth of voids so that a void does not encompass the full field. The final step in the parameter-free version of ZOBOV is to calculate the statistical significance of each identified void. In order to define the significance of a void,

ZOBOV exploits two density parameters: the minimum density of void v, $\rho_{\rm min}(v)$, and the minimum-density particle on the ridge of a void, $\rho_{\rm l}(v)$, beyond which lies a void with a deeper minimum. The ratio of these two densities, $r(v)$, defines a density contrast, which ZOBOV converts to a probability in comparison to a Poisson distribution. Since the distribution of underdensities in a Poisson Voronoi field is unknown, Neyrinck (2008) measure this distribution using a Monte-Carlo approach from a Poisson sampling. Considering that this method does not yield distinct voids but a *probability* of a region to be a void, the user can decide the significance level at which to accept objects as voids. In addition to the statistical criterion, the user can select voids based on a relatively simple physical criterion. As discussed in Section 3.2, the density associated with a spherical, top-hat void is $\rho_{\rm void} \approx 0.2$ at $z = 0$. This criterion could be incorporated into the significance estimation by calculating the probability of a 'fake' void with density $\rho_{\rm min} = 0.2$ existing in a Voronoi Poisson distribution. In the next section, I describe applying ZOBOV to the SLICS mock galaxy catalogues.

4.3 Voids in SLICS

The first step involved in measuring a void weak lensing signal from the SLICS simulation is to generate the inputs used by ZOBOV. Since ZOBOV identifies voids most accurately in a volume-limited sample, I use the apparent magnitude for each galaxy to create a volume-limited sample per redshift. I convert each galaxy's apparent magnitude into an absolute magnitude using its luminosity distance, using the public `FlatLambdaCDM` module within PYTHON's `astropy` numerical package, and find the brightest magnitude at the high-redshift end of each simulation box, $M_{\rm max,z}$. Using $M_{\rm max,z}$ I select all galaxies which are as bright as this limit and exclude any brighter galaxies, constructing a volume-limited sample per redshift bin. Fig. 4.3 shows the magnitude selection for one realisation. As mentioned in Section 4.1.1, due to the construction of the lightcone, correlations between galaxies are lost across each adjacent box. This means that in order to ensure that ZOBOV accounts for this loss of correlation, voids need to be identified in each individual box, which I refer to as a redshift bin. Furthermore, the coordinates of the galaxies need to be converted from RA/DEC/$z_{\rm spec}$ to Cartesian xyz coordinates. Since the SLICS are flat-sky mocks, this conversion can be achieved through simple geometry:

$$\begin{aligned} x_{\rm gal} &= z_{\rm gal} \tan({\rm RA}_{\rm gal} - 300), \\ y_{\rm gal} &= z_{\rm gal} \tan({\rm DEC}_{\rm gal} - 300), \end{aligned} \tag{4.10}$$

where $x_{\rm gal}$, $y_{\rm gal}$, and $z_{\rm gal}$ are Cartesian coordinates in units of h^{-1}Mpc and ${\rm RA}_{\rm gal}/{\rm DEC}_{\rm gal}$ are in units of arcmin. Since the mocks are aligned such that the redshift, $z_{\rm spec}$, aligns along the line-of-sight direction, a comoving distance formula yields the physical line-of-sight distance to that galaxy. The comoving

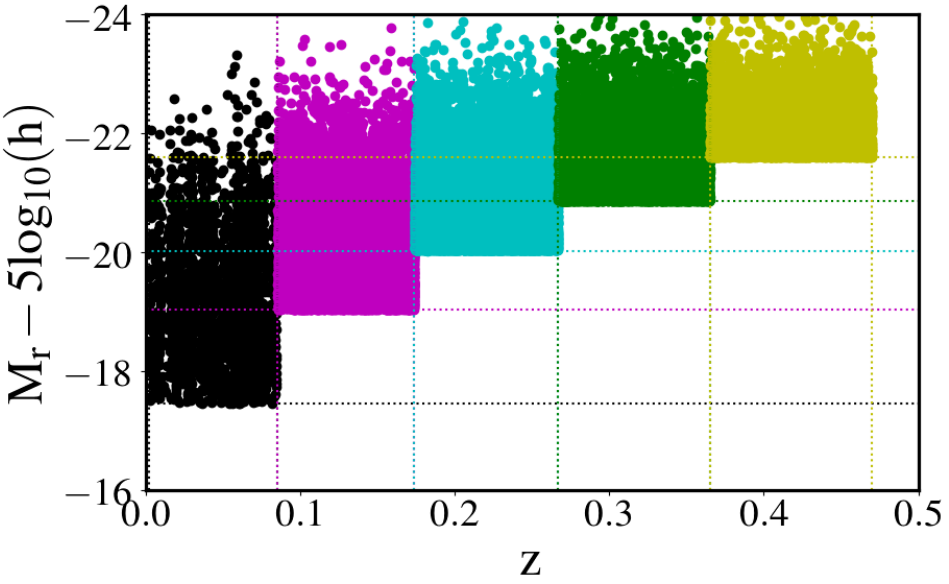

Figure 4.3 The magnitude selection applied to each redshift bin for one realisation from the GAMA HOD.

distances were calculated using the `astropy` package in PYTHON. Half of the box size (300 arcmin, which corresponds to a 5 degree angle) was subtracted in order to align the lightcones. Figs. 4.3 and 4.4 shows the magnitude selection and the geometry, respectively, of one realisation from the GAMA HOD used in the analysis. From Fig. 4.3 we notice that the magnitude decreases as a function of redshift. This occurs since less galaxies are observed at higher redshifts and those that are observed tend to be brighter. I make a selection on magnitude such that the magnitude of faintest galaxy at the high-redshift end of each redshift bin is the cutoff magnitude for that bin. Fig. 4.4 shows how the two different coordinate systems of the SLICS mocks appear. The upper panel shows the clustering coordinate system on which galaxy clustering is measured per redshift bin, whereas the lower panel shows the ray tracing coordinate system that the lensing measurements are made. In Section 4.3.2 I discuss the relation and transformation between these two coordinate systems. Fig. 4.5 shows a smoothed version of Fig. 4.4 in order to visualise the structure of the lightcone. As expected from the magnitude selection in Fig. 4.3, there is less visible structure at higher redshifts since there are less galaxies at higher redshifts. With the proper magnitude selection, I am able to mitigate the effect of a decreased number of tracer galaxies for void selection by creating a volume-limited galaxy sample. In order to define the simulation boundaries and prevent ZOBOV from overestimating the Voronoi volumes of voids at the edge of the SLICS catalogues, I define a set of dense 'buffer' particles that wrap around each redshift bin, taking advantage of the fact that SLICS are a flat-sky mock sample with no internal masks. I adapt this method of constructing buffer particles for observational data in order to account for masks (see Section 4.4).

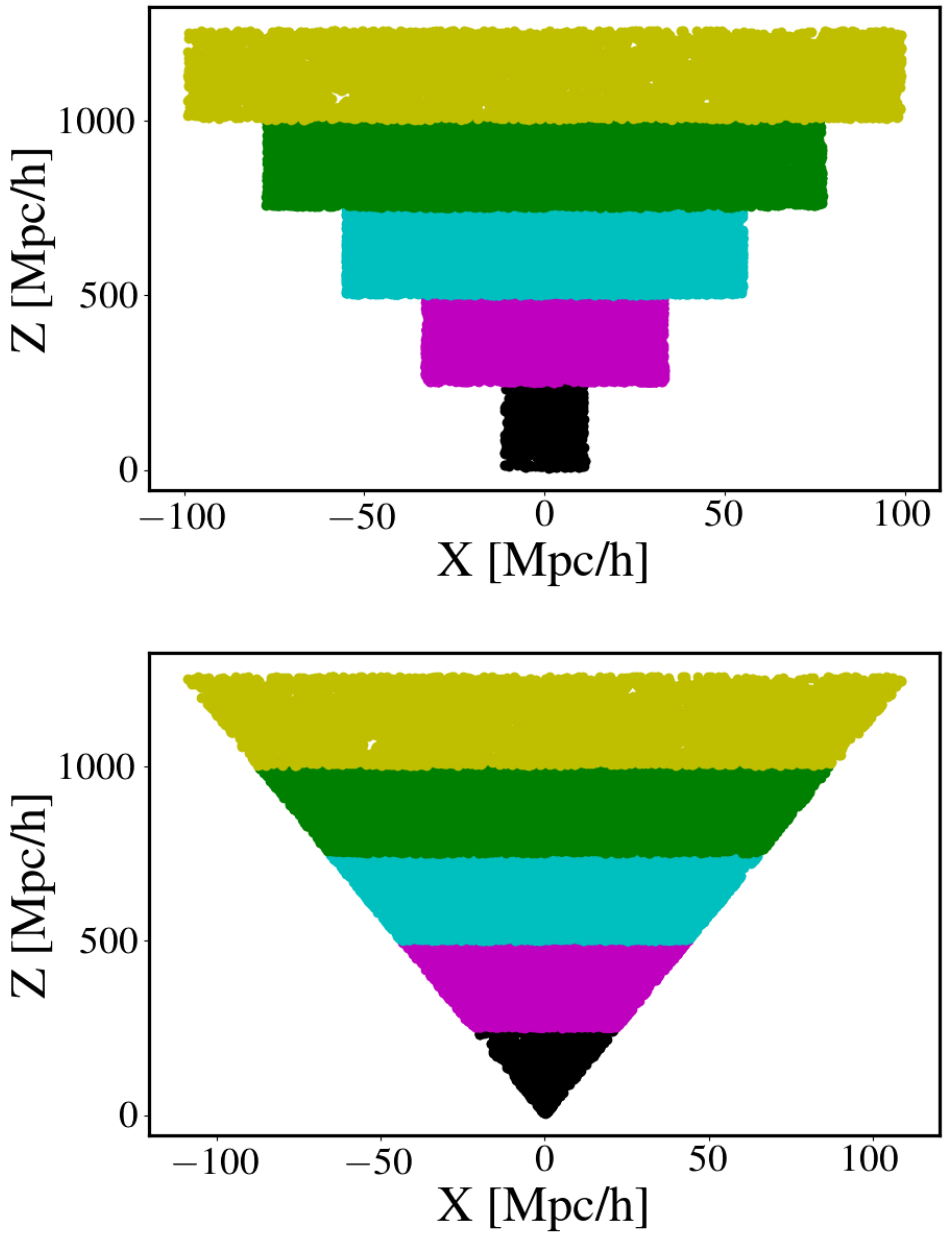

Figure 4.4 *Upper*: A scatter plot of the Cartesian clustering coordinates XZ, where Z is the line-of-sight direction. *Lower*: The same realisation with the lensing (ray-tracing) coordinates. Both sets of coordinates are split by redshift bins and magnitude selection as shown in Fig. 4.3.

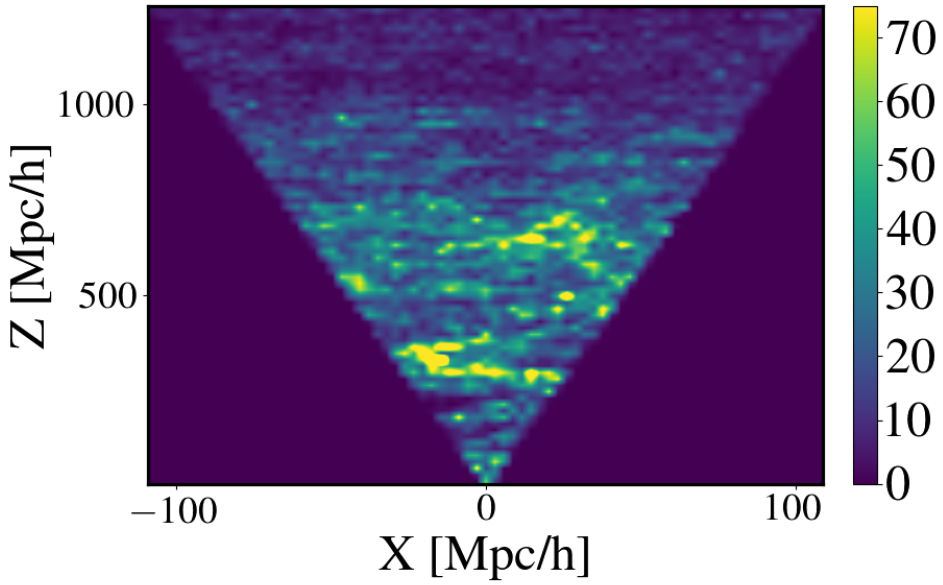

Figure 4.5 Smoothed version of the lensing coordinates (lower panel of Fig. 4.4) showing the structure along the line-of-sight direction for this realisation. The colorbar shows the number of galaxies per bin.

After identifying galaxies as well as buffer particles, I then use them as inputs for ZOBOV. ZOBOV's output contains 3 files: one with the volume of each cell, one with the adjacent particles of each particle, and one with the identified voids and their attributes such as the minimum-density centre, density, void radius, and others. From the raw ZOBOV output I calculate the volume-averaged centre of the void, as opposed to using the minimum-density centre. Also, it should be noted that since the shapes of voids found by ZOBOV are irregular, the void radius is an *effective* radius calculated by summing the volumes of all the Voronoi cells that constitute the void and solving for the radius assuming a spherical geometry. Next, I filter through the raw output of voids to exclude unrealistic voids. The first criterion I apply excludes voids that fall into the void-in-cloud category (Sheth and van de Weygaert, 2004). These objects correspond to voids located in a larger overdensity and are flagged if a particular voids density is larger or equal to that of the average density of the redshift bin. This mask confirms that all voids used are indeed underdense regions. The next selection applied is to the size of voids: only those with an effective radius greater than 10 h^{-1}Mpc are retained. When comparing the size of voids to the mean galaxy separation, since smaller voids tend to be more spurious or noisy, I remove them in order to have a sample of voids with smooth density profiles.

4.3.1 Density Profiles

The void density profile traced out by galaxies is in essence a void-galaxy correlation function, which can be computed using a tree algorithm. Since each individual void will have a noisy profile, multiple voids should be stacked to produce a statistically significant profile. However, since each void has a different size, I introduce a normalisation based on each void's individual radius. I measure the density profiles over 20 radial shells out to $2R_{\rm v}$, where $R_{\rm v}$ represents the void radius, for each void and stack the profiles. The density estimation technique counts the number of galaxies in each radial shell and uses the volume of the ZOBOV cells to calculate the number density in that radial shell. I then normalise the number density of galaxies to the total number density in the full redshift bin,

$$\delta_{\rm shell} = \frac{(N_{\rm bin}/\sum V_{\rm cell})}{n_{\rm tot}} - 1, \tag{4.11}$$

where $N_{\rm bin}$ is the number of galaxies in a radial shell each with a cell volume of $V_{\rm cell}$, and $n_{\rm tot}$ is the total number density of the full redshift bin. I refer to this density estimation as the 'tessellation' method.

Fig. 4.6 shows the density profile using the tessellation method (black) for voids from 40 realisations of the GAMA mocks with errors calculated as an error-on-the-mean from the 40 realisations. These ZOBOV void profiles exhibit the expected trends for large, underdense regions: underdense inner region, overdense peak at $\sim 1R_{\rm v}$, and a return to the average density on large scales (Sheth and van de Weygaert, 2004). Despite the seemingly good qualitative agreement with expectations, this method of density estimation carries a bias with it. The cell volume of each galaxy comes from the Voronoi volume after tessellation, meaning that each galaxy will occupy a different volume. Since the galaxies follow non-uniform clustering, a gradient in the Voronoi cell volume arises causing galaxies in denser environments to have smaller volumes. This yields a bias, which then propagates to the void radial density as calculated in Eq. 4.11. Furthermore, since the radial shells are spherical, they can slice through part of the Voronoi cells at the edges of the shell, which further biases the total volume of the shell. To alleviate this bias, I employ another density estimation method introduced by Davis and Peebles (1983),

$$\xi = \frac{N_{\rm rand,tot}}{N_{\rm gal,tot}} \frac{N_{\rm gal,shell}}{N_{\rm rand,shell}} - 1, \tag{4.12}$$

where ξ is the correlation function and $N_{\rm rand,tot}$ and $N_{\rm gal,tot}$ are the total number of random and real, respectively, galaxies in a redshift bin. I refer to this method as the 'correlation' method.

Since the correlation method requires randoms that follow the geometry and mask

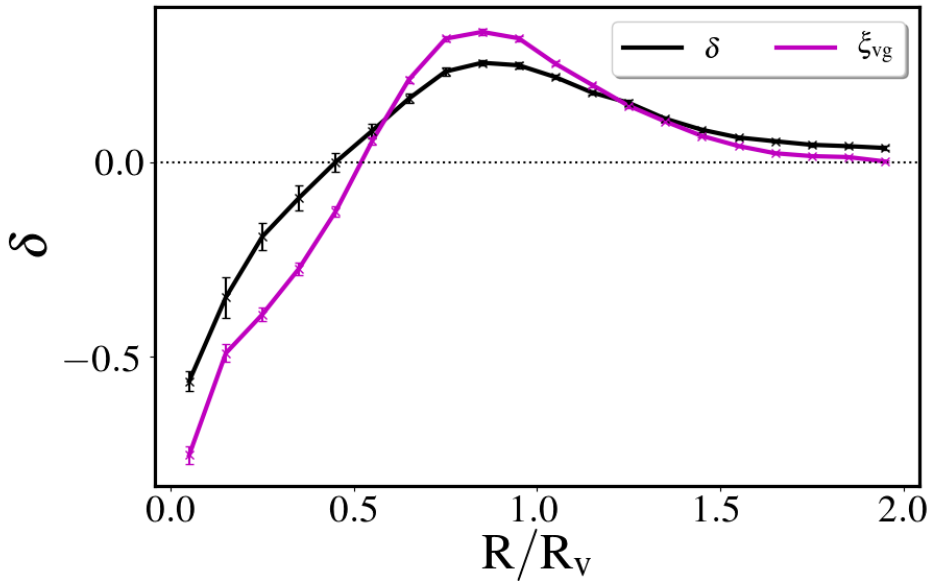

Figure 4.6 The stacked density profile, δ, of voids using the tessellation method defined in Eq. 4.11 (black) and the less biased void-galaxy correlation function, $\xi_{\rm vg}$, approach defined in Eq. 4.12 (magenta). 40 mock realisations were used for both estimators and the errors are calculated as an error-on-the-mean from these same 40 realisations.

of the considered survey, it automatically accounts for any masks and boundaries. This means that both the Voronoi cell gradient bias and the bias which arises from spherical shells slicing through Voronoi cells is eliminated. I create randoms that are 10 times as dense as the real galaxies (e.g. van Uitert et al., 2018). This amount of randoms suffices since the normalisation on large scales converges to the mean as seen by the correlation method profile (magenta) in Fig. 4.6, which shows a tighter peak distribution and better convergence to the mean on large scales as compared to the tessellation method.

Void Selection

As mentioned in Section 4.2.1, not all voids that ZOBOV identifies constitute bona fide voids, but rather come with a probability of them being real voids and not random Poisson fluctuations. However, I have several tools to use in the process of defining real voids. The simplest selection I explore comes from confirming that no selected voids reside in overdensities. To eliminate such objects from the void catalogue, I only use voids whose core particle density is less than the mean density of the Universe,

$$\delta_{\rm core} \leq 0. \tag{4.13}$$

One should keep in mind that this core particle defines the density minimum centre of the void, whereas I employ the volume averaged centre in the analysis. Nevertheless, this criteria helps me to determine truly underdense voids identified through ZOBOV.

Another way to select voids is to simply ignore voids that are below a certain radius. This will automatically alleviate most of the void-in-cloud issue since the smaller the void, the more likely it is a spurious void. Fig. 4.7 shows the void-galaxy cross-correlations calculated via the tessellation method (upper) and via the correlation method (lower) for the two void selection criteria discussed. As seen from the tessellation method panel, the core particle density method does not successfully select underdense regions as demonstrated by the positive density contrast inside the void, especially at the centre. However, a selection on void radius (solid black) only using voids whose radius exceeds 10 h^{-1}Mpc, shows expected trends in the density profile. This radius criteria depends on the mean particle separation and will differ between galaxy samples. The selection on void radii also dominates combination of the two criteria (cyan dot-dashed). Although the profiles from the correlation method (lower panel of Fig. 4.7) show qualitatively accurate trends, I see distinct differences among the void selection criteria. Voids selected using the core particle density selections show extremely wide peaks and do not converge to the mean density on large scales, suggesting that these voids do not represent true underdensities. As a further exploration, I plot the core particle density, $\delta_{\rm core}$, as a function of the void radius in Fig. 4.8 for all voids from the 40 mock realisations. This figure shows that the selection criteria, represented by the black horizontal and vertical lines, significantly reduces number of spurious voids and that the small voids affect the correlation function to a large degree. The selection based on the void radii (and the combination of both criteria) shows a much narrower density peak and converges to the mean density on large scales, as expected.

Since the void radii seems to be the main aspect governing the density profiles, I explore how a change in radius affects the profiles. Fig. 4.9 shows the density profiles via the tessellation method (upper) and the correlation method (lower) for void radius selection, where the minimum void radius is 5, 7, 10, and 12 h^{-1}Mpc as labelled in the legend. Again, the tessellation method helps us to understand how void radii selection affects the density of the voids. As seen from the black curve, voids with radius ≥ 5 h^{-1}Mpc show features of voids in overdense regions since their density is always above the mean density of the Universe. Increasing the requirement to voids with a radius of ≥ 7 h^{-1}Mpc improves the profile significantly by excluding voids which are in overdense regions, however only at a void radii of ≥ 10 h^{-1}Mpc does the profile begin to truly depict underdense voids. The correlation method (lower panel of Fig. 4.9) supports this claim by showing that only at a restriction of void radii ≥ 10 h^{-1}Mpc does the density peak narrow substantially and the large scales converge to the mean density.

From this analysis, I decide that the most optimal void selection criteria requires

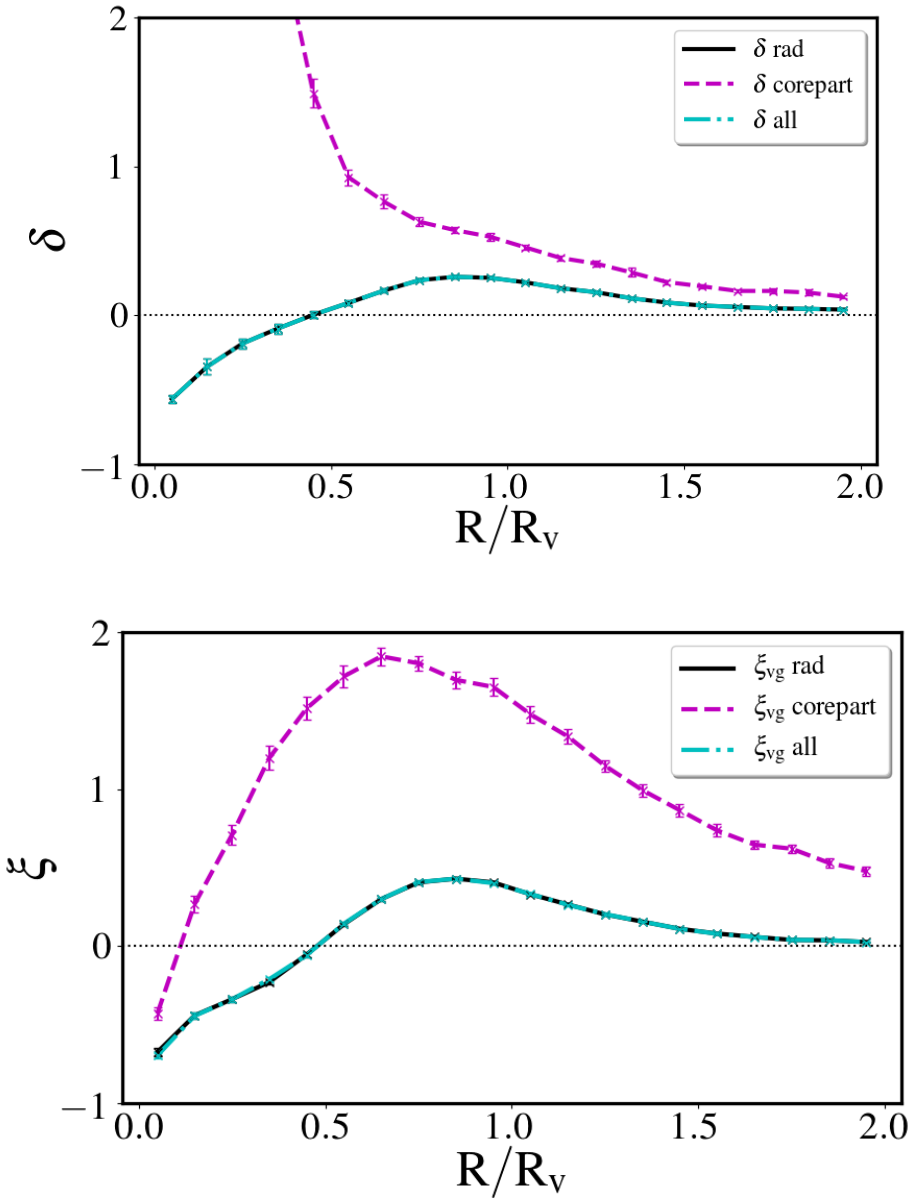

Figure 4.7 Effect of void selection criterion on the density profile using tessellation method (upper) and the correlation method (lower) from 40 GAMA mock realisations. The dashed magenta line represents a selection on voids requiring that their core particle volume is a true underdensity (corepart), the solid black line represents a selection on voids that are greater than 10 h^{-1}Mpc (rad), and the dot-dashed cyan line (all) combines both criteria. The errors are calculated as an error-on-the-mean from the 40 realisations.

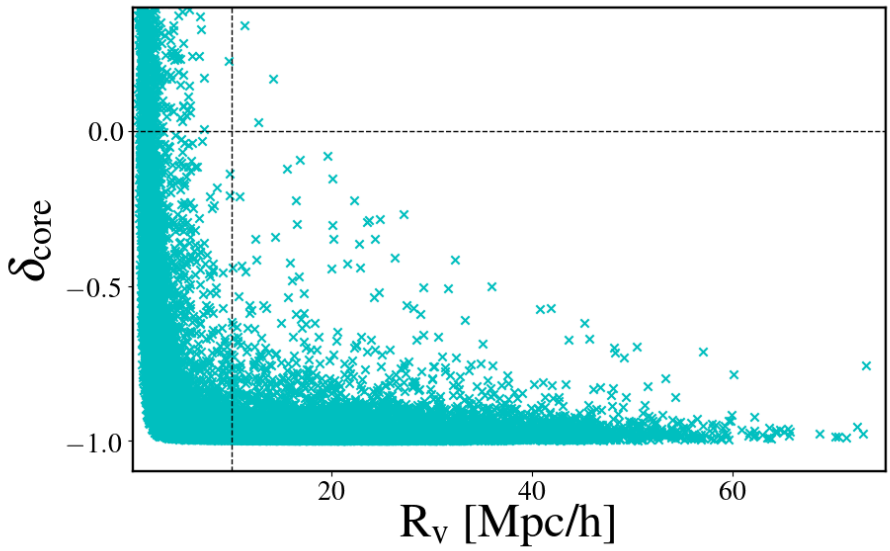

Figure 4.8 The void core particle density as a function of void radius for all voids from the 40 realisations. The horizontal and vertical black lines represent the void selection criteria as described in the text.

fundamentally underdense voids, which have a radius $\geq 10\,h^{-1}$Mpc[1]. The void selection criteria used for the density estimation in Fig. 4.6 and the analysis on the data in Section 4.4 can be summarised as:

$$\begin{aligned} \delta_{\rm core} &\leq 0, \\ R_{\rm void} &\geq 10\,h^{-1}{\rm Mpc}. \end{aligned} \tag{4.14}$$

This selection criteria mimics the one employed for the non-linear RSD prediction (see Section 3.8.1), however with a smaller void radius.

Growing Spheres

As discussed in Section 4.2, there exists no consensus on the definition of voids and no obvious way to define their radii. Sánchez et al. (2016) have opted for a different technique than the one used by ZOBOV. Rather than calculating an effective radius from summing the cells used to define the void, as carried out in ZOBOV, Sánchez et al. (2016) grow spheres around the void centre until the sphere reaches a predefined density, using the radius that reaches the density threshold as the void radius. Since identification of voids in a galaxy field requires accurate knowledge of galaxy locations, void finders such a ZOBOV may not be optimal for surveys with only photometric redshifts and no spectroscopic redshifts, such

[1]This value is intrinsically sample dependent and will differ between galaxy samples given their number density.

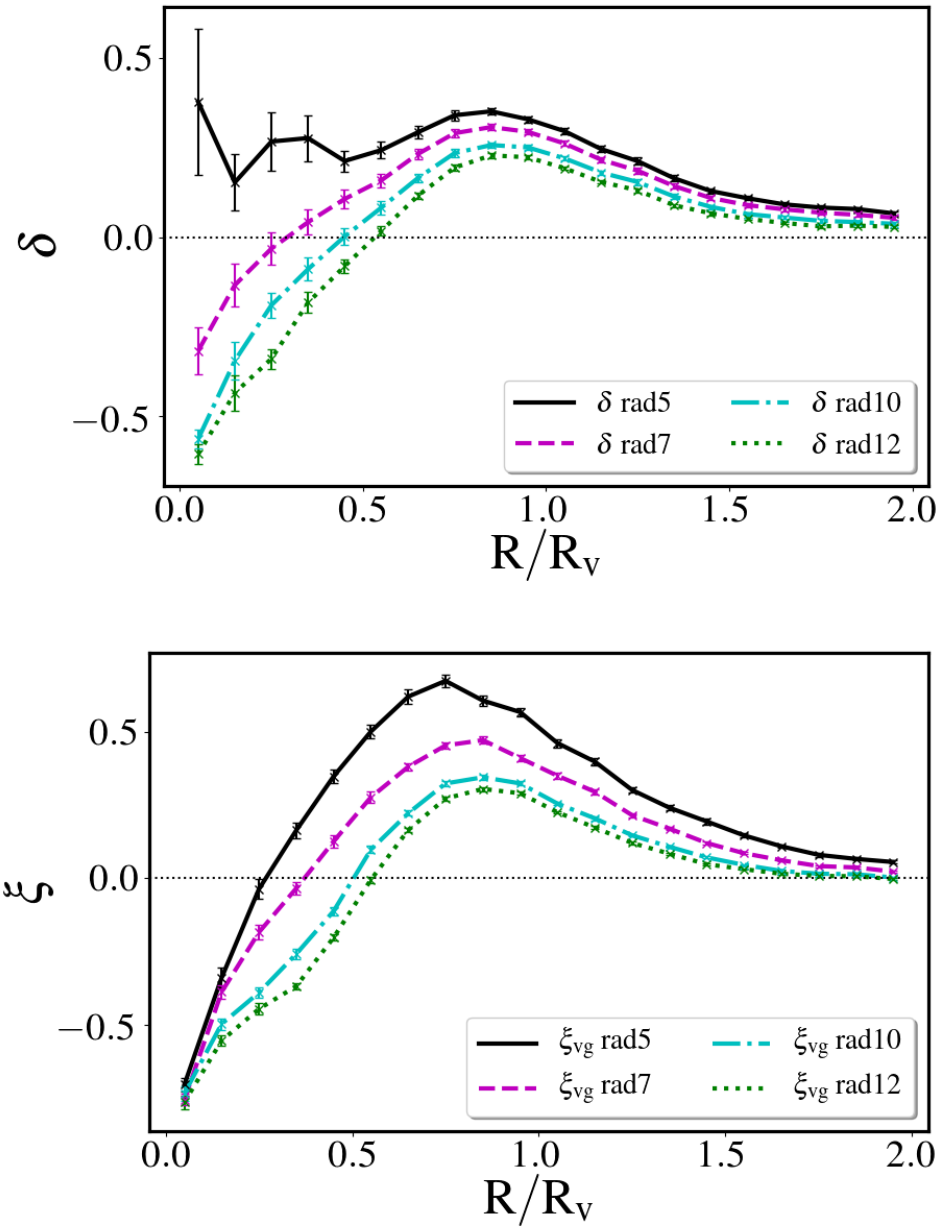

Figure 4.9 Effect of void radii selection on the density profile using tessellation method (upper) and the correlation method (lower) from 40 GAMA mock realisations. The value in the legend represents the minimum radius of voids considered in the analysis. The errors are calculated as an error-on-the-mean from the 40 realisations.

as the analysis of Sánchez et al. (2016), who identify voids in the Dark Energy Survey (DES) Science Verification (SV) dataset (Diehl et al., 2014; Dark Energy Survey Collaboration et al., 2016). Since I apply ZOBOV to a GAMA-like mock and the spectroscopic GAMA data (see Section 4.4), I do not encounter this issue. Nevertheless, in order to test the effect of a density-dependent void radius on the density profile, I create new void radii by growing spheres from the volume-weighted void centre until the sphere reaches a certain density threshold. The thresholds tested are $\rho_t = 0.2\bar{\rho}$, $0.5\bar{\rho}$, and $0.7\bar{\rho}$, where $\bar{\rho}$ is the mean density. These values were chosen to represent voids with various density properties and inspired by the density criteria of Sánchez et al. (2016). The algorithm begins at the void centre, c, and measures the number density of a sphere with radius d_i, where d_i is the distances to the ith nearest particle to c. Using the cell volume of all particles within d_i, the number density is calculated and compared to the threshold density, ρ_t. If the number density is greater than or equal to the threshold density, d_i is assigned as the void radius, if it is less, the sphere is grown to radius d_j, where d_j is the distance to the next nearest neighbour and the same calculations are made. Fig. 4.10 shows that there are more voids with smaller radii using this method when compared to ZOBOV's radii. As the vertical dotted lines show, the average radii increases as does the density threshold, ρ_t.

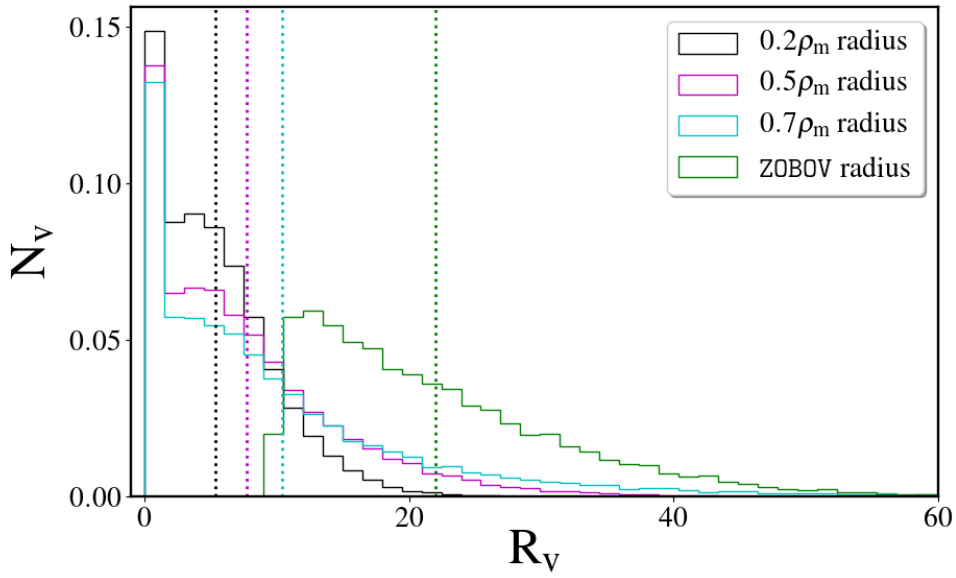

Figure 4.10 Normalised histogram of void radii comparing radii using the building spheres method to those from ZOBOV's effective radii. It's important to note that the ZOBOV voids are restricted to above 10 h^{-1}Mpc. The vertical dotted lines represent the mean void radius of each sample.

Fig. 4.11 shows the predicted profiles of stacked voids from 40 mock realisations using the ZOBOV void centres but radii calculated using the growing spheres method, where δ and ξ_{vg} represent the density estimated using the tessellation method and correlation method, respectively. When comparing these profiles to

those from ZOBOV voids in Fig. 4.6 there exists several distinct differences. The most notable difference is a much steeper density ridge with a narrower peak for voids identified using the growing spheres technique. This behaviour arises due to the nature of the growing spheres method, which halts the growth of the sphere once it reaches a preselected density threshold, $\rho_{\rm t}$. Another distinct feature of these density profiles is that the profiles converge to the mean density only when extracted to at least $4R_{\rm v}$, which results due to the smaller size of these voids. Furthermore, we find that tessellation method doesn't fully converge to the mean density, confirming that this method suffers from a bias, unlike the correlation method. Unlike ZOBOV void density profiles, these profiles have a large overdensity at the inner part of the void. This is due to the small size of the void and since, by construction, one or more galaxies reside in the first radial bin, this yields a very large overdensity that eventually smooths out as the radial profile grow. As Fig. 4.11 shows, as the density threshold, $\rho_{\rm t}$, reaches the mean density, the grown spheres begin to resemble statistically significant voids.

4.3.2 Coordinate Transformations

After selecting the voids and testing their density profiles, I compute the lensing signal around these stacked voids. In order to do this, a coordinate change needs to be performed. The reason for this lies in the inherent geometrical construction of the SLICS mocks. As discussed in Section 4.1, the SLICS are based on a flat-sky, multiple-plane geometry. This means that the cosmological volume contained in pixel p of the $i^{\rm th}$ mass plane comes from a projection of half the simulation box along the Cartesian coordinate, z. This coordinate functions as the radial, line-of-sight direction and provides both the redshift and comoving distances for the halos and galaxies in the lightcone. However, for objects at low redshifts, near field objects, or those objects with projected quantities in less than five parallel planes, this coordinate system is no longer accurate (Harnois-Déraps et al., 2018). Therefore, in order to have the most precise measurements, the SLICS mock catalogues provide two different coordinates. The 'ray-tracing' coordinate, $\boldsymbol{\theta}_{\rm ray\_tracing}$, which constitutes the mass projection coordinate, meaning that all objects that contribute to the same pixel in the mass/shear map share the same $\boldsymbol{\theta}_{\rm ray\_tracing}$ coordinate. We refer to this as the 'lensing' coordinate. The other coordinate, however, represents the *true* coordinate, $\boldsymbol{\theta}_{\rm clustering}$, and can deviate from the lensing coordinate, especially at low redshifts and at the edges of the lightcone. We refer to this as the 'clustering' coordinate. Fig. 4.4 presents the clustering coordinates (upper) and the lensing coordinate (lower) for a realisation of the GAMA HOD split by redshift bins. Note that exactly along the line-of-sight direction there exists no difference between these coordinates.

In order to properly identify voids in the SLICS, I use the clustering coordinates. However, when I measure the lensing signal around these voids, I must convert their centres to the lensing coordinate in order to ensure that the photon trajectories within the mock realisation are conserved. Due to the flat-sky

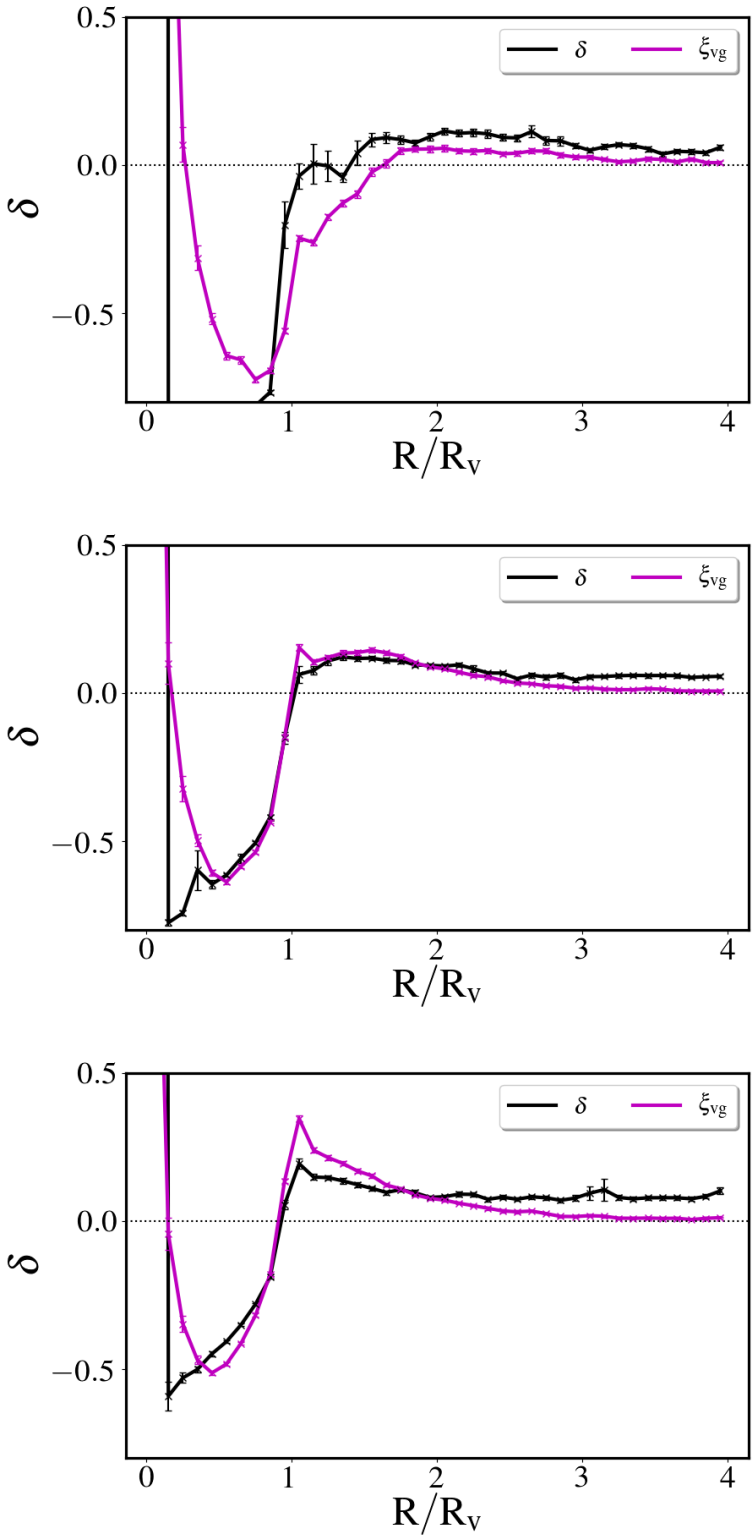

Figure 4.11 Stacked density profiles for voids from 40 GAMA realisations at ZOBOV identified void centres and radii obtained by growing spheres to density thresholds of $0.2\bar{\rho}$ (upper), $0.5\bar{\rho}$ (middle), and $0.7\bar{\rho}$ (lower). δ represents the density estimated with the tessellation method and $\xi_{\rm vg}$ represents the density estimation through the correlation method.

construction of the SLICS, applying the following geometrical transformation converts between clustering and lensing coordinates:

$$\begin{aligned} \Delta\chi &= z - d_{\text{nearest\_lens\_plane}} \\ \Delta x &= x_{\text{clustering}} \frac{\Delta\chi}{(z - \Delta\chi)} \\ x_{\text{lensing}} &= x_{\text{clustering}} + \Delta x, \end{aligned} \tag{4.15}$$

where z is the line-of-sight comoving distance in h^{-1}Mpc and doesn't change between the two coordinate systems, $d_{\text{nearest\_lens\_plane}}$ is the comoving distance to the nearest lens plane, $x_{\text{clustering}}$ is the x location of the void centre, and Δx is the conversion factor between the clustering coordinate and the lensing coordinate.

Fig. 4.12 shows the void locations for the realisation in Fig. 4.4 in the true clustering coordinates (cyan) and the lensing coordinates (magenta) converted using Eq. 4.15. As expected, the void centres located farther away from the line-of-sight direction visibly deviate more between the two coordinate systems compared to those locations along the line-of-sight direction. To confirm that the galaxy field correlates with the lensing field, Harnois-Déraps et al. (2018) compare the GGL signal from the SLICS HOD with the measurements from Amon et al. (2017), finding the agreement between the mocks and data to be within 1σ of the errors for scales of interest to this analysis.

Since the shear computation code TreeCorr (Jarvis et al., 2004) uses angular units, after transforming the void centres into lensing coordinates, these physical Cartesian coordinates and the void radius, both of which are in units of h^{-1}Mpc, need to be converted into angular coordinates. Utilising the geometry of the SLICS, I accomplish this with the following trigonometric equation:

$$\text{arcmin} = \arctan\left(\frac{x_{\text{lensing}}}{z}\right) + 300, \tag{4.16}$$

where the offset of 300 arcmin arises from the shift introduced in Eq. 4.10.

4.3.3 Lensing Measurements

After constructing the lenses (*i.e.* voids), I select the sources galaxies for the lensing measurement. The only selection criterion for the sources is a redshift selection of $0.4 < z_{\text{B}} < 0.9$, where z_{B} is the photometric redshift to mimic the selection made to the KiDS-450 data (Hildebrandt et al., 2017). Once the source galaxy selection is made, the lenses and source galaxies, with their observed ellipticities from Eq. 4.8, are used as inputs to TreeCorr's position-shape correlation function module, NGCorrelation. This module radially correlates the position of the lenses to the shapes of the sources for a predetermined number

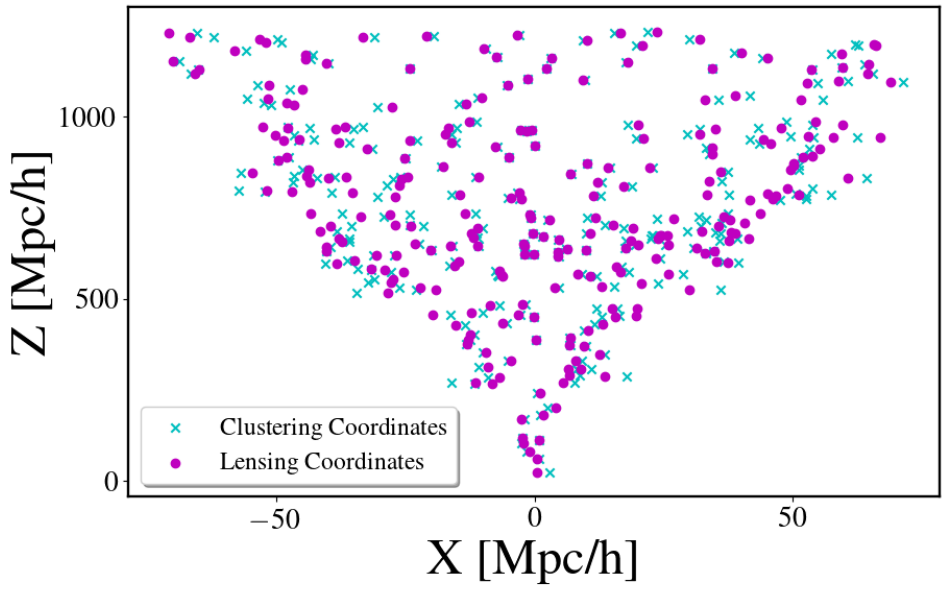

Figure 4.12 The comparison between void locations in the 'clustering' coordinate system (cyan) and those in the 'lensing' coordinate system (magenta). Note that the largest offset occurs at the edges of the light cone with no deviation at all along the line-of-sight direction.

of bins. This correlation is known as galaxy-galaxy lensing (void-galaxy lensing in this particular scenario) (see Section 2.3.3), where a non-zero tangential shear component, γ_t, is expected. Since I intend to stack the γ_t signal, this correlation needs to be calculated per void and normalised to the void radius. I measure the correlation function out to $2R_v$ in 100 logarithmic bins per void. After looping over all the voids, I rebin them all into 20 linear bins weighted by the number of pairs in each logarithmic bin, obtaining a weighted average of the tangential shear signal per linear bin. I choose to convert to linear bins to mitigate the effect of shot noise within the interior of the void.

Fig. 4.13 shows the tangential component of the shear (black) and the cross component of the shear (magenta) as a function of distance from the void centre normalised to the void radius using the ZOBOV void radius. The measurement averages 40 mock realisations, which is an effective area of $4000\,\mathrm{deg}^2$ close to DES's final area (Dark Energy Survey Collaboration et al., 2016). As expected, the cross shear is consistent with a null signal, while the tangential shear qualitatively resembles the void lensing signal. The negative tangential shear signal parallels that of an underdensity, increasing at $R > R_v$. The systematically positive signal on these large scales indicates that these voids are perhaps in overdense regions. This signal was calculated with KiDS-like shape noise and the errors are the error-on-the-mean, *i.e.* the standard deviation divided by the square root of the number of mock realisations giving an effective error about a $4000\,\mathrm{deg}^2$ KiDS-GAMA survey.

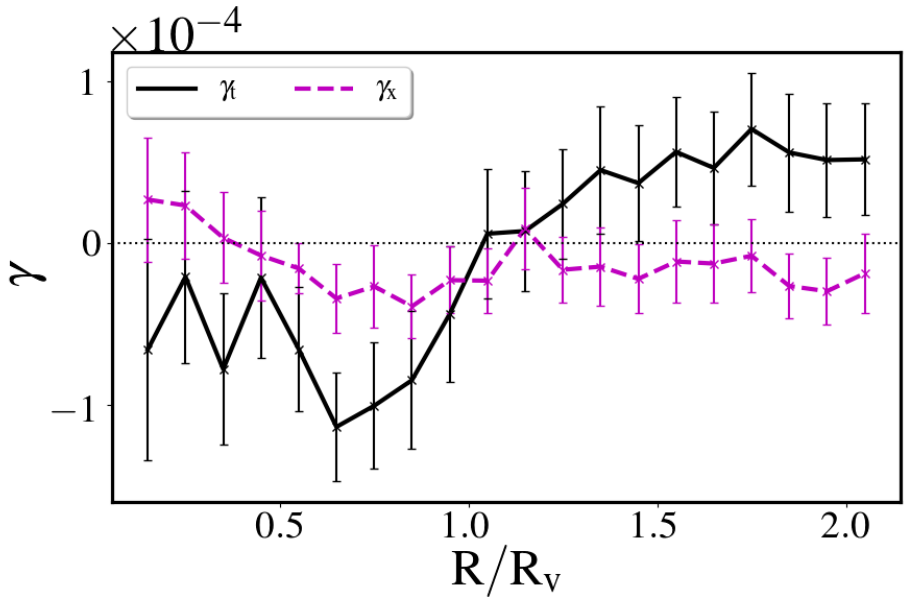

Figure 4.13 Tangential (black) and cross (magenta) shear components for voids from 40 SLICS GAMA HOD realisations using the KiDS-450 mocks as source galaxies. The errors are calculated as an error-on-the-mean.

Fig. 4.14 shows the shear signals for voids with radii defined using the growing spheres method as in Fig. 4.11. As expected from the behaviour in the upper panel of Fig. 4.11, the voids defined with density threshold $\rho_t = 0.2\bar{\rho}$ do not show any void lensing signal and resemble noisy, spurious voids. However, a distinct void lensing signal is measured from voids defined with $\rho_t = 0.5\bar{\rho}$ and an even cleaner signal for those with $\rho_t = 0.7\bar{\rho}$. This is due to larger size and higher statistical significance of voids with $\rho_t = 0.7\bar{\rho}$ as compared to the more spurious voids with $\rho_t = 0.2\bar{\rho}$.

Fig. 4.15 shows the excess surface density (Mandelbaum et al., 2005), $\Delta\Sigma$, measurement using the same voids as in the shear measurement (see Fig. 4.13). Measuring $\Delta\Sigma$ as opposed to γ_t has the advantage that $\Delta\Sigma$ utilises redshift information. I adopt the definition of $\Delta\Sigma$ from Amon et al. (2017) to calculate the mean excess surface mass density as discussed in Section 2.3.3, Eqs. 2.43 - 2.45. The calculation splits the distribution of the source galaxies into 70 bins in the redshift range $0 < z < 1.5$, which yields redshift 'slices' with width $\Delta z_l \approx 0.02$. The sources are chosen per void and depend on the redshift of the void. Therefore, for a given void v with void centre at z_v, the sources used to calculate $\Delta\Sigma$ would span $z_v < z_{spec} < 0.9$, where $z = 0.9$ represents the upper bound to which the photometric redshift estimation is considered reliable (Hildebrandt et al., 2017). In order to minimise source-lens contamination, Amon et al. (2017) show that calculating a 'boost factor' (Mandelbaum et al., 2006) to account for this source-lens contamination. Amon et al. (2017) discuss that an optimal buffer between the lens redshift and sources should be approximately $\Delta z = 0.1$, which would

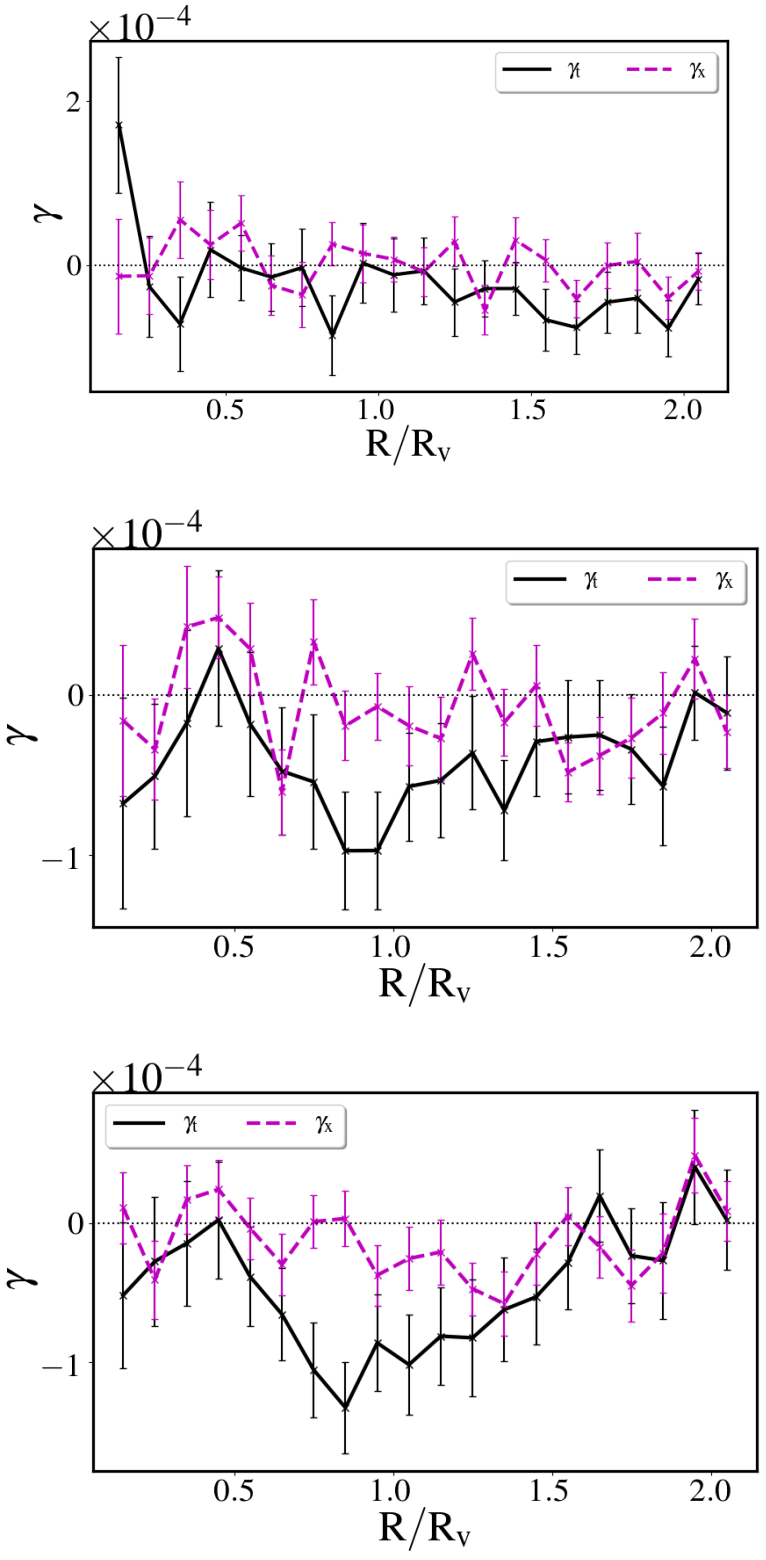

Figure 4.14 Shear signals from voids in 40 realisations of the GAMA HOD from SLICS defined using the growing spheres method. The solid black line shows the tangential shear, while the dashed magenta shows the cross shear. The errors are calculated as errors-on-mean. The upper, middle, and lower panels show signals from voids grown to $\rho_t = 0.2\bar{\rho}$, $0.5\bar{\rho}$, $0.7\bar{\rho}$, respectively.

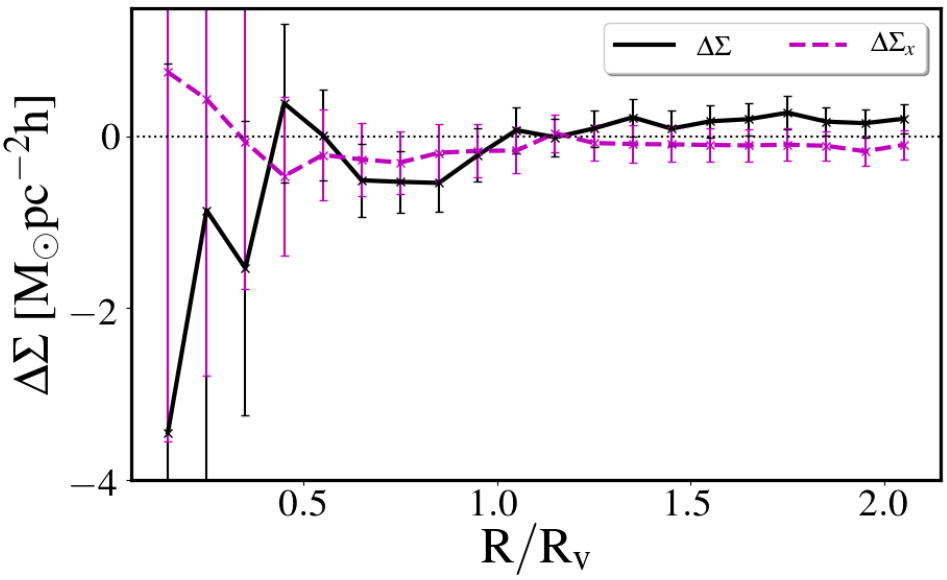

Figure 4.15 $\Delta\Sigma$ measurement of the same SLICS voids used to measure the tangential shear signal in Fig. 4.13. The solid black line shows the tangential component of $\Delta\Sigma$, while the dashed magenta shows the cross component. The errors are calculated are an error-on-the-mean.

change our selection of source to $z_v + 0.1 < z_{spec} < 0.9$. This would indeed lower the boost factor correction at the expense of also decreasing the signal to noise. Since the lens sample presented here consists of only several hundred voids, the effect of this correction will be insignificant at the large scales associated with voids.

4.4 Voids in Data

Transitioning from the real-space SLICS mocks to redshift-space observational data requires extra considerations in the void identification and measurement to account for the curved sky and masks in the data. In the next sections, I describe the GAMA and KiDS-450 data and the galaxy selection applied in order to identify voids and run a WL analysis. I then discuss modifications to the procedure in Section 4.3 to identify the voids, and finally present measurement of weak lensing around GAMA voids using KiDS-450 source galaxies.

4.4.1 GAMA Data

The Galaxy and Mass Assembly (GAMA) (Driver et al., 2011) is a galaxy redshift survey conducted on the Anglo-Australian Telescope (AAT) that has

yielded a complete, dense sample of the large-scale structure out to $z \approx 0.5$ with spectroscopic redshifts for galaxies with a magnitude of $r < 19.8$. The GAMA survey consists of five equatorial regions each covering $12 \times 5\,\mathrm{deg}^2$, however I only utilise the three in the northern regions centred on 09h, 12h, and 14h30, referred to G9, G12, and G15, respectively. Although KiDS-450 overlaps with G23 in the southern regions as well, since this field's completeness out to $r < 19.8$ is only 87%, I do not include it in this study.

The galaxies I use to define voids come from the TilingCatv43 GAMA catalogue (Liske et al., 2015). As discussed in the previous section, in order to make the most physically accurate void identification, I need precise measurements of galaxy locations. This requirement leads us to making several selections to the galaxy catalogue. For the first flag I apply the Survey_Class filter of SC ≥ 3, which selects the galaxies in the main survey samples of GAMA II and GAMA I. The next selection addresses redshift accuracy. From this main sample I select 98.4% of galaxies using the redshift criterion of nQ ≥ 3, which identifies those galaxies with a minimum of a 90% probability of having an accurate redshift estimation (Liske et al., 2015). These two selection criteria represent the main sample selection for the final GAMA data release and yields a magnitude completeness of $r < 19.4$ (G9,G15) and $r < 19.8$ (G12). I also impose a redshift cut of $0.002 < z < 0.5$.

In order to stay consistent with the SLICS analysis, I split the GAMA sample into the same redshift bins as in Section 4.3 (based on the redshift selections in Table 4.1). I further split these redshift bins based on their absolute magnitude as conducted in Fig. 4.3. To do this, I calculate the luminosity distance to each galaxy using the SLICS cosmology (see Section 4.1.1) and use it to convert the apparent r-band magnitude of each galaxy, R_PETRO, to its absolute magnitude via:

$$M_\mathrm{r} = m_\mathrm{r} - 5\log_{10}(d_\mathrm{L}), \tag{4.17}$$

where m_r is the r-band magnitude and d_L is the luminosity distance. Since zobov operates most optimally with a volume-limited sample, using the absolute magnitudes binned into redshifts, I exclude the first and the last redshift bins to avoid using the tail of the redshift distribution. Therefore, I use only 3 redshift bins in the analysis of the GAMA data spanning the redshift range $0.130 < z < 0.418$. Fig. 4.16 shows the $M_\mathrm{r}(z)$ for the 3 redshift bins used. This magnitude selection was performed in the same way as described in Section 4.3. Fig. 4.17 shows the redshift distribution of the GAMA main sample data (black) and the data after the redshift and absolute magnitude selections were applied (magenta). The total number of galaxies reduces from 182 178 to 81 651 after applying the magnitude criterion and I find a mean inter galaxy separation of $\sim 8\,h^{-1}$Mpc. After selecting the galaxies, I need to create buffer particles to wrap the GAMA galaxy sample as inputs to zobov, which requires an approach that incorporates a curved sky and survey masks.

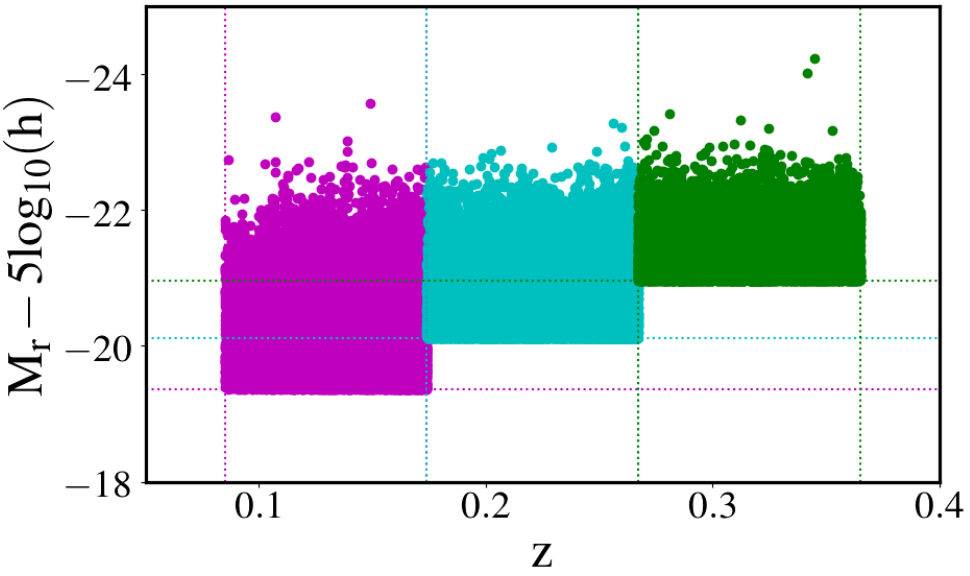

Figure 4.16 Absolute magnitude criterion as a function of redshift applied to the main sample of the GAMA II data. Note that these redshift bins are the same as those used in the SLICS HOD in Fig. 4.3.

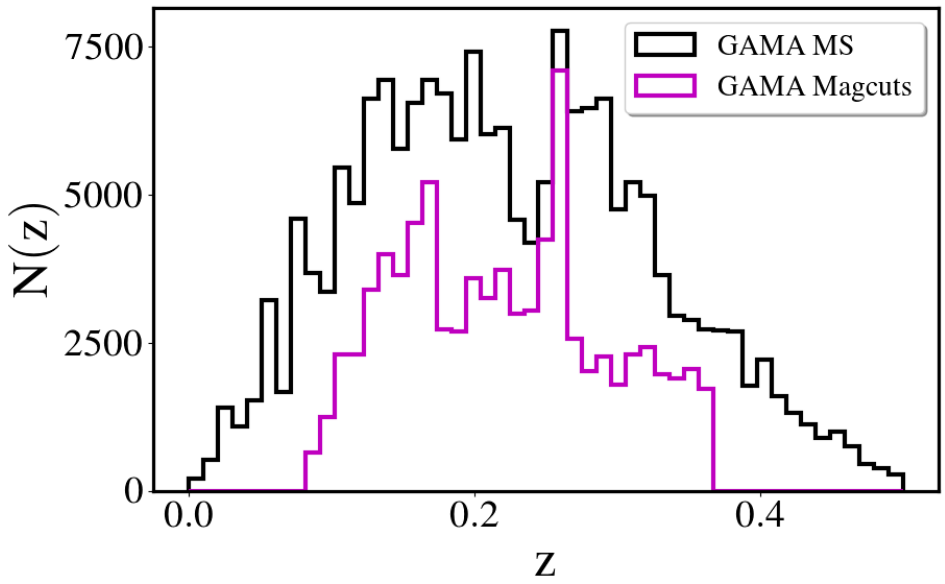

Figure 4.17 Redshift distribution of the GAMA II main sample (MS) (black) and the sample used for void selection (magenta), which excludes the first and last redshift bins and has the magnitude selection shown in Fig. 4.16.

4.4.2 KiDS Data

The imaging data I exploit for this analysis comes from the third release of the Kilo Degree Survey (KiDS) discussed in de Jong et al. (2017). The images were taken by the OmegaCAM camera (Kuijken, 2011) on the VLT Survey Telescope (VST, Capaccioli et al., 2012). The observations spanned the SDSS-like *ugri* bands targeting two strips of $\sim 10\,\mathrm{deg} \times 75\,\mathrm{deg}$ on the celestial equator (KiDS-N) and around the South Galactic Pole (KiDS-S). The survey consists of individual exposures that each cover a 'tile' of approximately $1\,\mathrm{deg}^2$. In order to optimise shear measurements, the observations were scheduled such that the r-band images were taken under the finest, dark-time conditions, u- and g-bands with progressively worse seeing conditions, and the i-band observations conducted under bright conditions. The final dataset used for this analysis spans 454 tiles and covers $449.7\,\mathrm{deg}^2$ on the sky, with a median r-band seeing of 0.66 arcsec (Hildebrandt et al., 2017).

In order to create shear catalogues from raw data, the KiDS-450 dataset undergoes several steps. First, the multi-colour data is processed through Astro-WISE (Valentijn et al., 2007; Begeman et al., 2013). Astro-WISE de-trends the raw data by considering de-biasing, correcting for cross-talk, satellite track removal, and other data reductions. It then photometrically calibrates the data and ensures that photometric redshifts are based on accurate colours using the Schlegel et al. (1998) maps to correct for the Galactic extinction for each individual star. Finally, the astrometric calibration utilises the 2MASS survey (Skrutskie et al., 2006) as the reference. After undergoing this calibration, the images are coadded and further defects are masked out. In order to meet the precision of data images needed for a robust weak lensing analysis, the data undergoes a second reduction pipeline, THELI (Erben et al., 2005), to further reduce the highest-quality r-band data. The most significant improvement for KiDS-450 over previous releases regarding the THELI reduction concerns an improvement in the astrometric calibration. After simultaneously calibrating all the data from a given field, SExtractor (Bertin and Arnouts, 1996) is run on the coadded THELI r-band images. After masking out any defects and ghosts found in the THELI images, the remaining $360.3\,\mathrm{deg}^2$ of data are used for the shape measurements and photometry.

Once THELI creates the main r-band catalogue, multi-colour photometry is then obtained for all of the objects in that catalogue from the Astro-WISE images in the *ugri*-bands. The modelling of the Point Spread Function (PSF) in the four bands results from using shapelets and a calculation of convolution kernels that transpose the PSFs into circular Gaussians. Once the images are convolved, Hildebrandt et al. (2017) extract the photometry from the images using elliptical Gaussian-weighted apertures. For this dataset, the tomographic bin selection relied on the photometric redshift estimation code BPZ (Benítez, 2000). In order to contain the outlier rate of galaxy redshift to less than 10%, the Bayesian estimations of the photometric redshifts, z_B, were chosen in the range of $0.1 < z_\mathrm{B} < 0.9$. Hildebrandt et al. (2017) defined outliers as galaxies

whose discrepancy between $z_{\rm B}$ and $z_{\rm spec}$ exceeds 15%. A $\Delta z_{\rm B} = 0.2$ was chosen for the tomographic binning to ensure sufficient resolution in the radial direction, while working within the limits of the photometric redshift estimation. These BPZ redshifts are only used to bin the data, while utilising a new method, which exploits spectroscopic training data to estimate the redshift distribution in each tomographic bin directly (discussed below).

Having completed the photometry and photo-z binning, the next step is to obtain shapes of the galaxies. To this end, Hildebrandt et al. (2017) exploit the likelihood based model-fitting method, *lens*fit (Miller et al., 2007, 2013; Fenech Conti et al., 2017), to estimate the shear from galaxy shapes. This method can successively 'self-calibrate' against noise bias effects analysed from image simulations. This noise bias arises when attempting to measure galaxy ellipticities from noise-bound, pixelated images. The 'self-calibration' technique uses a model for a measured galaxy, with model parameters obtained from a maximum likelihood estimator, and creates a simulated noise-free galaxy with those same parameters. This simulated galaxy's shape is then re-measured and the difference between the original galaxy ellipticity and the measured galaxy ellipticity is subtracted from that of the original galaxy, mitigating the effect of noise bias. Another major product of the shear estimation from *lens*fit is the weight given to each galaxy ellipticity. This weight accounts for both shape-noise variance from the measurements themselves, as well as ellipticity measurement variance from the estimation method. There arises a bias from a correlation between the PSF distortion and the intrinsic galaxy ellipticity, induced by the weighting the shears. In order to overcome this measurement noise bias, Fenech Conti et al. (2017) quantify the variance of the measured mean galaxy ellipticity and its dependence on galaxy ellipticity, signal-to-noise ratio, and isophotal area. They then place a requirement that these re-calibrated weights do not significantly depend on the observed ellipticity or the PSF-galaxy position angle. The final aspect of the shear measurements obtained by Hildebrandt et al. (2017) relies on a blinding scheme in order to suppress confirmation bias. The blinding scheme works by having three shear and shear weight catalogues: one that's the true data and two that are fake data with perturbed shears and weights. The perturbations are derived from a smooth function of the true data to prevent easy identification of the true data. The parameters of this function were known to an external blinder and were calibrated to ensure that offsets between the three datasets were 1-σ of the Planck best-fit for S_8.

The final step for creating the shear catalogue is the calibration of photometric redshifts. The DIR method constitutes the main approach chosen by Hildebrandt et al. (2017) for calibrating photometric redshifts and yields a weighted, direct calibration extracted from a magnitude-space re-weighting of spectroscopic redshift catalogues that overlap with KiDS. DIR approaches the spectroscopic sample in the same way as the photo-z sample and separates it into tomographic bins. Despite being a fairly straightforward approach, this technique reaches limitations due to a lack of spectroscopic completeness of representative shear catalogues and a concern of sample variance due to the typically smaller

coverage area of spectroscopic surveys compared to photometric ones. The way Hildebrandt et al. (2017) alleviate the effects of these limitations relies on a k-nearest neighbour approach to estimate the volume density of galaxies in a multi-dimensional magnitude space for both the spectroscopic and photometric samples. These estimates are then utilised to up/down weight the spectroscopic galaxies based on their representation in the magnitude space. In order for this approach to work optimally, the spectroscopic sample should cover the full photometric range. To this effect, Hildebrandt et al. (2017) exploit overlapping spectroscopic fields from three different samples: COSMOS (Scoville et al., 2007), Chandra Deep Field South (CDFS) (Vaccari et al., 2012), and DEEP2 (Newman et al., 2013). Hildebrandt et al. (2017) analysed and compared DIR to three other photo-z estimation methods (BPZ, cross-correlations, and a re-calibration of photometric $P(z)$) and decided to use DIR as the most robust and fiducial redshift estimator.

After the data undergoes the proper processing, reduction, tomographic binning, and shear estimations as described in Section 2 of Hildebrandt et al. (2017), the final catalogue yields shear measurements for ~ 15 million galaxies, with an effective number density of $n_{\rm eff} = 8.53$ galaxies per arcmin^2 over a total effective area of $360.3\,\deg^2$. Table 4.3 presents the distribution of the objects selected on these redshift bins with the effective number density, $n_{\rm eff}$, ellipticity dispersion, $\sigma_{\rm e}$, and the median calibrated redshift of the bin as calculate by the DIR method, $z_{\rm DIR}$ Hildebrandt et al. (2017).

Table 4.3 Source galaxy properties of the KiDS-450 dataset split by tomographic bins and for the full dataset taken from Hildebrandt et al. (2017). $z_{\rm B}$ represents the photometric redshift obtained through the BPZ method, $n_{\rm eff}$ represents the effective number density, $\sigma_{\rm e}$ is the ellipticity dispersion including uncertainties from the measurement, and the median $z_{\rm DIR}$ represents the median redshift of the bin using the DIR method.

Bin	$z_{\rm B}$ range	# of galaxies	$n_{\rm eff}$ [arcmin^{-2}]	$\sigma_{\rm e}$	median $z_{\rm DIR}$
1	$0.1 < z_{\rm B} < 0.3$	3 879 823	2.35	0.293	0.418 ± 0.041
2	$0.3 < z_{\rm B} < 0.5$	2 990 099	1.86	0.287	0.451 ± 0.012
3	$0.5 < z_{\rm B} < 0.7$	2 970 570	1.83	0.279	0.659 ± 0.003
4	$0.7 < z_{\rm B} < 0.9$	2 687 130	1.49	0.288	0.829 ± 0.004
Total	no $z_{\rm B}$ cuts	14 640 774	8.53	0.290	

4.4.3 ZOBOV on Data

In this section I describe how to apply ZOBOV to data. Since I now need to account for, not only survey geometry, but also survey masks, the setup of ZOBOV changes. By default, ZOBOV assumes periodic boundary conditions, however, there's an option to use the non-periodic boundaries and construct buffer particles that indicate where the survey's boundaries are. I discussed this approach in Section 4.3, however the buffer particles surrounding the SLICS simulation were

constructed on the basis of flat-sky geometry and no survey masks. For the GAMA data, I must account for both curved-sky geometry and survey masks, which account for any issues in the survey such as bright stars. This means that the buffer particles need to wrap around a truncated cone shape of each redshift bin of the lightcone, as well as several pixels within the lightcone which may be masked. To this end, I exploit the PYTHON package HEALPY, which uses HEALPIX [2] (Górski et al., 2005) as its basis. HEALPIX pixelates data from a spherical surface such that each pixel covers the same surface area. This allows for an accurate analysis and visualisation of all-sky maps. A parameter called $N_{\rm side}$ dictates the pixel resolution. I choose $N_{\rm side} = 2048$, which translates to a resolution of 1.72 arcmin/pixel. Using these on-sky pixels, I can then identify which galaxies reside within which pixels based on each galaxy's coordinates. I can use the same approach for the random galaxies and since the catalogue of random GAMA galaxies follows the mask and geometry of the survey and is highly dense, I can select the full set of pixels that are unmasked within each GAMA field. I achieve this by projecting all of the randoms onto a HEALPY map and using a binary criteria to determine which pixels are masked from the survey. By identifying those pixels that contain a real galaxies and those that contain random galaxies, I have a full set of unmasked pixels for each GAMA field. This, however, only determines the pixels *within* each field, but I also need to surround each field with buffer particles. This requires a creation of another, larger set of random galaxies that span beyond the GAMA survey boundaries. I generate these galaxies such that they are uniform in spherical coordinates and cover a slightly larger range in RA/DEC than each GAMA field. I generate enough randoms to fully cover a set of pixels on each side of the original GAMA randoms. This then allows me to identify only those pixels that surround each GAMA field, which I refer to as buffer particles. Knowing the pixels of the buffer particles and the redshift range, I can calculate the volume that these buffer particles occupy,

$$V_{\rm buffer} = SA_{\rm buffer}\frac{4\pi}{3}(d^3_{\rm max} - d^3_{\rm min}), \tag{4.18}$$

where $SA_{\rm buffer}$ represents the surface area of the sphere occupied by the buffer particles and $d_{\rm max/min}$ represents the comoving distance to the maximum/minimum redshift of each redshift bin. For the buffer particles to work properly and not make ZOBOV believe they represent real galaxies, they need to be sufficiently dense. Since I generate a large amount of randoms, the number density of the buffer particles is ~ 140 times greater than that of the actual GAMA galaxies. However, this approach only generates buffer particles that *surround* the light cone, but does not account for the 'front' and 'back' of the light cone. Using the number density of the original buffer particles, I construct an extra layer of buffer particles at the front and back of the each GAMA field with the same number density. This extra layer of particles spans 3 h^{-1}Mpc in thickness at $d_{\rm max}$ and $d_{\rm min}$, allowing me to fully cover each GAMA field.

[2] http://healpix.sourceforge.net

Once I have a set of buffer particles with a constant density that surround each GAMA field, I convert all of the galaxy and buffer particle coordinates to Cartesian units using HEALPY's ANG2VEC function. This function yields a unit vector per particle that I then translate to a physical coordinate using the comoving distance of each galaxy and buffer particle. I calculate the comoving distance from each galaxy's redshift using `astropy`'s COMOVING_DISTANCE module. For the randoms, I uniformly sample the comoving distances through a distance cubed formalism. Fig. 4.18 provides a visual representation of the chosen galaxies in the G9 field (magenta) as well as the buffer particles created to surround the field (black). I note that this figure shows a 2D projection but, in reality, the buffer particles fully surround the galaxies.

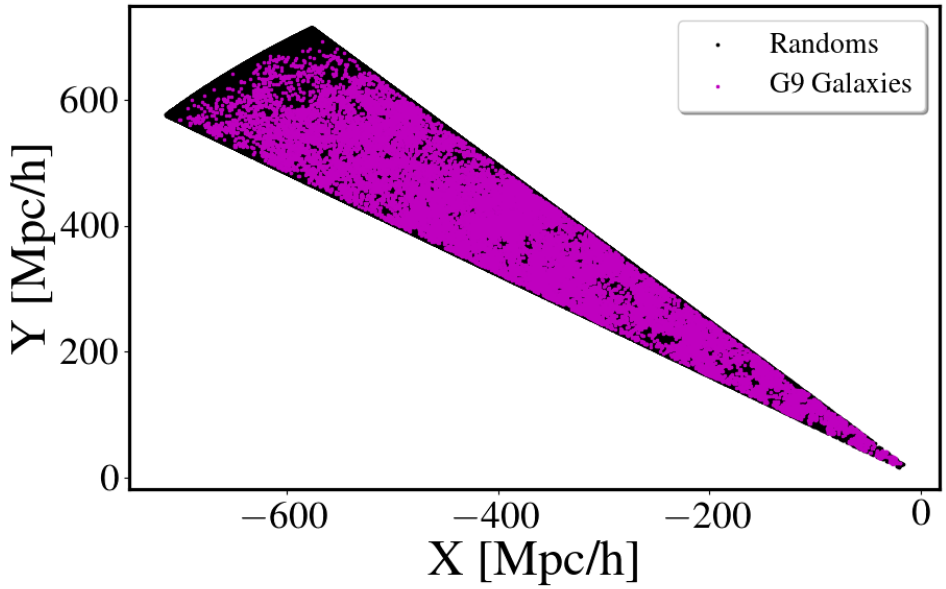

Figure 4.18 Scatter plot of the Cartesian locations of galaxies in the G9 field (magenta) as well as the buffer particles (black) created to surround the field and indicate masks and boundaries for ZOBOV.

After defining all of the galaxies and buffer particles in Cartesian coordinates, I use them as input for ZOBOV. Fig. 4.19 gives a broad overview of the process described above. Once ZOBOV identifies the voids, I can apply the same selection criteria as discussed in Section 4.3.1 and measure the correlation function. Fig. 4.20 shows the correlation function for voids in each GAMA field (upper) as well as the combined measurement (lower). Using the selection criteria, I identify a total of 423 voids with 158, 130, and 135 in the G9, G12, and G15 fields, respectively. The main feature to note is that seemingly only voids in the G12 field have their centres in underdense regions. Although I see the expected density peak from all three fields, G9 and G15 voids do not have underdense interiors. This indicates that these voids are likely to reside in large-scale overdensities. I do not see this behaviour from the mock predictions, so I do not believe it relies on the dense sampling of the GAMA survey. In Section 4.5 I discuss possible reasons for this unexpected behaviour.

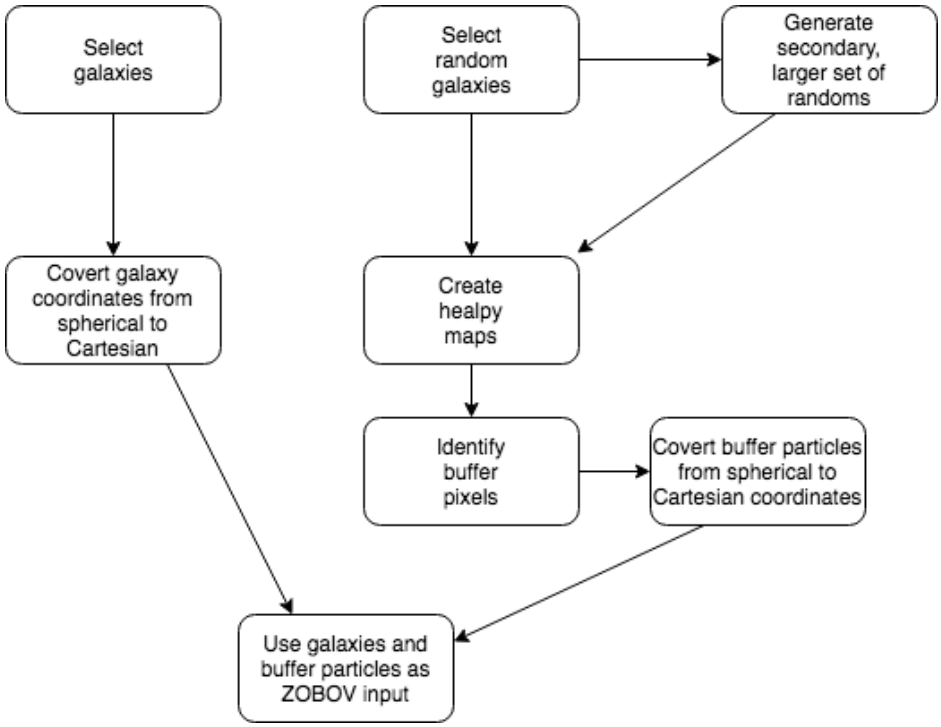

Figure 4.19 Overview of the steps taken to prepare GAMA data as an input for ZOBOV.

4.4.4 Weak Lensing of GAMA Voids

Coordinate Transforms and Source Selection

The output from ZOBOV provides the centre and radius of the void in physical, comoving units of h^{-1}Mpc. However, since lensing is a projected quantity, I need to convert the void locations into spherical units. The first transformation I apply converts the comoving distance of the void centre to a redshift. I use the distance modulus,

$$d = \sqrt{x^2 + y^2 + z^2}, \tag{4.19}$$

to calculate the comoving distance to the void centre and then employ ASTROPY's Z_AT_VALUE module to convert the comoving distance to a redshift given the cosmology. In the next step, I use HEALPY's VEC2ANG to convert the physical Cartesian coordinates into spherical coordinates. Using the void's comoving distance, I convert the void radius from comoving units to angular units using a similar approach as in Eq. 4.16 in Section 4.3.2, which assumes a flat-sky approximation for the conversion. Once the coordinate conversion is complete, I select voids based on the criterion discussed in Section 4.3.1. Fig 4.21 shows the distribution of void radii for the voids in the three GAMA fields that were chosen for the analysis.

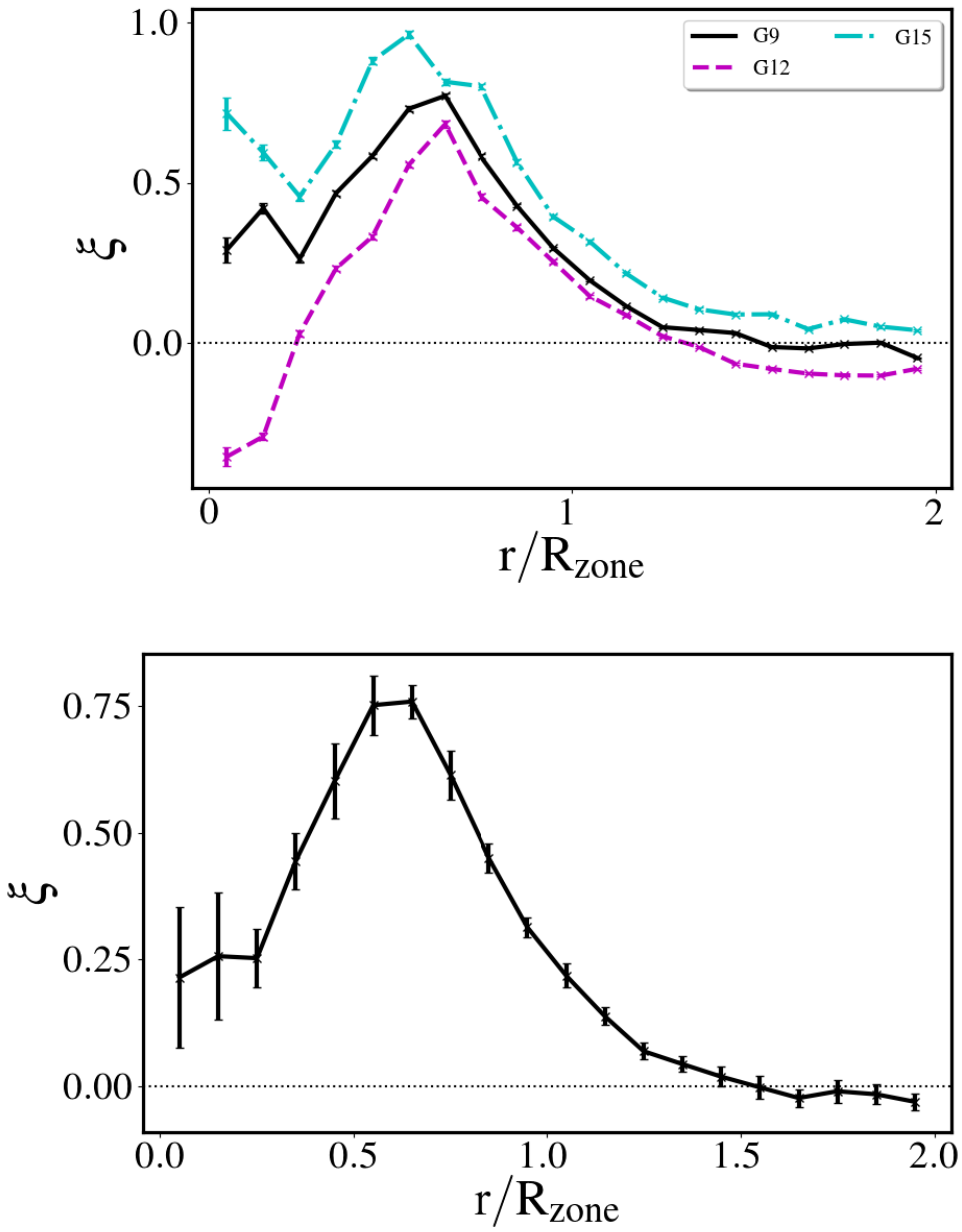

Figure 4.20 The stacked void-galaxy correlation function for voids found by ZOBOV in individual GAMA fields (upper) and all three fields combined (lower). The errors of each individual GAMA field are calculated as a standard deviation weighted by the number of counts per bin. For the errors on the combined correlation function (lower) I perform the same weighted standard deviation, but across the three fields.

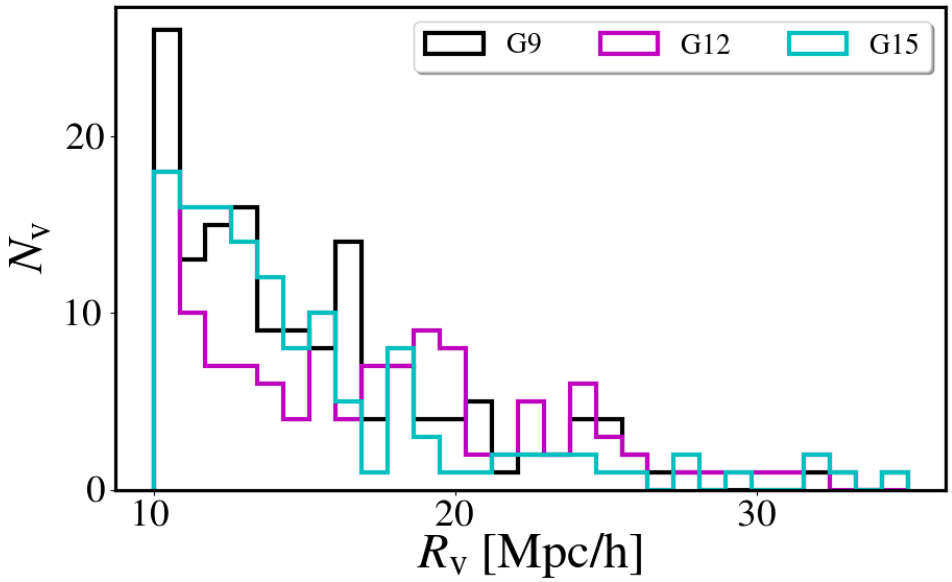

Figure 4.21 Void radius histogram for voids in the GAMA fields with void selection as described in Section 4.3.1.

Since I only consider the three GAMA patches in the northern sky, I therefore only utilise the three KiDS-N fields. I further make a selection on the photometric redshift of these galaxies to ensure that I only use source galaxies located behind the voids. Since the galaxies used to identify voids span a redshift of $0.130 < z < 0.418$, I limit the KiDS-450 source galaxies to $0.4 < z_B < 0.9$. Although with this selection there is an overlap between GAMA galaxies and KiDS-450 galaxies, due to our void selection criteria there exists no overlap between the voids and the KiDS-450 sources, where the maximum redshift for the analysed voids is $z_{max} = 0.32$. As discussed in Section 4.3.3, I could add a buffer of $\Delta z = 0.1$ to the lenses to account for source-lens contamination, but since the centre of the highest redshift void is $z_{max} = 0.32$, I decide not to restrict the sources any further. Table 4.4 shows number of KiDS-450 source galaxies per field. The KiDS-450 catalogue provides the RA/DEC, both ellipticity components, the *lensfit* weights for the ellipticities, and the photometric redshift for each galaxy. From each ellipticity component I subtract the mean of the ellipticity from all galaxies to account for the additive shear calibration, known as the c correction. Since I do not bin the source galaxies into redshift bins, I correct for the additive shear by taking the mean ellipticity from the full sample of KiDS-450, unlike the approach of Hildebrandt et al. (2017) who correct for the additive bias per tomographic bin. Furthermore, for the calculation of the critical surface density, Σ_c, defined in Eq. 2.44, I use the DIR weighted redshifts.

Table 4.4 Number of source galaxies in the three KiDS-N fields before and after the redshift selection ensuring no lens-source overlap.

Field	# of galaxies	# of galaxies after redshift selection
G9	1804859	845963
G12	3697711	1782278
G15	3549855	1730654
Total	9052425	4358895

Void-Galaxy Lensing with ZOBOV Voids

After completing the source galaxy and void selection and converting all quantities into spherical units, I use TreeCorr to calculate void position - galaxy shape correlation (VGL). I calculate this signal for each GAMA field out to $2R_{\rm v}$ and stack the signals together as described in Section 4.3.3. Fig. 4.22 shows the measured weak lensing shear signal of KiDS-450 source galaxies around GAMA voids. The upper panel of this figure shows the tangential shear, whereas the lower panel shows the cross component of the shear, which I expect to yield a signal consistent with zero by definition. In the upper panel of Fig. 4.22 I see that the signal for the individual GAMA fields varies. The voids in the G15 field (dot-dashed cyan) show signs of void-in-cloud since the signal on large scales is above zero, whereas the voids in the G9 field (solid black) are slightly below zero. I find that the signal in the G12 field (dashed magenta) is mostly dominated by noise. I obtain the errors on these signals by generating 20 realisations of random locations in each GAMA field with 10 times the number of voids in that particular field (e.g. van Uitert et al., 2018), where the void radii are sampled from the actual void radii distributions of each GAMA field. Taking the standard deviation over these 20 random realisations produces the error bars in Fig. 4.22. Using these same 20 realisations, I also subtract the random shear signal from each patch to suppress the effect of cosmic variance. Since the measurements for the individual GAMA fields in Fig. 4.22 show noisy behaviour and exhibit a high degree of correlation with one another, I decide not to combine them into one measurement.

Void-Galaxy Lensing with Empty Spheres

I also explore the lensing signal of GAMA voids identified in a different way than the zobov voids. This second catalogue of voids is created using the methodology of Micheletti et al. (2014). This method creates empty spheres within the galaxy distribution, selecting only those spheres that contain $\geq 80\%$ of their volume within the survey boundary. The algorithm then identifies 'maximal spheres', defined as the largest, non-overlapping, empty spheres in the galaxy sample. Hawken et al. (2019, in prep)[3] identify these maximal spheres in the three

[3]The voids discussed in this section were provided to me by private communication with Adam Hawken.

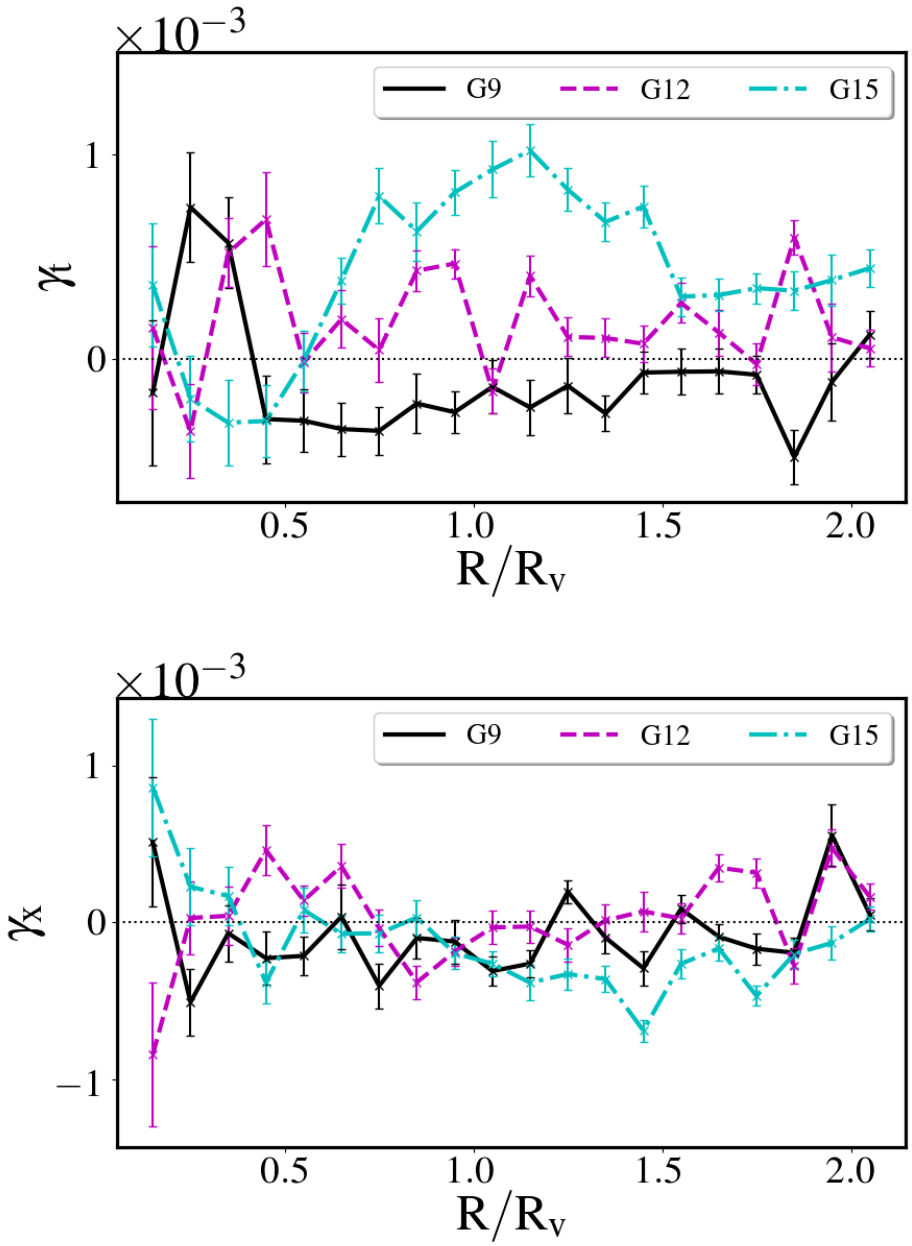

Figure 4.22 The upper panel shows the tangential shear signal for voids in the three GAMA fields, while the lower panel shows the cross component of the shear. The void selection is described in Section 4.3.1 and the errors are calculated from the standard deviation of the random signal described in the text.

northern GAMA fields. Since a constant number density as a function of redshift is important when searching for voids, Hawken et al. (2019, in prep) construct a volume limited sample from the main GAMA catalogue. They adopt a selection on the absolute rest frame r-band magnitude of $M_{\rm r} = -21.4$, which generates a catalogue that is complete up to $z = 0.4$ with a mean galaxy separation of $\sim 6\,h^{-1}$Mpc. The voids identified with this method will of course have low-luminosity galaxies inside of them and will not truly be empty spheres, however the imposed magnitude criterion allows Hawken et al. (2019, in prep) to measure void profiles within their most inner regions. Another systematic of this algorithm is that since 80% of the void volume is required to be within the survey boundary, large voids do not reside at the survey boundary. This means that small voids are more likely to reside at the survey boundary. This systematic resembles the one I find with ZOBOV voids, so I do not consider it as an issue for the comparison of the two void finding algorithms. Fig. 4.23 shows the distribution of void radii for this void identification method. I find that a similar distribution of these voids to the ZOBOV ones in Fig. 4.21 with 206, 206, and 196 voids in G9, G12, and G15, respectively, for voids whose radius exceeds 12 h^{-1}Mpc. If I make no restrictions on voids radius, the number of voids approximately doubles to 574, 590, and 583 for G9, G12, and G15, respectively. In Fig. 4.24 I present the correlation function for the voids used in the main analysis of Hawken et al. (2019, in prep) (*i.e.* $R_{\rm v} \geq 12\,h^{-1}$Mpc). I see that the correlation function of these voids resembles what we expect from underdense regions, noting the sharp increase at $R \approx R_{\rm v}$ and a convergence to the mean at $\approx 4R_{\rm v}$ as with the voids in Fig. 4.11.

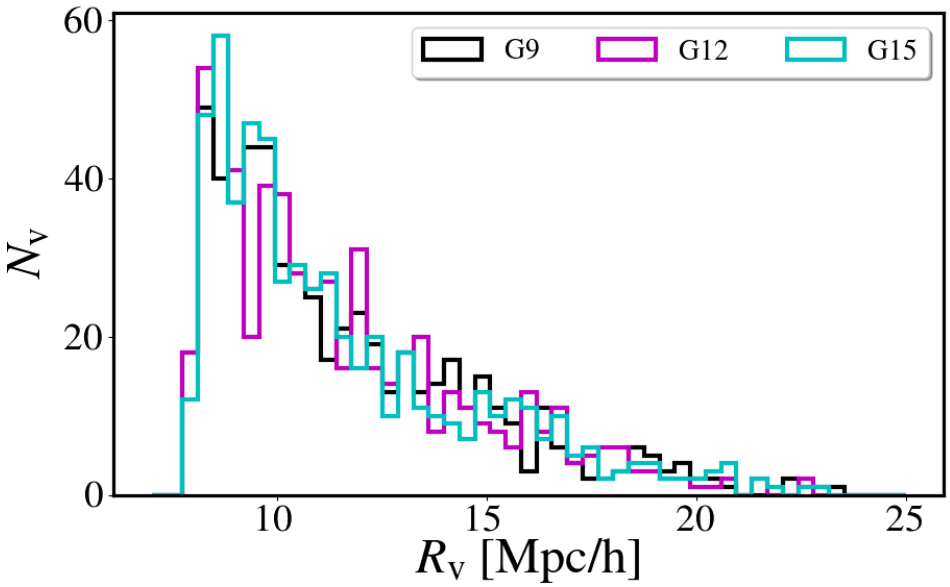

Figure 4.23 Void radii distribution for all voids from the empty spheres catalogue. The main analysis using these voids selected those with $R_{\rm v} \geq 12\,h^{-1}$Mpc.

Fig. 4.25 shows the tangential shear (upper) and cross shear (lower) of the void sample selected to have $R_{\rm v} \geq 12\ h^{-1}$Mpc. I find a cross shear component

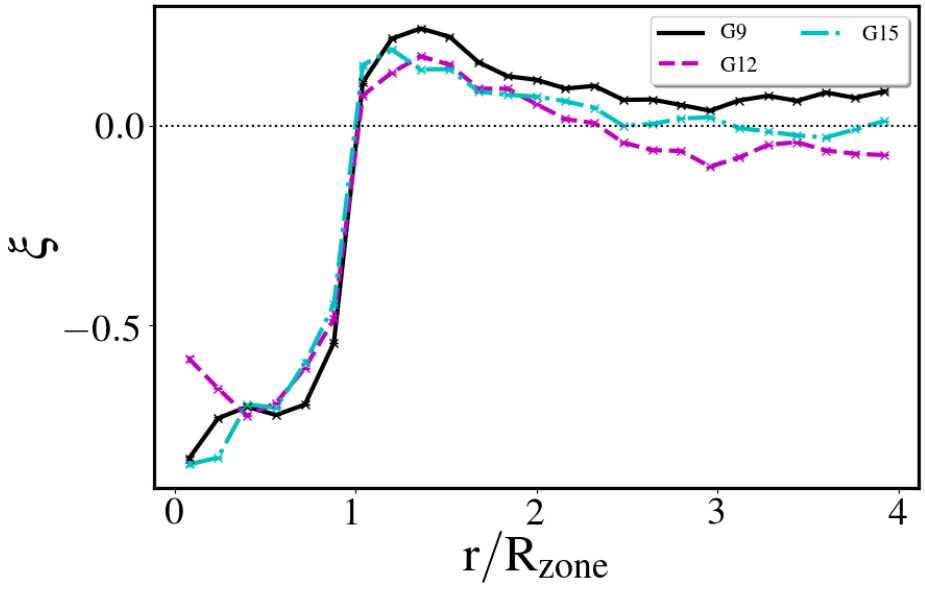

Figure 4.24 Correlation function for all voids from the empty spheres catalogue. The main analysis using these voids selected those with $R_v \geq 12\,h^{-1}$Mpc.

consistent with a null signal, but also a noisy tangential shear signal. Fig. 4.25 includes a subtraction of a random signal. I note that the lensing signal and the errors were calculated in the same way as for the ZOBOV voids. In essence, the only difference between the ZOBOV voids and the empty sphere voids is the number of voids, their location, and radius. Unlike in the mock voids in Section 4.3.3, there is no clear weak lensing signal in the GAMA data using either void catalogue. This, however, does not come as much of a surprise since the signal from the mocks assumes an effective area of $4000\,\mathrm{deg}^2$ with a GAMA-KiDS like galaxy sample.

4.5 Void Lensing Discussion and Conclusion

Through measuring the weak lensing signal from KiDS-450 galaxies around voids in the GAMA survey, I notice some trends that differ from the expectations I see in the mock data. The first difference arises when comparing the void-galaxy correlation function. From the mock data in Fig. 4.6, I see the expected shape of the correlation function with an underdense region inside the void radius, a density peak around the void radius, and convergence with the background density of the Universe outside of the void. However, when I measure the same correlation function for voids from the GAMA data, I find significant differences. As shown in Fig. 4.20, only the voids in the G12 have an underdense interior and only voids in G9 converge to the background density outside of the void

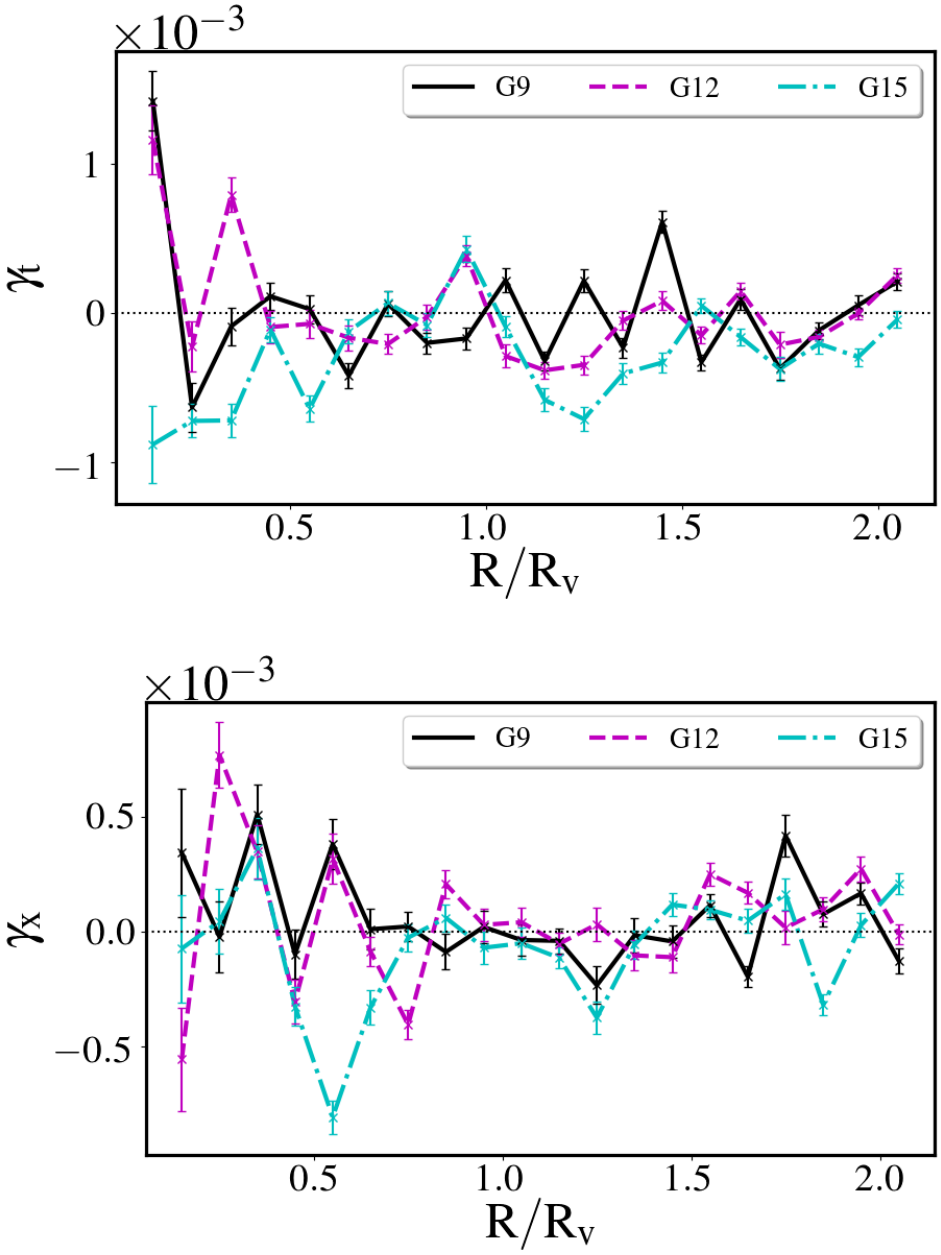

Figure 4.25 *Upper:* Tangential shear with a subtracted random signal for voids from the empty spheres catalogue selected on $R_v \geq 12$ in G9, G12, and G15. *Lower:* Cross shear with a subtracted random signal for voids from the empty spheres catalogue selected on $R_v \geq 12$ in G9, G12, and G15.

despite each void aligning with the criteria in Eq. 4.14. Several reason exist for such a behaviour. One reason indicates that the voids in the GAMA fields reside in a large-scale overdensity. This also explains the noisy behaviour of the shear signal in Fig. 4.22. Since the voids do not reside in truly underdense regions, the shear signal shows a positive amplitude on large-scales, mostly influenced by the voids in the G15 field since they reside in the most overdense environments as compared to the voids in G9 and G12. I find that this does not change when I compare two different void finding algorithms. Even when using the empty sphere voids of Hawken et al. (2019, in prep), which increases the number of voids for improved statistics, I still find no significant shear signal. Another reason for such behaviour is the inherent non-linear nature of the watershed void finding methodology. ZOBOV is optimised for large surveys or periodic boundary conditions, so the combination of a thin and narrow survey geometry, survey masks, and splitting the regions into redshift bins to compare the results with the SLICS mocks complicates the algorithm. I tested this by applying the galaxy selection from Hawken et al. (2019, in prep) to the GAMA data and using these galaxies as an input to ZOBOV. The void-galaxy correlation function contains similar features to Fig. 4.20, and although the voids tend to reside in slightly more underdense regions, the correlation function does not converge to the mean density of the Universe on large scales. This suggests that redshift cuts and galaxy selection, with complicated survey masks and geometry do not fare well for watershed void finding algorithms such as ZOBOV.

Due to small number statistics arising from the geometry and size of the GAMA survey, I chose to investigate the effect of survey geometry on void correlation functions. In order to do this, I use the DESI-like mock catalogue of Smith et al. (2017). This halo catalogue covers the full sky out to $z = 2.2$ with a mass resolution of $\sim 10^{11}\,h^{-1}\,\mathrm{M}_{\odot}$. Using it, Smith et al. (2017) construct a galaxy catalogue with a limiting r-band magnitude of $r < 20$ out to $z \sim 0.2$, mimicking the upcoming Bright Galaxy Survey sample from DESI. In practice, I select a region from the mock sample that spans the coordinates of the GAMA G9 field. Using this as my baseline, I utilise HEALPY's ROTATOR function to rotate the field in the range of RA: $[5, 75]$ deg and DEC: $[5, 80]$ deg. I chose this range on the requirement that any combination of the rotations in this range were within the full DESI mock area. In order to optimise the statistical sample of rotations, I decided to increase the amount of rotation in either RA/DEC by 5 deg per rotation generating 210 realisations of a G9-like field within the DESI mock area. The consequence of this choice is that not all of these rotations are fully independent. Since the ROTATOR function rotates the pixels of the all-sky map, I also retain the random mock galaxies that fall within the pixels of the rotated field. I also recalculate the total volume of each rotation in order to the get most accurate number density. Although the volumes for each rotation do not deviate much from the original G9-like baseline, due to the nature of rotated pixels, the surface area slightly changes per rotation thus changing the total volume. For each rotated field, I also create buffer particles as described in Section 4.4.3 to use as ZOBOV inputs. However, I do not consider masks within the rotated fields,

meaning that I only explore the effect of survey geometry for ZOBOV voids.

Fig. 4.26 compares the density profile from the tessellation method (upper) and void-galaxy correlation function (lower) for a single GAMA-like field (black) to a full DESI-like sample (cyan). The dashed magenta curve shows the average of 210 GAMA-like rotations. It's important to note that some of these rotated fields overlap with one another and are not fully independent. Nevertheless, I see a general trend for both the density profile from the tessellation method and correlation function. The first feature to note relates to the density depth of voids. As both the upper and lower panels of Fig. 4.26 show, the interior of voids from the full DESI mock appear to be ~ 2 times more underdense than the average voids in the GAMA-like fields. This likely arises due to a larger number of smaller voids in the GAMA-like fields, created by a limited volume and boundaries. This effect of survey geometry means that ZOBOV only identifies underdensities within the confined area of the GAMA-like field, limiting the size of the voids. This potentially leads to more void-in-cloud scenarios, especially if the GAMA-like overlaps with an overdense region of the full DESI mock. The second most notable features appears as a shift in the density peak between the averaged rotations and the full mock sample. Although with a broad spread, the full DESI mock density and correlation function peak at $\sim 1R_{\rm v}$, as expected, whereas the individual GAMA-like fields peak at $\sim 0.75R_{\rm v}$. I also see this behaviour in the GAMA data as shown in Fig. 4.20.

After comparing the behaviour of voids in the SLICS and DESI mocks and comparing them to the GAMA data, I conclude that galaxy selection, survey geometry, and complicated survey masks significantly affect void identification with watershed void finding algorithms and caution applying these algorithms to surveys with such narrow geometries. This highlights the possible effect of boundaries and masks on void identification and profile measurement, which may arise for surveys with larger areas as well. Moreover, the low numbers of voids in the patchy GAMA survey makes the signal-to-noise very low. Future galaxy redshift surveys with a larger, continuous area, such as DESI, will help to alleviate this void identification problem. However, as previously mentioned, in order to fully exploit the abilities of void weak lensing and employ our model from Chapter 3, we advocate for a symbiosis of weak lensing surveys and overlapping galaxy redshift surveys. In the Astro2020 White Paper by Pisani et al. (2019), we discuss an opportunity for WFIRST to create a wide and deep spectroscopic sample of galaxies that will overlap with the exquisite quality of the WFIRST lensing data, fuelling studies of void lensing, void RSDs, and environment dependent galaxy formation. We will now shift our attention away from the 3D underdensities of our Universe and focus on what information we can glean from projected 2D underdensities.

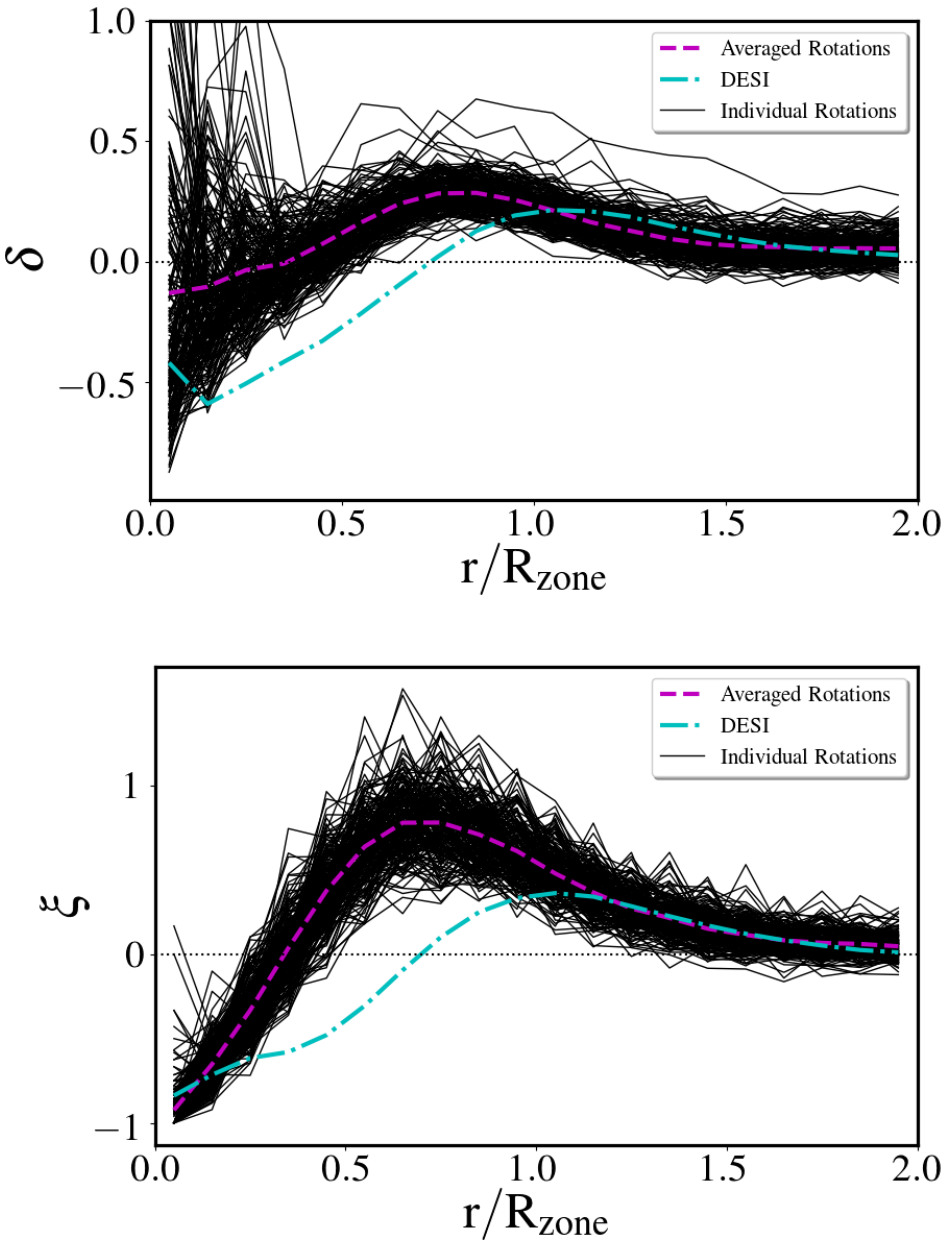

Figure 4.26 *Upper*: Density contrast using the tessellation approach for the full DESI mock (dot-dashed cyan), for 210 non-independent G9-like rotated fields (solid black), and the mean of those individual GAMA-like fields (dashed magenta). *Lower*: Same as the upper except showing the void-galaxy correlation function.

I also am other than what I imagine myself to be. To know this is forgiveness.

Simone Weil

5

Density Split Statistics

In Brouwer, Demchenko, et al. 2018 (BD18 hereafter), we report on the WL signal within projected, circular apertures using the KiDS-450 and GAMA datasets. We show the dependence of the WL amplitude on the density of the apertures. We then introduce an optimal weighting scheme to extract maximum signal-to-noise from these apertures and forecast the possibility of future WL surveys, such as Euclid and LSST, to constrain the evolution of these projected apertures by splitting them into tomographic bins. In this chapter, I directly include the parts of BD18 which describe the analysis that I led, with Section 5.2.3 published as Section 3.3, and Figs. 5.2, 5.3, and 5.1 published as Figs. 5, 6, and 8, respectively, in BD18. In the remainder of Section 5.2, I summarise our findings before moving on to the Density Split Statistics theory in Section 5.3. Sections 5.4 and 5.5 describe an analysis of Density Split Statistics using ΛCDM and non-ΛCDM simulations, respectively, while Section 5.6 concludes this chapter by providing an outlook for the future of Density Split Statistics.

5.1 Weak Lensing in Projected Density Bins

As shown in the results of Chapter 4, extracting the WL signal around voids in the GAMA dataset poses a challenge due to the survey geometry and low signal-to-noise (S/N). Furthermore, lensing is a projection effect and thus measuring it around 3D objects will yield a relatively low S/N measurement even in pristine conditions. Adding the difficulties of void identification and requiring spectroscopic galaxy redshift surveys to overlap with WL surveys makes WL with voids a viable task only for future surveys. However, a vast amount of information

exists within the underdense regions of our Universe and, as discussed in Section 1.8.3, these regions have the capability to shed light on theories of modified gravity and dark energy. To mitigate the difficulties of WL around voids, while still probing these underdense regions, Gruen et al. (2016) devised a way to measure WL around projected underdense regions they coined 'troughs.' The definitions of troughs is simply the most underdense circular regions on the sky in terms of the projected galaxy number density[1]. Since each trough exhibits a circular shape by definition, identifying the centre of the trough and stacking multiple troughs becomes a relatively simple task, as compared to stacking voids, yielding a shear signal that does not suffer from off-centring. Since troughs are defined as circular regions in *projected* space, they have 3D shapes of long conical frusta along the line-of-sight direction. This means that no overdensities (on average) will intrude into troughs. In essence, one can think of troughs as multiple voids stacked along the line of sight. However, unlike voids, troughs do not require a spectroscopic galaxy sample for accurate trough identification. Even if one wishes to identify projected underdenstities in tomographic bins, as long as the size of these redshift bins exceed the photometric redshift uncertainties, photometric redshifts will suffice (Clampitt and Jain, 2015; Sánchez et al., 2016). Using this approach, Gruen et al. (2016) measure a WL signal around troughs with a significance above 10σ using the DES Science Verification (DES-SV) dataset (Diehl et al., 2014).

Gruen et al. (2016) showed that, given the uncertainties of DES-SV dataset, their theoretical predictions using a Gaussian approximation for the matter density field agreed well with the data, although sensitivities to the galaxy bias arose. However, with current and upcoming datasets, a Gaussian assumption proves insufficient to accurately model the WL signal around troughs. To this end, Friedrich et al. (2018) further the concept of troughs by generalising the methodology to include not just the lowest projected density regions, but all density regions. This generalisation, known as 'Density Split Statistics' (DSS), allows the usage of the full density spectrum to measure not only WL observables, but also the skewness, stochasticity, and galaxy bias of the matter density field, making DSS a 3pt statistic. They introduce a log-normal, perturbation theory based model (see Section 5.3 for a description of the model) to predict the galaxy probability density function (PDF) and WL signal from projected circular apertures that span the full density range. Using this approach, Gruen et al. (2018) show that the 3pt statistic of DSS provides cosmological constraints comparable to those of DESY1 3×2pt results from Troxel et al. (2017).

Cautun et al. (2018) compared shear measurements from voids identified using various void finding algorithms with projected underdensity measurements in order to determine the most optimal method to compare various theories of gravity using WL around underdensities. For upcoming surveys such a Euclid and LSST, they find that the WL signal around troughs can constrain $f(R)$ gravity with a confidence level of ~ 30 times greater than voids alone. They also

[1]Gruen et al. (2016) define 'the most underdense' circular regions as those that have a number density in the lowest 20th percentile as compared to the mean number density.

propose a new method for identifying projected underdensities known as tunnels. Unlike troughs, which contain some amount of galaxies within them, Cautun et al. (2018) define tunnels as projected circular regions devoid of galaxies. In practice, they achieve this by constructing Delaunay tessellations of the projected galaxy field. Using the vertices of each Delaunay triangle they construct a circumcircle, which, by definition, will be empty of any galaxies. This method effectively creates empty, non-overlapping troughs of varying sizes. Since tunnels represent the most underdense regions, Cautun et al. (2018) find that they also yield a WL signal with the highest S/N among all the methods, surpassing troughs. Using this definition, they find that tunnels can distinguish the F5 and F6 $f(R)$ gravity models at 80σ and 11σ, respectively, with an LSST-like dataset. Davies et al. (2018) apply this approach to convergence maps and find a WL signal that is ~ 3 times more significant than the tunnels signal that uses galaxies as the tracers. Although tunnels produce a significant WL signal, since they are defined as regions devoid of galaxies, the size of tunnels will vary with the survey density. This means that as the number density of galaxies increases, the number of real tunnels will decrease and the Delaunay tessellation will identify spurious, empty regions and not true projected underdensities. Cautun et al. (2018) identified tunnels in a relatively underdense CMASS mock galaxy catalogue, however when applying their algorithm to the SLICS GAMA mock galaxy catalogue, I find that WL signal becomes noisy. This occurs because the size of these tunnels is extremely small leading to an identification of spurious tunnels. One can incorporate various cuts to the galaxy catalogue, but this will introduce a selection bias, which has not yet been studied for this type of measurement. In addition, no theory exists (yet) to model the WL signal from tunnels for a given cosmology and galaxy selection. Because of this I do not consider tunnels and focus the analysis on troughs, comparing simulation and data measurements to the predictions of Friedrich et al. (2018).

In the following sections I discuss the measurement of WL around troughs in simulations and data (Section 5.2). I then introduce the full DSS methodology (Section 5.3) and apply it to the SLICS mocks (Sections 5.4). I then introduce a new simulation suite that is an extension of the SLICS, but with non-ΛCDM cosmologies, *cosmo*-SLICS, and show how the DSS model can place constraints on non-ΛCDM cosmologies (Section 5.5.2). In the end, I conclude with an outlook to the future of DSS (Section 5.6).

5.2 Troughs and Ridges Measurements

In this section I summarise the analysis and results presented in BD18, where we apply the troughs measurement to the KiDS-450 and GAMA datasets.

5.2.1 Mocks and Data Galaxy Selection

In BD18, we use two observational datasets. The initial foreground sample considered is the GAMA dataset described in Section 4.4, although with a different galaxy selection. To compare the measurement with simulations, we mimic the mock galaxy selection by only using GAMA galaxies with absolute r-band magnitude $M_\mathrm{r} < -19.67$. This galaxy selection results in a sample of 159 519 galaxies (88.15% of the full catalogue), within the redshift range $0 < z_\mathrm{G} < 0.5$ and a mean redshift of $\overline{z_\mathrm{G}} = 0.24$. The average number density of this sample (including masks) is $\overline{n_\mathrm{g}} = 0.25\,\mathrm{arcmin}^{-2}$. However, at that time, the available area of the KiDS survey was ~ 2.5 times larger than that of the GAMA survey. Thus, since photometric redshifts are sufficient for trough identification, we decided to perform both the trough selection and lensing measurement using the KiDS galaxies alone, employing the full $454\,\mathrm{deg}^2$ area of the KiDS-450 dataset described in Section 4.4.2. To be able to compare the KiDS troughs to those obtained using GAMA, we select a sample of 'GAMA-like' (GL) KiDS galaxies that resembles the GAMA sample as closely as possible. In order to create this GL-KiDS galaxies, we match the KiDS and GAMA galaxies using their sky coordinates, and select the magnitude cut based on the completeness of this match. As mentioned in the previous section, one of the advantages of the trough analysis over voids is the ability to use photo-z's rather than needing spec-z's. However, in order to create a GL-KiDS sample, we cut the KiDS galaxies at the maximum redshift of GAMA: $z_\mathrm{G} < 0.5$. Contrary to the KiDS source redshifts used for the lensing measurement, where we can use the redshift probability distribution of the full population, the application of this cut and the use of KiDS galaxies as lenses both require individual galaxy redshifts. These photometric redshifts, z_ANN, are determined using the machine learning method ANNz2 (Sadeh et al., 2016; Bilicki et al., 2018), as described in Sect. 4.3 of de Jong et al. (2017). Finally, to mimic the galaxy sample corresponding to resolved halos in the mock catalogues, we apply the absolute r-band magnitude cut $M_\mathrm{r} < -19.67$ on the GL-KiDS sample. Using a selection to mimic both the mocks and GAMA data, the GL-KiDS catalogue consists of 309 021 KiDS galaxies. This is ~ 2 times the number of selected GAMA galaxies, which is a consequence of the completeness of GAMA compared to KiDS. The average galaxy number density of this fiducial sample (including masks) is $\overline{n_\mathrm{g}} = 0.33\,\mathrm{arcmin}^{-2}$.

In order to compare and interpret the results of the trough measurement from the GAMA and GL-KiDS data sets, we employ two sets of simulations. The first simulation considered is the MICE-GC N-body simulation presented by Fosalba et al. (2015a). It contains $\sim 7{\times}10^{10}$ DM particles in a $(3072\,h^{-1}\mathrm{Mpc})^3$ comoving volume, allowing the construction of an all-sky lightcone with a maximum redshift of $z = 1.4$. From this lightcone Crocce et al. (2015) built a halo and galaxy catalogue, using an HOD and Halo Abundance Matching (HAM) technique. The mock galaxy clustering as a function of luminosity has been constructed to reproduce observations from SDSS (Zehavi et al., 2011) at lower redshifts ($z < 0.25$), and has been validated against the COSMOS catalogue (Ilbert et al.,

2009) at higher redshifts ($0.45 < z < 1.1$). The MICE-GC simulation resolves DM halos down to a mass of $6 \times 10^{11}\, h^{-2}\mathrm{M}_{\odot}$ (corresponding to 20 particles), which host galaxies with an absolute magnitude $M_{\mathrm{r}} < -18.9$. Since this absolute magnitude includes a cosmology correction such that: $M_{\mathrm{r,MICE}} = M_{\mathrm{r}} - 5\log_{10}(h)$, where $h = 0.7$, we apply an $M_{\mathrm{r}} < -18.9 - 0.77 = -19.67$ cut to the GAMA and GL-KiDS samples in order to resemble the mock galaxy population. Each galaxy in the lightcone also carries the lensing shear values γ_1 and γ_2, which were calculated from the all-sky WL maps constructed by Fosalba et al. (2015b). We treat these shear values in the same way that we use the ellipticities observed by KiDS to obtain mock lensing profiles around troughs. To this end, we create a MICE background source sample with $0.1 < z < 0.9$ and $m_{\mathrm{r}} > 20$. This apparent magnitude cut equals the one applied to the KiDS background sources by Hildebrandt et al. (2017), and the redshift cut is analogous to their limit on the best-fit photometric redshift, z_{B}. We apply a further absolute magnitude cut of $M_{\mathrm{r}} > -19.3$ on the MICE mock galaxies in order to resemble the KiDS source redshift distribution more closely. The second suite of mock simulations that we use are the SLICS described in Section 4.1. Since SLICS has many realisations, we employ them to make quantitative estimates of the covariance matrices and error bars of the trough lensing signals (as described in Sect. 5.2.3), which can be compared to those from observations and used to predict the success of future measurements. One of the benefits of using both sets of simulations is our ability to compare the effects of cosmology on the trough measurement. In addition, the SLICS simulation suite provides us with a more robust covariance since we can employ multiple realisations, however the MICE simulation consists of a much larger volume, mitigating the effects of cosmic variance.

5.2.2 Trough Identification and Lensing Measurement

In order to identify troughs, in BD18 we follow the prescription of Gruen et al. (2016). Effectively, the procedure constitutes smoothing a low redshift, foreground galaxy population with a circular top-hat aperture and the smoothed density field is utilised to rank the apertures into similar density bins. We use apertures with 4 different angular top-hat radii for our analysis, $\theta_T = \{5, 10, 15, 20\}$ arcmin, choosing $\theta_T = 5$ arcmin as our fiducial case. We define the projected galaxy number density $n_{\mathrm{g}}(\vec{x}, \theta_T)$ of each aperture as the galaxy count within angular separation θ_T of the sky position $\vec{x}$, divided by the effective area of the corresponding circle on the sky, determined using the appropriate KiDS or GAMA mask, where each mask provides the survey area completeness. Following Gruen et al. (2016), we exclude apertures with less than 80% of their area completed. Next, for each circular aperture, we determine the percentile rank $P(\vec{x}, \theta_T)$: the fraction of equally sized apertures that have a lower galaxy density than the aperture considered. This type of ranking means that low-density apertures have a low value of P (down to $P = 0$), while high-density ones have a high P-value (up to $P = 1$), while an aperture containing the median density has the value $P = 0.5$. As in Gruen et al. (2016), we define all apertures in the lowest

quintile (20%) of galaxy density (*i.e.* $P(\vec{x}, \theta_T) < 0.2$) as troughs, while apertures in the highest quintile (*i.e.* $P(\vec{x}, \theta_T) > 0.8$) we define as 'ridges'.

We show that we can measure a substantial WL signal using both the GAMA and GL-KiDS samples and decide to use the GL-KiDS sample as the fiducial one due to the larger area of the KiDS-450 survey as compared to GAMA. For our main analysis, we decided to study *all* apertures as a function of their density percentile rank $P(\theta_T)$. Considering apertures of fixed radius θ_T, we split them into 20 samples of increasing P-value, using a bin width of $\mathrm{d}P = 0.05$. We then measure the shear profile $\gamma_\mathrm{t}(\theta)$ of each sample. Fig. 5.1 shows the GL-KiDS, MICE, and SLICS lensing profiles in the 20 P-bins for $\theta_T = 5\,\mathrm{arcmin}$.

The dotted vertical lines in Fig. 5.1 indicate the angular separation range: $1.2\,\theta_T < \theta < 70\,\mathrm{arcmin}$. We chose these scales because: 1) inside θ_T the lensing is insensitive to the full trough mass (where we leave a 20% buffer outside the trough edge), and 2) the random signal γ_0 for the KiDS shows systematic effects at $\theta > 70\,\mathrm{arcmin}$. Within this range, we find that the fiducial trough and ridge shear signals are well-described by a power law and therefore fit a relation $\gamma_\mathrm{t}(\theta) = A\,\theta^\alpha$ within the specified angular range, to obtain the best-fit amplitude A and index α of the lensing signal. Since our main interest is in the amplitude, we fix the value of α with the help of the MICE-GC simulations, finding a mean best-fit index value $\overline{\alpha}$ of -0.45 for the fiducial troughs and -0.55 for ridges. We therefore choose to fit all projected lensing profiles with the function:

$$\gamma_\mathrm{t}(\theta) = A/\sqrt{\theta}\,. \tag{5.1}$$

To each shear measurement in Fig. 5.1, we fit Eq. 5.1 within the indicated angular range, to measure the shear amplitude A. As expected, we find the apertures with lowest/highest P-values correspond to the strongest negative/positive shear signals. Furthermore, Fig. 5.1 shows an asymmetry between the troughs and ridges, where the lensing signal is stronger for the highest ridges than for the deepest troughs. This suggests that the known skewness of the matter density distribution manifests as a skewness in the galaxy number density distribution as well. The non-zero shear of apertures with $P \sim 0.5$ highlights this skewness.

5.2.3 Covariance Comparison

For all shear measurements created using the GL-KiDS and GAMA data, we compute the analytical covariance matrix as described in Sect. 3.4 of Viola et al. (2015). This covariance matrix is based on the contribution of each individual source to the stacked lensing signal, and takes into account the correlation between sources that contribute to the shear profile of multiple lenses. The errors on our shear profiles are estimated by the square-root of the diagonal of this analytical covariance matrix. However, these error bars could underestimate the uncertainties at larger scales, where sample variance

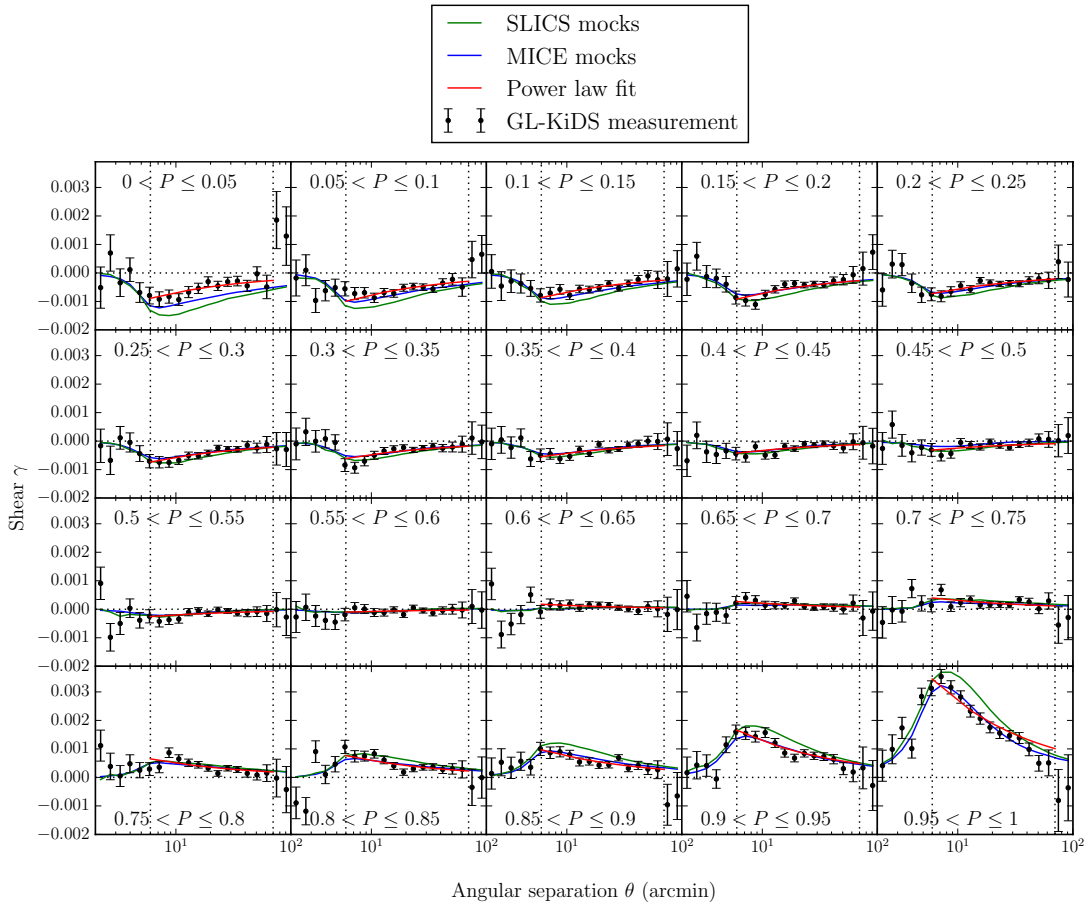

Figure 5.1 Each panel shows the GL-KiDS (black dots with 1σ errors), MICE (blue line) and SLICS (green line) shear profiles $\gamma_t(\theta)$, resulting from apertures of angular radius $\theta_T = 5\,\mathrm{arcmin}$. The shear profile of these apertures is stacked in 20 bins of increasing density percentile rank $P(\vec{x}, \theta_T = 5\,\mathrm{arcmin})$. A simple power law fit: $A/\sqrt{\theta}$ (red line), within the fitting range (dotted vertical lines) is used to obtain A as a function of P. For underdense apertures (troughs) the amplitude A of the lensing signal becomes negative outside the trough radius, while for overdense apertures (ridges) A becomes positive.

starts to play a significant role (Viola et al., 2015). We therefore compare the analytical covariance calculated using our GL-KiDS data to those based on the large ensemble of mock realisations from the SLICS mocks.

Utilising the SLICS HOD mock catalogues described in Sect. 4.1 we compute the covariance matrix using the following equation:

$$C^{ij} = \frac{1}{N-1}\sum_{n=1}^{N}(\gamma_{\mathrm{t},n}^{i} - \overline{\gamma_{\mathrm{t}}}^{i})(\gamma_{\mathrm{t},n}^{j} - \overline{\gamma_{\mathrm{t}}}^{j})\,, \tag{5.2}$$

where N is the number of mock realisations, ${\gamma_{\mathrm{t}}}^{i}$ is the tangential shear signal in the i-th angular bin of the n-th mock realisation, and $\overline{\gamma_{\mathrm{t}}}^{i}$ is the tangential shear average of the i-th bin from all used realisations. The covariance is then multiplied by the area factor:

$$f_{\mathrm{area}} = \frac{100}{360.3}\,, \tag{5.3}$$

in order to account for the difference in area between the SLICS mocks and the masked KiDS-450 data. The errors on the shear are then calculated using the square root of the diagonal of this scaled covariance matrix. Since we calculate the mock covariance from multiple realisations and use the total modelled ellipticities of the galaxies to calculate the tangential shear signal, the mock covariance accounts for shape noise, shot noise, and sample variance. Fig. 5.2 shows the correlation matrices, r_{corr}, for the mock and analytical covariances, respectively, where the correlation matrix is calculated using:

$$r_{\mathrm{corr}}^{ij} = \frac{C^{ij}}{\sqrt{C^{ii}C^{jj}}}\,. \tag{5.4}$$

We calculate the shear profiles and covariance using 349 realisations, but have also tested this analysis on 608 realisations. Having found no significant differences in our signal and covariance between 608 and 349 realisations, we opt to use 349 realisations throughout the analysis in order to save computational time.

Fig. 5.2 shows the data-based analytical (upper) and mock-based SLICS (lower) correlation matrices for the shear profiles $\gamma(\theta)$ of apertures with radius $\theta_T = 5\,\mathrm{arcmin}$, split into 20 bins based on their density percentile rank $P(\theta_T)$ (corresponding to the shear profiles shown in Fig. 5.1). Comparing the analytical and mock correlation matrices, we notice that those from the SLICS mocks are noisier compared those calculated analytically, due to the limited number of mock realisations in combination with the effects of sample variance. In addition, the correlation at large scales appears to be stronger for the mock results, which is also expected since the mock correlation incorporates the effects of sample variance (which the analytical covariance does not). Nevertheless, the analytically calculated correlation also increases at large scales, due to the increasing overlap of source galaxies with increasing radius. For both data and mocks, the covariance depends significantly on density, increasing at extremely low and high P-values. This is expected, since extremely low-density troughs (high-density ridges) tend to

cluster at the centres of larger low-density (high-density) regions. This clustering of extreme density regions increases the correlation between the lensing signals of the more extreme troughs and ridges.

Most importantly, we assess the agreement between the *diagonals* of the covariance matrices created by both methods, since the square-root of these diagonals defines the errors σ_γ on the measured shear profiles. Fig. 5.3 shows the $\sigma_\gamma(\theta)$ values of GL-KiDS and GAMA-selected fiducial troughs ($P(\vec{x}, \theta_T) < 0.2$), with a radius of $\theta_T = 5\,\mathrm{arcmin}$. As expected from its smaller survey area, the small-scale ($\theta < 30\,\mathrm{arcmin}$) error values from GAMA are a factor ~ 1.3 higher than those from KiDS. We compare these analytical covariance errors to those calculated from 349 SLICS mock realisations, adjusted using the area factor in Eq. 5.3 to resemble the KiDS survey. Up to a separation $\theta = 30\,\mathrm{arcmin}$ (half the size of a $1 \times 1\,\mathrm{deg}$ KiDS tile) the GL-KiDS and SLICS error values are in excellent agreement. Due to the patchy KiDS survey coverage beyond the GAMA fields, the KiDS errors increase rapidly at larger angular separations. For the GAMA survey, whose area is more contiguous, this increase in error values is much smaller. For the SLICS mocks, which consist of $10 \times 10\,\mathrm{deg}^2$ patches, it is completely absent. Because this effect dominates the error values at larger scales, we conclude that we do not need to worry about a possible underestimation of the analytical covariance errors at larger scales due to the lack of sample variance. However, we do use SLICS mock covariances to devise an optimal trough and ridge weighting scheme, and to predict the significance of future trough measurements, detailed in Section 4.3 and 5.4 of BD18 and reviewed in the next section.

5.2.4 Troughs and Ridges Conclusion and Outlook

Rather than selecting troughs and ridges with a 'hard cut' in the percentile rank $P(\vec{x}, \theta_T)$ of the apertures, we apply a more sophisticated S/N-based weighting scheme to stack the shear profiles of the apertures. In order to obtain the most significant stacked lensing detection, we suggest that the optimal weighting of each individual trough/ridge contributing to the stacked signal should be based on the $S/N \equiv A/\sigma_T$ of that contribution. To do this we employ the SLICS measurement and covariance and fit 5^{th}-order polynomials to the SLICS A/σ_T values, providing a lens weight for every individual aperture. With this weighting scheme, we find that our fiducial trough signal improves from a S/N of 12.3 to 16.8.

We explore the possibility of detecting trough/ridge evolution with upcoming high-redshift surveys such as Euclid and LSST. We effectively split the foreground galaxy sample into redshift bins with an equivalent comoving volume and measure the $\Delta\Sigma$ signal. Using the SLICS mocks, we find an indication that these surveys could observationally constrain the redshift evolution of troughs and ridges at $\gtrsim 7\sigma$ between every consecutive redshift bin. This type of measurement could be used to constrain the growth rate of structure and galaxy bias. However, to properly conduct a tomographic analysis of the foreground galaxies requires a

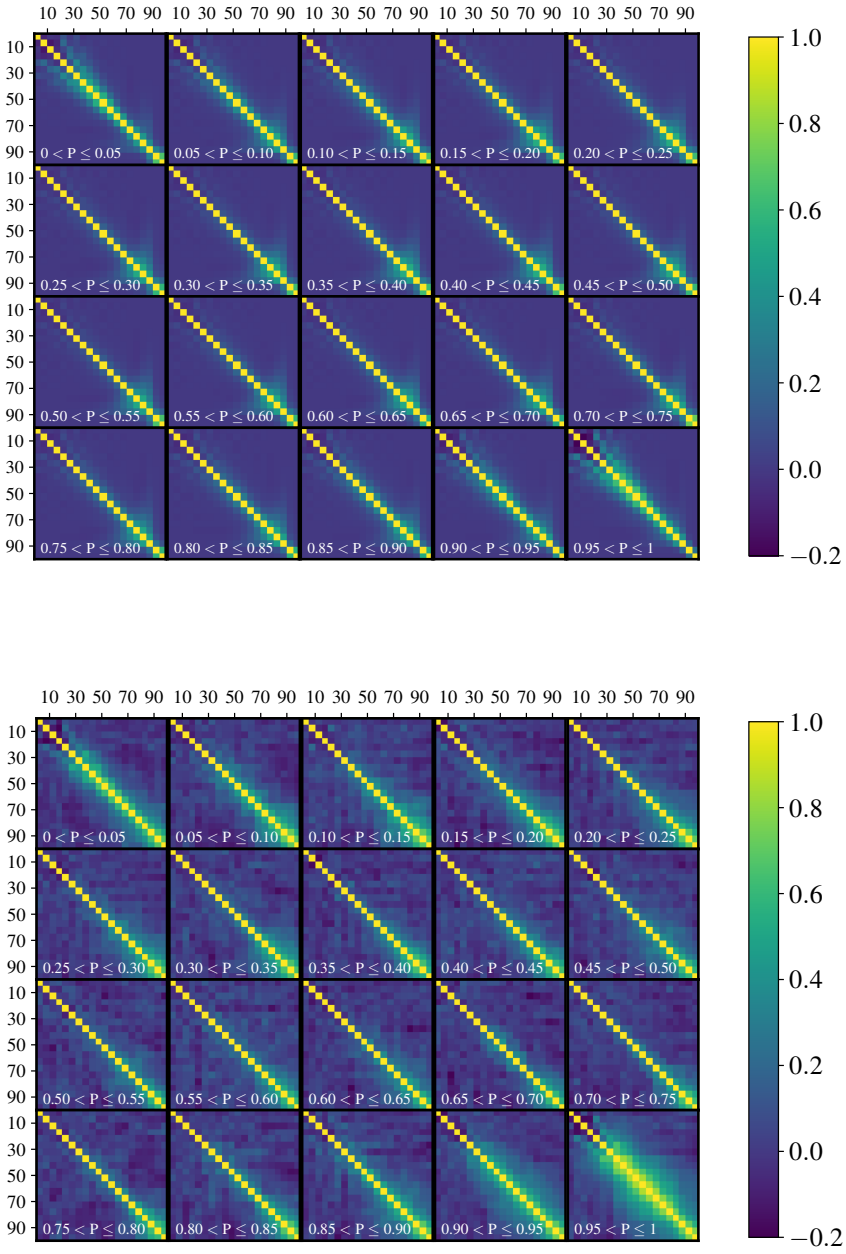

Figure 5.2 The two panels show the analytical GL-KiDS (upper) and SLICS GAMA HOD (lower) correlation matrices, resulting from apertures with an angular radius $\theta_T = 5\,\mathrm{arcmin}$. The correlation matrices are computed for 20 bins of increasing density percentile rank $P(\vec{x}, \theta_T = 5\,\mathrm{arcmin})$, corresponding to the shear profiles shown in Fig. 5.1. The increased correlation at large radii is caused by the overlap between sources (in the case of both GL-KiDS and SLICS) and by sample variance (in the case of SLICS). The increased correlation at extreme P-values is caused by the spatial clustering of low- and high-density regions.

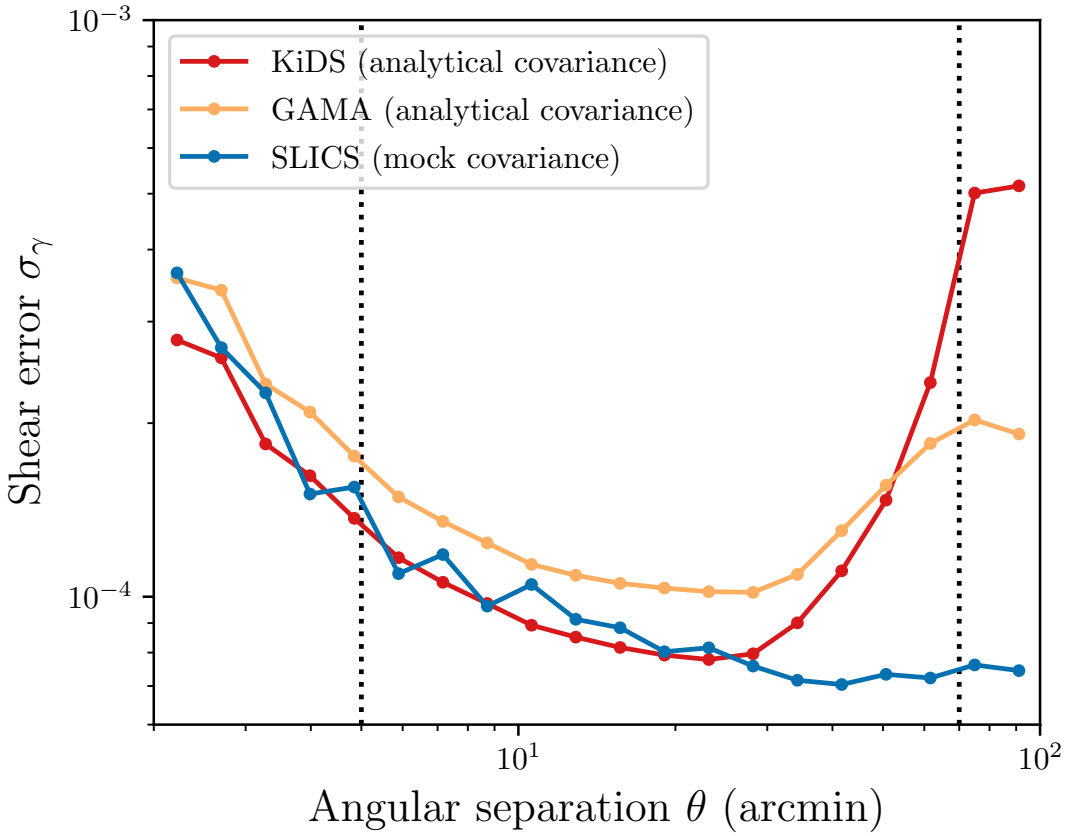

Figure 5.3 The error values $\sigma_\gamma(\theta)$ (as a function of angular separation θ) on the shear profile of the fiducial troughs ($P < 0.2$) with a radius of $\theta_T = 5\,\mathrm{arcmin}$. The GL-KiDS and GAMA errors are estimated using the diagonal of the analytical covariance matrix, while the mock errors are estimated from the covariance matrix calculated using 349 SLICS mock realisations. The GAMA errors are higher than those of GL-KiDS, as expected from its smaller survey area. The GL-KiDS errors are in reasonable agreement with the SLICS mock errors up to $\theta = 30\,\mathrm{arcmin}$, where they rise steeply as a result of the patchiness of the survey.

spec-z sample. We explore this possibility in Section 5.6. However, simulations are limited by the flexibility of model parameters, resolution, and size, making model fitting with data challenging. Moreover, we would like a more physical understanding of the WL signal from projected apertures. The DSS method presented in Friedrich et al. (2018) achieves this goal and so we now move on to a review of that method.

5.3 DSS Theory

The framework of DSS was developed by Friedrich et al. (2018), which I review in this section. Up to this point, we have considered the lensing signal in projected bins of varying density, which we can refer to as *density split lensing*. However, DSS takes this one step further by combining the counts-in-cells (CIC) measurement with the WL measurement. Since WL by itself is a 2pt statistic, the addition of CIC makes DSS a 3pt statistic, informing us not only about the amplitude of the density fluctuations, but also about the skewness of the matter density field. In practice, the DSS method functions as follows: the first step smooths a low redshift, foreground galaxy population with a circular top-hat aperture. Next, the smoothed density field is utilised to group areas on the sky into similar density bins. BD18 divided the sky into 20 bins, however Friedrich et al. (2018) split the sky into 5 density bins that they call quintiles. Using each of these density quintiles, the next step is to use a high redshift, source galaxy population to measure the tangential shear signal of all circular apertures within each quintile, creating 5 GGL signals. The lensing signal is then complemented by a CIC histogram of the foreground galaxy population, which constrains the bias and stochasticity of the foreground sample. The DSS methodology has several favourable features. The formulation of DSS lends itself to accurate analytical modelling through perturbation theory with a non-linear power spectrum (Friedrich et al., 2018). Furthermore, DSS avoids systematic effects from intrinsic alignment and additive shear bias (Gruen et al., 2018), which plagues cosmic shear analyses.

I will now discuss the components needed to model the DSS data vector. As presented by Friedrich et al. (2018), the data vector requires three ingredients:

(i) The PDF of the projected matter density field, smoothed with a top-hat filter with radius θ_T,

$$p(\delta_{m,T}). \tag{5.5}$$

(ii) The expectation value of the tangential shear within a distance θ given the density contrast within θ_T,

$$\langle \gamma_{\rm t}(\theta) | \delta_{m,T} \rangle = \langle \kappa_{<\theta} | \delta_{m,T} \rangle - \langle \kappa_{\theta} | \delta_{m,T} \rangle, \tag{5.6}$$

where κ is the convergence defined in Eq. 2.9.

(iii) The distribution of galaxy counts within the top-hat radius θ_T, N_T, given the projected density contrast within that radius,

$$P(N_T|\delta_{m,T}). \tag{5.7}$$

To calculate the projected density PDF, Friedrich et al. (2018) assume the smooth matter density field $\delta_{m,T}$ to behave as a log-normal random field. The PDF of a log-normal field depends on the variance, $\langle\delta^2_{m,T}\rangle$ and skewness, $\langle\delta^3_{m,T}\rangle$, of the field. Friedrich et al. (2018) calculate the variance from the non-linear power spectrum and then use leading order perturbation theory to compute a scaling relationship between the power spectrum and the bispectrum in order to estimate the skewness.

For the expectation value of the tangential shear given the density contrast, Friedrich et al. (2018) assume a joint log-normal PDF for $\delta_{m,T}$ and $\kappa_{<\theta}$, where the expectation value $\langle\kappa_{<\theta}|\delta_{m,T}\rangle$ is fixed by specifying the variance and skewness of the projected density field. Just as for the density PDF, second order moments are computed from the non-linear power spectrum while the third order moments are inferred from perturbation theory.

For the CIC distribution, Friedrich et al. (2018) consider two models to account for galaxy bias and stochasticity (see Dekel and Lahav, 1999, for a thorough discussion), however I will only focus on one of the models, which I adopt for this work. In this model, a galaxy density field is introduced, $\delta_{g,T}$, where the foreground galaxies are Poissonian tracers of the true density field. In this case, $\delta_{g,T}$ represents a smooth, shot-noise-free galaxy density contrast. Friedrich et al. (2018) then assume that $\delta_{g,T}$ and $\delta_{m,T}$ are joint log-normal variables with,

$$\begin{aligned}\langle\delta^2_{g,T}\rangle &= b^2\langle\delta^2_{m,T}\rangle\\ \langle\delta^3_{g,T}\rangle &= b^3\langle\delta^3_{m,T}\rangle\end{aligned} \tag{5.8}$$

and

$$\langle\delta_{g,T}\,\delta_{m,T}\rangle = br\langle\delta^2_{m,T}\rangle, \tag{5.9}$$

where b and r are the free parameters in the model known as galaxy bias and galaxy stochasticity, respectively. This is referred to as the linear bias model.

A drawback of the linear bias model is that it imposes a minimum scale for θ_T. This minimum scale arises due to two main reasons: the accuracy of the linear bias model itself and the accuracy of the PDF modelling on scales of $\theta_T < 20$ arcmin. To improve upon this, one could incorporate a scale-dependent galaxy bias model (e.g. Simon and Hilbert, 2018) into the DSS pipeline. This would allow for a more realistic bias assumption on all scales, however I leave this extension

to future DSS modelling. It should also be noted that Friedrich et al. (2018) test the fiducial, perturbation-theory-based models for (i) and (ii) described above by comparing them to an approach using cylindrical collapse, finding excellent agreement on all scales of interest. Furthermore, they note that they only trust this model on scales of $\theta_T \gtrsim 20$ arcmin since the accuracy of the density PDF and other assumptions in the theory degrade on scales smaller than this. In light of this, the remainder of this chapter uses apertures with $\theta_T = 20$ arcmin. For readers interested in a more thorough description of the DSS model, please refer to Section 4 of Friedrich et al. (2018).

To illustrate the cosmological dependence of the DSS model, I compare the WL lensing signals of troughs and ridges between the SLICS and MICE cosmologies. In Fig. 5.1, we find that the absolute amplitudes of the profiles predicted by the MICE mocks tend to be lower than those from SLICS, where the former predictions are in better agreement with the GL-KiDS measurements. This offset can be explained by the different background cosmologies chosen for the SLICS and MICE simulations, where higher values of σ_8 and Ω_m give rise to higher absolute lensing amplitudes. Fig. 5.4 compares the shear amplitude differences for troughs/ridges (cyan/red) for the SLICS (dashed) and MICE (dotted) cosmologies using the DSS prediction of Friedrich et al. (2018). Interestingly, the cosmological constraints from the cosmic shear analysis with KiDS-450 (Hildebrandt et al., 2017) suggest that the KiDS data prefer a cosmology with lower values of Ω_m and σ_8. These values are close to those adopted by the MICE simulations ($\sigma_8 = 0.8$, $\Omega_\mathrm{m} = 0.25$), and in slight tension with the Planck cosmology, which is similar to the WMAP9 + SN + BAO cosmology adopted by the SLICS simulation ($\sigma_8 = 0.826$, $\Omega_\mathrm{m} = 0.29$). Therefore, as shown through Fig. 5.4, we can exploit the shear measurement of troughs and ridges to identify any tensions in cosmology between different probes, such as seen with the Planck and KiDS-450 cosmic shear results.

5.3.1 DSS Pipeline Test

In order to test if my DSS measurement pipeline functions as intended, I initially tested it with an idealised test case before applying it to the SLICS mocks. I was provided[2] with a log-normal realisation of the matter density field for redMaGiC (Rozo et al., 2016) galaxies between $0.2 < z < 0.45$ created from the Buzzard mocks (DeRose et al., 2019), a corresponding all-sky, no-mask, Poisson-sampled galaxy catalogue with $b = 1$ and a number density of 0.05 gal/arcmin^2, and associated background galaxies with the shear components. If my DSS pipeline functions as expected, the measured CIC histogram and shear profiles for each quintile should align exactly with the modelling pipeline of Friedrich et al. (2018).

To perform the DSS analysis, I first identify the number of galaxies that reside within each circular aperture. In practice, I map the foreground galaxy catalogue

[2]Private communication with Daniel Gruen.

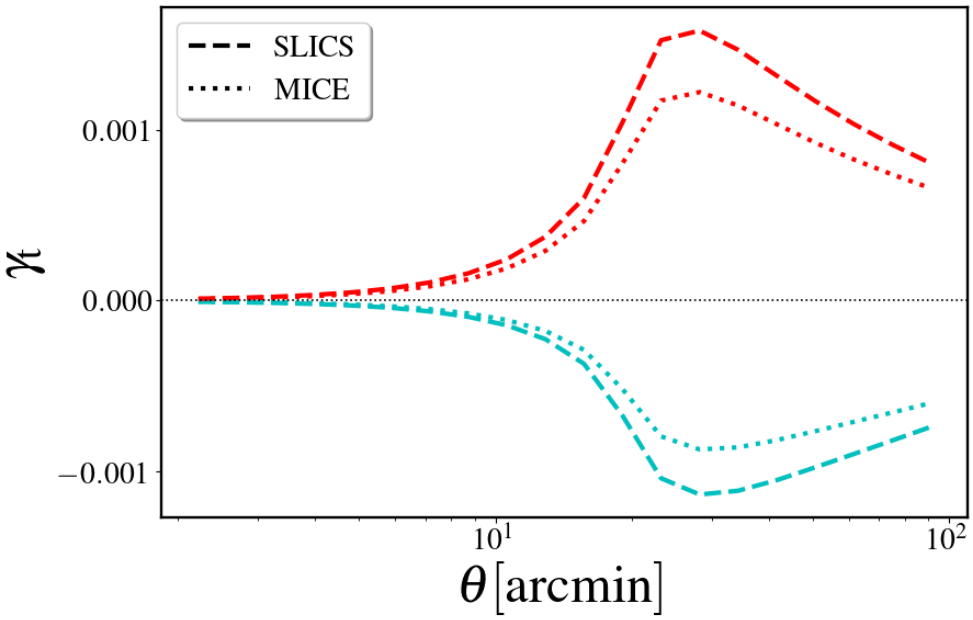

Figure 5.4 Comparison of the shear profiles for the SLICS GAMA sample (dashed) and MICE (dotted) cosmologies for troughs (cyan) and ridges (red). The profiles come from the theoretical prediction of Friedrich et al. (2018).

onto the sky using HEALPix (Górski et al., 2005). I then loop through each pixel location with a $\theta_T = 20$ arcmin radius around it and count how many galaxies reside within each pixel. Using the total sum of galaxies per pixel per aperture alongside a sample of randomly located galaxies allows me to estimate the number density within each aperture. The random galaxy sample functions as a weighting scheme where the galaxy number density per aperture is then the sum of the real galaxies weighted by the sum of the random galaxy sample within that same aperture. Furthermore, using a sample of randomly oriented galaxies, I can assign an effective area to each aperture. Although for the all-sky, no-mask case each aperture has its whole area on the sky covered, this will not be the case for the SLICS mocks and for data, thus the random sample and weighting scheme will be crucial to properly account for masks and survey boundaries. Having created a catalogue of apertures with their projected galaxy number density and effective area, I use this catalogue as a foreground sample for WL. For optimal accuracy in the WL measurement, I need to split the projected apertures into quintiles, remembering to carefully account for any apertures that reside on the border of two quintiles. To do this, I identify the percentage of galaxies in the border number density bin that will fall into the considered quintile and randomly subsample that amount of galaxies from the border number density bin, assigning them to the initial quintile. The remainder of the galaxies from that bin are assigned to the next quintile. Having accuratley separated the apertures into their quintiles, I then perform a GGL measurement on each quintile using the code TreeCorr discussed in Chapter 4. For the GGL measurement, I use 50

logarithmically spaced bins on scales of $2 < \theta < 100$ arcmin and then rebin the signal to 20 linearly spaced bins using the number of pairs per bin as a re-binning weight. Figs. 5.5 & 5.6 show the CIC histogram and shear profiles for the all-sky, Poisson test catalogue.

As shown in Fig. 5.5, the CIC histogram from the mocks (coloured lines) aligns perfectly with the prediction (dashed line), where each colour represents a separate density quintile. The CIC histogram depends significantly on the mean density of foreground galaxies (represented by the vertical dotted line) and a correct assumption of the galaxy bias. The shear profiles, on the other hand, rely strongly on the underlying cosmological parameters *i.e.* $\Omega_{\rm m}$ and σ_8. Fig. 5.6 suggests that my DSS pipeline works accurately since the lensing signals measured from the mocks (solid lines) lie on top of the predicted values (dashed lines), where the colours represent the different density quintiles as in Fig. 5.5. The intrinsic skewness of the matter density field is evident in both the CIC histogram and shear profiles. Namely, if the late-time matter density field followed a Gaussian distribution, both the CIC histogram and the shear profiles would be symmetric. Having proven that my DSS measurement pipeline reproduces the expected results, I then apply it to the SLICS simulations.

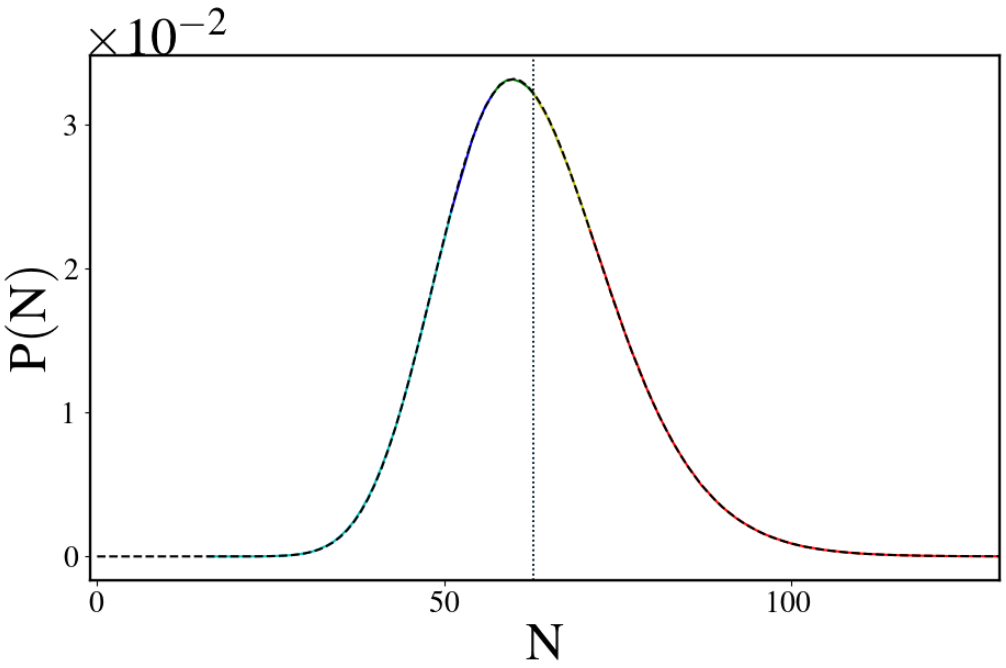

Figure 5.5 CIC histogram split into quintiles by colour of an all-sky Poisson mock described in the text with the DSS prediction of Friedrich et al. (2018) (dashed black).

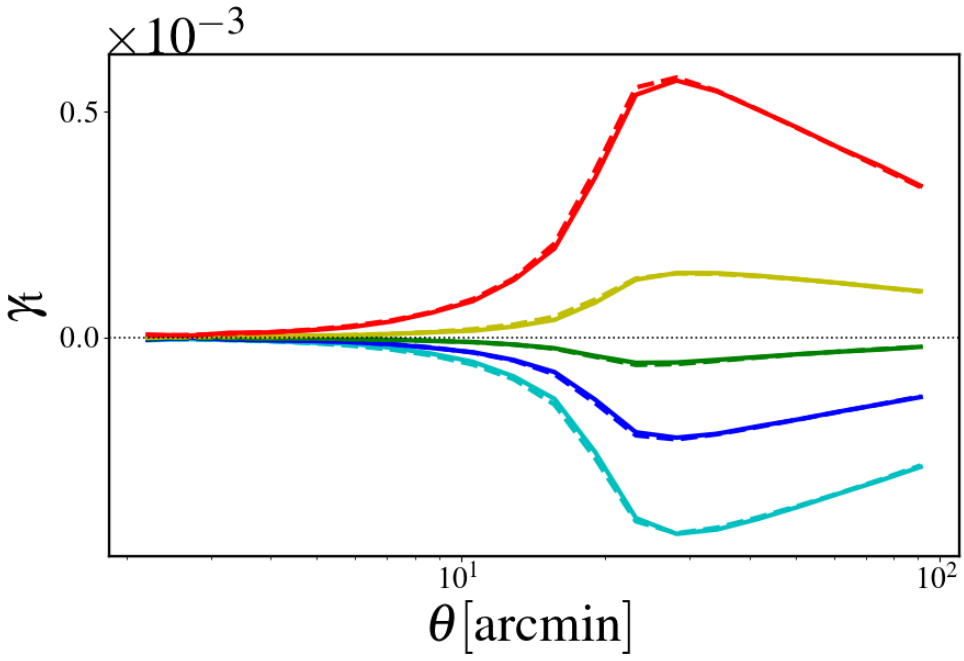

Figure 5.6 Shear quintiles (solid) of the all-sky Poisson mock with the DSS prediction of Friedrich et al. (2018) (dashed).

5.4 DSS with SLICS

Having confirmed my pipeline on an idealised test set in Section 5.3.1, I apply it to the SLICS mocks. I use the same 349 realisations as BD18 except using the SLICS LOWZ mock galaxies as the foreground sample rather than the GAMA mock galaxies. As we showed in BD18, the highest S/N from comes from a trough catalogue created using a circular aperture of $\theta_T = 5$ arcmin. However, in order to accurately compare my DSS measurement with the DSS prediction, I create a new catalogue with $\theta_T = 20$ since the perturbation theory prediction is inaccurate for apertures selected below this scale (Friedrich et al., 2018). Furthermore, unlike the all-sky Poisson sample, the SLICS lightcone only covers 100 deg^2. This means that some apertures at the edges will not fully overlap with the lightcone, inducing a bias in their number density that needs to be corrected for. To account for this bias, I use the effective area of each aperture as a masking criterion using only those apertures whose effective area is 1. This means that these apertures have no masks within them and are not located on the boundary of the lightcone. In essence, this creates a catalogue that resembles the same types of apertures as in Section 5.3.1, however with less apertures due to the difference in sky coverage. In order to minimize any overlap between the source and lens galaxy samples, I restrict the source galaxy selection to $\max(z)_{\rm lens} + \Delta z < z_{\rm B} < 0.9$ where $\Delta z = 0.1$ as per Amon et al. (2017) (see Section 4.3.3 for a discussion on the boost factor and the need for Δz), $z_{\rm B}$ is the photometric redshift of the source galaxies, and 0.9 is upper most reliability limit of the KiDS-450 redshift distribution (Hildebrandt et al., 2017).

To confirm the galaxy bias of the SLICS LOWZ sample, I measure the galaxy density as a function of the matter density. For this, I use the density maps of the four redshift bins from SLICS lightcone that correspond to the LOWZ redshift (see Section 4.1.1 for a discussion on the geometry of SLICS). Since the first and fourth redshift bin from SLICS extend beyond the redshift range of LOWZ (see Table 4.1), I weigh those two density maps by the fraction of overlapping volume between SLICS and LOWZ. Using these weighted maps, I combine them to construct an effective LOWZ matter density map. I then apply the procedure to calculate the galaxy number density described above, except on the total matter density maps. In essence, I take the average of the matter density contrast for each pixel within the lightcone. If the galaxies were populated as expected, the galaxy number density as a function of the total matter density should exhibit a bias of $b = 1.9$.

Fig. 5.7 shows the results of this test with 12 realisations for the fiducial case of $\theta_T = 20$ (upper panel) as well as the case where $\theta_T = 50$ (lower panel). From these plots one sees that the LOWZ HOD catalogues are constructed with a bias of $b = 1.9$ as expected (Harnois-Déraps et al., 2018). Since I know the cosmology of the SLICS mocks and have now confirmed the bias of the galaxy samples, I can compare the CIC histogram and shear profiles with the DSS prediction.

Figs. 5.8 & 5.9 show the CIC histogram and shear profiles for the 349 SLICS mock galaxy catalogues and the DSS prediction with $b = 1.9$ and SLICS cosmology (see Section 4.1.1). As Fig. 5.8 shows, the CIC histogram aligns well with the DSS prediction although a slight difference in the skewness between the SLICS mocks and prediction appears. This could be due to a scale-dependent galaxy bias. The shear profiles in Fig. 5.9 show good agreement between the SLICS mocks (solid lines) and prediction (dashed lines) with $\chi^2/\mathrm{dof} =$ 2.192, 0.490, 0.064, 0.240, and 3.682 from the lowest to highest density quintile. For the χ^2 estimation (Eq. 3.30), I use the mean γ_t from the SLICS realisations as the data vector and the DSS prediction as the model. The χ^2 estimation also takes into account the Hartlap factor (Hartlap et al., 2007), which de-biases the inverse of the covariance by taking into account the number of bins in the data vector and the number of simulation realisations used[3]. The larger χ^2 values at the extremes of the density spectrum are expected since the apertures that fall within the trough (ridge) quintile tend to exhibit stronger clustering at the centres of larger low (high) density regions as discussed in Section 5.2.3. The errorbars come from the diagonal of the covariance matrix shown in Fig. 5.10, which exhibit similar features to those seen in the BD18 analysis (lower panel of Fig. 5.2). Since I am making predictions for a LOWZ - KiDS-450 analysis, the errors are also scaled by an area factor,

$$f_{area} = \frac{100}{125}, \tag{5.10}$$

[3]It should be noted that the Hartlap factor fully removes the bias for an idealised case with Gaussian noise and independent data vectors. Since the quintiles are not independent data vectors, the reported χ^2 values are slightly underestimated.

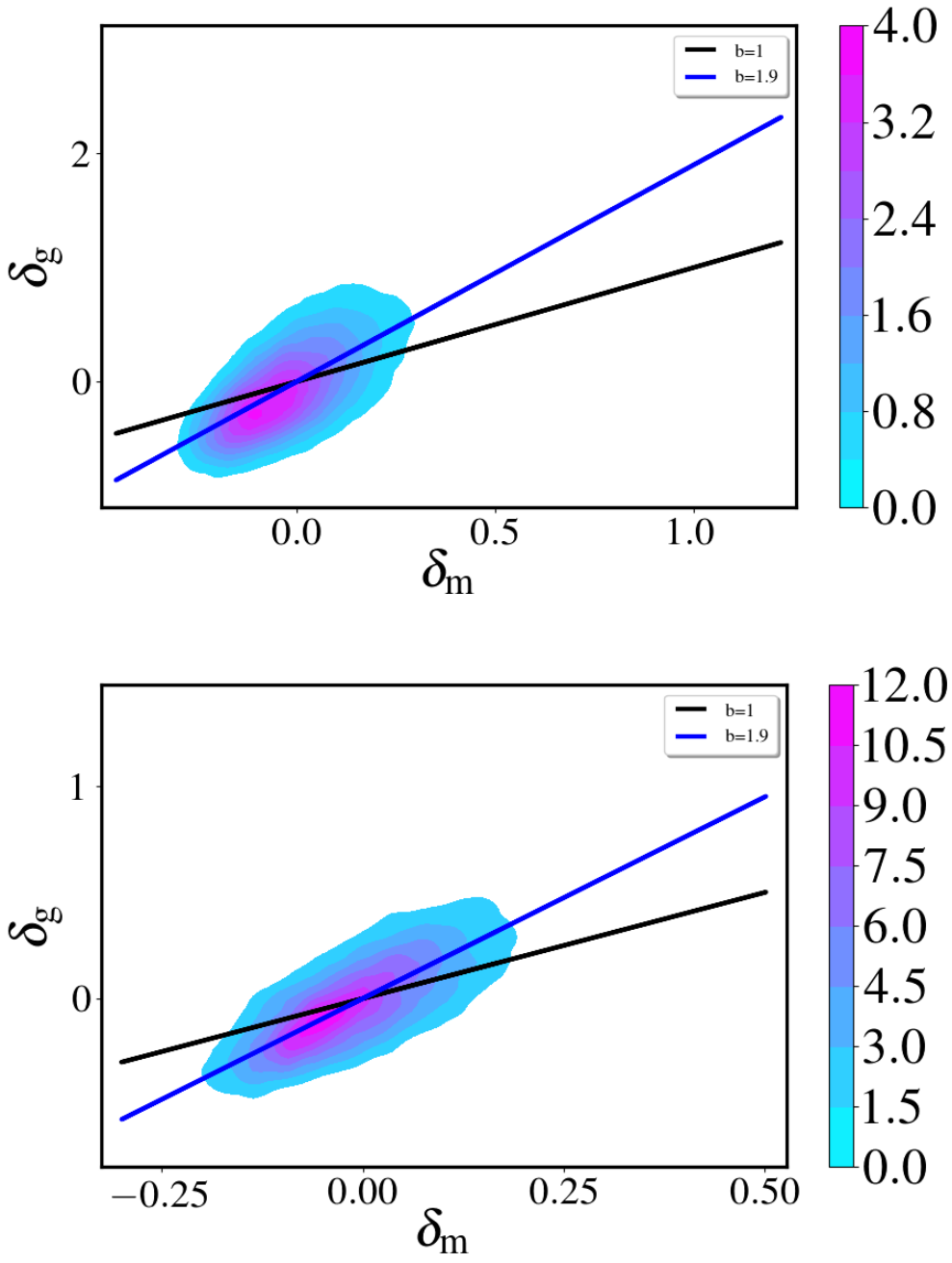

Figure 5.7 Galaxy density as a function of matter density for 12 LOS of LOWZ SLICS with an aperture of 20 (upper) and 50 (lower) arcmin. The colour scale indicates the the density of galaxies and the blue and black lines represent a bias model presented in the legend.

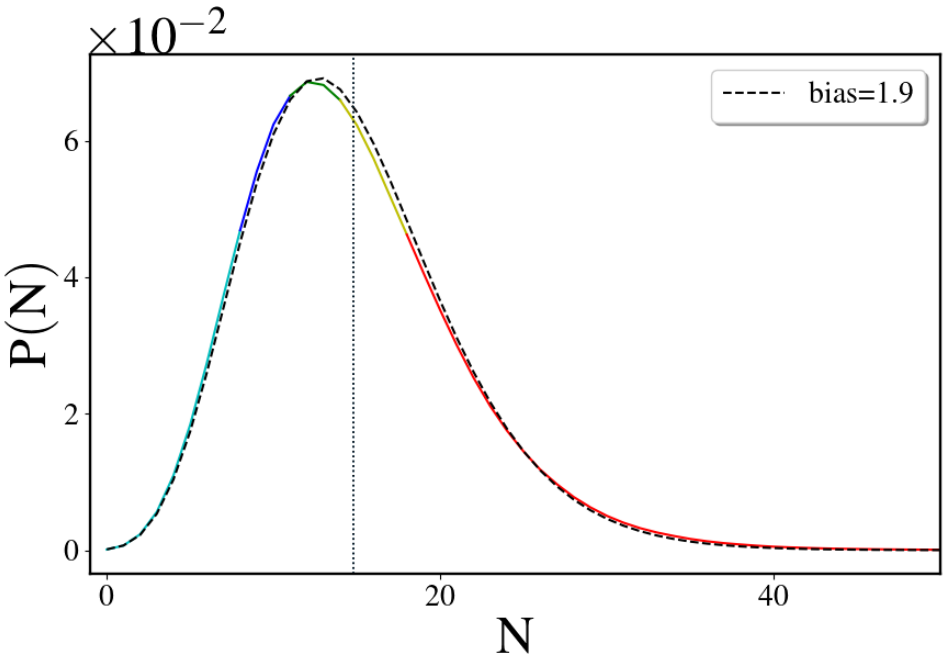

Figure 5.8 CIC histogram of a LOWZ SLICS mock with $b = 1.9$ from 349 LOS.

which takes into account the SLICS area relative to the effective overlap area between the LOWZ and KiDS-450 datasets (Amon et al., 2017).

I note that the errors in Fig. 5.9 are for a survey with 125 deg^2, however the measurement comes from the mean of 349 realisations, which equates to 34 900 deg^2. The fact that the DSS prediction does not match the measurement as well as in Fig. 5.6 suggests some limitations of the DSS model. To explore the validity of the DSS prediction as compared to the SLICS simulations, I explore $\Omega_\mathrm{m} - \sigma_8$ parameter space for the troughs and ridges and identify the cosmology for which the DSS prediction produces the minimum χ^2 value. To do this, I run predictions changing the DSS cosmology in the range of $\Omega_\mathrm{m} : [0.1, 0.5]$ and $\sigma_8 : [0.6, 1.2]$. I then calculate the χ^2 with Eq. 3.30 accounting for the Hartlap factor and area factor described above. I use the mean shear signal from the SLICS measurement as the data and the DSS prediction as the model. The covariance comes from the 349 SLICS realisations, with the area factor in Eq. 5.10 taken into account. As shown in upper panels of Fig. 5.11, the fiducial values for the SLICS simulation and the DSS prediction agree well, residing within the 68% Gaussian contours for both the troughs and ridges. I find that, as expected from the analysis of BD18, the ridges have tighter constraints due to a larger S/N. In the lower panels of Fig. 5.11, I explore the effects of removing data from scales of $\theta_T \leq 20$ arcmin. Friedrich et al. (2018) make these cuts in their analysis because they do not trust their modelling below these scales due to the accuracy of the density PDF and the assumption that the expected convergence within θ only depends on the total matter density contrast within θ_T. Furthermore, from Fig. 5.9, I note that the S/N begins to decrease on these scales, with shot noise increasing as progressively smaller scales are probed. Although the minimum χ^2

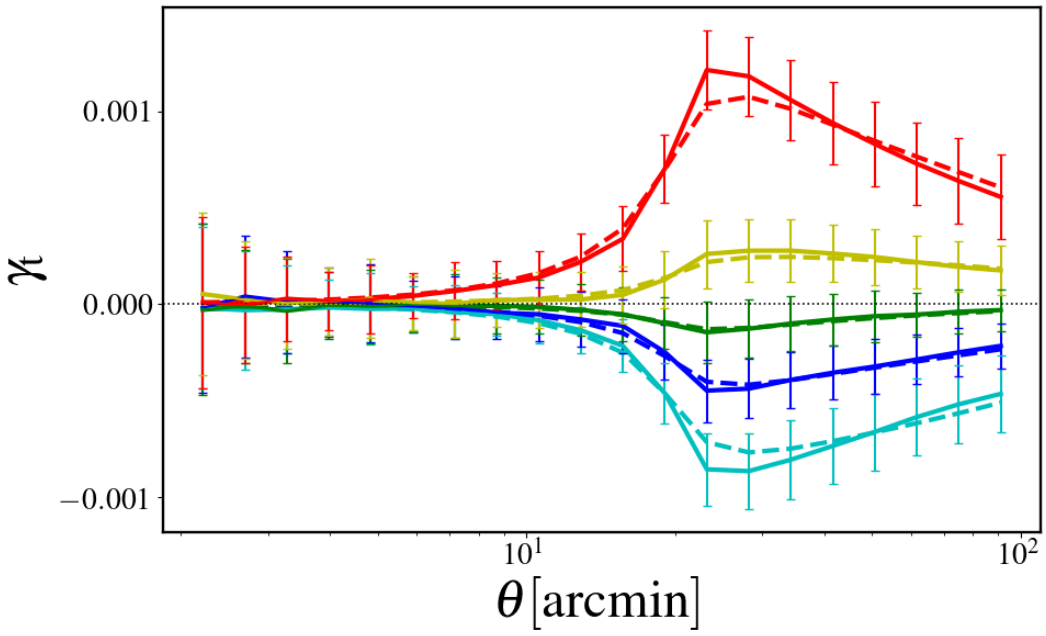

Figure 5.9 Shear quintiles of a LOWZ SLICS mock with $b = 1.9$ from 349 realisations. χ^2/dof values are 2.192, 0.490, 0.064, 0.240, and 3.682, from lowest to highest density quintiles.

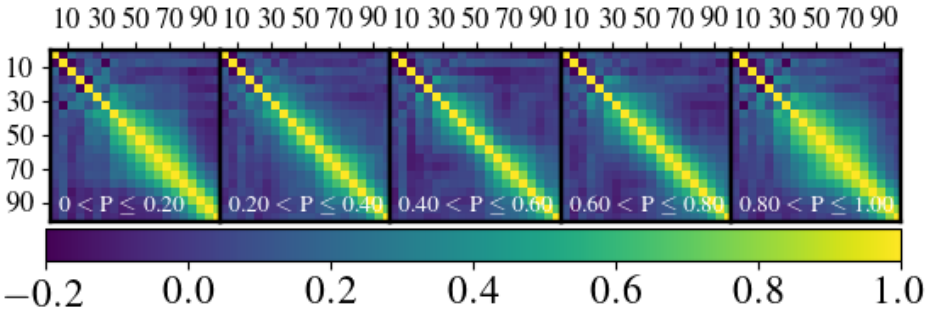

Figure 5.10 Covariance for quintiles of a LOWZ SLICS mock with $b = 1.9$ from 349 realisations.

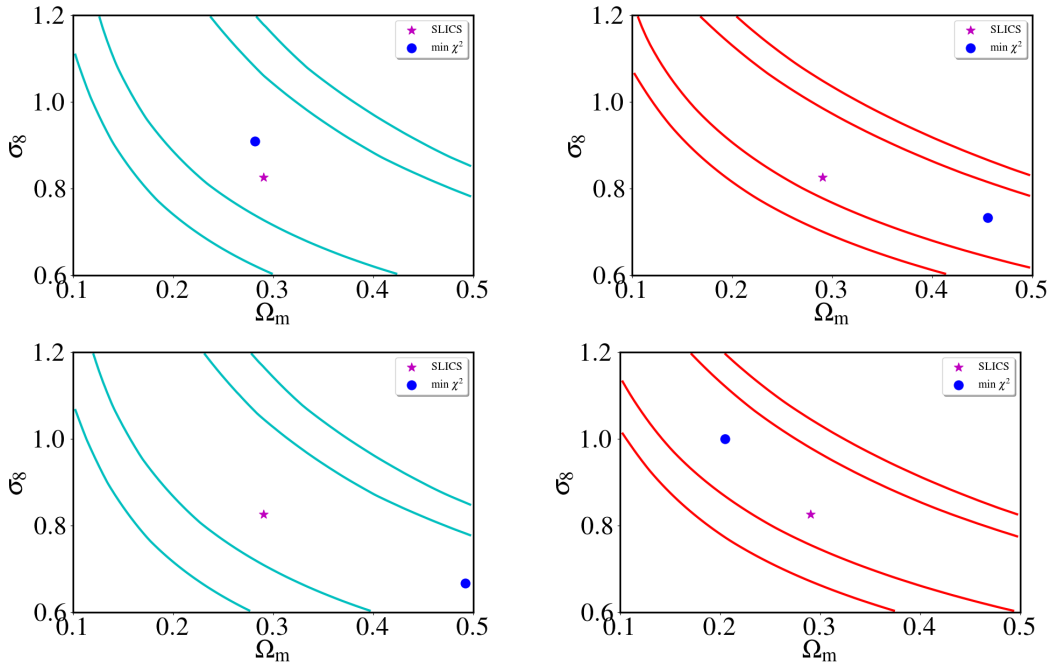

Figure 5.11 Constraints on the $\sigma_8 - \Omega_m$ plane using the SLICS LOWZ foreground sample and KiDS-450 source sample from 349 realisations. The left column is for the troughs and right column for the ridges. The first row shows the constraints from all scales, while the second row only uses scales of $\theta_T \geq 20$ arcmin. We do not see any significant change or bias in the contours from this scale cut. The contours represent 68% and 95% confidence intervals.

value shifts for both troughs and ridges, the shift is along the $\sigma_8 - \Omega_m$ degeneracy direction, so I do not consider it as an issue. Finding no significant differences by introducing cuts on the scales, in Fig. 5.12 I repeat this analysis, however applying an area factor of $f_{area} = \sqrt{\frac{100}{10000}}$ to the covariance to mimic an LSST-like sized survey. As expected, the contours shrink in size, with the SLICS fiducial cosmology lying on the curve of the 68% and 95% confidence interval for troughs and ridges, respectively. The lower panels of Fig. 5.12 shows that restricting the measurement to scales of $\theta_T \geq 20$ arcmin slightly shifts the contour for the ridges. Although the shift is along the degeneracy direction, one notices that the SLICS fiducial cosmology now lies on the 68% confidence interval rather than on the 95% confidence interval. Fig. 5.12 shows the power of increasing survey area for the DSS measurement, however for a more robust forecast, a thorough study with LSST mock source galaxies (e.g. Harnois-Déraps et al., 2018) would need to be executed.

These tests demonstrate the compatibility of the DSS model with the SLICS simulations. In the following section, I introduce the *cosmo*-SLICS simulations, which are extension to the SLICS, to test the DSS pipeline with non-ΛCDM cosmologies noting that from Figs. 5.9, 5.11, and 5.12 one sees that the DSS prediction works well for KiDS-450, but may be insufficient for a larger survey.

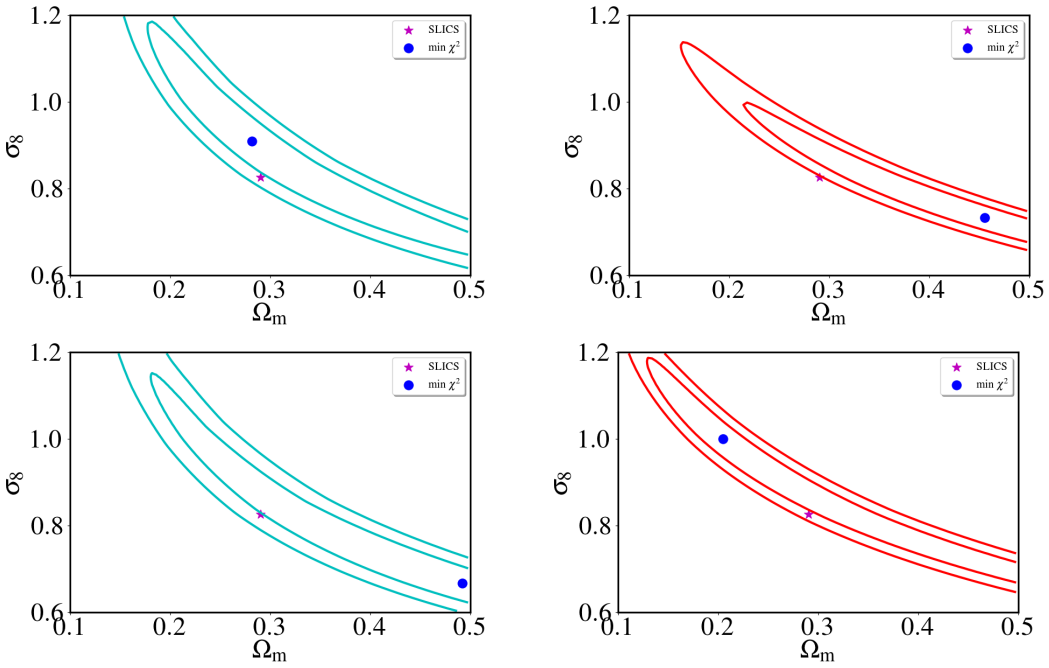

Figure 5.12 Same as Fig. 5.11 but with the covariance scaled to represent an LSST-like area *i.e.* 10 000 deg^2. We notice a slight shift in the contours along the degeneracy direction when making a scale cut of $\theta_T \geq 20$ arcmin. The contours represent 68% and 95% confidence intervals.

5.5 DSS with non-ΛCDM Simulations

5.5.1 The *cosmo*-SLICS Simulations

Having confirmed my pipeline and the DSS measurement on the SLICS mocks, I expand to the *cosmo*-SLICS simulation suite (Harnois-Déraps et al., 2019, HD19 hereafter) to test DSS's ability to predict the CIC histograms and shear profiles in wCDM cosmologies. The *cosmo*-SLICS simulations have the same global numerical setup (*i.e.* geometry, volume, and particle number) as the SLICS discussed in Section 4.1, however with a different underlying cosmology and covariance estimation. The primary science goal of these simulations is to provide simulations to execute alternative WL analyses of the KiDS, DES, HSC, and future WL surveys such as LSST and Euclid. These alternatives include beyond-2pt statistics analyses such as peaks statistics (e.g. Martinet et al., 2018), clipping (e.g. Giblin et al., 2018), bispectrum (e.g. Fu et al., 2014), and DSS (Brouwer et al., 2018; Gruen et al., 2018; Neyrinck et al., 2018). Considering the parameters of interest for a WL analysis, HD19 constructed *cosmo*-SLICS to model the parameters of $[\Omega_m, S_8, h, w_0]$. All other parameters such as n_s and Ω_b are fixed to the SLICS values. Fig. 5.13 shows the 26 (25 wCDM + 1 fiducial ΛCDM) cosmologies. From this figure, one sees that the choices of cosmological parameters broadly cover the range of parameter space without any preference

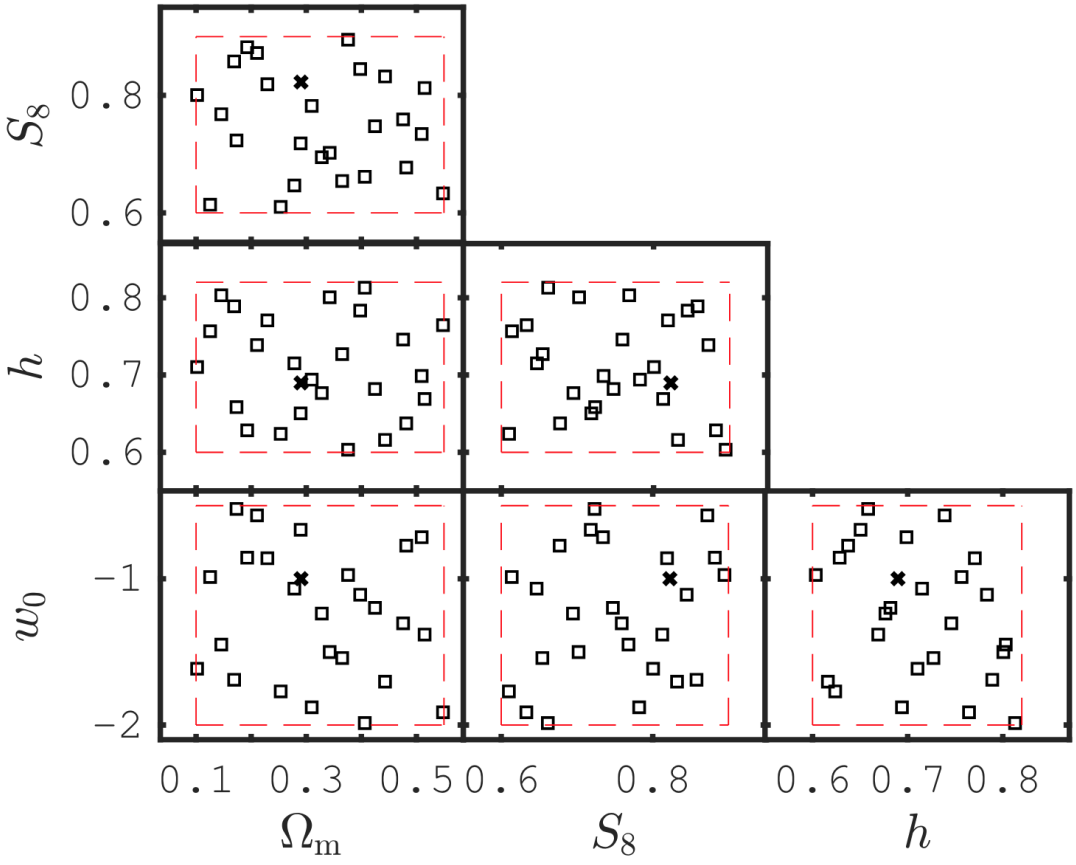

Figure 5.13 The nodes of the 4 parameters used for the *cosmo*-SLICS simulations. The black cross represents a ΛCDM cosmology. This plot is from Harnois-Déraps et al. (2019)

for a particular cosmology.

When choosing the cosmologies to explore, HD19 relied on the 2σ constraints of these four parameters from the KiDS-450 (Hildebrandt et al., 2017) and DES Y1 (Troxel et al., 2017) analyses. In order to select which sets of parameters to use for each cosmology, HD19 sample the four dimensional parameter space with a Latin Hypercube, which creates unique combinations of all four parameters, and then construct a Gaussian Process emulator to sample the space in between the 26 cosmologies. To ensure that the simulation sampling variance does not lead to mis-calibration, HD19 expand upon the matched pairs approach of Angulo and Pontzen (2016). They produce a pair of noise maps in which the sampling variance cancels almost entirely, such that the mean of any estimator extracted from the pair will be very close to the true ensemble mean. However, unlike the method presented in Angulo and Pontzen (2016), HD19 preserve Gaussianity in the initial density fields. To this end, HD19 follow two steps:

(i) Generate a large number of initial conditions at the fiducial ΛCDM cosmology, compute the mean power spectrum for all possible pair combinations, and finally select the pair whose mean is the closest to the theoretical

predictions, allowing a maximum of 5% residuals.

(ii) Demand that none of the pair members is a noise outlier, meaning that the fluctuations behave as Gaussian noise and scatter evenly across the theoretical power.

After constructing the matched pairs, the gravity solver CUBE^{3}PM (Harnois-Déraps et al., 2013) evolves the particles to $z = 0$ accounting for the background cosmology. A caveat of this matched-pairs approach is that it is only calibrated against 2pt functions and no mathematical proof exists to show that the sampling variance will cancel at the same level for higher-order statistics. Since this approach is relatively new, few studies exist to test its validity, however Villaescusa-Navarro et al. (2018) demonstrate that their matched-pair technique introduces no noticeable bias on the matter-matter, matter-halo, and halo-halo power spectra, nor on the halo mass function, void mass function, or matter PDF. HD19 then ray-trace 400 lightcones per simulation, creating a total of 800 *pseudo*-independent realisations of the lightcone for each matched pair to estimate the signal and covariance. The analysis in this thesis utilises only 50 realisations, since not all 800 are available yet for the full analysis. To test the accuracy of the covariance from the matched pair technique, HD19 compare it to 800 fully independent N-body realisations. Their analysis suggests that estimating the covariance matrix from *pseudo*-independent realisations using matched pairs is as accurate as one measured from fully independent realisations.

5.5.2 DSS with *cosmo*-SLICS

To test the DSS predictions capability with non-ΛCDM cosmologies, I use the *cosmo*-SLICS projected density maps and populate them with a $b = 1$ mock galaxy sample with a number density of $n_{\rm g} = 0.1\,{\rm gals/arcmin}^2$. I treat this galaxy sample as if it approximately spanned the LOWZ redshift range, meaning I use 4 redshift bins from the *cosmo*-SLICS lightcone geometry (see Fig. 4.4 for an example of the lightcone geometry) in the range of $0.15 \lesssim z \lesssim 0.43$. After populating the density maps with galaxies, I distribute the galaxies within each box using a R^3 distribution, where R refers to the lower and upper comoving distance of the box calculated from the redshift of the source planes (see Table 4.1 for an example). To properly account for the redshift-distance relation for each cosmology, I use the public `w0waCDM` module within PYTHON's `astropy.cosmology` numerical package. I call this type of galaxy foreground redshift distribution the 'saw-tooth' $n(z)$ and show the distribution of the $b = 1$ galaxies for the fiducial ΛCDM cosmology in the upper panel of Fig. 5.14. This panel shows that the density of galaxies increases as a function of R^3 per redshift bin, creating the saw-tooth distribution that I use for both the DSS pipeline and simulation measurements. The lower panel of Fig. 5.14 shows the source galaxy distribution for that same simulation cosmology. Unlike the SLICS simulations,

which based the source redshift distribution on the KiDS-450 analysis, *cosmo*-SLICS used the updated KiDS-VIKING-450 (KV450) (Hildebrandt et al., 2018) source redshift distribution. The KV450 dataset takes advantage of the extra infrared data from the VIKING survey (Edge et al., 2013) adding 5 more photometric bands to utilise for photometric redshift estimation. This allows Hildebrandt et al. (2018) to add a fifth tomographic bin, obtaining accurate photometric redshifts up to $z_{\rm B} = 1.2$, a significant improvement from the KiDS-450 limit of $z_{\rm B} = 0.9$. As discussed in Section 4.3.3, in order to minimise the effects of source-lens contamination (Amon et al., 2017), I add a buffer of $\Delta z = 0.1$ to the maximum lens redshift, which depends on the background cosmology. Therefore I select a source galaxy sample within the photometric redshift range $z_{{\rm max},c} + \Delta z < z_{\rm B} < 1.2$, where $z_{{\rm max},c}$ is the max lens redshift plane for cosmology c.

One aspect to consider is that since the box size used to create the lightcones has a fixed volume, this will vary the total number of redshift bins up to the final redshift, $z_{\rm max}$, due to the difference in the redshift-distance relation between cosmologies. Since the density maps for the *cosmo*-SLICS simulations are located at a single plane at the centre of box, this suggests that the 4 redshift bins I use to populate with galaxies will slightly vary between the cosmologies. The deviation in the comoving distance between cosmologies increases as a function of redshift, thus the largest offset occurs in the fourth bin. I find that the largest difference in the redshift amongst the box centres at which galaxies are populated is 28%. This may cause a slight difference in noise since each cosmology measurement will have a different number of source galaxies.

Having created the pipeline for a DSS measurement in a wCDM cosmology, I investigate the potential of the DSS methodology to distinguish between different cosmologies. To do this I use the procedures described in Section 5.4, applying them to the *cosmo*-SLICS with the exception that I use the noise-free shears of the source galaxies for this measurement. To concisely compare the agreement between *cosmo*-SLICS and the model of Friedrich et al. (2018), I use one radial bin per cosmology corresponding to the peak shear of the highest density quintile (ridges) and the absolute value of the peak shear of the lowest density quintile (troughs), which occurs at $\theta \approx 28$ arcmin. The reason I choose to focus on one data point rather than the full profile is as follows. As described in Gruen et al. (2016), the projected apertures on the sky overlap with one another and are thus highly correlated. In addition, the individual quintiles also exhibit a high degree of correlation. Furthermore, as shown in Fig. 5.9, the largest deviations between the DSS prediction (dashed lines) and the SLICS mocks (solid lines) occurs at the radial bin where the shear values peak with the largest discrepancies occurring in the lowest and highest density quintiles. Therefore, for the purposes of testing whether or not the DSS prediction yields reliable results when extended to wCDM, I choose to only use one radial bin corresponding to the peak shear values. Using both of the *cosmo*-SLICS seeds, I find the mean peak shear values for each cosmology and calculate the standard deviation across the 50 realisations. I then calculate the χ^2 between the *cosmo*-SLICS measurement and the DSS

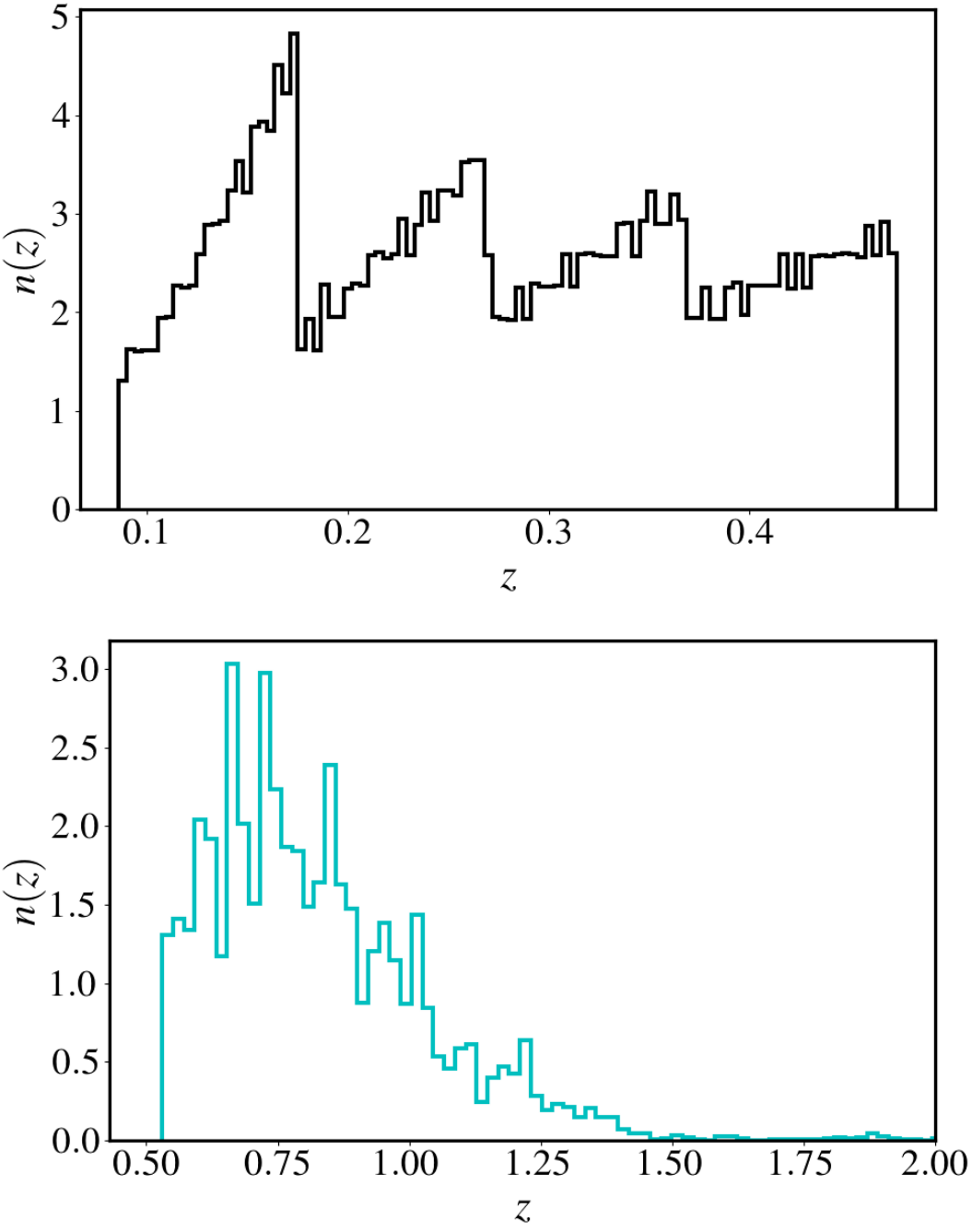

Figure 5.14 *Upper*: Redshift distribution of $b = 1$ galaxies for the fiducial ΛCDM cosmology of *cosmo*-SLICS with the saw-tooth distribution described in the text. *Lower*: Spectroscopic redshift distribution of KV450-like source galaxies from *cosmo*-SLICS selected within the redshift range $0.53 < z_{\rm B} < 1.2$.

prediction using,

$$\chi^2_{\rm peak} = \frac{(\gamma_{{\rm t},i}^{\rm mock} - \gamma_{{\rm t},i}^{\rm DSS})^2}{\sigma_i^2}, \tag{5.11}$$

where the i subscript refers to the quintile and σ_i is the error-on-the-mean from the 50 realisations for that particular cosmology.

I present my findings in the four panels of Fig. 5.15. The upper panels show the goodness of fit of the model to the *cosmo*-SLICS measurement for ridges (circles, upper left) and troughs (diamonds, upper right) in the $w_0 - S_8$ plane for all *cosmo*-SLICS cosmologies. I find good agreement between the *cosmo*-SLICS measurement and the DSS pipeline as indicated by the χ^2 values in the colorbar. The lower panels of Fig. 5.15 show the peak shear values for the ridges (circles, lower left) and peak of the absolute shear values for the troughs (diamonds, lower right). In both of the lower panels, one sees a clear trend for the shear to increase as a function of S_8 with higher peak values for the ridges than the troughs. This agrees well with our understanding of the shear amplitude increasing as clustering of galaxies increases as well as the asymmetry in the shear amplitudes between the lowest and highest density quintiles (Friedrich et al., 2018; Gruen et al., 2018; Brouwer et al., 2018). I find that the largest difference in shear amplitudes amongst the cosmologies is $\sim 67\%$ for the ridges and $\sim 92\%$ for the troughs. This suggests that, despite having a lower S/N, underdense regions can differentiate between cosmologies better than overdense regions for wCDM cosmologies. I discuss a potential cause for this in Section 5.6.

Having confirmed that the DSS pipeline and the *cosmo*-SLICS agree well and that substantial differences in the quintile shears exist amongst the cosmologies, I continue to a mock analysis in order explore the constraining power of DSS in wCDM cosmologies. To do this, I arbitrarily choose the '00' *cosmo*-SLICS cosmology with $\Omega_{\rm m} = 0.3282$, $S_8 = 0.6984$, $h = 0.6766$, and $w_0 = -1.2376$ as my fiducial test case. I then use the DSS prediction pipeline to create 400 predictions on a grid in the $w_0 - S_8$ plane and calculate the χ^2 (Eq. 3.30), locating the cosmology with the minimum χ^2. For the model vector, I use the average $\gamma_{\rm t}$ signal from all 50 realisations per quintile bin, which I also use for the covariance, taking into account the Hartlap factor and scaling it by the KiDS-450 - LOWZ overlap area (Eq. 5.10)[4]. Since from my analysis on the SLICS mocks (Fig. 5.9) I know that the lowest and highest density quintiles exhibit the largest deviations from the DSS prediction, I limit the analysis to only those quintiles. Fig. 5.16 shows the constraints for the lowest/highest density quintiles (troughs/ridges). The contours show the 68% and 95% confidence intervals with a Gaussian assumption for the errors. From this figure, I notice several aspects. The first noteworthy feature is the size and shape of the contours between the troughs and ridges. I find that the constraints from troughs have a slight rotation in the $w_0 - S_8$ degeneracy

[4]Technically, this area factor is negligible since I don't include shape noise in the measurement, but I include it to remain consitent with the analysis conducted on the SLICS.

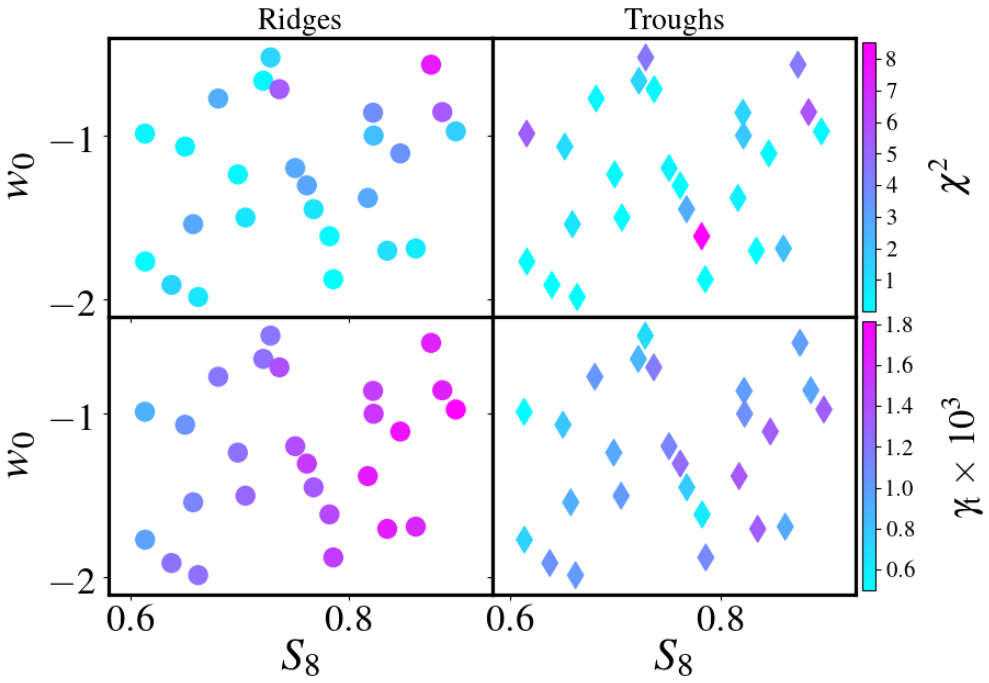

Figure 5.15 *Upper Left*: Ridges χ^2. *Upper Right*: Troughs χ^2. *Lower Left*: Ridges γ_t. *Lower Right*: Troughs γ_t. All panels use the combined 50 realisations from the two seeds.

as compared to the ridges. This clock-wise rotation resembles the constraints from cosmic shear (e.g. Joudaki et al., 2017). I also notice that, despite having a lower S/N, troughs have a higher constraining power as compared to ridges denoted by the noticeably smaller contours. This is the opposite of the SLICS analysis shown in Fig. 5.11 and I provide a possible explanation for this in Section 5.6.

However, I also see that the '00' cosmology lies outside the 68% confidence interval of the minimum χ^2 value. To investigate the cause of this offset, in Fig. 5.17 I show the *cosmo*-SLICS measurements for the '00' cosmology (solid; DSS-00), the DSS prediction for that cosmology (dashed), and the DSS prediction for the cosmology of the minimum χ^2 (dotted; DSS-$\chi^2_{\rm min}$) for both troughs (cyan) and ridges (red). At first glance, I see that the DSS-00 prediction and *cosmo*-SLICS measurement agree much better than the measurement and the DSS-$\chi^2_{\rm min}$ prediction. However, upon a closer investigation of Fig. 5.17 I realise that the DSS-$\chi^2_{\rm min}$ and the *cosmo*-SLICS measurement agree very well on scales of $\theta \lesssim 20$ arcmin. I note that, unlike the shear measurement for the LOWZ SLICS mocks in Fig. 5.9, the measurement in Fig. 5.17 has no shot noise or intrinsic shape noise, which underestimates the errors. For a large survey, such as LSST, this may be a reasonable assumption. Since the errors for the troughs are smaller and the agreement with the DSS-$\chi^2_{\rm min}$ is slightly better as compared to the ridges, I understand why the $\chi^2_{\rm min}$ cosmology for the troughs deviates from the '00' cosmology in Fig. 5.16. To test my assumption as to whether or not these small scales are the culprit, I only use scales of $\theta > 20$ arcmin for constraints in the

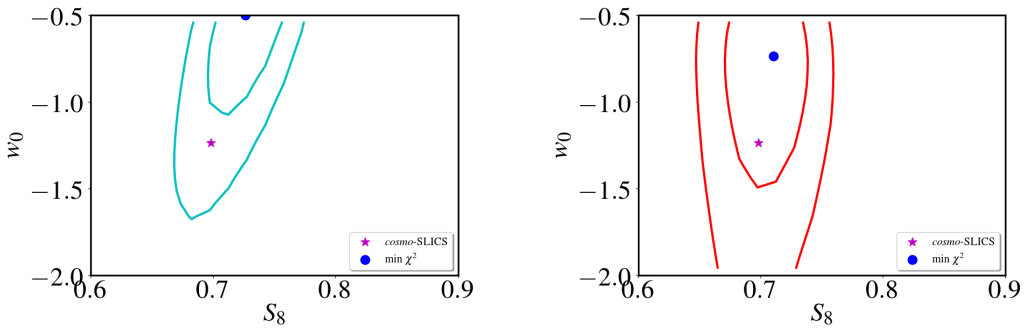

Figure 5.16 Constraints for the '00' *cosmo*-SLICS cosmology in the $w_0 - S_8$ plane for troughs (left) and for ridges (right). The magenta star shows the value for the '00' cosmology while the blue dot shows the minimum χ^2 value and the contours represent 68% and 95% confidence intervals.

$w_0 - S_8$ plane as done in Section 5.4. Fig. 5.18 shows that by removing the scales within the projected aperture, the $\chi^2_{\rm min}$ cosmology is within the 68% confidence interval of the '00' cosmology for both troughs and ridges. By excluding the small scales, Fig. 5.18 shows that I completely remove any constraining power on w_0, however the precision of the constraints from troughs still surpasses that of the ridges. This test confirms that an analysis using DSS for wCDM cosmologies will indeed work, but in order to quantify how well it will work, I need to include an estimate of the expected shot and shape noise in the covariance. As shown in Fig. 5.9, including shot and shape noise will increase the errors on $\theta \lesssim 20$ arcmin since the number of galaxies on those scales decreases. Since my goal for this analysis is to test the accuracy of the DSS pipeline on wCDM cosmologies, I leave a full cosmological analysis with accurate shape noise for future work. In the next section, I summarise my findings and discuss the future of DSS.

5.6 Discussion and the Future of DSS

In the previous sections, I have demonstrated that we can extend the DSS methodology to beyond-ΛCDM cosmologies. I have also shown the constraints on w_0 and S_8 using the shear profiles for the lowest and highest density quintiles in an idealised, noise-free setting. Using the *cosmo*-SLICS mocks, I show that, despite having a lower S/N, the variation in the peak shear value of the lowest density quintiles exceeds that of the highest density quintiles, indicating that these underdensities could have a stronger constraining power on cosmology. To demonstrate this, I chose an arbitrary *cosmo*-SLICS cosmology and conducted a mock analysis on the lowest and highest density quintiles showing that the lowest quintiles do indeed yield tighter constraints in the $w_0 - S_8$ plane. It may seem odd that a lower S/N measurement can produce tighter constraints, however one can understand this behaviour by referring back to the concepts discussed in Chapter 3. In that chapter we explored the dynamics of expansion for cosmic voids. Recall

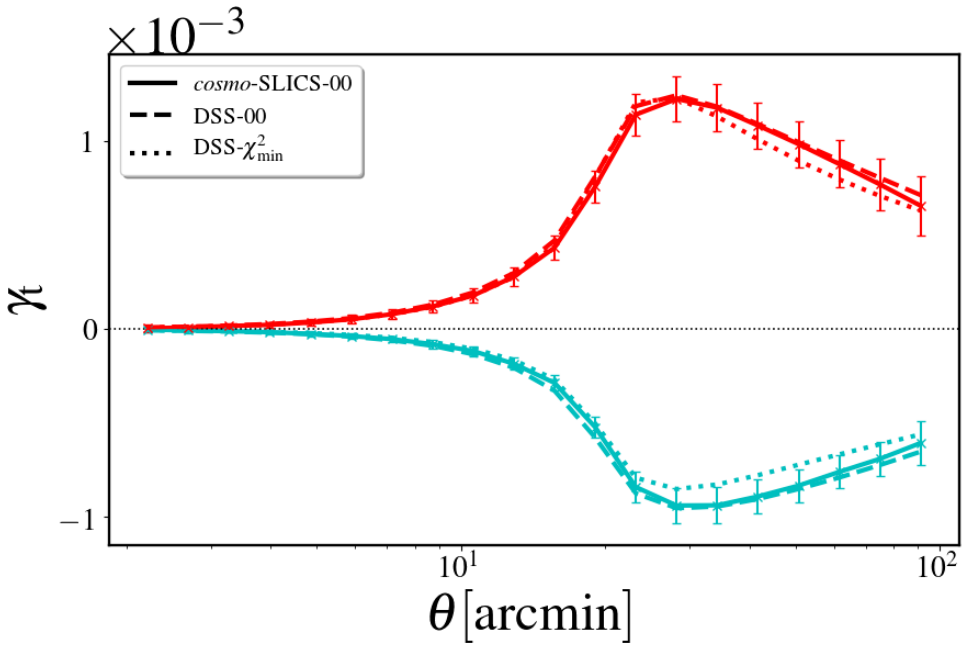

Figure 5.17 Shear measurement from 50 realisations of the *cosmo*-SLICS '00' cosmology (solid) for troughs (cyan) and ridges (red) compared to the DSS pipeline prediction for the '00' cosmology (dashed) and the cosmology of the minimum χ^2 (dotted). We see that for scales of $\theta \lesssim 20$ the measurement seems to agree better with the of the minimum χ^2. The errorbars are the diagonal of the covariance from the 50 realisations scaled by the KiDS-450-LOWZ overlap area (Eq. 5.10).

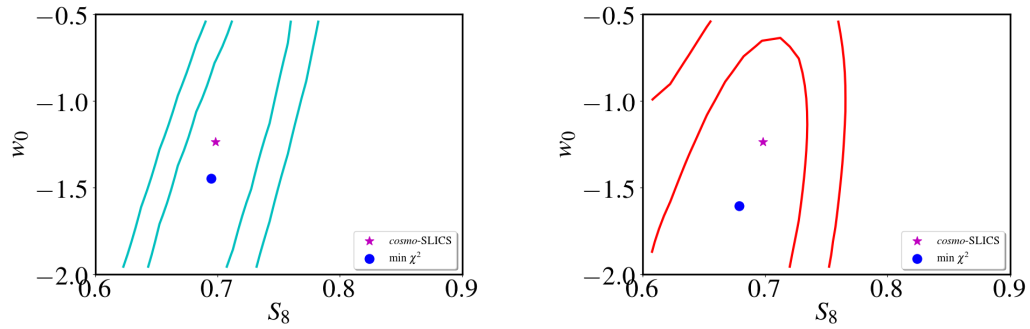

Figure 5.18 Constraints for the '00' *cosmo*-SLICS cosmology in the $w_0 - S_8$ plane for troughs (left) and for ridges (right) only using scales of $\theta > 20$ arcmin. The magenta star shows the value for the '00' cosmology while the blue dot shows the minimum χ^2 value and the contours represent 68% and 95% confidence intervals.

that the evolution equation (Eq. 3.8) essentially depends on two components: the matter term and the expansion term. As we decrease the amount of matter, the dark energy term dominates the dynamics. This suggests that underdense regions such as voids and the projected troughs are more sensitive to changes in dark energy as compared to their overdense counterparts. Thus, as we vary the present-day equation-of-state, w_0, the effects of this variation will manifest more prominently in the underdense regions of the Universe. I do note that to conduct a proper analysis and fully quantify the difference in the constraining power between troughs and ridges, I need to include realistic shape noise to the lensing measurement. This will indeed increase the size of the contours, but it will also alleviate the slight discrepancy between the minimum χ^2 and the expected value in Fig. 5.16. In addition, when the *cosmo*-SLICS suite increases from having 50 publicly available realisations per cosmology to 800, we will have the means to combine all quintiles into one data vector and calculate an accurate, invertible covariance, rather than relying on a single data point as I have done. Furthermore, to fully take advantage of the DSS method, I can also include the CIC histogram to the data vector and fully exploit the power of DSS. Gruen et al. (2018) showed how DSS can provide competitive constraints on cosmological parameters and galaxy bias when compared to the standard 3×2pt approach used by most WL surveys today. As the precision of our surveys increases, our analyses will need to have the capability to explore cosmologies beyond the standard ΛCDM paradigm. Using the *cosmo*-SLICS mocks, I have shown that the DSS pipeline presented by Friedrich et al. (2018) has this capability.

However the future of DSS extends beyond the examination of non-ΛCDM cosmologies. As shown in BD18, tomographically splitting the foreground galaxy sample could potentially constrain the evolution of troughs and ridges to significant precision. By furthering the analysis of BD18 to include the CIC histogram, *i.e.* conducting the full DSS analysis, this evolution could be identified to a higher degree. This could then provide crucial information on the evolution of galaxy bias as well as the growth rate of structure. Although the DSS approach has the advantage of not needing a spectroscopic foreground sample, to preform the most accurate DSS evolution analysis, we would need a spectroscopic galaxy redshift survey that overlaps with a WL survey as discussed in Section 3.9.1. As future spectroscopic galaxy redshift surveys and WL surveys increase their overlap area, we could broaden the capabilities of the DSS by combining it with my pipeline for measuring non-linear RSD (see Chapter 3) and conduct a density-dependent RSD analysis (Achitouv and Cai, 2018). This would allow us to effectively measure the growth rate in any density region with a fully non-linear model rather than limiting scales or relying upon linear modelling. Implementing a more accurate bias model presents another potential for the future of DSS. As discussed in Section 5.4, the offset for the extreme density regions between the SLICS measurement and the DSS prediction in Fig. 5.9 could arise due to a scale-dependent bias. Incorporating a scale-dependent bias (e.g. Simon and Hilbert, 2018) into the DSS formalism could increase the robustness of the model. Another future aspect of DSS is its compatibility with the 3×2pt approach for

WL. Since DSS technically only utilises one of the three 2pt statistics, namely GGL, one could consider combining DSS with galaxy clustering and cosmic shear to create a data vector that mixes both 2pt and 3pt statistics. One of the main difficulties for such an analysis would be obtaining an accurate covariance for this data vector. However, throughout this thesis, I have shown that simulations such as the SLICS and *cosmo*-SLICS have the capacity to provide an accurate covariance. Future, larger simulations would facilitate such a measurement that will surely provide the most precise cosmological constraints from WL to date.

The truth is simple. If it were complicated, everyone would understand it.

Walt Whitman

6 Conclusion

6.1 Overview

This thesis began with an overview of cosmology up the the present day, with a particular focus on the role played by the vast, underdense regions known as cosmic voids. Section 1.8 presented a historical overview of voids as a cosmological probe, followed by an overview of the seminal void evolution model of Sheth and van de Weygaert (2004), finishing off with a discussion of how voids function as a complementary probe for cosmology. In particular, I discussed how voids can be an effective tool to test theories of modified gravity through weak gravitational lensing, examined through the lens of redshift-space distortions to understand the growth rate of structure, and applied to the Alcock-Paczyński test. Interestingly enough, these three topics are fundamentally related such that progress in one, fuels progress in the others. Namely, I discussed how a combination of weak lensing and RSDs can help to constrain cosmological parameters and that the efficiency of the AP test depends on an accurate understanding of the RSD signal. One of the hindrances for present-day cosmologists is our capabilities to model information in the non-linear regimes. In an attempt to alleviate this hindrance, I began the work presented in this thesis with the goal of improving the modelling of void evolution for a more accurate analysis of large-scale structure through a combination of weak gravitational lensing and redshift-space distortions.

In the beginning of this journey, I focused on expanding upon the work of Sheth and van de Weygaert (2004) by extending the spherical void evolution model to ΛCDM and non-ΛCDM cosmologies (Chapter 3). I then applied this model, particularly the non-linear peculiar velocity profiles that it generates, to

predict fully non-linear RSDs around voids, using them to constrain cosmological parameters utilising information from all scales, including the non-linear regime. One advantageous feature of this approach is its simplicity, requiring only a late-time density profile. To this end, I delved into an analysis of extracting a weak lensing signal from voids using the spectroscopic galaxy redshift survey, GAMA, and an overlapping weak lensing survey, KiDS. With the aid of the SLICS simulation suite, I concluded that although extracting a weak lensing signal from voids identified in GAMA is possible, due to the survey geometry and relatively small overlap area, the measurement of the observational data is too noisy to yield any significant results (Chapter 4). With upcoming surveys that have a larger overlap between weak lensing and galaxy redshift surveys, a void lensing signal will indeed be possible, however, while we wait for those surveys to collect data, we can exploit the information contained within projected underdensities. Thus my journey took a detour from 3D voids to measure the weak lensing signal of projected underdensities known as troughs (Chapter 5). I further extended that analysis to include projected apertures that span the full density spectrum rather than only focusing on the underdense regions. Conveniently, Friedrich et al. (2018) created a model that combined the weak lensing signal from these projected apertures with a counts-in-cells methodology, coining this 3pt analysis as Density Split Statistics. In the vein of exploring the possibility of this method to predict measurements in non-ΛCDM cosmologies and to place constraints on cosmological parameters, I extended the DSS method to wCDM cosmologies with the *cosmo*-SLICS simulation suite, showing that the DSS model provides a good representation of the simulated data when extended to the wCDM regime.

The work in this thesis arrives at an important time in cosmology. As the precision of our observations increases, we require models that can accurately probe the non-linear regime to fully exploit observational data and make progressively meaningful claims about the constitution of our Universe. As a field, cosmology has tended to focus on the overdense regions of our Universe, with little attention paid to the vast emptiness occupying majority of the volume. However, over the past several decades, the cosmologists have begun to explore the underdense regions with more enthusiasm, realising that these regions can provide us with crucial, complementary information regarding modified gravity, dark energy, and neutrinos.

6.2 Future Outlook and Speculations

Throughout the duration of this thesis, the void community has made a significant amount of progress in exploiting underdense regions. Of particular interest is the advent of troughs and DSS (Gruen et al., 2016; Brouwer et al., 2018; Friedrich et al., 2018), measurement of RSDs around voids (Hamaus et al., 2017; Nadathur et al., 2019b), and the effect of massive neutrinos on void dynamics and evolution (Kreisch et al., 2018), although this is far from an exhaustive list. As our ability to extract information from overdensities begins to reach its limit due to advances

of modelling, the complementary, underdense regions will play a more significant role in furthering our knowledge of the Universe. Understanding and modelling non-linear regimes is the most pressing theoretical hurdle, which would allow us to extract information from a broader range of scales from upcoming large missions such as DESI[1], LSST[2], SPHEREx[3], Euclid[4], and WFIRST[5]. Although, I have shown that we currently cannot extract a weak lensing signal around voids using a spectroscopic foreground sample, this will become possible with larger spectroscopic surveys overlapping with weak lensing surveys. Voids are prime cosmological objects to probe for dark energy, study environment-dependent galaxy evolution, and test for deviations from general relativity, key science goals for upcoming surveys.

In an Astro2020 Science White Paper (Pisani et al., 2019), we present a case for allocating more observational resources aimed at optimising void science. One of the reasons observational void science has yet to reach its full potential is because it requires a survey with a large volume and large tracer density. Although some of the aforementioned surveys will improve the potential for void science, an amendment to the WFIRST survey strategy to consider extensions of the WFIRST high redshift spectroscopic program would complement spectroscopic surveys at low redshift. The combination of a large volume with the powerful imaging capabilities from WFIRST will fuel void science to an unprecedented level.

The contents of this thesis have the potential to improve cosmological measurements and shed light on fundamental aspect of our Universe. To conclude, I present a few of my personal thoughts about the future of cosmology:

It certainly is an exciting time in astrophysics and cosmology. During the duration of my Ph.D., not only were gravitational waves detected, but several weeks before the completion of this thesis, the Event Horizon Telescope revealed the first image of a black hole! I believe that the limitations of the next decade or so will be due to a lack of theoretical models explaining the physics on non-linear scales, for which we would need larger hydrodynamical simulations to aid theoretical progress. In terms of discoveries, I believe that pinning down the hierarchy and mass of neutrinos will manifest as the next major breakthrough in cosmology. Dark matter is not far behind, although I am unsure as to what kind of particle it will be (or if it's even a particle at all!). Although our observations seem to suggest that ΛCDM is the fundamental cosmology of our Universe, could we as a community be stuck in a massive confirmation bias? Until theorists concoct robust explanations surrounding the issues of ΛCDM discussed at the beginning of this thesis, I will remain a healthy sceptic of the model. Observing primordial B-modes will help support the theory of inflation, which will solidify ΛCDM, and may be possible

[1]https://www.desi.lbl.gov/
[2]https://www.lsst.org/
[3]http://spherex.caltech.edu/
[4]https://www.euclid-ec.org/
[5]https://wfirst.gsfc.nasa.gov/

with Stage IV CMB surveys. Regarding the $\sim 2\sigma$ 'tension' between the weak lensing measurements and the CMB, I believe that it's due to a combination of statistical fluctuations and systematic effects from both sides. I look forward to higher constraining power from lensing surveys to see if the tension persists, but that requires some ingenuity regarding our statistical analyses. I personally hope that the tension is indeed real and that present-day probes are detecting some sort of deviation from ΛCDM, but only time will tell. Overall, interest in cosmology keeps increasing and I believe the power of the main surveys of the 2020s, coupled with the brilliance of the scientists behind them, will yield more groundbreaking discoveries sooner than later. After all, Max Planck was initially discouraged from pursuing physics since his advisor, Philipp von Jolly, thought that 'all that remains is to fill a few unimportant holes.' I think we all know how that story ended.

And with that, dear distinguished reader, I thank you for letting me indulge you in some of my scientific musings and I bid you to be well wherever your journey may lead you in this wondrous Universe of ours.

Bibliography

Abbott, B. P., Abbott, R., Abbott, T. D., Abernathy, M. R., Acernese, F., Ackley, K., Adams, C., Adams, T., Addesso, P., Adhikari, R. X., and et al. (2016). Observation of Gravitational Waves from a Binary Black Hole Merger. , 116:061102.

Abbott, B. P., Abbott, R., Abbott, T. D., Acernese, F., Ackley, K., Adams, C., Adams, T., Addesso, P., Adhikari, R. X., Adya, V. B., and et al. (2017). Multi-messenger Observations of a Binary Neutron Star Merger. *ApJ*, 848:L12.

Acernese, F., Agathos, M., Agatsuma, K., Aisa, D., Allemandou, N., Allocca, A., Amarni, J., Astone, P., Balestri, G., Ballardin, G., Barone, F., Baronick, J. P., Barsuglia, M., Basti, A., Basti, F., Bauer, T. S., Bavigadda, V., Bejger, M., Beker, M. G., Belczynski, C., Bersanetti, D., Bertolini, A., Bitossi, M., Bizouard, M. A., Bloemen, S., Blom, M., Boer, M., Bogaert, G., Bondi, D., Bondu, F., Bonelli, L., Bonnand, R., Boschi, V., Bosi, L., Bouedo, T., Bradaschia, C., Branchesi, M., Briant, T., Brillet, A., Brisson, V., Bulik, T., Bulten, H. J., Buskulic, D., Buy, C., Cagnoli, G., Calloni, E., Campeggi, C., Canuel, B., Carbognani, F., Cavalier, F., Cavalieri, R., Cella, G., Cesarini, E., Chassande-Mottin, E., Chincarini, A., Chiummo, A., Chua, S., Cleva, F., Coccia, E., Cohadon, P. F., Colla, A., Colombini, M., Conte, A., Coulon, J. P., Cuoco, E., Dalmaz, A., D'Antonio, S., Dattilo, V., Davier, M., Day, R., Debreczeni, G., Degallaix, J., Deléglise, S., Del Pozzo, W., Dereli, H., De Rosa, R., Di Fiore, L., Di Lieto, A., Di Virgilio, A., Doets, M., Dolique, V., Drago, M., Ducrot, M., Endrőczi, G., Fafone, V., Farinon, S., Ferrante, I., Ferrini, F., Fidecaro, F., Fiori, I., Flaminio, R., Fournier, J. D., Franco, S., Frasca, S., Frasconi, F., Gammaitoni, L., Garufi, F., Gaspard, M., Gatto, A., Gemme, G., Gendre, B., Genin, E., Gennai, A., Ghosh, S., Giacobone, L., Giazotto, A., Gouaty, R., Granata, M., Greco, G., Groot, P., Guidi, G. M., Harms, J., Heidmann, A., Heitmann, H., Hello, P., Hemming, G., Hennes, E., Hofman, D., Jaranowski, P., Jonker, R. J. G., Kasprzack, M., Kéfélian, F., Kowalska, I., Kraan, M., Królak, A., Kutynia, A., Lazzaro, C., Leonardi, M., Leroy, N., Letendre, N., Li, T. G. F., Lieunard, B., Lorenzini, M., Loriette, V., Losurdo, G., Magazzù, C., Majorana, E., Maksimovic, I., Malvezzi, V., Man, N., Mangano, V., Mantovani, M., Marchesoni, F., Marion, F., Marque, J., Martelli, F., Martellini, L., Masserot, A., Meacher, D., Meidam, J., Mezzani, F., Michel, C., Milano, L., Minenkov, Y., Moggi, A., Mohan, M., Montani, M., Morgado, N., Mours, B., Mul, F., Nagy, M. F., Nardecchia, I., Naticchioni,

L., Nelemans, G., Neri, I., Neri, M., Nocera, F., Pacaud, E., Palomba, C., Paoletti, F., Paoli, A., Pasqualetti, A., Passaquieti, R., Passuello, D., Perciballi, M., Petit, S., Pichot, M., Piergiovanni, F., Pillant, G., Piluso, A., Pinard, L., Poggiani, R., Prijatelj, M., Prodi, G. A., Punturo, M., Puppo, P., Rabeling, D. S., Rácz, I., Rapagnani, P., Razzano, M., Re, V., Regimbau, T., Ricci, F., Robinet, F., Rocchi, A., Rolland, L., Romano, R., Rosińska, D., Ruggi, P., Saracco, E., Sassolas, B., Schimmel, F., Sentenac, D., Sequino, V., Shah, S., Siellez, K., Straniero, N., Swinkels, B., Tacca, M., Tonelli, M., Travasso, F., Turconi, M., Vajente, G., van Bakel, N., van Beuzekom, M., van den Brand, J. F. J., Van Den Broeck, C., van der Sluys, M. V., van Heijningen, J., Vasúth, M., Vedovato, G., Veitch, J., Verkindt, D., Vetrano, F., Viceré, A., Vinet, J. Y., Visser, G., Vocca, H., Ward, R., Was, M., Wei, L. W., Yvert, M., Zadro żny, A., and Zendri, J. P. (2015). Advanced Virgo: a second-generation interferometric gravitational wave detector. *Classical and Quantum Gravity*, 32(2):024001.

Achitouv, I. (2017). An improved model of redshift-space distortions around voids: application to quintessence dark energy. *ArXiv e-prints*.

Achitouv, I. and Blake, C. (2015). Improving reconstruction of the baryon acoustic peak: The effect of local environment. *Physical Review D*, 92(8):083523.

Achitouv, I., Blake, C., Carter, P., Koda, J., and Beutler, F. (2017). Consistency of the growth rate in different environments with the 6-degree Field Galaxy Survey: Measurement of the void-galaxy and galaxy-galaxy correlation functions. *Physical Review D*, 95(8):083502.

Achitouv, I. and Cai, Y.-C. (2018). Modeling the environmental dependence of the growth rate of cosmic structure. *Physical Review D*, 98:103502.

Ahmed, S. N., Anthony, A. E., Beier, E. W., Bellerive, A., Biller, S. D., Boger, J., Boulay, M. G., Bowler, M. G., Bowles, T. J., Brice, S. J., Bullard, T. V., Chan, Y. D., Chen, M., Chen, X., Cleveland, B. T., Cox, G. A., Dai, X., Dalnoki-Veress, F., Doe, P. J., Dosanjh, R. S., Doucas, G., Dragowsky, M. R., Duba, C. A., Duncan, F. A., Dunford, M., Dunmore, J. A., Earle, E. D., Elliott, S. R., Evans, H. C., Ewan, G. T., Farine, J., Fergani, H., Fleurot, F., Formaggio, J. A., Fowler, M. M., Frame, K., Fulsom, B. G., Gagnon, N., Graham, K., Grant, D. R., Hahn, R. L., Hall, J. C., Hallin, A. L., Hallman, E. D., Hamer, A. S., Handler, W. B., Hargrove, C. K., Harvey, P. J., Hazama, R., Heeger, K. M., Heintzelman, W. J., Heise, J., Helmer, R. L., Hemingway, R. J., Hime, A., Howe, M. A., Jagam, P., Jelley, N. A., Klein, J. R., Kos, M. S., Krumins, A. V., Kutter, T., Kyba, C. C., Labranche, H., Lange, R., Law, J., Lawson, I. T., Lesko, K. T., Leslie, J. R., Levine, I., Luoma, S., MacLellan, R., Majerus, S., Mak, H. B., Maneira, J., Marino, A. D., McCauley, N., McDonald, A. B., McGee, S., McGregor, G., Mifflin, C., Miknaitis, K. K., Miller, G. G., Moffat, B. A., Nally, C. W., Nickel, B. G., Noble, A. J., Norman, E. B., Oblath, N. S., Okada, C. E., Ollerhead, R. W., Orrell, J. L., Oser, S. M., Ouellet, C., Peeters, S. J., Poon, A. W., Robertson, B. C., Robertson, R. G., Rollin, E.,

Rosendahl, S. S., Rusu, V. L., Schwendener, M. H., Simard, O., Simpson, J. J., Sims, C. J., Sinclair, D., Skensved, P., Smith, M. W., Starinsky, N., Stokstad, R. G., Stonehill, L. C., Tafirout, R., Takeuchi, Y., Tešić, G., Thomson, M., Thorman, M., van Berg, R., van de Water, R. G., Virtue, C. J., Wall, B. L., Waller, D., Waltham, C. E., Tseung, H. W., Wark, D. L., West, N., Wilhelmy, J. B., Wilkerson, J. F., Wilson, J. R., Wouters, J. M., Yeh, M., and Zuber, K. (2004). Measurement of the Total Active ^{8}B Solar Neutrino Flux at the Sudbury Neutrino Observatory with Enhanced Neutral Current Sensitivity. *Physical Review Letters*, 92(18):181301.

Aiola, S., Kosowsky, A., and Wang, B. (2015). Gaussian approximation of peak values in the integrated Sachs-Wolfe effect. *PRD*, 91(4):043510.

Alam, S., Albareti, F. D., Allende Prieto, C., Anders, F., Anderson, S. F., Anderton, T., Andrews, B. H., Armengaud, E., Aubourg, É., Bailey, S., and et al. (2015). The Eleventh and Twelfth Data Releases of the Sloan Digital Sky Survey: Final Data from SDSS-III. *ApJS*, 219:12.

Alam, S., Ata, M., Bailey, S., Beutler, F., Bizyaev, D., Blazek, J. A., Bolton, A. S., Brownstein, J. R., Burden, A., Chuang, C.-H., Comparat, J., Cuesta, A. J., Dawson, K. S., Eisenstein, D. J., Escoffier, S., Gil-Marín, H., Grieb, J. N., Hand, N., Ho, S., Kinemuchi, K., Kirkby, D., Kitaura, F., Malanushenko, E., Malanushenko, V., Maraston, C., McBride, C. K., Nichol, R. C., Olmstead, M. D., Oravetz, D., Padmanabhan, N., Palanque-Delabrouille, N., Pan, K., Pellejero-Ibanez, M., Percival, W. J., Petitjean, P., Prada, F., Price-Whelan, A. M., Reid, B. A., Rodríguez-Torres, S. A., Roe, N. A., Ross, A. J., Ross, N. P., Rossi, G., Rubiño-Martín, J. A., Saito, S., Salazar-Albornoz, S., Samushia, L., Sánchez, A. G., Satpathy, S., Schlegel, D. J., Schneider, D. P., Scóccola, C. G., Seo, H.-J., Sheldon, E. S., Simmons, A., Slosar, A., Strauss, M. A., Swanson, M. E. C., Thomas, D., Tinker, J. L., Tojeiro, R., Magaña, M. V., Vazquez, J. A., Verde, L., Wake, D. A., Wang, Y., Weinberg, D. H., White, M., Wood-Vasey, W. M., Yèche, C., Zehavi, I., Zhai, Z., and Zhao, G.-B. (2017a). The clustering of galaxies in the completed SDSS-III Baryon Oscillation Spectroscopic Survey: cosmological analysis of the DR12 galaxy sample. *MNRAS*, 470:2617–2652.

Alam, S., Miyatake, H., More, S., Ho, S., and Mandelbaum, R. (2017b). Testing gravity on large scales by combining weak lensing with galaxy clustering using CFHTLenS and BOSS CMASS. *MNRAS*, 465:4853–4865.

Alarcon, A., Eriksen, M., and Gaztanaga, E. (2018). Cosmological constraints from multiple tracers in spectroscopic surveys. *MNRAS*, 473:1444–1460.

Alcock, C., Allsman, R. A., Alves, D. R., Axelrod, T. S., Becker, A. C., Bennett, D. P., Cook, K. H., Dalal, N., Drake, A. J., Freeman, K. C., Geha, M., Griest, K., Lehner, M. J., Marshall, S. L., Minniti, D., Nelson, C. A., Peterson, B. A., Popowski, P., Pratt, M. R., Quinn, P. J., Stubbs, C. W., Sutherland, W., Tomaney, A. B., Vand ehei, T., and Welch, D. (2000). The MACHO Project: Microlensing Results from 5.7 Years of Large Magellanic Cloud Observations. *ApJ*, 542:281–307.

Alcock, C. and Paczynski, B. (1979). An evolution free test for non-zero cosmological constant. *Nature*, 281:358.

Alpher, R. A. and Herman, R. (1948). Evolution of the Universe. , 162:774–775.

Amendola, L., Frieman, J. A., and Waga, I. (1999). Weak gravitational lensing by voids. *MNRAS*, 309:465–473.

Amon, A., Heymans, C., Klaes, D., Erben, T., Blake, C., Hildebrandt, H., Hoekstra, H., Kuijken, K., Miller, L., Morrison, C. B., Choi, A., de Jong, J. T. A., Glazebrook, K., Irissari, N., Joachimi, B., Joudaki, S., Kannawadi, A., Lidman, C., Napolitano, N., Parkinson, D., Schneider, P., van Uitert, E., Viola, M., and Wolf, C. (2017). KiDS-i-800: Comparing weak gravitational lensing measurements in same-sky surveys. *ArXiv e-prints*.

Angulo, R. E. and Pontzen, A. (2016). Cosmological N-body simulations with suppressed variance. *MNRAS*, 462:L1–L5.

Aragon-Calvo, M. A. and Szalay, A. S. (2013). The hierarchical structure and dynamics of voids. *MNRAS*, 428:3409–3424.

Bacon, D. J., Goldberg, D. M., Rowe, B. T. P., and Taylor, A. N. (2006). Weak gravitational flexion. *MNRAS*, 365:414–428.

Bacon, D. J., Refregier, A. R., and Ellis, R. S. (2000). Detection of weak gravitational lensing by large-scale structure. *MNRAS*, 318:625–640.

Bagla, J. S. (2002). TreePM: A Code for Cosmological N-Body Simulations. *Journal of Astrophysics and Astronomy*, 23:185–196.

Baker, T., Bellini, E., Ferreira, P. G., Lagos, M., Noller, J., and Sawicki, I. (2017). Strong Constraints on Cosmological Gravity from GW170817 and GRB 170817A. , 119:251301.

Baker, T., Clampitt, J., Jain, B., and Trodden, M. (2018). Void lensing as a test of gravity. *Physical Review D*, 98(2):023511.

Baldry, I. K., Liske, J., Brown, M. J. I., Robotham, A. S. G., Driver, S. P., Dunne, L., Alpaslan, M., Brough, S., Cluver, M. E., Eardley, E., Farrow, D. J., Heymans, C., Hildebrandt, H., Hopkins, A. M., Kelvin, L. S., Loveday, J., Moffett, A. J., Norberg, P., Owers, M. S., Taylor, E. N., Wright, A. H., Bamford, S. P., Bland-Hawthorn, J., Bourne, N., Bremer, M. N., Colless, M., Conselice, C. J., Croom, S. M., Davies, L. J. M., Foster, C., Grootes, M. W., Holwerda, B. W., Jones, D. H., Kafle, P. R., Kuijken, K., Lara-Lopez, M. A., López-Sánchez, Á. R., Meyer, M. J., Phillipps, S., Sutherland, W. J., van Kampen, E., and Wilkins, S. M. (2018). Galaxy And Mass Assembly: the G02 field, Herschel-ATLAS target selection and data release 3. *MNRAS*, 474:3875–3888.

Banerjee, A. and Dalal, N. (2016). Simulating nonlinear cosmological structure formation with massive neutrinos. , 11:015.

Bardeen, J. M., Bond, J. R., Kaiser, N., and Szalay, A. S. (1986). The statistics of peaks of gaussian random fields. *Astrophysical Journal*, 304:15–61.

Barreira, A., Cautun, M., Li, B., Baugh, C. M., and Pascoli, S. (2015). Weak lensing by voids in modified lensing potentials. *JCAP*, 8:028.

Bartelmann, M. (2010). TOPICAL REVIEW Gravitational lensing. *Classical and Quantum Gravity*, 27:233001.

Bartelmann, M. and Schneider, P. (2001). Weak gravitational lensing. *Physics Reports*, 340:291–472.

Begeman, K., Belikov, A. N., Boxhoorn, D. R., and Valentijn, E. A. (2013). The Astro-WISE datacentric information system. *Experimental Astronomy*, 35:1–23.

Behroozi, P. S., Wechsler, R. H., and Wu, H.-Y. (2013). The ROCKSTAR Phase-space Temporal Halo Finder and the Velocity Offsets of Cluster Cores. *ApJ*, 762:109.

Benítez, N. (2000). Bayesian Photometric Redshift Estimation. *ApJ*, 536:571–583.

Berlin, A., Hooper, D., Krnjaic, G., and McDermott, S. D. (2018). Severely Constraining Dark-Matter Interpretations of the 21-cm Anomaly. , 121(1):011102.

Bernstein, G. M. (2010). Shape measurement biases from underfitting and ellipticity gradients. *MNRAS*, 406:2793–2804.

Bernstein, G. M. and Cai, Y.-C. (2011). Cosmology without cosmic variance. *MNRAS*, 416:3009–3016.

Bernstein, G. M. and Jarvis, M. (2002). Shapes and Shears, Stars and Smears: Optimal Measurements for Weak Lensing. *AJ*, 123:583–618.

Bertin, E. and Arnouts, S. (1996). SExtractor: Software for source extraction. *AAPS*, 117:393–404.

Bertschinger, E. (1985). The self-similar evolution of holes in an Einstein-de Sitter universe. *ApJS*, 58:1–37.

Beutler, F., Blake, C., Colless, M., Jones, D. H., Staveley-Smith, L., Poole, G. B., Campbell, L., Parker, Q., Saunders, W., and Watson, F. (2012). The 6dF Galaxy Survey: z 0 measurements of the growth rate and σ_8. *MNRAS*, 423:3430–3444.

Beutler, F., Saito, S., Brownstein, J. R., Chuang, C.-H., Cuesta, A. J., Percival, W. J., Ross, A. J., Ross, N. P., Schneider, D. P., Samushia, L., Sánchez, A. G., Seo, H.-J., Tinker, J. L., Wagner, C., and Weaver, B. A. (2014). The clustering of galaxies in the SDSS-III Baryon Oscillation Spectroscopic Survey: signs of neutrino mass in current cosmological data sets. *MNRAS*, 444:3501–3516.

Bilicki, M., Hoekstra, H., Brown, M. J. I., Amaro, V., Blake, C., Cavuoti, S., de Jong, J. T. A., Georgiou, C., Hildebrandt, H., Wolf, C., Amon, A., Brescia, M., Brough, S., Costa-Duarte, M. V., Erben, T., Glazebrook, K., Grado, A., Heymans, C., Jarrett, T., Joudaki, S., Kuijken, K., Longo, G., Napolitano, N., Parkinson, D., Vellucci, C., Verdoes Kleijn, G. A., and Wang, L. (2018). Photometric redshifts for the Kilo-Degree Survey. Machine-learning analysis with artificial neural networks. *AAP*, 616:A69.

Bird, S., Cholis, I., Muñoz, J. B., Ali-Haïmoud, Y., Kamionkowski, M., Kovetz, E. D., Raccanelli, A., and Riess, A. G. (2016). Did ligo detect dark matter? *Phys. Rev. Lett.*, 116:201301.

Blake, C., Baldry, I. K., Bland-Hawthorn, J., Christodoulou, L., Colless, M., Conselice, C., Driver, S. P., Hopkins, A. M., Liske, J., Loveday, J., Norberg, P., Peacock, J. A., Poole, G. B., and Robotham, A. S. G. (2013). Galaxy And Mass Assembly (GAMA): improved cosmic growth measurements using multiple tracers of large-scale structure. *MNRAS*, 436:3089–3105.

Blanton, M. R., Bershady, M. A., Abolfathi, B., Albareti, F. D., Allende Prieto, C., Almeida, A., Alonso-García, J., Anders, F., Anderson, S. F., Andrews, B., and et al. (2017). Sloan Digital Sky Survey IV: Mapping the Milky Way, Nearby Galaxies, and the Distant Universe. *AJ*, 154:28.

Blazek, J., Vlah, Z., and Seljak, U. (2015). Tidal alignment of galaxies. , 8:015.

Blumenthal, G. R., da Costa, L. N., Goldwirth, D. S., Lecar, M., and Piran, T. (1992). The largest possible voids. *The Astrophysical Journal*, 388:234–241.

Bolton, A. S., Schlegel, D. J., Aubourg, É., Bailey, S., Bhardwaj, V., Brownstein, J. R., Burles, S., Chen, Y.-M., Dawson, K., Eisenstein, D. J., Gunn, J. E., Knapp, G. R., Loomis, C. P., Lupton, R. H., Maraston, C., Muna, D., Myers, A. D., Olmstead, M. D., Padmanabhan, N., Pâris, I., Percival, W. J., Petitjean, P., Rockosi, C. M., Ross, N. P., Schneider, D. P., Shu, Y., Strauss, M. A., Thomas, D., Tremonti, C. A., Wake, D. A., Weaver, B. A., and Wood-Vasey, W. M. (2012). Spectral Classification and Redshift Measurement for the SDSS-III Baryon Oscillation Spectroscopic Survey. *AJ*, 144:144.

Bond, J. R., Cole, S., Efstathiou, G., and Kaiser, N. (1991). Excursion set mass functions for hierarchical gaussian fluctuations. *The Astrophysical Journal*.

Bond, J. R., Kofman, L., and Pogosyan, D. (1996). How filaments of galaxies are woven into the cosmic web. *Nature*, 380:603–606.

Bonnett, C., Troxel, M. A., Hartley, W., Amara, A., Leistedt, B., Becker, M. R., Bernstein, G. M., Bridle, S. L., Bruderer, C., Busha, M. T., Carrasco Kind, M., Childress, M. J., Castander, F. J., Chang, C., Crocce, M., Davis, T. M., Eifler, T. F., Frieman, J., Gangkofner, C., Gaztanaga, E., Glazebrook, K., Gruen, D., Kacprzak, T., King, A., Kwan, J., Lahav, O., Lewis, G., Lidman, C., Lin, H., MacCrann, N., Miquel, R., O'Neill, C. R., Palmese, A., Peiris,

H. V., Refregier, A., Rozo, E., Rykoff, E. S., Sadeh, I., Sánchez, C., Sheldon, E., Uddin, S., Wechsler, R. H., Zuntz, J., Abbott, T., Abdalla, F. B., Allam, S., Armstrong, R., Banerji, M., Bauer, A. H., Benoit-Lévy, A., Bertin, E., Brooks, D., Buckley-Geer, E., Burke, D. L., Capozzi, D., Carnero Rosell, A., Carretero, J., Cunha, C. E., D'Andrea, C. B., da Costa, L. N., DePoy, D. L., Desai, S., Diehl, H. T., Dietrich, J. P., Doel, P., Fausti Neto, A., Fernandez, E., Flaugher, B., Fosalba, P., Gerdes, D. W., Gruendl, R. A., Honscheid, K., Jain, B., James, D. J., Jarvis, M., Kim, A. G., Kuehn, K., Kuropatkin, N., Li, T. S., Lima, M., Maia, M. A. G., March, M., Marshall, J. L., Martini, P., Melchior, P., Miller, C. J., Neilsen, E., Nichol, R. C., Nord, B., Ogando, R., Plazas, A. A., Reil, K., Romer, A. K., Roodman, A., Sako, M., Sanchez, E., Santiago, B., Smith, R. C., Soares- Santos, M., Sobreira, F., Suchyta, E., Swanson, M. E. C., Tarle, G., Thaler, J., Thomas, D., Vikram, V., Walker, A. R., and Dark Energy Survey Collaboration (2016). Redshift distributions of galaxies in the Dark Energy Survey Science Verification shear catalogue and implications for weak lensing. *Physical Review D*, 94:042005.

Born, M. (1926). Quantenmechanik der Stoßvorgänge. *Zeitschrift fur Physik*, 38:803–827.

Bos, E. G. P., van de Weygaert, R., Dolag, K., and Pettorino, V. (2012). The darkness that shaped the void: dark energy and cosmic voids. *MNRAS*, 426:440–461.

Bridle, S., Shawe-Taylor, J., Amara, A., Applegate, D., Balan, Berge, J. S. T., Bernstein, G., Dahle, H., Erben, T., Gill, M., Heavens, A., Heymans, C., High, F. W., Hoekstra, H., Jarvis, M., Kirk, D., Kitching, T., Kneib, J.-P., Kuijken, K., Lagatutta, D., Mandelbaum, R., Massey, R., Mellier, Y., Moghaddam, B., Moudden, Y., Nakajima, R., Paulin-Henriksson, S., Pires, S., Rassat, A., Refregier, A., Rhodes, J., Schrabback, T., Semboloni, E., Shmakova, M., van Waerbeke, L., Witherick, D., Voigt, L., and Wittman, D. (2009). Handbook for the GREAT08 Challenge: An image analysis competition for cosmological lensing. *Annals of Applied Statistics*, 3:6–37.

Bridle, S. L., Kneib, J.-P., Bardeau, S., and Gull, S. F. (2002). Bayesian Galaxy Shape Estimation. In Natarajan, P., editor, *The Shapes of Galaxies and their Dark Halos*, pages 38–46.

Brouwer, M. M., Demchenko, V., Harnois-Déraps, J., Bilicki, M., Heymans, C., Hoekstra, H., Kuijken, K., Alpaslan, M., Brough, S., Cai, Y.-C., Costa-Duarte, M. V., Dvornik, A., Erben, T., Hildebrandt, H., Holwerda, B. W., Schneider, P., Sifón, C., and van Uitert, E. (2018). Studying galaxy troughs and ridges using weak gravitational lensing with the Kilo-Degree Survey. *MNRAS*, 481:5189–5209.

Bullock, J. S., Kolatt, T. S., Sigad, Y., Somerville, R. S., Kravtsov, A. V., Klypin, A. A., Primack, J. R., and Dekel, A. (2001). Profiles of dark haloes: evolution, scatter and environment. *MNRAS*, 321:559–575.

Cabré, A., Vikram, V., Zhao, G.-B., Jain, B., and Koyama, K. (2012). Astrophysical tests of gravity: a screening map of the nearby universe. , 7:034.

Cacciato, M., van den Bosch, F. C., More, S., Mo, H., and Yang, X. (2013). Cosmological constraints from a combination of galaxy clustering and lensing - III. Application to SDSS data. *MNRAS*, 430:767–786.

Cai, Y.-C. and Bernstein, G. (2012). Combining weak-lensing tomography and spectroscopic redshift surveys. *MNRAS*, 422:1045–1056.

Cai, Y.-C., Neyrinck, M., Mao, Q., Peacock, J. A., Szapudi, I., and Berlind, A. A. (2017). The lensing and temperature imprints of voids on the cosmic microwave background. *MNRAS*, 466:3364–3375.

Cai, Y.-C., Neyrinck, M. C., Szapudi, I., Cole, S., and Frenk, C. S. (2014). A Possible Cold Imprint of Voids on the Microwave Background Radiation. *APJ*, 786:110.

Cai, Y.-C., Padilla, N., and Li, B. (2015). Testing gravity using cosmic voids. *MNRAS*, 451:1036–1055.

Cai, Y.-C., Taylor, A., Peacock, J. A., and Padilla, N. (2016). Redshift-space distortions around voids. *MNRAS*, 462:2465–2477.

Caldwell, R. R., Dave, R., and Steinhardt, P. J. (1998). Cosmological Imprint of an Energy Component with General Equation of State. , 80:1582–1585.

Capaccioli, M., Schipani, P., de Paris, G., Grado, A., Napolitano, N., Iodice, E., Marconi, M., Merluzzi, P., and Ripepi, V. (2012). VST: the VLT Survey Telescope. VST: An Overview. In *Science from the Next Generation Imaging and Spectroscopic Surveys*, page 1.

Carlson, J., Reid, B., and White, M. (2013). Convolution Lagrangian perturbation theory for biased tracers. *MNRAS*, 429:1674–1685.

Catelan, P., Kamionkowski, M., and Blandford, R. D. (2001). Intrinsic and extrinsic galaxy alignment. *MNRAS*, 320:L7–L13.

Cautun, M., Cai, Y.-C., and Frenk, C. S. (2015). The view from the boundary: a new void stacking method. *ArXiv e-prints*.

Cautun, M., Paillas, E., Cai, Y.-C., Bose, S., Armijo, J., Li, B., and Padilla, N. (2018). The Santiago-Harvard-Edinburgh-Durham void comparison - I. SHEDding light on chameleon gravity tests. *MNRAS*, 476:3195–3217.

Ceccarelli, L., Ruiz, A. N., Lares, M., Paz, D. J., Maldonado, V. E., Luparello, H. E., and Garcia Lambas, D. (2016). The sparkling Universe: a scenario for cosmic void motions. *MNRAS*, 461:4013–4021.

Chiba, T., Okabe, T., and Yamaguchi, M. (2000). Kinetically driven quintessence. *Phys. Rev. D*, 62:023511.

Chincarini, G. (1978). Clumpy structure of the universe and general field. , 272:515.

Chincarini, G. and Rood, H. J. (1980). The cosmic tapestry. *Sky and Telescope*, 59:364–371.

Clampitt, J., Cai, Y.-C., and Li, B. (2013). Voids in modified gravity: excursion set predictions. *MNRAS*, 431:749–766.

Clampitt, J. and Jain, B. (2015). Lensing measurements of the mass distribution in SDSS voids. *MNRAS*, 454:3357–3365.

Clifton, T., Ferreira, P. G., Padilla, A., and Skordis, C. (2012). Modified gravity and cosmology. *Physics Reports*, 513:1–189.

Clowe, D., Gonzalez, A., and Markevitch, M. (2004). Weak-Lensing Mass Reconstruction of the Interacting Cluster 1E 0657-558: Direct Evidence for the Existence of Dark Matter. *ApJ*, 604:596–603.

Colberg, J. M., Pearce, F., Foster, C., Platen, E., Brunino, R., Neyrinck, M., Basilakos, S., Fairall, A., Feldman, H., Gottlöber, S., Hahn, O., Hoyle, F., Müller, V., Nelson, L., Plionis, M., Porciani, C., Shandarin, S., Vogeley, M. S., and van de Weygaert, R. (2008). The Aspen-Amsterdam void finder comparison project. *MNRAS*, 387:933–944.

Cole, S., Fisher, K. B., and Weinberg, D. H. (1994). Fourier Analysis of Redshift Space Distortions and the Determination of Omega. *MNRAS*, 267:785.

Colless, M., Peterson, B. A., Jackson, C., Peacock, J. A., Cole, S., Norberg, P., Baldry, I. K., Baugh, C. M., and et al. (2003). The 2dF Galaxy Redshift Survey: Final Data Release. *ArXiv Astrophysics e-prints:astro-ph/0306581*.

Copeland, E. J., Sami, M., and Tsujikawa, S. (2006). Dynamics of Dark Energy. *International Journal of Modern Physics D*, 15:1753–1935.

Crocce, M., Castander, F. J., Gaztañaga, E., Fosalba, P., and Carretero, J. (2015). The MICE Grand Challenge lightcone simulation - II. Halo and galaxy catalogues. *MNRAS*, 453:1513–1530.

Crocce, M. and Scoccimarro, R. (2006). Renormalized cosmological perturbation theory. *Physical Review D*, 73:063519.

Croft, R. A. C. and Metzler, C. A. (2000). Weak-Lensing Surveys and the Intrinsic Correlation of Galaxy Ellipticities. *ApJ*, 545:561–571.

Dark Energy Survey Collaboration, Abbott, T., Abdalla, F. B., Aleksić, J., Allam, S., Amara, A., Bacon, D., Balbinot, E., Banerji, M., Bechtol, K., Benoit-Lévy, A., Bernstein, G. M., Bertin, E., Blazek, J., Bonnett, C., Bridle, S., Brooks, D., Brunner, R. J., Buckley-Geer, E., Burke, D. L., Caminha, G. B., Capozzi, D., Carlsen, J., Carnero-Rosell, A., Carollo, M., Carrasco-Kind, M., Carretero, J., Castander, F. J., Clerkin, L., Collett, T., Conselice, C., Crocce,

M., Cunha, C. E., D'Andrea, C. B., da Costa, L. N., Davis, T. M., Desai, S., Diehl, H. T., Dietrich, J. P., Dodelson, S., Doel, P., Drlica-Wagner, A., Estrada, J., Etherington, J., Evrard, A. E., Fabbri, J., Finley, D. A., Flaugher, B., Foley, R. J., Fosalba, P., Frieman, J., García-Bellido, J., Gaztanaga, E., Gerdes, D. W., Giannantonio, T., Goldstein, D. A., Gruen, D., Gruendl, R. A., Guarnieri, P., Gutierrez, G., Hartley, W., Honscheid, K., Jain, B., James, D. J., Jeltema, T., Jouvel, S., Kessler, R., King, A., Kirk, D., Kron, R., Kuehn, K., Kuropatkin, N., Lahav, O., Li, T. S., Lima, M., Lin, H., Maia, M. A. G., Makler, M., Manera, M., Maraston, C., Marshall, J. L., Martini, P., McMahon, R. G., Melchior, P., Merson, A., Miller, C. J., Miquel, R., Mohr, J. J., Morice-Atkinson, X., Naidoo, K., Neilsen, E., Nichol, R. C., Nord, B., Ogando, R., Ostrovski, F., Palmese, A., Papadopoulos, A., Peiris, H. V., Peoples, J., Percival, W. J., Plazas, A. A., Reed, S. L., Refregier, A., Romer, A. K., Roodman, A., Ross, A., Rozo, E., Rykoff, E. S., Sadeh, I., Sako, M., Sánchez, C., Sanchez, E., Santiago, B., Scarpine, V., Schubnell, M., Sevilla-Noarbe, I., Sheldon, E., Smith, M., Smith, R. C., Soares-Santos, M., Sobreira, F., Soumagnac, M., Suchyta, E., Sullivan, M., Swanson, M., Tarle, G., Thaler, J., Thomas, D., Thomas, R. C., Tucker, D., Vieira, J. D., Vikram, V., Walker, A. R., Wechsler, R. H., Weller, J., Wester, W., Whiteway, L., Wilcox, H., Yanny, B., Zhang, Y., and Zuntz, J. (2016). The Dark Energy Survey: more than dark energy - an overview. *MNRAS*, 460:1270–1299.

Davies, C. T., Cautun, M., and Li, B. (2018). Weak lensing by voids in weak lensing maps. *MNRAS*, 480:L101–L105.

Davis, M. and Peebles, P. J. E. (1983). A survey of galaxy redshifts. V - The two-point position and velocity correlations. *ApJ*, 267:465–482.

de Jong, J. T. A., Verdoes Kleijn, G. A., Boxhoorn, D. R., Buddelmeijer, H., Capaccioli, M., Getman, F., Grado, A., Helmich, E., Huang, Z., Irisarri, N., Kuijken, K., La Barbera, F., McFarland, J. P., Napolitano, N. R., Radovich, M., Sikkema, G., Valentijn, E. A., Begeman, K. G., Brescia, M., Cavuoti, S., Choi, A., Cordes, O.-M., Covone, G., Dall'Ora, M., Hildebrandt, H., Longo, G., Nakajima, R., Paolillo, M., Puddu, E., Rifatto, A., Tortora, C., van Uitert, E., Buddendiek, A., Harnois-Déraps, J., Erben, T., Eriksen, M. B., Heymans, C., Hoekstra, H., Joachimi, B., Kitching, T. D., Klaes, D., Koopmans, L. V. E., Köhlinger, F., Roy, N., Sifón, C., Schneider, P., Sutherland, W. J., Viola, M., and Vriend, W.-J. (2015). The first and second data releases of the Kilo-Degree Survey. *AAP*, 582:A62.

de Jong, J. T. A., Verdoes Kleijn, G. A., Erben, T., Hildebrandt, H., Kuijken, K., Sikkema, G., Brescia, M., Bilicki, M., Napolitano, N. R., Amaro, V., Begeman, K. G., Boxhoorn, D. R., Buddelmeijer, H., Cavuoti, S., Getman, F., Grado, A., Helmich, E., Huang, Z., Irisarri, N., La Barbera, F., Longo, G., McFarland, J. P., Nakajima, R., Paolillo, M., Puddu, E., Radovich, M., Rifatto, A., Tortora, C., Valentijn, E. A., Vellucci, C., Vriend, W., Amon, A., Blake, C., Choi, A., Fenech Conti, I., Herbonnet, R., Heymans, C., Hoekstra, H., Klaes, D., Merten,

J., Miller, L., Schneider, P., and Viola, M. (2017). The third data release of the Kilo-Degree Survey and associated data products. *ArXiv e-prints*.

de Jong, J. T. A., Verdoes Kleijn, G. A., Kuijken, K. H., and Valentijn, E. A. (2013). The Kilo-Degree Survey. *Experimental Astronomy*, 35:25–44.

de la Torre, S. and Guzzo, L. (2012). Modelling non-linear redshift-space distortions in the galaxy clustering pattern: systematic errors on the growth rate parameter. *MNRAS*, 427:327–342.

de la Torre, S., Guzzo, L., Peacock, J. A., Branchini, E., Iovino, A., Granett, B. R., Abbas, U., Adami, C., Arnouts, S., Bel, J., Bolzonella, M., Bottini, D., Cappi, A., Coupon, J., Cucciati, O., Davidzon, I., De Lucia, G., Fritz, A., Franzetti, P., Fumana, M., Garilli, B., Ilbert, O., Krywult, J., Le Brun, V., Le Fèvre, O., Maccagni, D., Małek, K., Marulli, F., McCracken, H. J., Moscardini, L., Paioro, L., Percival, W. J., Polletta, M., Pollo, A., Schlagenhaufer, H., Scodeggio, M., Tasca, L. A. M., Tojeiro, R., Vergani, D., Zanichelli, A., Burden, A., Di Porto, C., Marchetti, A., Marinoni, C., Mellier, Y., Monaco, P., Nichol, R. C., Phleps, S., Wolk, M., and Zamorani, G. (2013). The VIMOS Public Extragalactic Redshift Survey (VIPERS) . Galaxy clustering and redshift-space distortions at z 0.8 in the first data release. *AAP*, 557:A54.

de la Torre, S., Jullo, E., Giocoli, C., Pezzotta, A., Bel, J., Granett, B. R., Guzzo, L., Garilli, B., Scodeggio, M., Bolzonella, M., Abbas, U., Adami, C., Bottini, D., Cappi, A., Cucciati, O., Davidzon, I., Franzetti, P., Fritz, A., Iovino, A., Krywult, J., Le Brun, V., Le Fèvre, O., Maccagni, D., Małek, K., Marulli, F., Polletta, M., Pollo, A., Tasca, L. A. M., Tojeiro, R., Vergani, D., Zanichelli, A., Arnouts, S., Branchini, E., Coupon, J., De Lucia, G., Ilbert, O., Moutard, T., Moscardini, L., Peacock, J. A., Metcalf, R. B., Prada, F., and Yepes, G. (2017). The VIMOS Public Extragalactic Redshift Survey (VIPERS). Gravity test from the combination of redshift-space distortions and galaxy-galaxy lensing at 0.5 z 1.2. *AAP*, 608:A44.

de Lapparent, V., Geller, M. J., and Huchra, J. P. (1986). A slice of the universe. , 302:L1–L5.

Dekel, A. and Lahav, O. (1999). Stochastic Nonlinear Galaxy Biasing. *ApJ*, 520:24–34.

Demchenko, V., Cai, Y.-C., Heymans, C., and Peacock, J. A. (2016). Testing the spherical evolution of cosmic voids. *MNRAS*, 463:512–519.

DeRose, J., Wechsler, R. H., Becker, M. R., Busha, M. T., Rykoff, E. S., MacCrann, N., Erickson, B., Evrard, A. E., Kravtsov, A., Gruen, D., Allam, S., Avila, S., Bridle, S., Brooks, D., Buckley-Geer, E., Carnero Rosell, A., Carrasco Kind, M., Carretero, J., Castander, F. J., Cawthon, R., Crocce, M., da Costa, L. N., Davis, C., De Vicente, J., Dietrich, J. P., Doel, P., Drlica-Wagner, A., Fosalba, P., Frieman, J., Garcia-Bellido, J., Gutierrez, G., Hartley, W. G., Hollowood, D. L., Hoyle, B., James, D. J., Krause, E., Kuehn, K.,

Kuropatkin, N., Lima, M., Maia, M. A. G., Menanteau, F., Miller, C. J., Miquel, R., Ogando, R. L. C., Plazas Malagón, A., Romer, A. K., Sanchez, E., Schindler, R., Serrano, S., Sevilla-Noarbe, I., Smith, M., Suchyta, E., Swanson, M. E. C., Tarle, G., and Vikram, V. (2019). The Buzzard Flock: Dark Energy Survey Synthetic Sky Catalogs. *arXiv e-prints*.

DESI Collaboration, Aghamousa, A., Aguilar, J., Ahlen, S., Alam, S., Allen, L. E., Allende Prieto, C., Annis, J., Bailey, S., Balland, C., and et al. (2016). The DESI Experiment Part I: Science,Targeting, and Survey Design. *ArXiv e-prints*.

Dicke, R. H., Peebles, P. J. E., Roll, P. G., and Wilkinson, D. T. (1965). Cosmic Black-Body Radiation. *ApJ*, 142:414–419.

Diehl, H. T., Abbott, T. M. C., Annis, J., Armstrong, R., Baruah, L., Bermeo, A., Bernstein, G., Beynon, E., Bruderer, C., Buckley-Geer, E. J., Campbell, H., Capozzi, D., Carter, M., Casas, R., Clerkin, L., Covarrubias, R., Cuhna, C., D'Andrea, C., da Costa, L., Das, R., DePoy, D. L., Dietrich, J., Drlica-Wagner, A., Elliott, A., Eifler, T., Estrada, J., Etherington, J., Flaugher, B. L., Frieman, J., Fausti Neto, A., Gelman, M., Gerdes, D., Gruen, D., Gruendl, R., Hao, J., Head, H., Helsby, J., Hoffman, K., Honscheid, K., James, D., Johnson, M., Kacprzac, T., Katsaros, J., Kennedy, R., Kent, S., Kessler, R., Kim, A., Krause, E., Kron, R., Kuhlmann, S., Kunder, A., Li, T., Lin, H., Maccrann, N., March, M., Marshall, J., Neilsen, E., Nugent, P., Martini, P., Melchior, P., Menanteau, F., Nichol, R. C., Nord, B., Ogando, R., Old, L., Papadopoulos, A., Patton, K., Petravick, D., Plazas, A. A., Poulton, R., Pujol, A., Reil, K., Rigby, T., Romer, A., Roodman, A., Rooney, P., Sanchez Alvaro, E., Serrano, S., Sheldon, E., Smith, A., Smith, R. C., Soares-Santos, M., Soumagnac, M., Spinka, H., Suchyta, E., Tucker, D., Walker, A. R., Wester, W., Wiesner, M., Wilcox, H., Williams, R., Yanny, B., and Zhang, Y.-. (2014). The Dark Energy Survey and operations: Year 1. In *Observatory Operations: Strategies, Processes, and Systems V*, volume 9149 of , page 91490V.

Doroshkevich, A. G. and Novikov, I. D. (1964). Mean Density of Radiation in the Metagalaxy and Certain Problems in Relativistic Cosmology. *Soviet Physics Doklady*, 9:111.

Driver, S. P., Hill, D. T., Kelvin, L. S., Robotham, A. S. G., Liske, J., Norberg, P., Baldry, I. K., Bamford, S. P., Hopkins, A. M., Loveday, J., Peacock, J. A., Andrae, E., Bland-Hawthorn, J., Brough, S., Brown, M. J. I., Cameron, E., Ching, J. H. Y., Colless, M., Conselice, C. J., Croom, S. M., Cross, N. J. G., de Propris, R., Dye, S., Drinkwater, M. J., Ellis, S., Graham, A. W., Grootes, M. W., Gunawardhana, M., Jones, D. H., van Kampen, E., Maraston, C., Nichol, R. C., Parkinson, H. R., Phillipps, S., Pimbblet, K., Popescu, C. C., Prescott, M., Roseboom, I. G., Sadler, E. M., Sansom, A. E., Sharp, R. G., Smith, D. J. B., Taylor, E., Thomas, D., Tuffs, R. J., Wijesinghe, D., Dunne, L., Frenk, C. S., Jarvis, M. J., Madore, B. F., Meyer, M. J., Seibert, M., Staveley-Smith, L., Sutherland, W. J., and Warren, S. J. (2011). Galaxy and

Mass Assembly (GAMA): survey diagnostics and core data release. *MNRAS*, 413:971–995.

Dubinski, J., da Costa, L. N., Goldwirth, D., Lecar, M., and Piran, T. (1993). Void evolution and the large-scale structure. *The Astrophysical Journal*, 410:458–468.

Dvornik, A., Hoekstra, H., Kuijken, K., Schneider, P., Amon, A., Nakajima, R., Viola, M., Choi, A., Erben, T., Farrow, D. J., Heymans, C., Hildebrandt, H., Sifón, C., and Wang, L. (2018). Unveiling galaxy bias via the halo model, KiDS, and GAMA. *MNRAS*, 479:1240–1259.

Eddington, A. S. (1926). *The Internal Constitution of the Stars*. Cambridge Science Classics. Cambridge University Press.

Edge, A., Sutherland, W., Kuijken, K., Driver, S., McMahon, R., Eales, S., and Emerson, J. P. (2013). The VISTA Kilo-degree Infrared Galaxy (VIKING) Survey: Bridging the Gap between Low and High Redshift. *The Messenger*, 154:32–34.

Eisenstein, D. J. (2005). Dark energy and cosmic sound [review article]. *NAR*, 49:360–365.

Eisenstein, D. J., Zehavi, I., Hogg, D. W., Scoccimarro, R., Blanton, M. R., Nichol, R. C., Scranton, R., Seo, H.-J., Tegmark, M., Zheng, Z., Anderson, S. F., Annis, J., Bahcall, N., Brinkmann, J., Burles, S., Castander, F. J., Connolly, A., Csabai, I., Doi, M., Fukugita, M., Frieman, J. A., Glazebrook, K., Gunn, J. E., Hendry, J. S., Hennessy, G., Ivezić, Z., Kent, S., Knapp, G. R., Lin, H., Loh, Y.-S., Lupton, R. H., Margon, B., McKay, T. A., Meiksin, A., Munn, J. A., Pope, A., Richmond, M. W., Schlegel, D., Schneider, D. P., Shimasaku, K., Stoughton, C., Strauss, M. A., SubbaRao, M., Szalay, A. S., Szapudi, I., Tucker, D. L., Yanny, B., and York, D. G. (2005). Detection of the Baryon Acoustic Peak in the Large-Scale Correlation Function of SDSS Luminous Red Galaxies. *APJ*, 633:560–574.

Eke, V. R., Cole, S., and Frenk, C. S. (1996). Cluster evolution as a diagnostic for Omega. *MNRAS*, 282:263.

Epstein, R. I. (1983). Proto-galactic perturbations. *MNRAS*, 205:207–229.

Erben, T., Schirmer, M., Dietrich, J. P., Cordes, O., Haberzettl, L., Hetterscheidt, M., Hildebrandt, H., Schmithuesen, O., Schneider, P., Simon, P., Deul, E., Hook, R. N., Kaiser, N., Radovich, M., Benoist, C., Nonino, M., Olsen, L. F., Prandoni, I., Wichmann, R., Zaggia, S., Bomans, D., Dettmar, R. J., and Miralles, J. M. (2005). GaBoDS: The Garching-Bonn Deep Survey. IV. Methods for the image reduction of multi-chip cameras demonstrated on data from the ESO Wide-Field Imager. *Astronomische Nachrichten*, 326:432–464.

Falck, B., Koyama, K., Zhao, G.-B., and Cautun, M. (2018). Using voids to unscreen modified gravity. *MNRAS*, 475:3262–3272.

Fenech Conti, I., Herbonnet, R., Hoekstra, H., Merten, J., Miller, L., and Viola, M. (2017). Calibration of weak-lensing shear in the Kilo-Degree Survey. *MNRAS*, 467:1627–1651.

Flender, S., Hotchkiss, S., and Nadathur, S. (2013). The stacked ISW signal of rare superstructures in ΛCDM. *JCAP*, 2:13.

Foreman-Mackey, D., Hogg, D. W., Lang, D., and Goodman, J. (2013). emcee: The MCMC Hammer. *Publications of the Astronomical Society of the Pacific*, 125:306.

Fosalba, P., Crocce, M., Gaztañaga, E., and Castander, F. J. (2015a). The MICE grand challenge lightcone simulation - I. Dark matter clustering. *MNRAS*, 448:2987–3000.

Fosalba, P., Gaztañaga, E., Castander, F. J., and Crocce, M. (2015b). The MICE Grand Challenge light-cone simulation - III. Galaxy lensing mocks from all-sky lensing maps. *MNRAS*, 447:1319–1332.

Friedmann, A. (1922). Über die Krümmung des Raumes. *Zeitschrift fur Physik*, 10:377–386.

Friedrich, O., Gruen, D., DeRose, J., Kirk, D., Krause, E., McClintock, T., Rykoff, E. S., Seitz, S., Wechsler, R. H., Bernstein, G. M., Blazek, J., Chang, C., Hilbert, S., Jain, B., Kovacs, A., Lahav, O., Abdalla, F. B., Allam, S., Annis, J., Bechtol, K., Benoit-Lévy, A., Bertin, E., Brooks, D., Carnero Rosell, A., Carrasco Kind, M., Carretero, J., Cunha, C. E., D'Andrea, C. B., da Costa, L. N., Davis, C., Desai, S., Diehl, H. T., Dietrich, J. P., Drlica-Wagner, A., Eifler, T. F., Fosalba, P., Frieman, J., García-Bellido, J., Gaztanaga, E., Gerdes, D. W., Giannantonio, T., Gruendl, R. A., Gschwend, J., Gutierrez, G., Honscheid, K., James, D. J., Jarvis, M., Kuehn, K., Kuropatkin, N., Lima, M., March, M., Marshall, J. L., Melchior, P., Menanteau, F., Miquel, R., Mohr, J. J., Nord, B., Plazas, A. A., Sanchez, E., Scarpine, V., Schindler, R., Schubnell, M., Sevilla-Noarbe, I., Sheldon, E., Smith, M., Soares-Santos, M., Sobreira, F., Suchyta, E., Swanson, M. E. C., Tarle, G., Thomas, D., Troxel, M. A., Vikram, V., Weller, J., and DES Collaboration (2018). Density split statistics: Joint model of counts and lensing in cells. *Physical Review D*, 98(2):023508.

Frieman, J. A., Turner, M. S., and Huterer, D. (2008). Dark Energy and the Accelerating Universe. *ARAA*, 46:385–432.

Fu, L., Kilbinger, M., Erben, T., Heymans, C., Hildebrandt, H., Hoekstra, H., Kitching, T. D., Mellier, Y., Miller, L., Semboloni, E., Simon, P., Van Waerbeke, L., Coupon, J., Harnois-Déraps, J., Hudson, M. J., Kuijken, K., Rowe, B., Schrabback, T., Vafaei, S., and Velander, M. (2014). CFHTLenS: cosmological constraints from a combination of cosmic shear two-point and three-point correlations. *MNRAS*, 441:2725–2743.

Gamow, G. (1948a). The Evolution of the Universe. , 162:680–682.

Gamow, G. (1948b). The Origin of Elements and the Separation of Galaxies. *Physical Review*, 74:505–506.

Gamow, G. (1956). The Evolutionary Universe. *Scientific American*, 195:136–156.

Gao, L. and Theuns, T. (2007). Lighting the Universe with Filaments. *Science*, 317:1527.

Georgiou, C., Johnston, H., Hoekstra, H., Viola, M., Kuijken, K., Joachimi, B., Chisari, N. E., Hildebrandt, H., and Kannawadi, A. (2018). The dependence of intrinsic alignment of galaxies on wavelength using KiDS and GAMA. *ArXiv e-prints*.

Giblin, B., Cataneo, M., Moews, B., and Heymans, C. (2019). On the road to per cent level accuracy II: calibration of the non-linear matter power spectrum for arbitrary cosmologies. *arXiv e-prints*, page arXiv:1906.02742.

Giblin, B., Heymans, C., Harnois-Déraps, J., Simpson, F., Dietrich, J. P., Van Waerbeke, L., Amon, A., Asgari, M., Erben, T., Hildebrandt, H., Joachimi, B., Kuijken, K., Martinet, N., Schneider, P., and Tröster, T. (2018). KiDS-450: enhancing cosmic shear with clipping transformations. *MNRAS*, 480:5529–5549.

Goldberg, D. M. and Vogeley, M. S. (2004). Simulating Voids. *ApJ*, 605:1–6.

Goodman, J. and Weare, J. (2010). Ensemble samplers with affine invariance. *Communications in Applied Mathematics and Computational Science, Vol. 5, No. 1, p. 65-80, 2010*, 5:65–80.

Górski, K. M., Hivon, E., Banday, A. J., Wandelt, B. D., Hansen, F. K., Reinecke, M., and Bartelmann, M. (2005). HEALPix: A Framework for High-Resolution Discretization and Fast Analysis of Data Distributed on the Sphere. *ApJ*, 622:759–771.

Granett, B. R., Neyrinck, M. C., and Szapudi, I. (2008). An Imprint of Superstructures on the Microwave Background due to the Integrated Sachs-Wolfe Effect. *APJL*, 683:L99–L102.

Green, J., Schechter, P., Baltay, C., Bean, R., Bennett, D., Brown, R., Conselice, C., Donahue, M., Fan, X., Gaudi, B. S., Hirata, C., Kalirai, J., Lauer, T., Nichol, B., Padmanabhan, N., Perlmutter, S., Rauscher, B., Rhodes, J., Roellig, T., Stern, D., Sumi, T., Tanner, A., Wang, Y., Weinberg, D., Wright, E., Gehrels, N., Sambruna, R., Traub, W., Anderson, J., Cook, K., Garnavich, P., Hillenbrand, L., Ivezic, Z., Kerins, E., Lunine, J., McDonald, P., Penny, M., Phillips, M., Rieke, G., Riess, A., van der Marel, R., Barry, R. K., Cheng, E., Content, D., Cutri, R., Goullioud, R., Grady, K., Helou, G., Jackson, C.,

Kruk, J., Melton, M., Peddie, C., Rioux, N., and Seiffert, M. (2012). Wide-Field InfraRed Survey Telescope (WFIRST) Final Report. *arXiv e-prints*, page arXiv:1208.4012.

Gregory, S. A. and Thompson, L. A. (1978). The Coma/A1367 supercluster and its environs. *ApJ*, 222:784–799.

Griest, K. (1991). Galactic microlensing as a method of detecting massive compact halo objects. *ApJ*, 366:412–421.

Grogin, N. A. and Geller, M. J. (1999). An Imaging and Spectroscopic Survey of Galaxies within Prominent Nearby Voids. I. The Sample and Luminosity Distribution. *AJ*, 118:2561–2580.

Gruen, D., Friedrich, O., Amara, A., Bacon, D., Bonnett, C., Hartley, W., Jain, B., Jarvis, M., Kacprzak, T., Krause, E., Mana, A., Rozo, E., Rykoff, E. S., Seitz, S., Sheldon, E., Troxel, M. A., Vikram, V., Abbott, T. M. C., Abdalla, F. B., Allam, S., Armstrong, R., Banerji, M., Bauer, A. H., Becker, M. R., Benoit-Lévy, A., Bernstein, G. M., Bernstein, R. A., Bertin, E., Bridle, S. L., Brooks, D., Buckley-Geer, E., Burke, D. L., Capozzi, D., Carnero Rosell, A., Carrasco Kind, M., Carretero, J., Crocce, M., Cunha, C. E., D'Andrea, C. B., da Costa, L. N., DePoy, D. L., Desai, S., Diehl, H. T., Dietrich, J. P., Doel, P., Eifler, T. F., Neto, A. F., Fernandez, E., Flaugher, B., Fosalba, P., Frieman, J., Gerdes, D. W., Gruendl, R. A., Gutierrez, G., Honscheid, K., James, D. J., Kuehn, K., Kuropatkin, N., Lahav, O., Li, T. S., Lima, M., Maia, M. A. G., March, M., Martini, P., Melchior, P., Miller, C. J., Miquel, R., Mohr, J. J., Nord, B., Ogando, R., Plazas, A. A., Reil, K., Romer, A. K., Roodman, A., Sako, M., Sanchez, E., Scarpine, V., Schubnell, M., Sevilla-Noarbe, I., Smith, R. C., Soares-Santos, M., Sobreira, F., Suchyta, E., Swanson, M. E. C., Tarle, G., Thaler, J., Thomas, D., Walker, A. R., Wechsler, R. H., Weller, J., Zhang, Y., and Zuntz, J. (2016). Weak lensing by galaxy troughs in DES Science Verification data. *MNRAS*, 455:3367–3380.

Gruen, D., Friedrich, O., Krause, E., DeRose, J., Cawthon, R., Davis, C., Elvin-Poole, J., Rykoff, E. S., Wechsler, R. H., Alarcon, A., Bernstein, G. M., Blazek, J., Chang, C., Clampitt, J., Crocce, M., De Vicente, J., Gatti, M., Gill, M. S. S., Hartley, W. G., Hilbert, S., Hoyle, B., Jain, B., Jarvis, M., Lahav, O., MacCrann, N., McClintock, T., Prat, J., Rollins, R. P., Ross, A. J., Rozo, E., Samuroff, S., Sánchez, C., Sheldon, E., Troxel, M. A., Zuntz, J., Abbott, T. M. C., Abdalla, F. B., Allam, S., Annis, J., Bechtol, K., Benoit-Lévy, A., Bertin, E., Bridle, S. L., Brooks, D., Buckley-Geer, E., Carnero Rosell, A., Carrasco Kind, M., Carretero, J., Cunha, C. E., D'Andrea, C. B., da Costa, L. N., Desai, S., Diehl, H. T., Dietrich, J. P., Doel, P., Drlica-Wagner, A., Fernandez, E., Flaugher, B., Fosalba, P., Frieman, J., García-Bellido, J., Gaztanaga, E., Giannantonio, T., Gruendl, R. A., Gschwend, J., Gutierrez, G., Honscheid, K., James, D. J., Jeltema, T., Kuehn, K., Kuropatkin, N., Lima, M., March, M., Marshall, J. L., Martini, P., Melchior, P., Menanteau, F., Miquel, R., Mohr, J. J., Plazas, A. A., Roodman, A., Sanchez, E., Scarpine,

V., Schubnell, M., Sevilla-Noarbe, I., Smith, M., Smith, R. C., Soares-Santos, M., Sobreira, F., Swanson, M. E. C., Tarle, G., Thomas, D., Vikram, V., Walker, A. R., Weller, J., Zhang, Y., and DES Collaboration (2018). Density split statistics: Cosmological constraints from counts and lensing in cells in DES Y1 and SDSS data. *Physical Review D*, 98(2):023507.

Guillaume, C. E. (1896). La Température de L'Espace. *La Nature*, 24:210–234.

Gunn, J. E. and Gott, III, J. R. (1972). On the Infall of Matter Into Clusters of Galaxies and Some Effects on Their Evolution. *APJ*, 176:1.

Guth, A. H. (1981). Inflationary universe: A possible solution to the horizon and flatness problems. *Phys. Rev. D*.

Hahn, O., Porciani, C., Carollo, C. M., and Dekel, A. (2007). Properties of dark matter haloes in clusters, filaments, sheets and voids. *MNRAS*, 375:489–499.

Hamaus, N., Cousinou, M.-C., Pisani, A., Aubert, M., Escoffier, S., and Weller, J. (2017). Multipole analysis of redshift-space distortions around cosmic voids. , 7:014.

Hamaus, N., Pisani, A., Sutter, P. M., Lavaux, G., Escoffier, S., Wandelt, B. D., and Weller, J. (2016). Constraints on Cosmology and Gravity from the Dynamics of Voids. *Physical Review Letters*, 117(9):091302.

Hamaus, N., Seljak, U., and Desjacques, V. (2012). Optimal weighting in galaxy surveys: Application to redshift-space distortions. *Physical Review D*, 86(10):103513.

Hamaus, N., Sutter, P. M., Lavaux, G., and Wandelt, B. D. (2015). Probing cosmology and gravity with redshift-space distortions around voids. , 11:036.

Hamilton, A. J. S. (1992). Measuring Omega and the real correlation function from the redshift correlation function. , 385:L5–L8.

Hamilton, A. J. S. (1998). Linear Redshift Distortions: a Review. In Hamilton, D., editor, *The Evolving Universe*, volume 231 of *Astrophysics and Space Science Library*, page 185.

Harnois-Déraps, J., Amon, A., Choi, A., Demchenko, V., Heymans, C., Kannawadi, A., Nakajima, R., Sirks, E., van Waerbeke, L., Cai, Y.-C., Giblin, B., Hildebrandt, H., Hoekstra, H., Miller, L., and Tröster, T. (2018). Cosmological simulations for combined-probe analyses: covariance and neighbour-exclusion bias. *MNRAS*, 481:1337–1367.

Harnois-Déraps, J., Giblin, B., and Joachimi, B. (2019). Cosmic Shear Covariance Matrix in wCDM: Cosmology Matters. *arXiv e-prints*, page arXiv:1905.06454.

Harnois-Déraps, J., Pen, U.-L., Iliev, I. T., Merz, H., Emberson, J. D., and Desjacques, V. (2013). High-performance P^3M N-body code: CUBEP^{3}M. *MNRAS*, 436:540–559.

Harnois-Déraps, J., Vafaei, S., and Van Waerbeke, L. (2012). Gravitational lensing simulations - I. Covariance matrices and halo catalogues. *MNRAS*, 426:1262–1279.

Harnois-Déraps, J. and van Waerbeke, L. (2015). Simulations of weak gravitational lensing - II. Including finite support effects in cosmic shear covariance matrices. *MNRAS*, 450:2857–2873.

Hartlap, J., Simon, P., and Schneider, P. (2007). Why your model parameter confidences might be too optimistic. Unbiased estimation of the inverse covariance matrix. *AAP*, 464:399–404.

Hastings, W. K. (1970). Monte Carlo Sampling Methods using Markov Chains and their Applications. *Biometrika, Vol. 57, No. 1, p. 97-109, 1970*, 57:97–109.

Hawken, A. J., Granett, B. R., Iovino, A., Guzzo, L., Peacock, J. A., de la Torre, S., Garilli, B., Bolzonella, M., Scodeggio, M., Abbas, U., Adami, C., Bottini, D., Cappi, A., Cucciati, O., Davidzon, I., Fritz, A., Franzetti, P., Krywult, J., Le Brun, V., Le Fèvre, O., Maccagni, D., Małek, K., Marulli, F., Polletta, M., Pollo, A., Tasca, L. A. M., Tojeiro, R., Vergani, D., Zanichelli, A., Arnouts, S., Bel, J., Branchini, E., De Lucia, G., Ilbert, O., Moscardini, L., and Percival, W. J. (2017). The VIMOS Public Extragalactic Redshift Survey. Measuring the growth rate of structure around cosmic voids. *AAP*, 607:A54.

Heavens, A., Refregier, A., and Heymans, C. (2000). Intrinsic correlation of galaxy shapes: implications for weak lensing measurements. *MNRAS*, 319:649–656.

Heymans, C., Brown, M. L., Barden, M., Caldwell, J. A. R., Jahnke, K., Peng, C. Y., Rix, H.-W., Taylor, A., Beckwith, S. V. W., Bell, E. F., Borch, A., Häußler, B., Jogee, S., McIntosh, D. H., Meisenheimer, K., Sánchez, S. F., Somerville, R., Wisotzki, L., and Wolf, C. (2005). Cosmological weak lensing with the HST GEMS survey. *MNRAS*, 361:160–176.

Heymans, C. and Heavens, A. (2003). Weak gravitational lensing: reducing the contamination by intrinsic alignments. *MNRAS*, 339:711–720.

Heymans, C., White, M., Heavens, A., Vale, C., and van Waerbeke, L. (2006). Potential sources of contamination to weak lensing measurements: constraints from N-body simulations. *MNRAS*, 371:750–760.

Hikage, C., Oguri, M., Hamana, T., More, S., Mandelbaum, R., Takada, M., Köhlinger, F., Miyatake, H., Nishizawa, A. J., Aihara, H., Armstrong, R., Bosch, J., Coupon, J., Ducout, A., Hsieh, B.-C., Komiyama, Y., Lanusse, F., Leauthaud, A., Medezinski, E., Mineo, S., Miyazaki, S., Murata, R., Murayama, H., Shirasaki, M., Sifón, C., Simet, M., Speagle, J., Spergel, D. N., Strauss, M. A., Sugiyama, N., Tanaka, M., and Wang, S.-Y. (2018). Cosmology from cosmic shear power spectra with Subaru Hyper Suprime-Cam first-year data. *ArXiv e-prints*.

Hilbert, S., Xu, D., Schneider, P., Springel, V., Vogelsberger, M., and Hernquist, L. (2017). Intrinsic alignments of galaxies in the Illustris simulation. *MNRAS*, 468:790–823.

Hildebrandt, H., Arnouts, S., Capak, P., Moustakas, L. A., Wolf, C., Abdalla, F. B., Assef, R. J., Banerji, M., Benítez, N., Brammer, G. B., Budavári, T., Carliles, S., Coe, D., Dahlen, T., Feldmann, R., Gerdes, D., Gillis, B., Ilbert, O., Kotulla, R., Lahav, O., Li, I. H., Miralles, J.-M., Purger, N., Schmidt, S., and Singal, J. (2010). PHAT: PHoto-z Accuracy Testing. *AAP*, 523:A31.

Hildebrandt, H., Erben, T., Kuijken, K., van Waerbeke, L., Heymans, C., Coupon, J., Benjamin, J., Bonnett, C., Fu, L., Hoekstra, H., Kitching, T. D., Mellier, Y., Miller, L., Velander, M., Hudson, M. J., Rowe, B. T. P., Schrabback, T., Semboloni, E., and Benítez, N. (2012). CFHTLenS: improving the quality of photometric redshifts with precision photometry. *MNRAS*, 421:2355–2367.

Hildebrandt, H., Köhlinger, F., van den Busch, J. L., Joachimi, B., Heymans, C., Kannawadi, A., Wright, A. H., Asgari, M., Blake, C., Hoekstra, H., Joudaki, S., Kuijken, K., Miller, L., Morrison, C. B., Tröster, T., Amon, A., Archidiacono, M., Brieden, S., Choi, A., de Jong, J. T. A., Erben, T., Giblin, B., Mead, A., Peacock, J. A., Radovich, M., Schneider, P., Sifón, C., and Tewes, M. (2018). KiDS+VIKING-450: Cosmic shear tomography with optical+infrared data. *arXiv e-prints*, page arXiv:1812.06076.

Hildebrandt, H., Viola, M., Heymans, C., Joudaki, S., Kuijken, K., Blake, C., Erben, T., Joachimi, B., Klaes, D., Miller, L., Morrison, C. B., Nakajima, R., Verdoes Kleijn, G., Amon, A., Choi, A., Covone, G., de Jong, J. T. A., Dvornik, A., Fenech Conti, I., Grado, A., Harnois-Déraps, J., Herbonnet, R., Hoekstra, H., Köhlinger, F., McFarland, J., Mead, A., Merten, J., Napolitano, N., Peacock, J. A., Radovich, M., Schneider, P., Simon, P., Valentijn, E. A., van den Busch, J. L., van Uitert, E., and Van Waerbeke, L. (2017). KiDS-450: cosmological parameter constraints from tomographic weak gravitational lensing. *MNRAS*, 465:1454–1498.

Hinshaw, G., Larson, D., Komatsu, E., Spergel, D. N., Bennett, C. L., Dunkley, J., Nolta, M. R., Halpern, M., Hill, R. S., Odegard, N., Page, L., Smith, K. M., Weiland, J. L., Gold, B., Jarosik, N., Kogut, A., Limon, M., Meyer, S. S., Tucker, G. S., Wollack, E., and Wright, E. L. (2013). Nine-year Wilkinson Microwave Anisotropy Probe (WMAP) Observations: Cosmological Parameter Results. *APJS*, 208:19.

Hirata, C. M., Mandelbaum, R., Seljak, U., Guzik, J., Padmanabhan, N., Blake, C., Brinkmann, J., Budávari, T., Connolly, A., Csabai, I., Scranton, R., and Szalay, A. S. (2004). Galaxy-galaxy weak lensing in the Sloan Digital Sky Survey: intrinsic alignments and shear calibration errors. *MNRAS*, 353:529–549.

Hirata, C. M. and Seljak, U. (2004). Intrinsic alignment-lensing interference as a contaminant of cosmic shear. *Physical Review D*, 70(6):063526.

Hockney, R. W. and Eastwood, J. W. (1981). *Computer Simulation Using Particles*.

Hoekstra, H., Franx, M., Kuijken, K., and Squires, G. (1998). Weak Lensing Analysis of CL 1358+62 Using Hubble Space Telescope Observations. *ApJ*, 504:636–660.

Hoffman, Y. and Shaham, J. (1982). On the origin of the voids in the galaxy distribution. , 262:L23–L26.

Hogg, D. W., Baldry, I. K., Blanton, M. R., and Eisenstein, D. J. (2002). The K correction. *arXiv e-prints*, pages astro–ph/0210394.

Hotchkiss, S., Nadathur, S., Gottlöber, S., Iliev, I. T., Knebe, A., Watson, W. A., and Yepes, G. (2015). The Jubilee ISW Project - II. Observed and simulated imprints of voids and superclusters on the cosmic microwave background. *mnras*, 446:1321–1334.

Hoyle, B., Gruen, D., Bernstein, G. M., Rau, M. M., De Vicente, J., Hartley, W. G., Gaztanaga, E., DeRose, J., Troxel, M. A., Davis, C., Alarcon, A., MacCrann, N., Prat, J., Sánchez, C., Sheldon, E., Wechsler, R. H., Asorey, J., Becker, M. R., Bonnett, C., Carnero Rosell, A., Carollo, D., Carrasco Kind, M., Castander, F. J., Cawthon, R., Chang, C., Childress, M., Davis, T. M., Drlica-Wagner, A., Gatti, M., Glazebrook, K., Gschwend, J., Hinton, S. R., Hoormann, J. K., Kim, A. G., King, A., Kuehn, K., Lewis, G., Lidman, C., Lin, H., Macaulay, E., Maia, M. A. G., Martini, P., Mudd, D., Möller, A., Nichol, R. C., Ogando, R. L. C., Rollins, R. P., Roodman, A., Ross, A. J., Rozo, E., Rykoff, E. S., Samuroff, S., Sevilla-Noarbe, I., Sharp, R., Sommer, N. E., Tucker, B. E., Uddin, S. A., Varga, T. N., Vielzeuf, P., Yuan, F., Zhang, B., Abbott, T. M. C., Abdalla, F. B., Allam, S., Annis, J., Bechtol, K., Benoit-Lévy, A., Bertin, E., Brooks, D., Buckley-Geer, E., Burke, D. L., Busha, M. T., Capozzi, D., Carretero, J., Crocce, M., D'Andrea, C. B., da Costa, L. N., DePoy, D. L., Desai, S., Diehl, H. T., Doel, P., Eifler, T. F., Estrada, J., Evrard, A. E., Fernandez, E., Flaugher, B., Fosalba, P., Frieman, J., García-Bellido, J., Gerdes, D. W., Giannantonio, T., Goldstein, D. A., Gruendl, R. A., Gutierrez, G., Honscheid, K., James, D. J., Jarvis, M., Jeltema, T., Johnson, M. W. G., Johnson, M. D., Kirk, D., Krause, E., Kuhlmann, S., Kuropatkin, N., Lahav, O., Li, T. S., Lima, M., March, M., Marshall, J. L., Melchior, P., Menanteau, F., Miquel, R., Nord, B., O'Neill, C. R., Plazas, A. A., Romer, A. K., Sako, M., Sanchez, E., Santiago, B., Scarpine, V., Schindler, R., Schubnell, M., Smith, M., Smith, R. C., Soares-Santos, M., Sobreira, F., Suchyta, E., Swanson, M. E. C., Tarle, G., Thomas, D., Tucker, D. L., Vikram, V., Walker, A. R., Weller, J., Wester, W., Wolf, R. C., Yanny, B., and Zuntz, J. (2018). Dark Energy Survey Year 1 Results: redshift distributions of the weak-lensing source galaxies. *MNRAS*, 478:592–610.

Hoyle, F. and Vogeley, M. S. (2002). Voids in the Point Source Catalogue Survey and the Updated Zwicky Catalog. *ApJ*, 566:641–651.

Hubble, E. (1929). A Relation between Distance and Radial Velocity among Extra-Galactic Nebulae. *Proceedings of the National Academy of Science*, 15:168–173.

Huff, E. and Mandelbaum, R. (2017). Metacalibration: Direct Self-Calibration of Biases in Shear Measurement. *ArXiv e-prints*.

Hui, L., Nicolis, A., and Stubbs, C. W. (2009). Equivalence principle implications of modified gravity models. *Physical Review D*, 80(10):104002.

Huterer, D., Takada, M., Bernstein, G., and Jain, B. (2006). Systematic errors in future weak-lensing surveys: requirements and prospects for self-calibration. *MNRAS*, 366:101–114.

Icke, V. (1984). Voids and filaments. *The Monthly Notices of the Royal Astronomical Society*, 206.

Ilbert, O., Arnouts, S., McCracken, H. J., Bolzonella, M., Bertin, E., Le Fèvre, O., Mellier, Y., Zamorani, G., Pellò, R., Iovino, A., Tresse, L., Le Brun, V., Bottini, D., Garilli, B., Maccagni, D., Picat, J. P., Scaramella, R., Scodeggio, M., Vettolani, G., Zanichelli, A., Adami, C., Bardelli, S., Cappi, A., Charlot, S., Ciliegi, P., Contini, T., Cucciati, O., Foucaud, S., Franzetti, P., Gavignaud, I., Guzzo, L., Marano, B., Marinoni, C., Mazure, A., Meneux, B., Merighi, R., Paltani, S., Pollo, A., Pozzetti, L., Radovich, M., Zucca, E., Bondi, M., Bongiorno, A., Busarello, G., de La Torre, S., Gregorini, L., Lamareille, F., Mathez, G., Merluzzi, P., Ripepi, V., Rizzo, D., and Vergani, D. (2006). Accurate photometric redshifts for the CFHT legacy survey calibrated using the VIMOS VLT deep survey. *AAP*, 457:841–856.

Ilbert, O., Capak, P., Salvato, M., Aussel, H., McCracken, H. J., Sanders, D. B., Scoville, N., Kartaltepe, J., Arnouts, S., Le Floc'h, E., Mobasher, B., Taniguchi, Y., Lamareille, F., Leauthaud, A., Sasaki, S., Thompson, D., Zamojski, M., Zamorani, G., Bardelli, S., Bolzonella, M., Bongiorno, A., Brusa, M., Caputi, K. I., Carollo, C. M., Contini, T., Cook, R., Coppa, G., Cucciati, O., de la Torre, S., de Ravel, L., Franzetti, P., Garilli, B., Hasinger, G., Iovino, A., Kampczyk, P., Kneib, J. P., Knobel, C., Kovac, K., Le Borgne, J. F., Le Brun, V., Le Fèvre, O., Lilly, S., Looper, D., Maier, C., Mainieri, V., Mellier, Y., Mignoli, M., Murayama, T., Pellò, R., Peng, Y., Pérez-Montero, E., Renzini, A., Ricciardelli, E., Schiminovich, D., Scodeggio, M., Shioya, Y., Silverman, J., Surace, J., Tanaka, M., Tasca, L., Tresse, L., Vergani, D., and Zucca, E. (2009). Cosmos Photometric Redshifts with 30-Bands for 2-deg^2. *ApJ*, 690:1236–1249.

Ilić, S., Langer, M., and Douspis, M. (2013). Detecting the integrated Sachs-Wolfe effect with stacked voids. *AAP*, 556:A51.

Iršič, V., Viel, M., Haehnelt, M. G., Bolton, J. S., Cristiani, S., Becker, G. D., D'Odorico, V., Cupani, G., Kim, T.-S., Berg, T. A. M., López, S., Ellison, S., Christensen, L., Denney, K. D., and Worseck, G. (2017). New constraints on the free-streaming of warm dark matter from intermediate and small scale Lyman-α forest data. *Physical Review D*, 96(2):023522.

Jackson, J. C. (1972). A critique of Rees's theory of primordial gravitational radiation. *MNRAS*, 156:1P.

Jain, B. (2011). Designing surveys for tests of gravity. *Philosophical Transactions of the Royal Society of London Series A*, 369:5081–5089.

Jain, B. and VanderPlas, J. (2011). Tests of modified gravity with dwarf galaxies. , 10:032.

Jarvis, M., Bernstein, G., and Jain, B. (2004). The skewness of the aperture mass statistic. *MNRAS*, 352:338–352.

Jennings, E., Baugh, C. M., and Pascoli, S. (2011). Modelling redshift space distortions in hierarchical cosmologies. *MNRAS*, 410:2081–2094.

Joachimi, B., Semboloni, E., Hilbert, S., Bett, P. E., Hartlap, J., Hoekstra, H., and Schneider, P. (2013). Intrinsic galaxy shapes and alignments - II. Modelling the intrinsic alignment contamination of weak lensing surveys. *MNRAS*, 436:819–838.

Joeveer, M. and Einasto, J. (1978). Has the universe the cell structure. In Longair, M. S. and Einasto, J., editors, *Large Scale Structures in the Universe*, volume 79 of *IAU Symposium*, pages 241–250.

Johnston, H., Georgiou, C., Joachimi, B., Hoekstra, H., Chisari, N. E., Farrow, D., Fortuna, M. C., Heymans, C., Joudaki, S., Kuijken, K., and Wright, A. (2018). KiDS+GAMA: Intrinsic alignment model constraints for current and future weak lensing cosmology. *arXiv e-prints*.

Joudaki, S., Mead, A., Blake, C., Choi, A., de Jong, J., Erben, T., Fenech Conti, I., Herbonnet, R., Heymans, C., Hildebrandt, H., Hoekstra, H., Joachimi, B., Klaes, D., Köhlinger, F., Kuijken, K., McFarland, J., Miller, L., Schneider, P., and Viola, M. (2017). KiDS-450: testing extensions to the standard cosmological model. *MNRAS*, 471:1259–1279.

Joyce, A., Lombriser, L., and Schmidt, F. (2016). Dark Energy Versus Modified Gravity. *Annual Review of Nuclear and Particle Science*, 66:95–122.

Jungman, G., Kamionkowski, M., and Griest, K. (1996). Supersymmetric dark matter. *Physics Reports*, 267:195–373.

Kaiser, N. (1987). Clustering in real space and in redshift space. *MNRAS*, 227:1–21.

Kaiser, N. (2000). A New Shear Estimator for Weak-Lensing Observations. *ApJ*, 537:555–577.

Kaiser, N., Squires, G., and Broadhurst, T. (1995). A Method for Weak Lensing Observations. *ApJ*, 449:460.

Kannawadi, A., Hoekstra, H., Miller, L., Viola, M., Conti, I. F., Herbonnet, R., Erben, T., Heymans, C., Hildebrandt, H., Kuijken, K., Vakili, M., and Wright, A. H. (2018). Towards emulating cosmic shear data: revisiting the calibration of the shear measurements for the Kilo-Degree Survey. *arXiv e-prints*, page arXiv:1812.03983.

Khoury, J. and Weltman, A. (2004). Chameleon cosmology. *PRD*, 69(4):044026.

Kilbinger, M. (2015). Cosmology with cosmic shear observations: a review. *Reports on Progress in Physics*, 78:086901.

Kilbinger, M., Bonnett, C., and Coupon, J. (2014). athena: Tree code for second-order correlation functions. Astrophysics Source Code Library.

Kimura, R., Suyama, T., Yamaguchi, M., Yamauchi, D., and Yokoyama, S. (2018). Are redshift-space distortions actually a probe of growth of structure? *Publications of the Astronomical Society of Japan*, 70:L5.

Kirshner, R. P., Oemler, Jr., A., Schechter, P. L., and Shectman, S. A. (1981). A million cubic megaparsec void in Bootes. , 248:L57–L60.

Kirshner, R. P., Oemler, Jr., A., Schechter, P. L., and Shectman, S. A. (1987). A survey of the Bootes void. *APJ*, 314:493–506.

Kitaura, F.-S., Chuang, C.-H., Liang, Y., Zhao, C., Tao, C., Rodríguez-Torres, S., Eisenstein, D. J., Gil-Marín, H., Kneib, J.-P., McBride, C., Percival, W. J., Ross, A. J., Sánchez, A. G., Tinker, J., Tojeiro, R., Vargas-Magana, M., and Zhao, G.-B. (2016). Signatures of the Primordial Universe from Its Emptiness: Measurement of Baryon Acoustic Oscillations from Minima of the Density Field. *Physical Review Letters*, 116(17):171301.

Kitching, T. D., Miller, L., Heymans, C. E., van Waerbeke, L., and Heavens, A. F. (2008). Bayesian galaxy shape measurement for weak lensing surveys - II. Application to simulations. *MNRAS*, 390:149–167.

Kovács, A. (2018). The part and the whole: voids, supervoids, and their ISW imprint. *MNRAS*, 475:1777–1790.

Kovács, A. and Granett, B. R. (2015). Cold imprint of supervoids in the cosmic microwave background re-considered with Planck and Baryon Oscillation Spectroscopic Survey DR10. *MNRAS*, 452:1295–1302.

Kovács, A., Sánchez, C., García-Bellido, J., Elvin-Poole, J., Hamaus, N., Miranda, V., Nadathur, S., Abbott, T., Abdalla, F. B., Annis, J., Avila, S., Bertin, E., Brooks, D., Burke, D. L., Carnero Rosell, A., Carrasco Kind, M.,

Carretero, J., Cawthon, R., Crocce, M., Cunha, C., da Costa, L. N., Davis, C., De Vicente, J., DePoy, D., Desai, S., Diehl, H. T., Doel, P., Fernandez, E., Flaugher, B., Fosalba, P., Frieman, J., Gaztañaga, E., Gerdes, D., Gruendl, R., Gutierrez, G., Hartley, W., Hollowood, D. L., Honscheid, K., Hoyle, B., James, D. J., Krause, E., Kuehn, K., Kuropatkin, N., Lahav, O., Lima, M., Maia, M., March, M., Marshall, J., Melchior, P., Menanteau, F., Miller, C. J., Miquel, R., Mohr, J., Plazas, A. A., Romer, K., Rykoff, E., Sanchez, E., Scarpine, V., Schindler, R., Schubnell, M., Sevilla-Noarbe, I., Smith, M., Smith, R. C., Soares-Santos, M., Sobreira, F., Suchyta, E., Swanson, M., Tarle, G., Thomas, D., Vikram, V., and Weller, J. (2019). More out of less: an excess integrated Sachs-Wolfe signal from supervoids mapped out by the Dark Energy Survey. *MNRAS*.

Kragh, H. (1999). *Cosmology and Controversy: The Historical Development of Two Theories of the Universe.*

Kraljic, K., Arnouts, S., Pichon, C., Laigle, C., de la Torre, S., Vibert, D., Cadiou, C., Dubois, Y., Treyer, M., Schimd, C., Codis, S., de Lapparent, V., Devriendt, J., Hwang, H. S., Le Borgne, D., Malavasi, N., Milliard, B., Musso, M., Pogosyan, D., Alpaslan, M., Bland-Hawthorn, J., and Wright, A. H. (2018). Galaxy evolution in the metric of the cosmic web. *MNRAS*, 474:547–571.

Krause, E., Chang, T.-C., Doré, O., and Umetsu, K. (2013). The Weight of Emptiness: The Gravitational Lensing Signal of Stacked Voids. , 762:L20.

Kravtsov, A. V., Berlind, A. A., Wechsler, R. H., Klypin, A. A., Gottlöber, S., Allgood, B., and Primack, J. R. (2004). The Dark Side of the Halo Occupation Distribution. *ApJ*, 609:35–49.

Kreisch, C. D., Pisani, A., Carbone, C., Liu, J., Hawken, A. J., Massara, E., Spergel, D. N., and Wandelt, B. D. (2018). Massive Neutrinos Leave Fingerprints on Cosmic Voids. *arXiv e-prints*.

Kristian, J. and Sachs, R. K. (1966). Observations in Cosmology. *ApJ*, 143:379.

Kuijken, K. (1999). Weak weak lensing: correcting weak shear measurements accurately for PSF anisotropy. *AAP*, 352:355–362.

Kuijken, K. (2011). OmegaCAM: ESO's Newest Imager. *The Messenger*, 146:8–11.

Kuijken, K., Heymans, C., Hildebrandt, H., Nakajima, R., Erben, T., de Jong, J. T. A., Viola, M., Choi, A., Hoekstra, H., Miller, L., van Uitert, E., Amon, A., Blake, C., Brouwer, M., Buddendiek, A., Conti, I. F., Eriksen, M., Grado, A., Harnois-Déraps, J., Helmich, E., Herbonnet, R., Irisarri, N., Kitching, T., Klaes, D., La Barbera, F., Napolitano, N., Radovich, M., Schneider, P., Sifón, C., Sikkema, G., Simon, P., Tudorica, A., Valentijn, E., Verdoes Kleijn, G., and van Waerbeke, L. (2015). Gravitational lensing analysis of the Kilo-Degree Survey. *MNRAS*, 454:3500–3532.

Laigle, C., McCracken, H. J., Ilbert, O., Hsieh, B. C., Davidzon, I., Capak, P., Hasinger, G., Silverman, J. D., Pichon, C., Coupon, J., Aussel, H., Le Borgne, D., Caputi, K., Cassata, P., Chang, Y. Y., Civano, F., Dunlop, J., Fynbo, J., Kartaltepe, J. S., Koekemoer, A., Le Fèvre, O., Le Floc'h, E., Leauthaud, A., Lilly, S., Lin, L., Marchesi, S., Milvang- Jensen, B., Salvato, M., Sanders, D. B., Scoville, N., Smolcic, V., Stockmann, M., Taniguchi, Y., Tasca, L., Toft, S., Vaccari, M., and Zabl, J. (2016). The COSMOS2015 Catalog: Exploring the 1 < z < 6 Universe with Half a Million Galaxies. *The Astrophysical Journal Supplement Series*, 224:24.

Lam, T. Y., Clampitt, J., Cai, Y.-C., and Li, B. (2015). Voids in modified gravity reloaded: Eulerian void assignment. *MNRAS*, 450:3319–3330.

Landy, S. D. and Szalay, A. S. (1993). Bias and variance of angular correlation functions. *ApJ*, 412:64–71.

Laureijs, R., Amiaux, J., Arduini, S., Augueres, J. L., Brinchmann, J., Cole, R., Cropper, M., Dabin, C., Duvet, L., Ealet, A., Garilli, B., Gondoin, P., Guzzo, L., Hoar, J., Hoekstra, H., Holmes, R., Kitching, T., Maciaszek, T., Mellier, Y., Pasian, F., Percival, W., Rhodes, J., Saavedra Criado, G., Sauvage, M., Scaramella, R., Valenziano, L., Warren, S., Bender, R., Castander, F., Cimatti, A., Le Fèvre, O., Kurki-Suonio, H., Levi, M., Lilje, P., Meylan, G., Nichol, R., Pedersen, K., Popa, V., Rebolo Lopez, R., Rix, H. W., Rottgering, H., Zeilinger, W., Grupp, F., Hudelot, P., Massey, R., Meneghetti, M., Miller, L., Paltani, S., Paulin-Henriksson, S., Pires, S., Saxton, C., Schrabback, T., Seidel, G., Walsh, J., Aghanim, N., Amendola, L., Bartlett, J., Baccigalupi, C., Beaulieu, J. P., Benabed, K., Cuby, J. G., Elbaz, D., Fosalba, P., Gavazzi, G., Helmi, A., Hook, I., Irwin, M., Kneib, J. P., Kunz, M., Mannucci, F., Moscardini, L., Tao, C., Teyssier, R., Weller, J., Zamorani, G., Zapatero Osorio, M. R., Boulade, O., Foumond, J. J., Di Giorgio, A., Guttridge, P., James, A., Kemp, M., Martignac, J., Spencer, A., Walton, D., Blümchen, T., Bonoli, C., Bortoletto, F., Cerna, C., Corcione, L., Fabron, C., Jahnke, K., Ligori, S., Madrid, F., Martin, L., Morgante, G., Pamplona, T., Prieto, E., Riva, M., Toledo, R., Trifoglio, M., Zerbi, F., Abdalla, F., Douspis, M., Grenet, C., Borgani, S., Bouwens, R., Courbin, F., Delouis, J. M., Dubath, P., Fontana, A., Frailis, M., Grazian, A., Koppenhöfer, J., Mansutti, O., Melchior, M., Mignoli, M., Mohr, J., Neissner, C., Noddle, K., Poncet, M., Scodeggio, M., Serrano, S., Shane, N., Starck, J. L., Surace, C., Taylor, A., Verdoes-Kleijn, G., Vuerli, C., Williams, O. R., Zacchei, A., Altieri, B., Escudero Sanz, I., Kohley, R., Oosterbroek, T., Astier, P., Bacon, D., Bardelli, S., Baugh, C., Bellagamba, F., Benoist, C., Bianchi, D., Biviano, A., Branchini, E., Carbone, C., Cardone, V., Clements, D., Colombi, S., Conselice, C., Cresci, G., Deacon, N., Dunlop, J., Fedeli, C., Fontanot, F., Franzetti, P., Giocoli, C., Garcia-Bellido, J., Gow, J., Heavens, A., Hewett, P., Heymans, C., Holland, A., Huang, Z., Ilbert, O., Joachimi, B., Jennins, E., Kerins, E., Kiessling, A., Kirk, D., Kotak, R., Krause, O., Lahav, O., van Leeuwen, F., Lesgourgues, J., Lombardi, M., Magliocchetti, M., Maguire, K., Majerotto, E., Maoli, R.,

Marulli, F., Maurogordato, S., McCracken, H., McLure, R., Melchiorri, A., Merson, A., Moresco, M., Nonino, M., Norberg, P., Peacock, J., Pello, R., Penny, M., Pettorino, V., Di Porto, C., Pozzetti, L., Quercellini, C., Radovich, M., Rassat, A., Roche, N., Ronayette, S., Rossetti, E., Sartoris, B., Schneider, P., Semboloni, E., Serjeant, S., Simpson, F., Skordis, C., Smadja, G., Smartt, S., Spano, P., Spiro, S., Sullivan, M., Tilquin, A., Trotta, R., Verde, L., Wang, Y., Williger, G., Zhao, G., Zoubian, J., and Zucca, E. (2011). Euclid Definition Study Report. *arXiv e-prints*, page arXiv:1110.3193.

Lavaux, G. and Wandelt, B. D. (2010). Precision cosmology with voids: definition, methods, dynamics. *The Monthly Notices of the Royal Astronomical Society*, 403:1392–1408.

Lavaux, G. and Wandelt, B. D. (2012). Precision Cosmography with Stacked Voids. *ApJ*, 754:109.

Lee, J. and Park, D. (2009). Constraining the Dark Energy Equation of State with Cosmic Voids. *APJL*, 696:L10–L12.

Lemaître, G. (1927). Un Univers homogène de masse constante et de rayon croissant rendant compte de la vitesse radiale des nébuleuses extra-galactiques. *Annales de la Société Scientifique de Bruxelles*, 47:49–59.

Li, B., Zhao, G.-B., and Koyama, K. (2012). Haloes and voids in f(R) gravity. *MNRAS*, 421:3481–3487.

Liang, Y., Zhao, C., Chuang, C.-H., Kitaura, F.-S., and Tao, C. (2016). Measuring baryon acoustic oscillations from the clustering of voids. *MNRAS*, 459:4020–4028.

LIGO Scientific Collaboration, Aasi, J., Abbott, B. P., Abbott, R., Abbott, T., Abernathy, M. R., Ackley, K., Adams, C., Adams, T., Addesso, P., and et al. (2015). Advanced LIGO. *Classical and Quantum Gravity*, 32(7):074001.

Lilje, P. B. and Lahav, O. (1991). Evolution of velocity and density fields around clusters of galaxies. *ApJ*, 374:29–43.

Linde, A. D. (1982). A new inflationary universe scenario: A possible solution of the horizon, flatness, homogeneity, isotropy and primordial monopole problems. *Physics Letters B*, 108(6):389–393.

Liske, J., Baldry, I. K., Driver, S. P., Tuffs, R. J., Alpaslan, M., Andrae, E., Brough, S., Cluver, M. E., Grootes, M. W., Gunawardhana, M. L. P., Kelvin, L. S., Loveday, J., Robotham, A. S. G., Taylor, E. N., Bamford, S. P., Bland-Hawthorn, J., Brown, M. J. I., Drinkwater, M. J., Hopkins, A. M., Meyer, M. J., Norberg, P., Peacock, J. A., Agius, N. K., Andrews, S. K., Bauer, A. E., Ching, J. H. Y., Colless, M., Conselice, C. J., Croom, S. M., Davies, L. J. M., De Propris, R., Dunne, L., Eardley, E. M., Ellis, S., Foster, C., Frenk, C. S., Häußler, B., Holwerda, B. W., Howlett, C., Ibarra, H., Jarvis, M. J.,

Jones, D. H., Kafle, P. R., Lacey, C. G., Lange, R., Lara-López, M. A., López-Sánchez, Á. R., Maddox, S., Madore, B. F., McNaught-Roberts, T., Moffett, A. J., Nichol, R. C., Owers, M. S., Palamara, D., Penny, S. J., Phillipps, S., Pimbblet, K. A., Popescu, C. C., Prescott, M., Proctor, R., Sadler, E. M., Sansom, A. E., Seibert, M., Sharp, R., Sutherland, W., Vázquez-Mata, J. A., van Kampen, E., Wilkins, S. M., Williams, R., and Wright, A. H. (2015). Galaxy And Mass Assembly (GAMA): end of survey report and data release 2. *MNRAS*, 452:2087–2126.

Lombriser, L. and Taylor, A. (2016). Breaking a dark degeneracy with gravitational waves. *Journal of Cosmology and Astro-Particle Physics*, 2016:031.

Longair, M. S. (2008). *Galaxy Formation*.

Lovelock, D. (1971). The einstein tensor and its generalizations. *Journal of Mathematical Physics*, 12(3):498–501.

LSST Science Collaboration, Abell, P. A., Allison, J., Anderson, S. F., Andrew, J. R., Angel, J. R. P., Armus, L., Arnett, D., Asztalos, S. J., Axelrod, T. S., Bailey, S., Ballantyne, D. R., Bankert, J. R., Barkhouse, W. A., Barr, J. D., Barrientos, L. F., Barth, A. J., Bartlett, J. G., Becker, A. C., Becla, J., Beers, T. C., Bernstein, J. P., Biswas, R., Blanton, M. R., Bloom, J. S., Bochanski, J. J., Boeshaar, P., Borne, K. D., Bradac, M., Brandt, W. N., Bridge, C. R., Brown, M. E., Brunner, R. J., Bullock, J. S., Burgasser, A. J., Burge, J. H., Burke, D. L., Cargile, P. A., Chand rasekharan, S., Chartas, G., Chesley, S. R., Chu, Y.-H., Cinabro, D., Claire, M. W., Claver, C. F., Clowe, D., Connolly, A. J., Cook, K. H., Cooke, J., Cooray, A., Covey, K. R., Culliton, C. S., de Jong, R., de Vries, W. H., Debattista, V. P., Delgado, F., Dell'Antonio, I. P., Dhital, S., Di Stefano, R., Dickinson, M., Dilday, B., Djorgovski, S. G., Dobler, G., Donalek, C., Dubois-Felsmann, G., Durech, J., Eliasdottir, A., Eracleous, M., Eyer, L., Falco, E. E., Fan, X., Fassnacht, C. D., Ferguson, H. C., Fernandez, Y. R., Fields, B. D., Finkbeiner, D., Figueroa, E. E., Fox, D. B., Francke, H., Frank, J. S., Frieman, J., Fromenteau, S., Furqan, M., Galaz, G., Gal-Yam, A., Garnavich, P., Gawiser, E., Geary, J., Gee, P., Gibson, R. R., Gilmore, K., Grace, E. A., Green, R. F., Gressler, W. J., Grillmair, C. J., Habib, S., Haggerty, J. S., Hamuy, M., Harris, A. W., Hawley, S. L., Heavens, A. F., Hebb, L., Henry, T. J., Hileman, E., Hilton, E. J., Hoadley, K., Holberg, J. B., Holman, M. J., Howell, S. B., Infante, L., Ivezic, Z., Jacoby, S. H., Jain, B., R, Jedicke, Jee, M. J., Garrett Jernigan, J., Jha, S. W., Johnston, K. V., Jones, R. L., Juric, M., Kaasalainen, M., Styliani, Kafka, Kahn, S. M., Kaib, N. A., Kalirai, J., Kantor, J., Kasliwal, M. M., Keeton, C. R., Kessler, R., Knezevic, Z., Kowalski, A., Krabbendam, V. L., Krughoff, K. S., Kulkarni, S., Kuhlman, S., Lacy, M., Lepine, S., Liang, M., Lien, A., Lira, P., Long, K. S., Lorenz, S., Lotz, J. M., Lupton, R. H., Lutz, J., Macri, L. M., Mahabal, A. A., Mandelbaum, R., Marshall, P., May, M., McGehee, P. M., Meadows, B. T., Meert, A., Milani, A., Miller, C. J., Miller, M., Mills, D., Minniti, D., Monet, D., Mukadam, A. S., Nakar, E., Neill, D. R., Newman, J. A., Nikolaev, S.,

Nordby, M., O'Connor, P., Oguri, M., Oliver, J., Olivier, S. S., Olsen, J. K., Olsen, K., Olszewski, E. W., Oluseyi, H., Padilla, N. D., Parker, A., Pepper, J., Peterson, J. R., Petry, C., Pinto, P. A., Pizagno, J. L., Popescu, B., Prsa, A., Radcka, V., Raddick, M. J., Rasmussen, A., Rau, A., Rho, J., Rhoads, J. E., Richards, G. T., Ridgway, S. T., Robertson, B. E., Roskar, R., Saha, A., Sarajedini, A., Scannapieco, E., Schalk, T., Schindler, R., Schmidt, S., Schmidt, S., Schneider, D. P., Schumacher, G., Scranton, R., Sebag, J., Seppala, L. G., Shemmer, O., Simon, J. D., Sivertz, M., Smith, H. A., Allyn Smith, J., Smith, N., Spitz, A. H., Stanford, A., Stassun, K. G., Strader, J., Strauss, M. A., Stubbs, C. W., Sweeney, D. W., Szalay, A., Szkody, P., Takada, M., Thorman, P., Trilling, D. E., Trimble, V., Tyson, A., Van Berg, R., Vand en Berk, D., VanderPlas, J., Verde, L., Vrsnak, B., Walkowicz, L. M., Wand elt, B. D., Wang, S., Wang, Y., Warner, M., Wechsler, R. H., West, A. A., Wiecha, O., Williams, B. F., Willman, B., Wittman, D., Wolff, S. C., Wood-Vasey, W. M., Wozniak, P., Young, P., Zentner, A., and Zhan, H. (2009). LSST Science Book, Version 2.0. *arXiv e-prints*, page arXiv:0912.0201.

Luppino, G. A. and Kaiser, N. (1997). Detection of Weak Lensing by a Cluster of Galaxies at z = 0.83. *ApJ*, 475:20–28.

Macciò, A. V., Dutton, A. A., van den Bosch, F. C., Moore, B., Potter, D., and Stadel, J. (2007). Concentration, spin and shape of dark matter haloes: scatter and the dependence on mass and environment. *MNRAS*, 378:55–71.

Mackey, J., White, M., and Kamionkowski, M. (2002). Theoretical estimates of intrinsic galaxy alignment. *MNRAS*, 332:788–798.

Madhavacheril, M. S., Battaglia, N., and Miyatake, H. (2017). Fundamental physics from future weak-lensing calibrated Sunyaev-Zel'dovich galaxy cluster counts. *Physical Review D*, 96(10):103525.

Majaess, D. J., Turner, D. G., and Lane, D. J. (2009). Characteristics of the Galaxy according to Cepheids. *MNRAS*, 398:263–270.

Mandelbaum, R. (2018). Weak Lensing for Precision Cosmology. , 56:393–433.

Mandelbaum, R., Hirata, C. M., Seljak, U., Guzik, J., Padmanabhan, N., Blake, C., Blanton, M. R., Lupton, R., and Brinkmann, J. (2005). Systematic errors in weak lensing: application to SDSS galaxy-galaxy weak lensing. *MNRAS*, 361:1287–1322.

Mandelbaum, R., Seljak, U., Baldauf, T., and Smith, R. E. (2010). Precision cluster mass determination from weak lensing. *MNRAS*, 405:2078–2102.

Mandelbaum, R., Seljak, U., Kauffmann, G., Hirata, C. M., and Brinkmann, J. (2006). Galaxy halo masses and satellite fractions from galaxy-galaxy lensing in the Sloan Digital Sky Survey: stellar mass, luminosity, morphology and environment dependencies. *MNRAS*, 368:715–731.

Mao, Q., Berlind, A. A., Scherrer, R. J., Neyrinck, M. C., Scoccimarro, R., Tinker, J. L., McBride, C. K., and Schneider, D. P. (2017). Cosmic Voids in the SDSS DR12 BOSS Galaxy Sample: The Alcock-Paczynski Test. *ApJ*, 835:160.

Markevitch, M., Gonzalez, A. H., Clowe, D., Vikhlinin, A., Forman, W., Jones, C., Murray, S., and Tucker, W. (2004). Direct Constraints on the Dark Matter Self-Interaction Cross Section from the Merging Galaxy Cluster 1E 0657-56. *APJ*, 606:819–824.

Martinet, N., Schneider, P., Hildebrandt, H., Shan, H., Asgari, M., Dietrich, J. P., Harnois-Déraps, J., Erben, T., Grado, A., Heymans, C., Hoekstra, H., Klaes, D., Kuijken, K., Merten, J., and Nakajima, R. (2018). KiDS-450: cosmological constraints from weak-lensing peak statistics - II: Inference from shear peaks using N-body simulations. *MNRAS*, 474:712–730.

Massara, E. and Sheth, R. K. (2018). Density and velocity profiles around cosmic voids. *arXiv e-prints*.

Massara, E., Villaescusa-Navarro, F., Viel, M., and Sutter, P. M. (2015). Voids in massive neutrino cosmologies. *JCAP*, 11:018.

Massey, R., Schrabback, T., Cordes, O., Marggraf, O., Israel, H., Miller, L., Hall, D., Cropper, M., Prod'homme, T., and Niemi, S.-M. (2014). An improved model of charge transfer inefficiency and correction algorithm for the Hubble Space Telescope. *MNRAS*, 439:887–907.

Matsubara, T. (2008). Nonlinear perturbation theory with halo bias and redshift-space distortions via the Lagrangian picture. *Physical Review D*, 78(8):083519.

McDonald, P. and Seljak, U. (2009). How to evade the sample variance limit on measurements of redshift-space distortions. *Journal of Cosmology and Astro-Particle Physics*, 2009:007.

Melchior, P., Sutter, P. M., Sheldon, E. S., Krause, E., and Wandelt, B. D. (2014). First measurement of gravitational lensing by cosmic voids in sdss. *The Monthly Notices of the Royal Astronomical Society*, 440:2922–2927.

Melchior, P. and Viola, M. (2012). Means of confusion: how pixel noise affects shear estimates for weak gravitational lensing. *MNRAS*, 424:2757–2769.

Melchior, P., Viola, M., Schäfer, B. M., and Bartelmann, M. (2011). Weak gravitational lensing with DEIMOS. *MNRAS*, 412:1552–1558.

Micheletti, D., Iovino, A., Hawken, A. J., Granett, B. R., Bolzonella, M., Cappi, A., Guzzo, L., Abbas, U., Adami, C., Arnouts, S., Bel, J., Bottini, D., Branchini, E., Coupon, J., Cucciati, O., Davidzon, I., De Lucia, G., de la Torre, S., Fritz, A., Franzetti, P., Fumana, M., Garilli, B., Ilbert, O., Krywult, J., Le Brun, V., Le Fèvre, O., Maccagni, D., Małek, K., Marulli, F., McCracken, H. J., Polletta, M., Pollo, A., Schimd, C., Scodeggio, M., Tasca, L. A. M., Tojeiro, R., Vergani, D., Zanichelli, A., Burden, A., Di Porto, C., Marchetti, A., Marinoni,

C., Mellier, Y., Moutard, T., Moscardini, L., Nichol, R. C., Peacock, J. A., Percival, W. J., and Zamorani, G. (2014). The VIMOS Public Extragalactic Redshift Survey. Searching for cosmic voids. *AAP*, 570:A106.

Miller, L., Heymans, C., Kitching, T. D., van Waerbeke, L., Erben, T., Hildebrandt, H., Hoekstra, H., Mellier, Y., Rowe, B. T. P., Coupon, J., Dietrich, J. P., Fu, L., Harnois-Déraps, J., Hudson, M. J., Kilbinger, M., Kuijken, K., Schrabback, T., Semboloni, E., Vafaei, S., and Velander, M. (2013). Bayesian galaxy shape measurement for weak lensing surveys - III. Application to the Canada-France-Hawaii Telescope Lensing Survey. *MNRAS*, 429:2858–2880.

Miller, L., Kitching, T. D., Heymans, C., Heavens, A. F., and van Waerbeke, L. (2007). Bayesian galaxy shape measurement for weak lensing surveys - I. Methodology and a fast-fitting algorithm. *MNRAS*, 382:315–324.

Miyazaki, S., Komiyama, Y., Nakaya, H., Kamata, Y., Doi, Y., Hamana, T., Karoji, H., Furusawa, H., Kawanomoto, S., Morokuma, T., Ishizuka, Y., Nariai, K., Tanaka, Y., Uraguchi, F., Utsumi, Y., Obuchi, Y., Okura, Y., Oguri, M., Takata, T., Tomono, D., Kurakami, T., Namikawa, K., Usuda, T., Yamanoi, H., Terai, T., Uekiyo, H., Yamada, Y., Koike, M., Aihara, H., Fujimori, Y., Mineo, S., Miyatake, H., Yasuda, N., Nishizawa, J., Saito, T., Tanaka, M., Uchida, T., Katayama, N., Wang, S.-Y., Chen, H.-Y., Lupton, R., Loomis, C., Bickerton, S., Price, P., Gunn, J., Suzuki, H., Miyazaki, Y., Muramatsu, M., Yamamoto, K., Endo, M., Ezaki, Y., Itoh, N., Miwa, Y., Yokota, H., Matsuda, T., Ebinuma, R., and Takeshi, K. (2012). Hyper Suprime-Cam. In *Ground-based and Airborne Instrumentation for Astronomy IV*, volume 8446 of , page 84460Z.

Moore, B. and Silk, J. (1995). Dynamical and observable constraints on RAMBOs: Robust associations of massive baryonic objects. , 442:L5–L8.

Nadathur, S., Carter, P., and Percival, W. J. (2019a). A Zeldovich reconstruction method for measuring redshift space distortions using cosmic voids. *MNRAS*, 482:2459–2470.

Nadathur, S., Carter, P. M., Percival, W. J., Winther, H. A., and Bautista, J. (2019b). Beyond BAO: improving cosmological constraints from BOSS with measurement of the void-galaxy cross-correlation. *arXiv e-prints*, page arXiv:1904.01030.

Nadathur, S., Hotchkiss, S., and Sarkar, S. (2012). The integrated Sachs-Wolfe imprint of cosmic superstructures: a problem for ΛCDM. *JCAP*, 6:42.

Nadathur, S. and Percival, W. J. (2019). An accurate linear model for redshift space distortions in the void-galaxy correlation function. *MNRAS*, 483:3472–3487.

Naselsky, P. D., Novikov, D. I., and Novikov, I. D. (2006). *The Physics of the Cosmic Microwave Background*.

Navarro, J. F., Frenk, C. S., and White, S. D. M. (1996). The Structure of Cold Dark Matter Halos. *ApJ*, 462:563.

Newman, J. A., Abate, A., Abdalla, F. B., Allam, S., Allen, S. W., Ansari, R., Bailey, S., Barkhouse, W. A., Beers, T. C., Blanton, M. R., Brodwin, M., Brownstein, J. R., Brunner, R. J., Carrasco Kind, M., Cervantes-Cota, J. L., Cheu, E., Chisari, N. E., Colless, M., Comparat, J., Coupon, J., Cunha, C. E., de la Macorra, A., Dell'Antonio, I. P., Frye, B. L., Gawiser, E. J., Gehrels, N., Grady, K., Hagen, A., Hall, P. B., Hearin, A. P., Hildebrandt, H., Hirata, C. M., Ho, S., Honscheid, K., Huterer, D., Ivezić, Ž., Kneib, J.-P., Kruk, J. W., Lahav, O., Mandelbaum, R., Marshall, J. L., Matthews, D. J., Ménard, B., Miquel, R., Moniez, M., Moos, H. W., Moustakas, J., Myers, A. D., Papovich, C., Peacock, J. A., Park, C., Rahman, M., Rhodes, J., Ricol, J.-S., Sadeh, I., Slozar, A., Schmidt, S. J., Stern, D. K., Anthony Tyson, J., von der Linden, A., Wechsler, R. H., Wood-Vasey, W. M., and Zentner, A. R. (2015). Spectroscopic needs for imaging dark energy experiments. *Astroparticle Physics*, 63:81–100.

Newman, J. A., Cooper, M. C., Davis, M., Faber, S. M., Coil, A. L., Guhathakurta, P., Koo, D. C., Phillips, A. C., Conroy, C., Dutton, A. A., Finkbeiner, D. P., Gerke, B. F., Rosario, D. J., Weiner, B. J., Willmer, C. N. A., Yan, R., Harker, J. J., Kassin, S. A., Konidaris, N. P., Lai, K., Madgwick, D. S., Noeske, K. G., Wirth, G. D., Connolly, A. J., Kaiser, N., Kirby, E. N., Lemaux, B. C., Lin, L., Lotz, J. M., Luppino, G. A., Marinoni, C., Matthews, D. J., Metevier, A., and Schiavon, R. P. (2013). The DEEP2 Galaxy Redshift Survey: Design, Observations, Data Reduction, and Redshifts. *ApJS*, 208:5.

Neyrinck, M. C. (2008). Zobov: a parameter-free void-finding algorithm. *The Monthly Notices of the Royal Astronomical Society*, 386:2101–2109.

Neyrinck, M. C., Aragón-Calvo, M. A., Jeong, D., and Wang, X. (2014). A halo bias function measured deeply into voids without stochasticity. *MNRAS*, 441:646–655.

Neyrinck, M. C., Szapudi, I., McCullagh, N., Szalay, A. S., Falck, B., and Wang, J. (2018). Density-dependent clustering - I. Pullingback the curtains on motions of the BAO peak. *MNRAS*, 478:2495–2504.

Ngan, W., van Waerbeke, L., Mahdavi, A., Heymans, C., and Hoekstra, H. (2009). Sérsiclets - a matched filter extension of Shapelets for weak lensing studies. *MNRAS*, 396:1211–1216.

Okabe, A., Boots, B., Sugihara, K., and Chiu, S. N. (2000). *Spatial tessellations: concepts and algorithms of Voronoi diagrams*. J. Wiley Sons.

Okumura, T., Hikage, C., Totani, T., Tonegawa, M., Okada, H., Glazebrook, K., Blake, C., Ferreira, P. G., More, S., Taruya, A., Tsujikawa, S., Akiyama, M., Dalton, G., Goto, T., Ishikawa, T., Iwamuro, F., Matsubara, T., Nishimichi, T., Ohta, K., Shimizu, I., Takahashi, R., Takato, N., Tamura, N., Yabe, K., and

Yoshida, N. (2016). The Subaru FMOS galaxy redshift survey (FastSound). IV. New constraint on gravity theory from redshift space distortions at z 1.4. , 68:38.

Oort, J. H. (1940). Some Problems Concerning the Structure and Dynamics of the Galactic System and the Elliptical Nebulae NGC 3115 and 4494. *ApJ*, 91:273.

Padilla, N. D., Ceccarelli, L., and Lambas, D. G. (2005). Spatial and dynamical properties of voids in a Λ cold dark matter universe. *MNRAS*, 363:977–990.

Panagia, N. (1998). New Distance Determination to the LMC. , 69:225.

Peacock, J. A. (1999). *Cosmological Physics*.

Peacock, J. A. (2007). Testing anthropic predictions for Λ and the cosmic microwave background temperature. *MNRAS*, 379:1067–1074.

Peacock, J. A., Cole, S., Norberg, P., Baugh, C. M., Bland-Hawthorn, J., Bridges, T., Cannon, R. D., Colless, M., Collins, C., Couch, W., Dalton, G., Deeley, K., De Propris, R., Driver, S. P., Efstathiou, G., Ellis, R. S., Frenk, C. S., Glazebrook, K., Jackson, C., Lahav, O., Lewis, I., Lumsden, S., Maddox, S., Percival, W. J., Peterson, B. A., Price, I., Sutherland, W., and Taylor, K. (2001). A measurement of the cosmological mass density from clustering in the 2dF Galaxy Redshift Survey. , 410:169–173.

Peacock, J. A. and Smith, R. E. (2000). Halo occupation numbers and galaxy bias. *MNRAS*, 318:1144–1156.

Peccei, R. D. and Quinn, H. R. (1977). CP conservation in the presence of pseudoparticles. *Physical Review Letters*, 38:1440–1443.

Peebles, P. (1980). *The Large-scale Structure of the Universe*. Princeton UP.

Peebles, P. (1993). *Principles of Physical Cosmology*. Princeton University Press.

Peebles, P. J. E. (2001). The Void Phenomenon. *APJ*, 557:495–504.

Pen, U.-L. (2004). Beating lensing cosmic variance with galaxy tomography. *MNRAS*, 350:1445–1448.

Penrose, R. (1989). Difficulties with inflationary cosmology. *Annals of the New York Academy of Sciences*, 571:249–264.

Penzias, A. A. and Wilson, R. W. (1965). A Measurement of Excess Antenna Temperature at 4080 Mc/s. *ApJ*, 142:419–421.

Perlmutter, S., Aldering, G., Goldhaber, G., Knop, R. A., Nugent, P., Castro, P. G., Deustua, S., Fabbro, S., Goobar, A., Groom, D. E., Hook, I. M., Kim, A. G., Kim, M. Y., Lee, J. C., Nunes, N. J., Pain, R., Pennypacker, C. R., Quimby, R., Lidman, C., Ellis, R. S., Irwin, M., McMahon, R. G.,

Ruiz-Lapuente, P., Walton, N., Schaefer, B., Boyle, B. J., Filippenko, A. V., Matheson, T., Fruchter, A. S., Panagia, N., Newberg, H. J. M., Couch, W. J., and Project, T. S. C. (1999). Measurements of Ω and Λ from 42 High-Redshift Supernovae. *APJ*, 517:565–586.

Phillips, M. M., Wells, L. A., Suntzeff, N. B., Hamuy, M., Leibundgut, B., Kirshner, R. P., and Foltz, C. B. (1992). SN 1991T - Further evidence of the heterogeneous nature of type IA supernovae. *AJ*, 103:1632–1637.

Pietrzynski, G., Graczyk, D., Gallenne, A., Gieren, W., Thompson, I. B., Pilecki, B., Karczmarek, P., Gorski, M., Suchomska, K., Taormina, M., Zgirski, B., Wielgorski, P., Kolaczkowski, Z., Konorski, P., Villanova, S., Nardetto, N., Kervella, P., Bresolin, F., Kudritzki, R. P., Storm, J., Smolec, R., and Narloch, W. (2019). A distance to the Large Magellanic Cloud that is precise to one per cent. *arXiv e-prints*, page arXiv:1903.08096.

Pisani, A., Lavaux, G., Sutter, P. M., and Wandelt, B. D. (2014). Real-space density profile reconstruction of stacked voids. *MNRAS*, 443:3238–3250.

Pisani, A., Massara, E., Spergel, D. N., Alonso, D., Baker, T., Cai, Y.-C., Cautun, M., Davies, C., Demchenko, V., Doré, O., Goulding, A., Habouzit, M., Hamaus, N., Hawken, A., Hirata, C. M., Ho, S., Jain, B., Kreisch, C. D., Marulli, F., Padilla, N., Pollina, G., Sahlén, M., Sheth, R. K., Somerville, R., Szapudi, I., van de Weygaert, R., Villaescusa-Navarro, F., Wandelt, B. D., and Wang, Y. (2019). Cosmic voids: a novel probe to shed light on our Universe. *arXiv e-prints*, page arXiv:1903.05161.

Pisani, A., Sutter, P. M., Hamaus, N., Alizadeh, E., Biswas, R., Wandelt, B. D., and Hirata, C. M. (2015). Counting voids to probe dark energy. *Physical Review D*, 92(8):083531.

Planck Collaboration, Ade, P. A. R., Aghanim, N., Armitage-Caplan, C., Arnaud, M., Ashdown, M., Atrio-Barandela, F., Aumont, J., Baccigalupi, C., Banday, A. J., and et al. (2014). Planck 2013 results. XIX. The integrated Sachs-Wolfe effect. *AAP*, 571:A19.

Planck Collaboration, Ade, P. A. R., Aghanim, N., Arnaud, M., Ashdown, M., Aumont, J., Baccigalupi, C., Banday, A. J., Barreiro, R. B., Bartolo, N., and et al. (2015). Planck 2015 results. XXI. The integrated Sachs-Wolfe effect. *ArXiv e-prints:1502.01595*.

Planck Collaboration, Aghanim, N., Akrami, Y., Ashdown, M., Aumont, J., Baccigalupi, C., Ballardini, M., Banday, A. J., Barreiro, R. B., Bartolo, N., Basak, S., Battye, R., Benabed, K., Bernard, J. P., Bersanelli, M., Bielewicz, P., Bock, J. J., Bond, J. R., Borrill, J., Bouchet, F. R., Boulanger, F., Bucher, M., Burigana, C., Butler, R. C., Calabrese, E., Cardoso, J. F., Carron, J., Challinor, A., Chiang, H. C., Chluba, J., Colombo, L. P. L., Combet, C., Contreras, D., Crill, B. P., Cuttaia, F., de Bernardis, P., de Zotti, G., Delabrouille, J., Delouis, J. M., Di Valentino, E., Diego, J. M., Doré, O., Douspis, M., Ducout,

A., Dupac, X., Dusini, S., Efstathiou, G., Elsner, F., Enßlin, T. A., Eriksen, H. K., Fantaye, Y., Farhang, M., Fergusson, J., Fernandez-Cobos, R., Finelli, F., Forastieri, F., Frailis, M., Franceschi, E., Frolov, A., Galeotta, S., Galli, S., Ganga, K., Génova-Santos, R. T., Gerbino, M., Ghosh, T., González-Nuevo, J., Górski, K. M., Gratton, S., Gruppuso, A., Gudmundsson, J. E., Hamann, J., Handley, W., Herranz, D., Hivon, E., Huang, Z., Jaffe, A. H., Jones, W. C., Karakci, A., Keihänen, E., Keskitalo, R., Kiiveri, K., Kim, J., Kisner, T. S., Knox, L., Krachmalnicoff, N., Kunz, M., Kurki-Suonio, H., Lagache, G., Lamarre, J. M., Lasenby, A., Lattanzi, M., Lawrence, C. R., Le Jeune, M., Lemos, P., Lesgourgues, J., Levrier, F., Lewis, A., Liguori, M., Lilje, P. B., Lilley, M., Lindholm, V., López-Caniego, M., Lubin, P. M., Ma, Y. Z., Macías-Pérez, J. F., Maggio, G., Maino, D., Mandolesi, N., Mangilli, A., Marcos-Caballero, A., Maris, M., Martin, P. G., Martinelli, M., Martínez-González, E., Matarrese, S., Mauri, N., McEwen, J. D., Meinhold, P. R., Melchiorri, A., Mennella, A., Migliaccio, M., Millea, M., Mitra, S., Miville-Deschênes, M. A., Molinari, D., Montier, L., Morgante, G., Moss, A., Natoli, P., Nørgaard-Nielsen, H. U., Pagano, L., Paoletti, D., Partridge, B., Patanchon, G., Peiris, H. V., Perrotta, F., Pettorino, V., Piacentini, F., Polastri, L., Polenta, G., Puget, J. L., Rachen, J. P., Reinecke, M., Remazeilles, M., Renzi, A., Rocha, G., Rosset, C., Roudier, G., Rubiño-Martín, J. A., Ruiz-Granados, B., Salvati, L., Sandri, M., Savelainen, M., Scott, D., Shellard, E. P. S., Sirignano, C., Sirri, G., Spencer, L. D., Sunyaev, R., Suur-Uski, A. S., Tauber, J. A., Tavagnacco, D., Tenti, M., Toffolatti, L., Tomasi, M., Trombetti, T., Valenziano, L., Valiviita, J., Van Tent, B., Vibert, L., Vielva, P., Villa, F., Vittorio, N., Wandelt, B. D., Wehus, I. K., White, M., White, S. D. M., Zacchei, A., and Zonca, A. (2018a). Planck 2018 results. VI. Cosmological parameters. *arXiv e-prints*, page arXiv:1807.06209.

Planck Collaboration, Akrami, Y., Arroja, F., Ashdown, M., Aumont, J., Baccigalupi, C., Ballardini, M., Banday, A. J., Barreiro, R. B., Bartolo, N., Basak, S., Battye, R., Benabed, K., Bernard, J. P., Bersanelli, M., Bielewicz, P., Bock, J. J., Bond, J. R., Borrill, J., Bouchet, F. R., Boulanger, F., Bucher, M., Burigana, C., Butler, R. C., Calabrese, E., Cardoso, J. F., Carron, J., Casaponsa, B., Challinor, A., Chiang, H. C., Colombo, L. P. L., Combet, C., Contreras, D., Crill, B. P., Cuttaia, F., de Bernardis, P., de Zotti, G., Delabrouille, J., Delouis, J. M., Désert, F. X., Di Valentino, E., Dickinson, C., Diego, J. M., Donzelli, S., Doré, O., Douspis, M., Ducout, A., Dupac, X., Efstathiou, G., Elsner, F., Enßlin, T. A., Eriksen, H. K., Falgarone, E., Fantaye, Y., Fergusson, J., Fernandez-Cobos, R., Finelli, F., Forastieri, F., Frailis, M., Franceschi, E., Frolov, A., Galeotta, S., Galli, S., Ganga, K., Génova-Santos, R. T., Gerbino, M., Ghosh, T., González-Nuevo, J., Górski, K. M., Gratton, S., Gruppuso, A., Gudmundsson, J. E., Hamann, J., Hand ley, W., Hansen, F. K., Helou, G., Herranz, D., Hivon, E., Huang, Z., Jaffe, A. H., Jones, W. C., Karakci, A., Keihänen, E., Keskitalo, R., Kiiveri, K., Kim, J., Kisner, T. S., Knox, L., Krachmalnicoff, N., Kunz, M., Kurki-Suonio, H., Lagache, G., Lamarre, J. M., Langer, M., Lasenby, A., Lattanzi, M., Lawrence, C. R., Le Jeune, M., Leahy, J. P., Lesgourgues, J., Levrier, F.,

Lewis, A., Liguori, M., Lilje, P. B., Lilley, M., Lindholm, V., López-Caniego, M., Lubin, P. M., Ma, Y. Z., Macías-Pérez, J. F., Maggio, G., Maino, D., Mand olesi, N., Mangilli, A., Marcos-Caballero, A., Maris, M., Martin, P. G., Martínez-González, E., Matarrese, S., Mauri, N., McEwen, J. D., Meerburg, P. D., Meinhold, P. R., Melchiorri, A., Mennella, A., Migliaccio, M., Millea, M., Mitra, S., Miville-Deschênes, M. A., Molinari, D., Moneti, A., Montier, L., Morgante, G., Moss, A., Mottet, S., Münchmeyer, M., Natoli, P., Nørgaard-Nielsen, H. U., Oxborrow, C. A., Pagano, L., Paoletti, D., Partridge, B., Patanchon, G., Pearson, T. J., Peel, M., Peiris, H. V., Perrotta, F., Pettorino, V., Piacentini, F., Polastri, L., Polenta, G., Puget, J. L., Rachen, J. P., Reinecke, M., Remazeilles, M., Renzi, A., Rocha, G., Rosset, C., Roudier, G., Rubiño-Martín, J. A., Ruiz-Granados, B., Salvati, L., Sandri, M., Savelainen, M., Scott, D., Shellard, E. P. S., Shiraishi, M., Sirignano, C., Sirri, G., Spencer, L. D., Sunyaev, R., Suur-Uski, A. S., Tauber, J. A., Tavagnacco, D., Tenti, M., Terenzi, L., Toffolatti, L., Tomasi, M., Trombetti, T., Valiviita, J., Van Tent, B., Vibert, L., Vielva, P., Villa, F., Vittorio, N., Wandelt, B. D., Wehus, I. K., White, M., White, S. D. M., Zacchei, A., and Zonca, A. (2018b). Planck 2018 results. I. Overview and the cosmological legacy of Planck. *arXiv e-prints*, page arXiv:1807.06205.

Platen, E., van de Weygaert, R., and Jones, B. J. T. (2007). A cosmic watershed: the WVF void detection technique. *MNRAS*, 380:551–570.

Pogosyan, D., Bond, J. R., Kofman, L., and Wadsley, J. (1998). Cosmic web: Origin and observables. *Wide Field Surveys in Cosmology*, page 61.

Pollina, G., Baldi, M., Marulli, F., and Moscardini, L. (2016). Cosmic voids in coupled dark energy cosmologies: the impact of halo bias. *MNRAS*, 455:3075–3085.

Pollina, G., Hamaus, N., Paech, K., Dolag, K., Weller, J., Sánchez, C., Rykoff, E. S., Jain, B., Abbott, T. M. C., Allam, S., Avila, S., Bernstein, R. A., Bertin, E., Brooks, D., Burke, D. L., Carnero Rosell, A., Carrasco Kind, M., Carretero, J., Cunha, C. E., D'Andrea, C. B., da Costa, L. N., De Vicente, J., DePoy, D. L., Desai, S., Diehl, H. T., Doel, P., Evrard, A. E., Flaugher, B., Fosalba, P., Frieman, J., García-Bellido, J., Gerdes, D. W., Giannantonio, T., Gruen, D., Gschwend, J., Gutierrez, G., Hartley, W. G., Hollowood, D. L., Honscheid, K., Hoyle, B., James, D. J., Jeltema, T., Kuehn, K., Kuropatkin, N., Lima, M., March, M., Marshall, J. L., Melchior, P., Menanteau, F., Miquel, R., Plazas, A. A., Romer, A. K., Sanchez, E., Scarpine, V., Schindler, R., Schubnell, M., Sevilla-Noarbe, I., Smith, M., Soares-Santos, M., Sobreira, F., Suchyta, E., Tarle, G., Walker, A. R., and Wester, W. (2018). On the relative bias of void tracers in the Dark Energy Survey. *arXiv e-prints*.

Press, W. H. and Schechter, P. (1974). Formation of galaxies and clusters of galaxies by self-similar gravitational condensation. *Astrophysical Journal*, 187:425–438.

Refregier, A. (2003). Shapelets - I. A method for image analysis. *MNRAS*, 338:35–47.

Refregier, A. and Bacon, D. (2003). Shapelets - II. A method for weak lensing measurements. *MNRAS*, 338:48–56.

Refregier, A., Kacprzak, T., Amara, A., Bridle, S., and Rowe, B. (2012). Noise bias in weak lensing shape measurements. *MNRAS*, 425:1951–1957.

Regos, E. & Geller, M. J. (1991). The evolution of void-filled cosmological structures. *apj*, 377:14–28.

Reid, B., Ho, S., Padmanabhan, N., Percival, W. J., Tinker, J., Tojeiro, R., White, M., Eisenstein, D. J., Maraston, C., Ross, A. J., Sánchez, A. G., Schlegel, D., Sheldon, E., Strauss, M. A., Thomas, D., Wake, D., Beutler, F., Bizyaev, D., Bolton, A. S., Brownstein, J. R., Chuang, C.-H., Dawson, K., Harding, P., Kitaura, F.-S., Leauthaud, A., Masters, K., McBride, C. K., More, S., Olmstead, M. D., Oravetz, D., Nuza, S. E., Pan, K., Parejko, J., Pforr, J., Prada, F., Rodríguez-Torres, S., Salazar-Albornoz, S., Samushia, L., Schneider, D. P., Scóccola, C. G., Simmons, A., and Vargas-Magana, M. (2016). SDSS-III Baryon Oscillation Spectroscopic Survey Data Release 12: galaxy target selection and large-scale structure catalogues. *MNRAS*, 455:1553–1573.

Reid, B. A., Samushia, L., White, M., Percival, W. J., Manera, M., Padmanabhan, N., Ross, A. J., Sánchez, A. G., Bailey, S., Bizyaev, D., Bolton, A. S., Brewington, H., Brinkmann, J., Brownstein, J. R., Cuesta, A. J., Eisenstein, D. J., Gunn, J. E., Honscheid, K., Malanushenko, E., Malanushenko, V., Maraston, C., McBride, C. K., Muna, D., Nichol, R. C., Oravetz, D., Pan, K., de Putter, R., Roe, N. A., Ross, N. P., Schlegel, D. J., Schneider, D. P., Seo, H.-J., Shelden, A., Sheldon, E. S., Simmons, A., Skibba, R. A., Snedden, S., Swanson, M. E. C., Thomas, D., Tinker, J., Tojeiro, R., Verde, L., Wake, D. A., Weaver, B. A., Weinberg, D. H., Zehavi, I., and Zhao, G.-B. (2012). The clustering of galaxies in the SDSS-III Baryon Oscillation Spectroscopic Survey: measurements of the growth of structure and expansion rate at z = 0.57 from anisotropic clustering. *MNRAS*, 426:2719–2737.

Reid, B. A., Seo, H.-J., Leauthaud, A., Tinker, J. L., and White, M. (2014). A 2.5 per cent measurement of the growth rate from small-scale redshift space clustering of SDSS-III CMASS galaxies. *MNRAS*, 444:476–502.

Reid, B. A. and White, M. (2011). Towards an accurate model of the redshift-space clustering of haloes in the quasi-linear regime. *MNRAS*, 417:1913–1927.

Rhodes, J., Leauthaud, A., Stoughton, C., Massey, R., Dawson, K., Kolbe, W., and Roe, N. (2010). The Effects of Charge Transfer Inefficiency (CTI) on Galaxy Shape Measurements. *PASP*, 122:439.

Ricciardelli, E., Cava, A., Varela, J., and Quilis, V. (2014). The star formation activity in cosmic voids. *MNRAS*, 445:4045–4054.

Riess, A. G., Casertano, S., Yuan, W., Macri, L. M., and Scolnic, D. (2019). Large Magellanic Cloud Cepheid Standards Provide a 1% Foundation for the Determination of the Hubble Constant and Stronger Evidence for Physics Beyond LambdaCDM. *arXiv e-prints*, page arXiv:1903.07603.

Riess, A. G., Filippenko, A. V., Challis, P., Clocchiatti, A., Diercks, A., Garnavich, P. M., Gilliland, R. L., Hogan, C. J., Jha, S., Kirshner, R. P., Leibundgut, B., Phillips, M. M., Reiss, D., Schmidt, B. P., Schommer, R. A., Smith, R. C., Spyromilio, J., Stubbs, C., Suntzeff, N. B., and Tonry, J. (1998). Observational Evidence from Supernovae for an Accelerating Universe and a Cosmological Constant. *AJ*, 116:1009–1038.

Riess, A. G., Macri, L. M., Hoffmann, S. L., Scolnic, D., Casertano, S., Filippenko, A. V., Tucker, B. E., Reid, M. J., Jones, D. O., Silverman, J. M., Chornock, R., Challis, P., Yuan, W., Brown, P. J., and Foley, R. J. (2016). A 2.4% Determination of the Local Value of the Hubble Constant. *ApJ*, 826:56.

Robotham, A. S. G., Norberg, P., Driver, S. P., Baldry, I. K., Bamford, S. P., Hopkins, A. M., Liske, J., Loveday, J., Merson, A., Peacock, J. A., Brough, S., Cameron, E., Conselice, C. J., Croom, S. M., Frenk, C. S., Gunawardhana, M., Hill, D. T., Jones, D. H., Kelvin, L. S., Kuijken, K., Nichol, R. C., Parkinson, H. R., Pimbblet, K. A., Phillipps, S., Popescu, C. C., Prescott, M., Sharp, R. G., Sutherland, W. J., Taylor, E. N., Thomas, D., Tuffs, R. J., van Kampen, E., and Wijesinghe, D. (2011). Galaxy and Mass Assembly (GAMA): the GAMA galaxy group catalogue (G^3Cv1). *MNRAS*, 416:2640–2668.

Rojas, R. R., Vogeley, M. S., Hoyle, F., and Brinkmann, J. (2004). Photometric Properties of Void Galaxies in the Sloan Digital Sky Survey. *ApJ*, 617:50–63.

Rozo, E., Rykoff, E. S., Abate, A., Bonnett, C., Crocce, M., Davis, C., Hoyle, B., Leistedt, B., Peiris, H. V., Wechsler, R. H., Abbott, T., Abdalla, F. B., Banerji, M., Bauer, A. H., Benoit-Lévy, A., Bernstein, G. M., Bertin, E., Brooks, D., Buckley-Geer, E., Burke, D. L., Capozzi, D., Rosell, A. C., Carollo, D., Kind, M. C., Carretero, J., Castander, F. J., Childress, M. J., Cunha, C. E., D'Andrea, C. B., Davis, T., DePoy, D. L., Desai, S., Diehl, H. T., Dietrich, J. P., Doel, P., Eifler, T. F., Evrard, A. E., Neto, A. F., Flaugher, B., Fosalba, P., Frieman, J., Gaztanaga, E., Gerdes, D. W., Glazebrook, K., Gruen, D., Gruendl, R. A., Honscheid, K., James, D. J., Jarvis, M., Kim, A. G., Kuehn, K., Kuropatkin, N., Lahav, O., Lidman, C., Lima, M., Maia, M. A. G., March, M., Martini, P., Melchior, P., Miller, C. J., Miquel, R., Mohr, J. J., Nichol, R. C., Nord, B., O'Neill, C. R., Ogando, R., Plazas, A. A., Romer, A. K., Roodman, A., Sako, M., Sanchez, E., Santiago, B., Schubnell, M., Sevilla-Noarbe, I., Smith, R. C., Soares-Santos, M., Sobreira, F., Suchyta, E., Swanson, M. E. C., Thaler, J., Thomas, D., Uddin, S., Vikram, V., Walker, A. R., Wester, W., Zhang, Y., and da Costa, L. N. (2016). redMaGiC: selecting luminous red galaxies from the DES Science Verification data. *MNRAS*, 461:1431–1450.

Rubin, V. C. and Ford, Jr., W. K. (1970). Rotation of the Andromeda Nebula from a Spectroscopic Survey of Emission Regions. *ApJ*, 159:379.

Rubin, V. C., Ford, Jr., W. K., and Thonnard, N. (1978). Extended rotation curves of high-luminosity spiral galaxies. IV - Systematic dynamical properties, SA through SC. , 225:L107–L111.

Rubin, V. C., Ford, Jr., W. K., and Thonnard, N. (1980). Rotational properties of 21 SC galaxies with a large range of luminosities and radii, from NGC 4605 /R = 4kpc/ to UGC 2885 /R = 122 kpc/. *ApJ*, 238:471–487.

Ryden, B. S. (1995). Measuring q_0 from the Distortion of Voids in Redshift Space. *APJ*, 452:25.

Sachs, R. K. and Wolfe, A. M. (1967). Perturbations of a Cosmological Model and Angular Variations of the Microwave Background. *APJ*, 147:73.

Sadeh, I., Abdalla, F. B., and Lahav, O. (2016). ANNz2: Photometric Redshift and Probability Distribution Function Estimation using Machine Learning. *PASP*, 128(10):104502.

Salvato, M., Ilbert, O., and Hoyle, B. (2018). The many flavours of photometric redshifts. *Nature Astronomy*, page 68.

Samuroff, S., Blazek, J., Troxel, M. A., MacCrann, N., Krause, E., Leonard, C. D., Prat, J., Gruen, D., Dodelson, S., Eifler, T. F., Gatti, M., Hartley, W. G., Hoyle, B., Larsen, P., Zuntz, J., Abbott, T. M. C., Allam, S., Annis, J., Bernstein, G. M., Bertin, E., Bridle, S. L., Brooks, D., Carnero Rosell, A., Carrasco Kind, M., Carretero, J., Castander, F. J., Cunha, C. E., da Costa, L. N., Davis, C., De Vicente, J., DePoy, D. L., Desai, S., Diehl, H. T., Dietrich, J. P., Doel, P., Flaugher, B., Fosalba, P., Frieman, J., García-Bellido, J., Gaztanaga, E., Gerdes, D. W., Gruendl, R. A., Gschwend, J., Gutierrez, G., Hollowood, D. L., Honscheid, K., James, D. J., Kuehn, K., Kuropatkin, N., Lima, M., Maia, M. A. G., March, M., Marshall, J. L., Martini, P., Melchior, P., Menanteau, F., Miller, C. J., Miquel, R., Ogando, R. L. C., Plazas, A. A., Sanchez, E., Scarpine, V., Schindler, R., Schubnell, M., Serrano, S., Sevilla-Noarbe, I., Sheldon, E., Smith, M., Sobreira, F., Suchyta, E., Tarle, G., Thomas, D., and Vikram, V. (2018). Dark Energy Survey Year 1 Results: Constraints on Intrinsic Alignments and their Colour Dependence from Galaxy Clustering and Weak Lensing. *ArXiv e-prints*.

Samushia, L., Reid, B. A., White, M., Percival, W. J., Cuesta, A. J., Zhao, G.-B., Ross, A. J., Manera, M., Aubourg, É., Beutler, F., Brinkmann, J., Brownstein, J. R., Dawson, K. S., Eisenstein, D. J., Ho, S., Honscheid, K., Maraston, C., Montesano, F., Nichol, R. C., Roe, N. A., Ross, N. P., Sánchez, A. G., Schlegel, D. J., Schneider, D. P., Streblyanska, A., Thomas, D., Tinker, J. L., Wake, D. A., Weaver, B. A., and Zehavi, I. (2014). The clustering of galaxies in the SDSS-III Baryon Oscillation Spectroscopic Survey: measuring growth rate and geometry with anisotropic clustering. *MNRAS*, 439:3504–3519.

Sánchez, C., Clampitt, J., Kovacs, A., Jain, B., García-Bellido, J., Nadathur, S., Gruen, D., Hamaus, N., Huterer, D., Vielzeuf, P., Amara, A., Bonnett,

C., DeRose, J., Hartley, W. G., Jarvis, M., Lahav, O., Miquel, R., Rozo, E., Rykoff, E. S., Sheldon, E., Wechsler, R. H., Zuntz, J., Abbott, T. M. C., Abdalla, F. B., Annis, J., Benoit-Lévy, A., Bernstein, G. M., Bernstein, R. A., Bertin, E., Brooks, D., Buckley-Geer, E., Carnero Rosell, A., Carrasco Kind, M., Carretero, J., Crocce, M., Cunha, C. E., D'Andrea, C. B., da Costa, L. N., Desai, S., Diehl, H. T., Dietrich, J. P., Doel, P., Evrard, A. E., Fausti Neto, A., Flaugher, B., Fosalba, P., Frieman, J., Gaztanaga, E., Gruendl, R. A., Gutierrez, G., Honscheid, K., James, D. J., Krause, E., Kuehn, K., Lima, M., Maia, M. A. G., Marshall, J. L., Melchior, P., Plazas, A. A., Reil, K., Romer, A. K., Sanchez, E., Schubnell, M., Sevilla-Noarbe, I., Smith, R. C., Soares-Santos, M., Sobreira, F., Suchyta, E., Tarle, G., Thomas, D., Walker, A. R., and Weller, J. (2016). Cosmic Voids and Void Lensing in the Dark Energy Survey Science Verification Data. *ArXiv e-prints:1605.03982*.

Schaap, W. E. (2007). *DTFE: the Delaunay Tessellation Field Estimator*. PhD thesis, Kapteyn Astronomical Institute <EMAIL>w_schaap@live.nl</EMAIL>.

Schlegel, D. J., Finkbeiner, D. P., and Davis, M. (1998). Maps of Dust Infrared Emission for Use in Estimation of Reddening and Cosmic Microwave Background Radiation Foregrounds. *ApJ*, 500:525–553.

Schneider, M. D. and Bridle, S. (2010). A halo model for intrinsic alignments of galaxy ellipticities. *MNRAS*, 402:2127–2139.

Schneider, P. (2005). Weak Gravitational Lensing. *ArXiv Astrophysics e-prints*.

Schneider, P. and Seitz, C. (1995). Steps towards nonlinear cluster inversion through gravitational distortions. 1: Basic considerations and circular clusters. *AAP*, 294:411–431.

Scoccimarro, R. (2004). Redshift-space distortions, pairwise velocities, and nonlinearities. *Physical Review D*, 70:083007.

Scoville, N., Aussel, H., Brusa, M., Capak, P., Carollo, C. M., Elvis, M., Giavalisco, M., Guzzo, L., Hasinger, G., Impey, C., Kneib, J.-P., LeFevre, O., Lilly, S. J., Mobasher, B., Renzini, A., Rich, R. M., Sanders, D. B., Schinnerer, E., Schminovich, D., Shopbell, P., Taniguchi, Y., and Tyson, N. D. (2007). The Cosmic Evolution Survey (COSMOS): Overview. *ApJS*, 172:1–8.

Seitz, C. and Schneider, P. (1997). Steps towards nonlinear cluster inversion through gravitational distortions. III. Including a redshift distribution of the sources. *AAP*, 318:687–699.

Seitz, S., Schneider, P., and Ehlers, J. (1994). Light propagation in arbitrary spacetimes and the gravitational lens approximation. *Classical and Quantum Gravity*, 11:2345–2373.

Seljak, U. (2000). Analytic model for galaxy and dark matter clustering. *MNRAS*, 318:203–213.

Seljak, U. and McDonald, P. (2011). Distribution function approach to redshift space distortions. *Journal of Cosmology and Astro-Particle Physics*, 2011:039.

Sersic, J. L. (1968). *Atlas de Galaxias Australes*.

Shafieloo, A. and Clarkson, C. (2010). Model independent tests of the standard cosmological model. *Physical Review D*, 81(8):083537.

Sheldon, E. S. and Huff, E. M. (2017). Practical Weak-lensing Shear Measurement with Metacalibration. *ApJ*, 841:24.

Sheth, R. K. and van de Weygaert, R. (2004). A hierarchy of voids: much ado about nothing. *MNRAS*, 350:517–538.

Simon, P. and Hilbert, S. (2018). Scale dependence of galaxy biasing investigated by weak gravitational lensing: An assessment using semi-analytic galaxies and simulated lensing data. *AAP*, 613:A15.

Singh, S. and Mandelbaum, R. (2016). Intrinsic alignments of BOSS LOWZ galaxies - II. Impact of shape measurement methods. *MNRAS*, 457:2301–2317.

Skrutskie, M. F., Cutri, R. M., Stiening, R., Weinberg, M. D., Schneider, S., Carpenter, J. M., Beichman, C., Capps, R., Chester, T., Elias, J., Huchra, J., Liebert, J., Lonsdale, C., Monet, D. G., Price, S., Seitzer, P., Jarrett, T., Kirkpatrick, J. D., Gizis, J. E., Howard, E., Evans, T., Fowler, J., Fullmer, L., Hurt, R., Light, R., Kopan, E. L., Marsh, K. A., McCallon, H. L., Tam, R., Van Dyk, S., and Wheelock, S. (2006). The Two Micron All Sky Survey (2MASS). *AJ*, 131:1163–1183.

Slipher, V. M. (1917). Nebulae. *Proceedings of the American Philosophical Society*, 56:403–409.

Smith, A., Cole, S., Baugh, C., Zheng, Z., Angulo, R., Norberg, P., and Zehavi, I. (2017). A lightcone catalogue from the Millennium-XXL simulation. *MNRAS*, 470:4646–4661.

Smoot, G. F., Bennett, C. L., Kogut, A., Wright, E. L., Aymon, J., Boggess, N. W., Cheng, E. S., de Amici, G., Gulkis, S., Hauser, M. G., Hinshaw, G., Jackson, P. D., Janssen, M., Kaita, E., Kelsall, T., Keegstra, P., Lineweaver, C., Loewenstein, K., Lubin, P., Mather, J., Meyer, S. S., Moseley, S. H., Murdock, T., Rokke, L., Silverberg, R. F., Tenorio, L., Weiss, R., and Wilkinson, D. T. (1992). Structure in the COBE differential microwave radiometer first-year maps. , 396:L1–L5.

Sollerman, J., Mörtsell, E., Davis, T. M., Blomqvist, M., Bassett, B., Becker, A. C., Cinabro, D., Filippenko, A. V., Foley, R. J., Frieman, J., Garnavich, P., Lampeitl, H., Marriner, J., Miquel, R., Nichol, R. C., Richmond, M. W., Sako, M., Schneider, D. P., Smith, M., Vanderplas, J. T., and Wheeler, J. C. (2009). First-Year Sloan Digital Sky Survey-II (SDSS-II) Supernova Results: Constraints on Nonstandard Cosmological Models. *ApJ*, 703:1374–1385.

Springel, V., White, S. D. M., Jenkins, A., Frenk, C. S., Yoshida, N., Gao, L., Navarro, J., Thacker, R., Croton, D., Helly, J., Peacock, J. A., Cole, S., Thomas, P., Couchman, H., Evrard, A., Colberg, J., and Pearce, F. (2005). Simulations of the formation, evolution and clustering of galaxies and quasars. *Nature*, 435:629–636.

Starobinsky, A. A. (1980). A new type of isotropic cosmological models without singularity. *Physics Letters B*, 91:99–102.

Sutter, P. M., Carlesi, E., Wandelt, B. D., and Knebe, A. (2015). On the observability of coupled dark energy with cosmic voids. *MNRAS*, 446:L1–L5.

Sutter, P. M., Lavaux, G., Wandelt, B. D., and Weinberg, D. H. (2012a). A First Application of the Alcock-Paczynski Test to Stacked Cosmic Voids. *ApJ*, 761:187.

Sutter, P. M., Lavaux, G., Wandelt, B. D., and Weinberg, D. H. (2012b). A Public Void Catalog from the SDSS DR7 Galaxy Redshift Surveys Based on the Watershed Transform. *ApJ*, 761:44.

Sutter, P. M., Pisani, A., Wandelt, B. D., and Weinberg, D. H. (2014). A measurement of the Alcock-Paczyński effect using cosmic voids in the SDSS. *MNRAS*, 443:2983–2990.

Suzuki, N., Rubin, D., Lidman, C., Aldering, G., Amanullah, R., Barbary, K., Barrientos, L. F., Botyanszki, J., Brodwin, M., Connolly, N., Dawson, K. S., Dey, A., Doi, M., Donahue, M., Deustua, S., Eisenhardt, P., Ellingson, E., Faccioli, L., Fadeyev, V., Fakhouri, H. K., Fruchter, A. S., Gilbank, D. G., Gladders, M. D., Goldhaber, G., Gonzalez, A. H., Goobar, A., Gude, A., Hattori, T., Hoekstra, H., Hsiao, E., Huang, X., Ihara, Y., Jee, M. J., Johnston, D., Kashikawa, N., Koester, B., Konishi, K., Kowalski, M., Linder, E. V., Lubin, L., Melbourne, J., Meyers, J., Morokuma, T., Munshi, F., Mullis, C., Oda, T., Panagia, N., Perlmutter, S., Postman, M., Pritchard, T., Rhodes, J., Ripoche, P., Rosati, P., Schlegel, D. J., Spadafora, A., Stanford, S. A., Stanishev, V., Stern, D., Strovink, M., Takanashi, N., Tokita, K., Wagner, M., Wang, L., Yasuda, N., Yee, H. K. C., and Supernova Cosmology Project, T. (2012). The Hubble Space Telescope Cluster Supernova Survey. V. Improving the Dark-energy Constraints above z > 1 and Building an Early-type-hosted Supernova Sample. *ApJ*, 746(1):85.

Takada, M., Ellis, R. S., Chiba, M., Greene, J. E., Aihara, H., Arimoto, N., Bundy, K., Cohen, J., Doré, O., Graves, G., Gunn, J. E., Heckman, T., Hirata, C. M., Ho, P., Kneib, J.-P., Le Fèvre, O., Lin, L., More, S., Murayama, H., Nagao, T., Ouchi, M., Seiffert, M., Silverman, J. D., Sodré, L., Spergel, D. N., Strauss, M. A., Sugai, H., Suto, Y., Takami, H., and Wyse, R. (2014). Extragalactic science, cosmology, and Galactic archaeology with the Subaru Prime Focus Spectrograph. , 66:R1.

Takahashi, R., Sato, M., Nishimichi, T., Taruya, A., and Oguri, M. (2012). Revising the Halofit Model for the Nonlinear Matter Power Spectrum. *ApJ*, 761:152.

Taruya, A., Nishimichi, T., and Saito, S. (2010). Baryon acoustic oscillations in 2D: Modeling redshift-space power spectrum from perturbation theory. *Physical Review D*, 82:063522.

Taylor, E. N., Hopkins, A. M., Baldry, I. K., Brown, M. J. I., Driver, S. P., Kelvin, L. S., Hill, D. T., Robotham, A. S. G., Bland-Hawthorn, J., Jones, D. H., Sharp, R. G., Thomas, D., Liske, J., Loveday, J., Norberg, P., Peacock, J. A., Bamford, S. P., Brough, S., Colless, M., Cameron, E., Conselice, C. J., Croom, S. M., Frenk, C. S., Gunawardhana, M., Kuijken, K., Nichol, R. C., Parkinson, H. R., Phillipps, S., Pimbblet, K. A., Popescu, C. C., Prescott, M., Sutherland, W. J., Tuffs, R. J., van Kampen, E., and Wijesinghe, D. (2011). Galaxy And Mass Assembly (GAMA): stellar mass estimates. *MNRAS*, 418:1587–1620.

Taylor, W., Cirasuolo, M., Afonso, J., Carollo, M., Evans, C., Flores, H., Maiolino, R., Paltani, S., Vanzi, L., Abreu, M., Amans, J.-P., Atkinson, D., Barrett, J., Beard, S., Béchet, C., Black, M., Boettger, D., Brierley, S., Buscher, D., Cabral, A., Cochrane, W., Coelho, J., Colling, M., Conzelmann, R., Dalessio, F., Dauvin, L., Davidson, G., Drass, H., Dünner, R., Fairley, A., Fasola, G., Ferruzzi, D., Fisher, M., Flores, M., Garilli, B., Gaudemard, J., Gonzalez, O., Guinouard, I., Gutierrez, P., Hammersley, P., Haigron, R., Haniff, C., Hayati, M., Ives, D., Iwert, O., Laporte, P., Lee, D., Li Causi, G., Luco, Y., Macleod, A., Mainieri, V., Maire, C., Melse, B.-T., Nix, J., Oliva, E., Oliveira, A., Origlia, L., Parry, I., Pedichini, F., Piazzesi, R., Rees, P., Reix, F., Rodrigues, M., Rojas, F., Rota, S., Royer, F., Santos, P., Schnell, R., Shen, T.-C., Sordet, M., Strachan, J., Sun, X., Tait, G., Torres, M., Tozzi, A., Tulloch, S., Navarro, Á. V., Von Dran, L., Waring, C., Watson, S., Woodward, B., and Yang, Y. (2018). Rising MOONS: an update on the VLT's next multi-object spectrograph as it begins to grow. In *Ground-based and Airborne Instrumentation for Astronomy VII*, volume 10702 of *Society of Photo-Optical Instrumentation Engineers (SPIE) Conference Series*, page 107021G.

Tinker, J. L. and Conroy, C. (2009). The Void Phenomenon Explained. *ApJ*, 691:633–639.

Tisserand, P., Le Guillou, L., Afonso, C., Albert, J. N., Andersen, J., Ansari, R., Aubourg, É., Bareyre, P., Beaulieu, J. P., Charlot, X., Coutures, C., Ferlet, R., Fouqué, P., Glicenstein, J. F., Goldman, B., Gould, A., Graff, D., Gros, M., Haissinski, J., Hamadache, C., de Kat, J., Lasserre, T., Lesquoy, É., Loup, C., Magneville, C., Marquette, J. B., Maurice, É., Maury, A., Milsztajn, A., Moniez, M., Palanque-Delabrouille, N., Perdereau, O., Rahal, Y. R., Rich, J., Spiro, M., Vidal-Madjar, A., Vigroux, L., Zylberajch, S., and EROS-2 Collaboration (2007). Limits on the Macho content of the Galactic Halo from the EROS-2 Survey of the Magellanic Clouds. *AAP*, 469:387–404.

Troxel, M. A., MacCrann, N., Zuntz, J., Eifler, T. F., Krause, E., Dodelson, S., Gruen, D., Blazek, J., Friedrich, O., Samuroff, S., Prat, J., Secco, L. F., Davis, C., Ferté, A., DeRose, J., Alarcon, A., Amara, A., Baxter, E., Becker, M. R., Bernstein, G. M., Bridle, S. L., Cawthon, R., Chang, C., Choi, A., De Vicente, J., Drlica-Wagner, A., Elvin-Poole, J., Frieman, J., Gatti, M., Hartley, W. G., Honscheid, K., Hoyle, B., Huff, E. M., Huterer, D., Jain, B., Jarvis, M., Kacprzak, T., Kirk, D., Kokron, N., Krawiec, C., Lahav, O., Liddle, A. R., Peacock, J., Rau, M. M., Refregier, A., Rollins, R. P., Rozo, E., Rykoff, E. S., Sánchez, C., Sevilla-Noarbe, I., Sheldon, E., Stebbins, A., Varga, T. N., Vielzeuf, P., Wang, M., Wechsler, R. H., Yanny, B., Abbott, T. M. C., Abdalla, F. B., Allam, S., Annis, J., Bechtol, K., Benoit-Lévy, A., Bertin, E., Brooks, D., Buckley-Geer, E., Burke, D. L., Carnero Rosell, A., Carrasco Kind, M., Carretero, J., Castander, F. J., Crocce, M., Cunha, C. E., D'Andrea, C. B., da Costa, L. N., DePoy, D. L., Desai, S., Diehl, H. T., Dietrich, J. P., Doel, P., Fernandez, E., Flaugher, B., Fosalba, P., García-Bellido, J., Gaztanaga, E., Gerdes, D. W., Giannantonio, T., Goldstein, D. A., Gruendl, R. A., Gschwend, J., Gutierrez, G., James, D. J., Jeltema, T., Johnson, M. W. G., Johnson, M. D., Kent, S., Kuehn, K., Kuhlmann, S., Kuropatkin, N., Li, T. S., Lima, M., Lin, H., Maia, M. A. G., March, M., Marshall, J. L., Martini, P., Melchior, P., Menanteau, F., Miquel, R., Mohr, J. J., Neilsen, E., Nichol, R. C., Nord, B., Petravick, D., Plazas, A. A., Romer, A. K., Roodman, A., Sako, M., Sanchez, E., Scarpine, V., Schindler, R., Schubnell, M., Smith, M., Smith, R. C., Soares-Santos, M., Sobreira, F., Suchyta, E., Swanson, M. E. C., Tarle, G., Thomas, D., Tucker, D. L., Vikram, V., Walker, A. R., Weller, J., and Zhang, Y. (2017). Dark Energy Survey Year 1 Results: Cosmological Constraints from Cosmic Shear. *ArXiv e-prints*.

Tully, R. B., Shaya, E. J., Karachentsev, I. D., Courtois, H. M., Kocevski, D. D., Rizzi, L., and Peel, A. (2008). Our Peculiar Motion Away from the Local Void. *ApJ*, 676:184–205.

Vaccari, M., Cappellaro, E., Covone, G., Pignata, G., Grado, L., Limatola, L., Marchetti, L., Paolillo, M., Radovich, M., Capaccioli, M., Franceschini, A., Napolitano, N., and Botticella, M. T. (2012). The SUDARE/VOICE INAF VST GT Survey. Galaxy Evolution, AGN Variability and Supernova Host Galaxies with VST. In *Science from the Next Generation Imaging and Spectroscopic Surveys*, page 49.

Vainshtein, A. I. (1972). To the problem of nonvanishing gravitation mass. *Physics Letters B*, 39:393–394.

Valdes, F., Tyson, J. A., and Jarvis, J. F. (1983). Alignment of faint galaxy images - Cosmological distortion and rotation. *ApJ*, 271:431–441.

Vale, C. and White, M. (2003). Simulating Weak Lensing by Large-Scale Structure. *ApJ*, 592:699–709.

Valentijn, E. A., McFarland, J. P., Snigula, J., Begeman, K. G., Boxhoorn, D. R., Rengelink, R., Helmich, E., Heraudeau, P., Verdoes Kleijn, G., Vermeij, R.,

Vriend, W.-J., Tempelaar, M. J., Deul, E., Kuijken, K., Capaccioli, M., Silvotti, R., Bender, R., Neeser, M., Saglia, R., Bertin, E., and Mellier, Y. (2007). Astro-WISE: Chaining to the Universe. In Shaw, R. A., Hill, F., and Bell, D. J., editors, *Astronomical Data Analysis Software and Systems XVI*, volume 376 of *Astronomical Society of the Pacific Conference Series*, page 491.

van de Weygaert, R. (1991). *Voids and the Large Scale Structure of the Universe*. PhD thesis, Leiden University.

van de Weygaert, R., editor (2002). *Proceedings 2nd Hellenic Cosmology Workshop*, volume 276. Astrophysics and Space Science Library.

van de Weygaert, R., Kreckel, K., Platen, E., Beygu, B., van Gorkom, J. H., van der Hulst, J. M., Aragón-Calvo, M. A., Peebles, P. J. E., Jarrett, T., Rhee, G., Kovač, K., and Yip, C.-W. (2011). The Void Galaxy Survey. *Astrophysics and Space Science Proceedings*, 27:17.

van de Weygaert, R. and Schaap, W. (2009). The Cosmic Web: Geometric Analysis. In Martínez, V. J., Saar, E., Martínez-González, E., and Pons-Bordería, M.-J., editors, *Data Analysis in Cosmology*, volume 665 of *Lecture Notes in Physics, Berlin Springer Verlag*, pages 291–413.

van de Weygaert, R. and van Kampen, E. (1993). Voids in Gravitational Instability Scenarios - Part One - Global Density and Velocity Fields in an Einstein - De-Sitter Universe. *MNRAS*, 263:481.

van Uitert, E., Joachimi, B., Joudaki, S., Amon, A., Heymans, C., Köhlinger, F., Asgari, M., Blake, C., Choi, A., Erben, T., Farrow, D. J., Harnois-Déraps, J., Hildebrandt, H., Hoekstra, H., Kitching, T. D., Klaes, D., Kuijken, K., Merten, J., Miller, L., Nakajima, R., Schneider, P., Valentijn, E., and Viola, M. (2018). KiDS+GAMA: cosmology constraints from a joint analysis of cosmic shear, galaxy-galaxy lensing, and angular clustering. *MNRAS*, 476(4):4662–4689.

Van Waerbeke, L., Mellier, Y., Erben, T., Cuillandre, J. C., Bernardeau, F., Maoli, R., Bertin, E., McCracken, H. J., Le Fèvre, O., Fort, B., Dantel-Fort, M., Jain, B., and Schneider, P. (2000). Detection of correlated galaxy ellipticities from CFHT data: first evidence for gravitational lensing by large-scale structures. *AAP*, 358:30–44.

Villaescusa-Navarro, F., Naess, S., Genel, S., Pontzen, A., Wandelt, B., Anderson, L., Font-Ribera, A., Battaglia, N., and Spergel, D. N. (2018). Statistical Properties of Paired Fixed Fields. *ApJ*, 867:137.

Viola, M., Cacciato, M., Brouwer, M., Kuijken, K., Hoekstra, H., Norberg, P., Robotham, A. S. G., van Uitert, E., Alpaslan, M., Baldry, I. K., Choi, A., de Jong, J. T. A., Driver, S. P., Erben, T., Grado, A., Graham, A. W., Heymans, C., Hildebrandt, H., Hopkins, A. M., Irisarri, N., Joachimi, B., Loveday, J., Miller, L., Nakajima, R., Schneider, P., Sifón, C., and Verdoes Kleijn, G. (2015). Dark matter halo properties of GAMA galaxy groups from 100 square degrees of KiDS weak lensing data. *MNRAS*, 452:3529–3550.

Vlah, Z. and White, M. (2018). Exploring redshift-space distortions in large-scale structure. *arXiv e-prints*.

Voigt, L. M. and Bridle, S. L. (2010). Limitations of model-fitting methods for lensing shear estimation. *MNRAS*, 404:458–467.

Wambsganss, J. (1998). Gravitational lensing in astronomy. *Living Reviews in Relativity*, 1(1):12.

Wang, L., Gonzalez-Perez, V., Xie, L., Cooper, A. P., Frenk, C. S., Gao, L., Hellwing, W. A., Helly, J., Lovell, M. R., and Jiang, L. (2017). The galaxy population in cold and warm dark matter cosmologies. *MNRAS*, 468:4579–4591.

Wang, L., Reid, B., and White, M. (2014). An analytic model for redshift-space distortions. *MNRAS*, 437:588–599.

Wang, Y. and Tegmark, M. (2005). Uncorrelated measurements of the cosmic expansion history and dark energy from supernovae. *Physical Review D*, 71(10):103513.

Wang, Y., Zhao, G.-B., Chuang, C.-H., Pellejero-Ibanez, M., Zhao, C., Kitaura, F.-S., and Rodriguez-Torres, S. (2018). The clustering of galaxies in the completed SDSS-III Baryon Oscillation Spectroscopic Survey: a tomographic analysis of structure growth and expansion rate from anisotropic galaxy clustering. *MNRAS*, 481:3160–3166.

Weinberg, S. (1987). Anthropic bound on the cosmological constant. *Physical Review Letters*, 59:2607–2610.

Weinberg, S. (1989). The cosmological constant problem. *Reviews of Modern Physics*, 61:1–23.

White, M., Hernquist, L., and Springel, V. (2002). Simulating the Sunyaev-Zeldovich Effect(s): Including Radiative Cooling and Energy Injection by Galactic Winds. *ApJ*, 579:16–22.

White, M., Song, Y.-S., and Percival, W. J. (2009). Forecasting cosmological constraints from redshift surveys. *MNRAS*, 397:1348–1354.

Will, C. M. (2014). The Confrontation between General Relativity and Experiment. *Living Reviews in Relativity*, 17:4.

Wittman, D. M., Tyson, J. A., Kirkman, D., Dell'Antonio, I., and Bernstein, G. (2000). Detection of weak gravitational lensing distortions of distant galaxies by cosmic dark matter at large scales. , 405:143–148.

Wojtak, R., Powell, D., and Abel, T. (2016). Voids in cosmological simulations over cosmic time. *MNRAS*, 458:4431–4442.

Yang, L. F., Neyrinck, M. C., Aragón-Calvo, M. A., Falck, B., and Silk, J. (2015). Warmth elevating the depths: shallower voids with warm dark matter. *MNRAS*, 451:3606–3614.

Zehavi, I., Zheng, Z., Weinberg, D. H., Blanton, M. R., Bahcall, N. A., Berlind, A. A., Brinkmann, J., Frieman, J. A., Gunn, J. E., Lupton, R. H., Nichol, R. C., Percival, W. J., Schneider, D. P., Skibba, R. A., Strauss, M. A., Tegmark, M., and York, D. G. (2011). Galaxy Clustering in the Completed SDSS Redshift Survey: The Dependence on Color and Luminosity. *APJ*, 736:59.

Zeldovich, I. B., Einasto, J., and Shandarin, S. F. (1982). Giant voids in the universe. , 300:407–413.

Zel'dovich, Y. B. (1970). Gravitational instability: An approximate theory for large density perturbations. *AAP*, 5:84–89.

Zhao, C., Chuang, C.-H., Liang, Y., Kitaura, F.-S., Vargas-Magaña, M., Tao, C., Pellejero-Ibanez, M., and Yepes, G. (2018). Improving baryon acoustic oscillation measurement with the combination of cosmic voids and galaxies. *arXiv e-prints*.

Zhao, G.-B., Giannantonio, T., Pogosian, L., Silvestri, A., Bacon, D. J., Koyama, K., Nichol, R. C., and Song, Y.-S. (2010). Probing modifications of general relativity using current cosmological observations. *Physical Review D*, 81(10):103510.

Zheng, Z., Berlind, A. A., Weinberg, D. H., Benson, A. J., Baugh, C. M., Cole, S., Davé, R., Frenk, C. S., Katz, N., and Lacey, C. G. (2005). Theoretical Models of the Halo Occupation Distribution: Separating Central and Satellite Galaxies. *ApJ*, 633:791–809.

Zivick, P., Sutter, P. M., Wandelt, B. D., Li, B., and Lam, T. Y. (2015). Using cosmic voids to distinguish f(R) gravity in future galaxy surveys. *MNRAS*, 451:4215–4222.

Zuntz, J., Kacprzak, T., Voigt, L., Hirsch, M., Rowe, B., and Bridle, S. (2013). IM3SHAPE: a maximum likelihood galaxy shear measurement code for cosmic gravitational lensing. *MNRAS*, 434:1604–1618.

Zuntz, J., Sheldon, E., Samuroff, S., Troxel, M. A., Jarvis, M., MacCrann, N., Gruen, D., Prat, J., Sánchez, C., Choi, A., Bridle, S. L., Bernstein, G. M., Dodelson, S., Drlica-Wagner, A., Fang, Y., Gruendl, R. A., Hoyle, B., Huff, E. M., Jain, B., Kirk, D., Kacprzak, T., Krawiec, C., Plazas, A. A., Rollins, R. P., Rykoff, E. S., Sevilla-Noarbe, I., Soergel, B., Varga, T. N., Abbott, T. M. C., Abdalla, F. B., Allam, S., Annis, J., Bechtol, K., Benoit-Lévy, A., Bertin, E., Buckley-Geer, E., Burke, D. L., Carnero Rosell, A., Carrasco Kind, M., Carretero, J., Castander, F. J., Crocce, M., Cunha, C. E., D'Andrea, C. B., da Costa, L. N., Davis, C., Desai, S., Diehl, H. T., Dietrich, J. P., Doel, P., Eifler, T. F., Estrada, J., Evrard, A. E., Neto, A. F., Fernandez, E., Flaugher,

B., Fosalba, P., Frieman, J., García-Bellido, J., Gaztanaga, E., Gerdes, D. W., Giannantonio, T., Gschwend, J., Gutierrez, G., Hartley, W. G., Honscheid, K., James, D. J., Jeltema, T., Johnson, M. W. G., Johnson, M. D., Kuehn, K., Kuhlmann, S., Kuropatkin, N., Lahav, O., Li, T. S., Lima, M., Maia, M. A. G., March, M., Martini, P., Melchior, P., Menanteau, F., Miller, C. J., Miquel, R., Mohr, J. J., Neilsen, E., Nichol, R. C., Ogando, R. L. C., Roe, N., Romer, A. K., Roodman, A., Sanchez, E., Scarpine, V., Schindler, R., Schubnell, M., Smith, M., Smith, R. C., Soares-Santos, M., Sobreira, F., Suchyta, E., Swanson, M. E. C., Tarle, G., Thomas, D., Tucker, D. L., Vikram, V., Walker, A. R., Wechsler, R. H., and Zhang, Y. (2018). Dark Energy Survey Year 1 results: weak lensing shape catalogues. *MNRAS*, 481:1149–1182.

Zwicky, F. (1933). Die Rotverschiebung von extragalaktischen Nebeln. *Helvetica Physica Acta*, 6:110–127.

Zwicky, F. (1937). On the Masses of Nebulae and of Clusters of Nebulae. *ApJ*, 86:217.